Tsunami wave interaction with a coastal structure. Focus on the Tohoku tsunami case and the flip-through impact

Manuel Martin-Medina

N° attribué par la bibliothèque

THÈSE

PRÉSENTÉE À

L'UNIVERSITÉ DE PAU ET DES PAYS DE L'ADOUR

ÉCOLE DOCTORALE DES SCIENCES EXACTES ET DE LEURS APPLICATIONS

PAR

Manuel Martin-Medina

POUR OBTENIR LE GRADE DE

DOCTEUR

Spécialité : Génie Civil

20 décembre 2017

Tsunami wave interaction with a coastal structure. Focus on the Tohoku tsunami case and the flip-through impact.

Après avis de :

Hocine Oumeraci, Emeritus Professor, TU Braunschweig	.....	Rapporteur
Olivier Kimmoun, Associate Professor, HDR, École Centrale Marseille	.....	Rapporteur

Devant la commission d'examen formée de :

Stéphane Abadie, Full Professor, UPPA	.....	Directeur de thése
Denis Morichon, Associate Professor, UPPA	.....	Co-Directeur de thése
Pierre Lubin, Full Professor, I2M	.....	Examinateur
Philippe Bonneton, CNRS research director	.....	Examinateur
Yves-Marie Scolan, Associate Professor, HDR	.....	Examinateur

Contents

List of Figures

List of Tables

List of Symbols

α	Free surface inclination
G_0	Constant value of the pressure at h_1
I	Integral of the pressure profile on the wall
$R(t)$	Resulting horizontal force
s_p	Vertical velocity of the first point of the pressure distribution
α_m	Maximum elevation slope
β	Bottom slope
η	Free surface height
γ	Breaking parameter
μ	Friction coefficient
ϕ	Porosity
ρ_s	Caisson density
ρ_w	Water density
a_i	First tsunami wave amplitude
a_u	First undulation bore amplitude
c_b	Bore celerity
F_h	Horizontal force
F_u	Vertical force
Fr	Froude number nomenclature
$G(s)$	Pressure profile due to a water wedge impact in the self-similar plan
h_0	Initial free surface before the FTI
h_1	Free surface at the begining of FTI
h_2	Maximal height reached by the FTI
h_c, h	Breakwater caisson height
H_w	Wave height generating a FTI
k	Intrinsic permeability
m	Caisson mass

m_a	hydrodynamic added mass
M_e	Moment about the heel of the caisson
M_h	Horizontal moment
M_u	Vertical moment
M_w	Stabilizing moment
p_e	Bearing pressure at the heel
$P_{imp}(z,t)$	Dynamic pressure distribution generated by a water wedge impact
$P_{sub}(z)$	Pressure distribution on the submerged part of caissons generated by a water wedge impact
S	Total sliding of a caisson breakwater submitted to water wedges
s	Position in the self-similar plan
T	Wave period
t_p	Time of the force increase
$U(t)$	Uplift force generated by a water wedge impact
u_0	Average fluid velocity before the bore arrives
V_0	Horizontal velocity of water wedge
V_c	Solitary wave celerity
$v_x(t)$	Caisson velocity
W	Dry weight of the caisson
W_e	Normal force of the caisson
NRMSD	Normalized root-mean-square deviation
S.F.	Safety Factors regarding sliding
S.F.m	Safety Factors regarding overturning

Résumé

Lors du tsunami de Tohoku en 2011, des relevés de terrain sur les côtes japonaises ont montré la fragilité des structures côtières, où le plus grand brise-lames du monde (brise-lames de Kamaishi) a été fortement endommagé dû à cet événement. Dans ce doctorat, l'objectif est d'étudier l'interaction entre les brise-lames , les structures côtières les plus communes protégeant les zones urbaines et les entrées des ports, et les vagues, en particulier les tsunamis.

Dans la première partie de ce travail, la transformation du tsunami en bore ondulaire dans les zones côtières est étudiée numériquement avec le code de calcul BOSZ (modèle Boussinesq). Les résultats montrent que la deuxième vague générée par le tsunami de Tohoku s'est transformée en un bore ondulaire. En revanche, la première vague n'était pas assez cambrée pour permettre une telle transformation. Les forces et les moments dus aux vagues ainsi que la contrainte normale appliquée par la base arrière du caisson sur le sol de fondation sont calculés à l'aide de deux modèles numériques différents: BOSZ et THETIS (modèle Navier-Stokes). Les résultats de BOSZ sont comparés avec THETIS pour l'interaction tsunami-structure. L'étude d'impact est réalisée à relativement grande échelle dans le but d'obtenir une première estimation des efforts d'un tsunami.

Par la suite, une expérience numérique utilisant le modèle THETIS a été réalisée pour étudier les impacts du type flip-through sur des brise-lames. Ces impacts de vagues sans air emprisonné sont considérés comme le type d'impact le plus extrême dans la littérature (e.g. Cooker & Peregrine (1992), Hofland et al. (2011)). L'influence de l'inclinaison de l'interface sur la dynamique d'impact et les pressions générées sont analysées dans une configuration de brise-lames réelle. Le modèle d'onde solitaire est utilisé pour générer trois impacts caractéristiques du type flip-through: peu cambré, moyen et très cambré. Le champ de vitesses et la pression à l'intérieur de la fondation sont également étudiés dans cette partie. Les forces horizontales et verticales appliquées sur le caisson sont estimées en intégrant les distributions de pression données par THETIS.

La dernière partie de ces travaux montre la stabilité des caissons de brise-lames soumis à des impacts du type flip-through, qui sont ici assimilés à un jet triangulaire (e.g. Cumberbatch (1960), Kihara et al. (2015)). Cette approche simple permet de formuler un modèle semi-analytique pour prédire le mouvement des caissons dû à ce type d'impacts. Après validation avec des simulations numériques, la méthode du jet triangulaire permet d'obtenir des informations sur les forces, la durée du mouvement et le déplacement total en fonction des caractéristiques de la vague et des dimensions du caisson du brise-lames impacté.

Abstract

During the Tohoku tsunami in 2011, field surveys of the east coast of Japan showed the weakness of coastal defences, as even the world largest tsunami breakwater (Kamaishi) almost completely collapsed due to this event. In this PhD, the aim is to investigate the interaction between breakwaters, the most common offshore coastal structures protecting urban areas and harbour entries, and waves and especially tsunami waves.

In the first part of the work, the generation of undular bores in the near-shore area of Sendai during the Tohoku event is numerically investigated with the numerical model BOSZ (Boussinesq-type model). It is shown that the second wave, which stroke the coast during this event, transformed into an undular bore, whereas the first wave did not due to steepness differences. Tsunami loads, moments and bearing stress applied on the offshore breakwater of the Soma Port are calculated using two models: BOSZ and THETIS (Navier-Stokes VOF model). BOSZ results are compared to THETIS for the tsunami wave-breakwater interaction. The impact study is carried out at a relatively large scale aiming to have a first estimation of tsunami efforts.

Then, a numerical experiment using THETIS is carried out to investigate flip-through impacts on vertical breakwaters. This non-aerated wave impact is considered as the most severe type of impact in the literature (e.g. Cooker & Peregrine (1992), Hofland et al. (2011)) in terms of maximum pressure generated. The influence of the front interface on the impact dynamics and the pressure induced is analysed in a realistic breakwater configuration. Solitary waves are used to obtain three characteristic flip-through impacts involving least steep, medium steep and steepest wave front. The flow field and pressure inside the porous rubble mound are then investigated as well as horizontal and uplift forces applied on the breakwater caisson.

The last part of this study is devoted to the stability of breakwater caissons submitted to flip-through impacts. The latter are here assimilated to water wedges (e.g. Cumberbatch (1960), Kihara et al. (2015)). This simple approach allows to formulate a semi-analytical model to predict caisson motion due to this type of impacts. After validation with numerical results, the water wedge method gives rich informations about forces, motion duration and sliding distance depending on the wave impact characteristics and breakwater caisson dimensions.

Acknowledgements

This PhD has been carried out at the SIAME laboratory of the University of Pau et Pays de l'Adour (UPPA) under the supervision of Stéphane Abadie and Denis Morichon. This work started on September 2014 and it has been completed in a bit more of three years (December 2017).

The PIA RSNR French program TANDEM (Grant No.: ANR-11-RSNR-00023-01) funded this research. It also allowed me to meet the best researchers in France working on tsunamis. I would like to thank the TANDEM collaborators who participate actively in my PhD: BRGM (Sylvestre Leroy, Rodrigo Pedreros, Anne Lemoine), Principia (Richard Marcer, Kevin Pons) and INRIA (Mario Ricchiuto, Maria Kazolea). The FP7 EU research program ASTARTE (Grant No.:603839) is acknowledged for funding my participation in the laboratory experiments carried out by IH Cantabria where a composite breakwater is under tsunami attack. Mauricio González and Iñigo Aniel-Quiroga are thanked for their good reception during my stays in Santander.

First of all, I would like to acknowledge Pr. Hocine Oumeraci and Dr. Olivier Kimmoun for accepting to correct my manuscript and for their valuable remarks. I would also like to thank the jury president Pr. Pierre Lubin and the rest of members of the jury Dr. Philippe Bonneton and Dr. Yves-Marie Scolan. Of course, special mention goes to my supervisors Stéphane and Denis for their support, motivation, help and rich scientific discussions. This has been indispensable to accomplish this research work. Apart from work, I appreciate very much their friendship with many great moments. I want to thank Volker Roeber and Jeremy Bricker for their advices and guidance on the numerical study of the Tohoku tsunami in Soma port.

During these three years at the SIAME laboratory, I have to underline the professionalism and human values of all my colleagues. Above all, I thank my office mates: Cyril for giving me the throne of Flip-through, Benoît for the best "cannelés" of the world, Iñaki for the cooking-football lessons, Olivier N. for keeping me informed, Beñat for the notions of Euskera, Lucie for showing me that Le Mans is not only a 24 hours car race, Serge for our rugby-NBA-cycling conversations, Florian B. for his help as Master of Python and Sophie for the fishing tales. I want also to thank to the "Others": Walter, Hatem, Thomas, Lionel, Hui and Alessia; and the new doctorates Delphine and Amaia. I would like to mention the support of the whole family of ISA BTP engineering school.

Last but most important, I would like to thank my parents, my sister and my brother. Maina, You+Me, I can not thank you enough for all the magic.

Chapter 1

Introduction

This PhD thesis presents a part of the research carried out in the Risks and Structure group of SIAME laboratory. The aim of this work is to improve the current knowledge on tsunami impact on offshore vertical breakwaters.

Tsunamis are very destructive and unusual events that might impact several coastal areas in the world at the same time. The catastrophic effects of the Boxing day tsunami in 2004 and specially the Tohoku tsunami in 2011 in Japan illustrated the weakness of coastal structures submitted to tsunami wave impacts. The March 11 in 2011, an earthquake magnitude 9.0 strikes east of Sendai coast triggering the largest tsunami observed until now. This event caused large human and economic losses, and a major accident in the Daiichi nuclear power plant of Fukushima. The PIA RSNR TANDEM project (Tsunamis en Atlantique et Manche: Définition des effets par modélisation), which funds this PhD, has been established after this event in order to assess the effects of a tsunami on the French coasts (Atlantic and De La Manche). In the framework of this project, this thesis focuses on the study of tsunami wave impacts and interaction with vertical breakwaters protecting urban coastal areas.

1.1 Tsunami propagation on near-shore areas

Tsunami are composed of several waves which have been generated by a sudden elevation/depression of the ocean bottom or a submarine landslide. This induces a variation of the free surface that becomes the initial tsunami wave. This wave is characterized by a large length compared to depth. The shape of a tsunami wave approaching the coast depends directly on the shore characteristics (depth, shore slope, etc.), amplitude and

period of the wave. We focus on the two latest tsunami (in 2004 and 2011) because of the quantity of available data. In the Indian Ocean tsunami, the wave propagated towards several countries (Indonesia, Sri Lanka, India, Malaysia, etc.) presenting different shapes (Glimsdal et al. (2006), Horrillo et al. (2006) and Grue et al. (2008)) ranging from undular bore to flooding events (fig.1.1). In the Tohoku tsunami, the event was very well documented with measurements along the east coast of Japan and video observations at the shore (Mori & Takahashi (2012) and Mikami et al. (2012)).

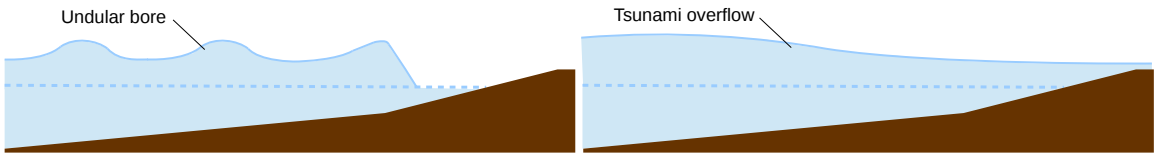

Figure 1.1: Shapes of tsunami waves arriving to the coast: undular bore (left) and overflow (right).

During the Indian Ocean tsunami, Glimsdal et al. (2006) numerically studied the tsunami propagation finding that flooding overflow events were observed in areas near to the source. In contrast, when the tsunami propagated in shallow waters, undular bores appeared as the one observed in Thailand (fig.1.2). This was also confirmed by the numerical simulations carried out in Grue et al. (2008), where the formation and propagation of undular bores were studied in the strait of Malacca.

Focusing on the Japanese tsunami, a fast flooding event was observed in the Sanriku coast (fig.1.3) which is characterized by the presence of very steep and narrow bays (Mori & Takahashi (2012)). This bathymetry shape does not induce significant changes in the tsunami approaching the coast, which means that very long waves that were propagating offshore will come in onshore with similar characteristics (length of several kms and period of 10-20 min).

Murashima et al. (2012) and Baba et al. (2015) showed that undular bores were observed near the Sendai Bay coast. For instance, in Sendai City, it was recorded from the helicopter that 10-20 short waves were riding on top of the tsunami (fig.1.4). The work of Murashima et al. (2012) showed that the period and length of these short waves were respectively $10-14s$ and $100-300m$. In contrast to the Sanriku coast, Sendai Bay is a large flat region which favours tsunami transformation into an undular bore.

Figure 1.2: Undular bore hitting the coast of Thailand during the Indian Ocean tsunami. Copyright by Anders Grawin, 2006.

1.2 Interaction between coastal structures and tsunamis

In the case of the Tohoku tsunami, Japan was a well prepared country to face such a catastrophic event. Urban areas were protected by breakwaters, dykes and seawalls. Some of them designed to mitigate the destructive effects of tsunamis. Nevertheless, many of these coastal structures have been partially or totally damaged after the Tohoku tsunami.

Mikami et al. (2012), Suppasri et al. (2012) and Mori et al. (2013) agreed that the effectiveness of coastal protection structures depended on the location. Mikami et al. (2012) carried out a field survey that can be divided in two parts: the rias coastal area of the Sanriku coast and the coastal plain area of the Sendai Bay. In the rias coastal area, the authors showed that tsunami heights were higher than $10m$ inundating the inner part of the rias. Due to the steep bathymetry, the long waves did not generate violent impacts and the arrival of tsunami looked like more as a fast tide that started to overflow the protection structures. The most populated bays in this area are often protected by tsunami breakwaters which allowed to mitigate damages resisting partially the tsunami overflow and reflecting part of the wave as shown in Mori et al. (2013) for the case of Kamaishi Bay. But some villages, protected by wind waves coastal structures (offshore

Figure 1.3: Tsunami overflow above a coastal seawall in Sanriku coast during the Tohoku tsunami in 2011.

breakwater or onshore seawalls), were totally destroyed by the effects of tsunami overflow as in Minami-Sanriku or Onawaga (Suppasri et al. (2012), Mikami et al. (2012)).

In the southern part of plains, where the propagation of undular bore were observed, inundation heights were between $5-10m$ and the tsunami bore penetrated several kms inland. The Sendai plain, considered as a place with low tsunami risk in Japan, was protected against storms by coastal levees built along the shore (Mano et al. (2013)). These structures, usually of $6m$ or $7m$ high, were damaged by the impact of undulations and overtopped by the tsunami body without avoiding flooding of inland urban areas (Suppasri et al. (2012)). The breakwaters protecting some important spots of Sendai Bay, as the port of Soma and the Fukushima Daiichi nuclear power station, also failed to mitigate the catastrophic effects of the tsunami. Large damages and even a nuclear incident were reported after the tsunami (Tsimopoulou (2011)).

1.3 Failure mechanisms of composite breakwaters submitted to tsunami waves

After the tsunami in 2011, different failure mechanisms of coastal protection structures were reported. Among them, motion of caissons and seawall parapets, scouring due

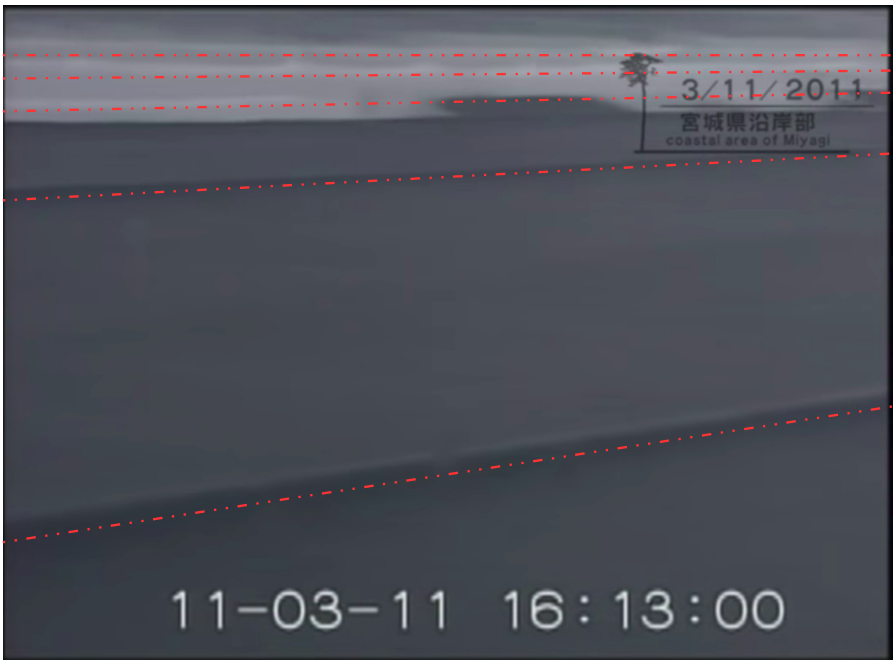

Figure 1.4: Tsunami undular bore propagating towards the shore recorded in helicopter video.

to overtopping or destabilization of rubble mound foundations were the most frequent. In this work, the scope is put on the rupture mechanism of primary coastal defences that are first impacted when tsunamis arrive to the coast: offshore vertical breakwaters (fig.1.5). These structures are built offshore protecting the entry of harbors from storm waves and tsunamis. They are composed of concrete caissons placed over porous rubble mound foundations.

The failure mechanisms of offshore breakwaters (fig. 1.6) are identified in Oumeraci (1994) and Takahashi et al. (2001): Motion of caissons, global stability and scouring of the rubble mound.

The arrival of the Tohoku tsunami in the rias coast generated significant damages in almost all the offshore breakwaters. The field work presented in Mikami et al. (2012) examined the cases of two small bays in Sanriku coast as Onagawa or Takenoura, where ports were protected by composite breakwaters designed for wind waves. When these breakwaters were submitted to the Tohoku tsunami attack, many caissons slid and failed due to the large forces. The reduction of tsunami inundation heights inside the bays was minimum.

In the Sendai plain, the southern part of the area impacted by the tsunami, caisson

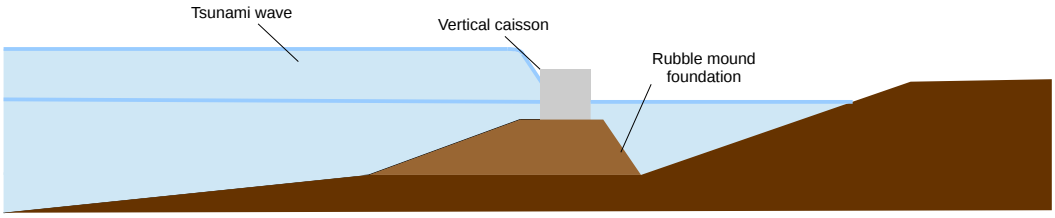

Figure 1.5: Coastal structures studied in this work: Offshore composite breakwater composed of a vertical caisson placed over a porous rubble mound.

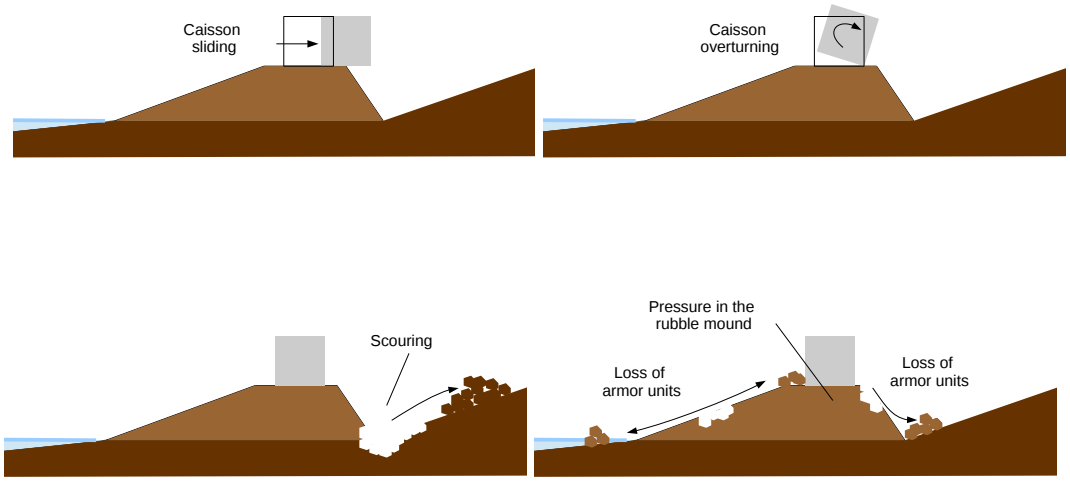

Figure 1.6: Failure mechanisms of offshore breakwaters: Sliding and tilting of caissons, global stability and scouring of rubble mound foundations.

sliding was also reported as a failure mechanism. In the ports of Ishinomaki and Sendai City, some of the caissons were partially displaced, but in general the breakwaters resisted well to the impact. This was not the case in the port of Soma. The field work carried out by Tsimopoulou (2011) showed large damages in the Soma offshore breakwater designed for storm waves (fig.1.7). Only a few caissons (of 546 in total) remained in place and the rest of them were displaced and totally or partially inundated.

Even the largest offshore breakwater in the world located in Kamaishi Bay was destabilised due to such event (fig.1.8). The failure mechanism of this breakwater, designed for tsunami mitigation, has been investigated in Arikawa et al. (2012). The authors carried out laboratory experiments and numerical simulations to find the causes of the breakwater collapse. This study concluded that the failure was caused by the difference

Figure 1.7: Caisson displaced in the offshore breakwater of the Port of Soma (from Tsimopoulou (2011)).

of water level between the ocean and port side during a long period of time. The scouring in the back side of the caissons was also identified as a phenomena that weakens the rubble mound breakwater. In Bricker et al. (2013), excessive bearing stress in the rubble mound was also found to be another failure cause.

Figure 1.8: Damages in the north part of the Kamaishi breakwater.

1.4 Study of tsunami impacts and similarities to common wave impacts

At Sanriku coast, Arikawa et al. (2012) and Bricker et al. (2013) showed that the main stability issues of coastal structures were linked to tsunami overflowing. Impulsive loads generated by tsunami impact were not reported as a major failure cause of the Kamaishi breakwater.

However, Grue et al. (2008), Madsen et al. (2008) and Mano et al. (2013) pointed out

that when the tsunami wave transforms into a bore near the coast, coastal structures are susceptible to be impacted by the broken leading front of a turbulent bore or the short waves generated on top of an undular bore. For tsunami-like undular bores, the breakwater stability might be compromised by a series of loads due to successive wave impacts as illustrated in fig.1.9. In that case, the study of single impacts is justified and needed to correctly estimate efforts on coastal structures.

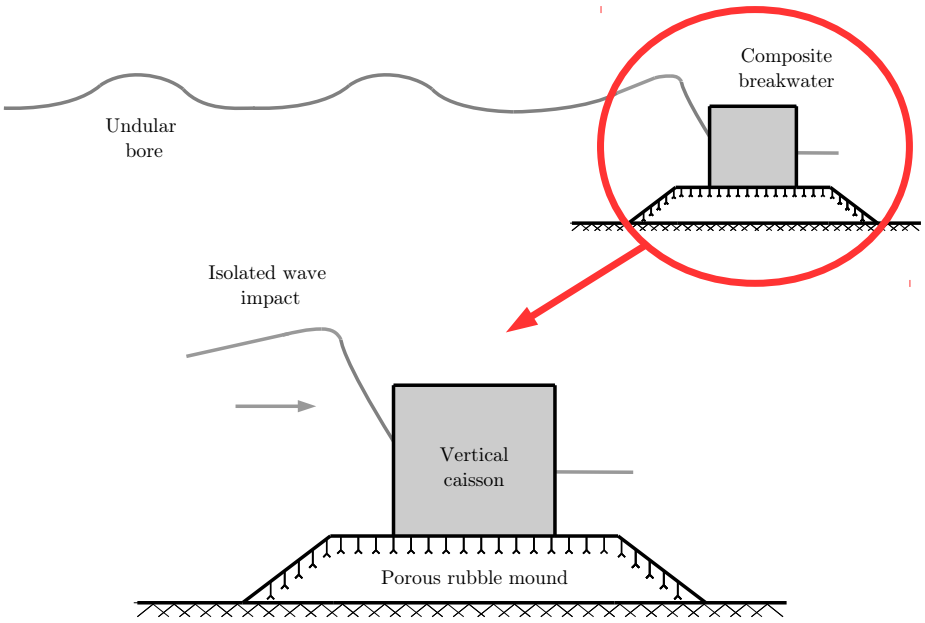

Figure 1.9: Isolated wave impact on a vertical breakwater during the arrival of a tsunami undular bore.

Focusing on the literature of common wave impacts, it has been shown that the generated pressure signals are composed by an impulsive part characterized by a very high magnitude and a short duration, followed by a longer part controlled by the pressure peak and hydrostatic pressure. Impulsive loads have been reported for storm waves (Takahashi et al. (1992), Hattori et al. (1994), Bullock et al. (2007)), but also for tsunamis (Ramsden & Raichlen (1990), Kato et al. (2006), Arikawa (2009), Nouri et al. (2010), Nistor et al. (2011)). Researchers as Bagnold (1939), Kirkgöz (1991), Hull & Müller (2002), Bullock et al. (2007) and Abadie & Mokrani (2012) agree that to know the value of impulsive pressure peak, the wave shape at impact needs to be carefully investigated. Bagnold (1939) was the first study to identify large pressures when waves impact vertical walls entrapping an air pocket during the collision. Later, in the laboratory experiments of Mitsuyasu (1966), Chan (1994) and Hull & Müller (2002), the authors observed that pressures were very sensitive to slight variations on the wave kinematic or the amount

of entrapped air. But when vertical walls are submitted to non-aerated breaking wave impacts, even larger pressures were reported in the numerical work of Cooker & Peregrine (1990) and Cooker & Peregrine (1992): the so-called flip-through phenomenon (fig.1.10).

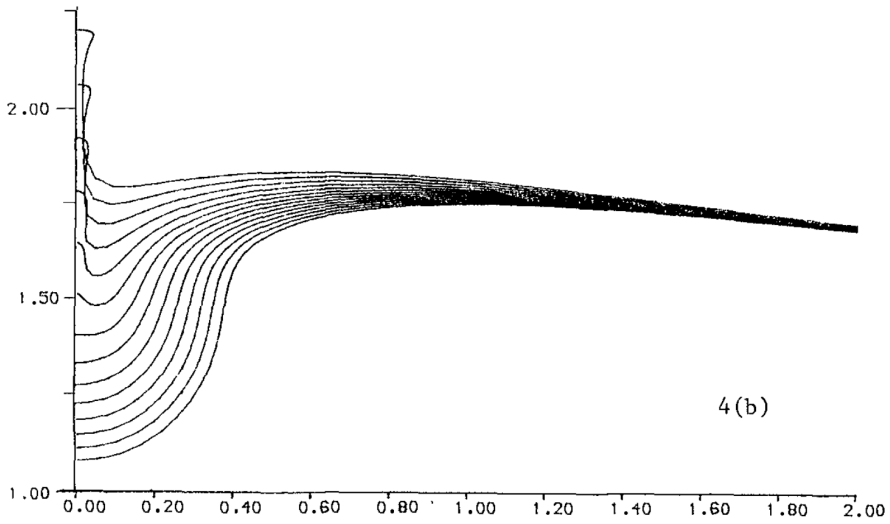

Figure 1.10: Water interface evolution during a flip-through impact (Cooker & Peregrine (1990)).

The flip-through impacts are generated without any entrapped air when the wave crest and trough flow converge at the wall and give birth to a small scale ascending jet associated to accelerations orders of magnitude larger than in other parts of the wave. Hattori et al. (1994), Bullock et al. (2007), Kaminski et al. (2009) and Hofland et al. (2011) experimentally studied several kinds of wave impact (broken wave, plunging breaking wave and non-aerated wave impacts) concluding that the most extreme pressures corresponded to flip-through cases.

1.5 Tsunami wave approaches

Several researchers (Cross (1967), Ramsden (1996), Asakura et al. (2003), Ikeno et al. (2007), Nouri et al. (2010), Kihara et al. (2015)) have used laboratory experiments to improve the knowledge on tsunami-coastal structure interaction. The limitations of laboratory facilities bring some authors to use simple approaches for tsunamis. Synolakis (1987), Grilli et al. (1994) and Li & Raichlen (2001) proposed the use of solitary waves to investigate the run-up of tsunamis. In the same way, Hsiao & Lin (2010) investigated tsunami loads on coastal structures using the solitary wave approach. In contrast, Madsen et al. (2008) questioned this approach showing the limitations of its applicability. This work concluded that the characteristics of solitary waves are more related to short

waves than long waves as tsunamis. This approach could, therefore, hold for modelling the impact of storm waves or undular bore short waves.

On the other hand, Chanson (2006) proposed the dam-break flow to simplify the shape of tsunamis impacting the coast. In this work, the dam-break approach is compared with measures of the Indonesian tsunami obtaining a satisfactory agreement. This approach has been recently adopted in laboratory experiments (Nouri et al. (2010), Kihara et al. (2015)) to investigate loads induced by tsunami bores on coastal structures.

1.6 Modelling of tsunami propagation and wave impact

The correct numerical modelling of tsunami waves is indispensable when investigating their effect on coastal structures. Three models have been mainly used over the years: nonlinear shallow water, nonlinear Boussinesq and full Navier-Stokes models. The first one solving the shallow water equations is very extended for preliminary tsunami forecasting because of the simplicity and rapidity of this kind of models. Nevertheless, as shown in Horrillo et al. (2006) and Arcas & Segur (2012), these models are not able to reproduce the exact wave shape near the coast due to inherent approximation. To take into account dispersive effects and the nonhydrostatic component of pressure, models using the Boussinesq approach (Peregrine (1972)) are proposed for tsunami modelling. Glimsdal et al. (2006) and Madsen et al. (2008) have demonstrated the ability of these models to simulate the propagation of long waves from deep to shallow water, the transformation of wave regime into undular bore regime and the tsunami arrival to the shore. The Navier-Stokes models are less common on tsunami propagation due to their expensive cost in terms of computation time. Horrillo et al. (2006) run a full Navier-Stokes model to investigate the propagation of the Indonesian tsunami. The authors considered this model as a reference to validate the results given by two models based on the nonlinear shallow water and nonlinear boussinesq equations. On near-shore areas, the comparison showed a good agreement between the Navier-Stokes and Boussineq model, but less precise results are obtained for the shallow water code as mentioned before. Dispersive models are, therefore, needed for accurate simulation of tsunamis interacting with coastal structures.

For real-scale experiments of tsunami impacts on coastal structures, numerical models have become useful tool. Despite the criticism from the work of Madsen et al. (2008), authors as Jianhong et al. (2013) and Jiang et al. (2016) kept using the controversial solitary wave approach to numerically (RANS simulations) investigate tsunami impinging coastal structures. In contrast, the numerical experiments with a Navier-Stokes code

presented in Mikami & Shibayama (2013) and Jayaratne et al. (2014) used the dam-break set-up to show the effects of tsunamis impacting and overflowing coastal levees. The dam-break flow is also the base of the studies published by Wei et al. (2015) and St-Germain et al. (2013) which applied a SPH model to estimate tsunami forces on coastal structures.

With respect to past numerical works of stability of vertical breakwater submitted to tsunamis, apart from the already mentioned Hsiao & Lin (2010) and Jianhong et al. (2013) based on the solitary wave theory, Arikawa et al. (2012) studied the rupture mechanism of the Kamishi breakwater imposing a realistic signal in a Navier-Stokes model (CADMAS-SURF/3D). A good agreement was found between the numerical results and large-scale experiments. Bricker et al. (2013) also carried out Navier-Stokes simulations with InterFOAM VOF to test the influence of different turbulence models on the Kamaishi breakwater stability. In this case, the tsunami signal was previously computed by a Boussinesq model from the source to near-shore areas.

1.7 Thesis structure

This literature review raised the following questions still not answered in our scientific community:

- Undular bores were observed in the two last tsunamis, but how and when did they appear during the arrival of these long waves? Which are the effects of undular bore short waves on the stability of offshore breakwaters?
- Knowing that breakwaters might be impacted by tsunami-like undular bores, could their undulations be isolated to estimate loads individually?
- In that case and considering the flip-through phenomenon as the most severe case of wave impact in terms of pressures, what are the factors that control the pressure variability for apparently similar flip-through impacts?
- If a vertical breakwater is subjected to flip-through impacts, how might the stability of caissons be compromised by such extreme impacts?

To clarify these questions, a Navier-Stokes model (THETIS), which allows to simulate tsunami-breakwater interaction, is used as main investigation tool. The model equation are presented in Chapter 2. The BOSZ (Boussinesq Ocean & Surf Zone) model is used for the propagation of tsunamis. This code, based on the Boussinesq equations, is described in the second part of the Chapter 2.

As a first step of this research work, the propagation and formation mechanism of undular bores near Soma city (Sendai bay) is shown during the Tohoku tsunami in 2011 in Chapter 3. After this, the failure process of the offshore breakwater located at the port of Soma is investigated with BOSZ and THETIS.

In Chapter 4, the efforts induced on breakwaters by the undular bore short waves are analysed as a single event at a fine scale. The literature showed that the flip-through phenomenon is considered the most extreme case of impact in terms of pressures and forces. This chapter focuses, therefore, on this severe non-aerated impact and proposes to investigate the influence of the wave front inclination at impact on the flow field and pressure variability.

After Chapter 4, the next step in Chapter 5 is to enlarge the knowledge on how the stability of breakwaters varies depending on the flip-through case. To do that, a semi-analytical model based on the simple water wedge theory is formulated for least steep, medium steep and steepest wave face. After validation with the numerical results presented in Chapter 4, this method is used to plot useful graphs from an engineering point of view, which contains forces, impact durations and caisson displacements for hypothetical cases of flip-through. The studies about the flip-through phenomenon included in Chapter 4 and 5 can be overall applicable for all kinds of short waves generated by either tsunami undular bores or storms.

The conclusions of this research work are drawn at the end of each chapter. Chapter 6 summarizes the main results and proposes new possibilities of research for the future.

Chapter 2

Description of the numerical models

2.1 THETIS model

The numerical simulation of wave-structure interaction problems needs to properly describe the flow and wave interface taking into account several phases (water and air). The literature has shown that the most extended and accurate numerical models for such problems are based in the Navier-Stokes equations. Among all the available codes using this formulation (OpenFoam, Fluent, Fun3D, etc.), the chosen model is THETIS, a versatile code which has been developed over the last years at Trefle laboratory (Bordeaux). This choice is motivated by the ability of this model to simulate incompressible/slightly compressible problems, multi-phasic flows and solid obstacles. The potential of the code in the field of fluid flow problems has been proven in the following published works: wave propagation (Abadie et al. (2012)), breaking process (Kazolea et al. (2017)), fluid-structure interaction (Mokrani & Abadie (2016), Ducassou et al. (2017) and Martin-Medina, Abadie, Mokrani & Morichon (2017)) and surface-subsurface flows (Desombre et al. (2012)).

2.1.1 Governing equations

An incompressible flow composed of two unmiscible phases is considered: water and air. If we assume continuity of fluid velocity through the interface and neglect surface tension effects, the governing equations are simply the incompressible Navier-Stokes equations (NS) obviously valid in each phase to which an interface evolution equation is added. $\mathbf{u} = (u, v, w)$, p, ρ, μ, t, and $\mathbf{g}$ are respectively the velocity, pressure, fluid density,

dynamic viscosity, time and gravity. The system of equations is then the following:

$$\begin{cases} \nabla.\mathbf{u} = 0 \\ \rho\left(\dfrac{\partial \mathbf{u}}{\partial t} + (\mathbf{u}.\nabla)\mathbf{u}\right) = \rho\mathbf{g} - \nabla p + \nabla.\left[\mu(\nabla\mathbf{u} + \nabla^t\mathbf{u})\right] \end{cases} \tag{2.1}$$

2.1.2 Boundary conditions and obstacles

The boundary conditions in THETIS are implemented using the technique proposed by Angot (1989) and Khadra (1994). This technique consists in adding a penalty term in the Navier-Stokes equations. For these simulations, two kinds of boundary conditions are considered:

i) a free slip condition which imposes a Neumann condition on the tangential component to the boundary and a nil normal velocity. This condition allows the fluid motion in the parallel direction with respect to the obstacle.

ii) a non-slip condition which imposes a nil velocity in all the directions. In this case, the fluid is blocked at the boundary which allows, for instance, to simulate the boundary layer.

Taking into account this penalty term ($\mathbf{B_u}$), the system (2.1) reads as follows:

$$\begin{cases} \nabla.\mathbf{u} = 0 \\ \\ \rho\left(\dfrac{\partial \mathbf{u}}{\partial t} + (\mathbf{u}.\nabla)\mathbf{u}\right) + \mathbf{B_u}(\mathbf{u} - \mathbf{u}_\infty) = \rho\mathbf{g} - \nabla p + \nabla.\left[\mu(\nabla\mathbf{u} + \nabla^t\mathbf{u})\right] \end{cases} \tag{2.2}$$

To model an obstacle in THETIS, three different approaches can be used:

i) The first method consists in penalizing the velocity with the penalty term defined before in the matrix coefficients $\mathbf{B_u}$. Since this term is present in the equation governing the fluid motion, it allows to change the velocity values in any point of the model. The obstacle can, therefore, be built by simply imposing nil velocities in the place of the solid.

ii) The second method is inspired by the Brinkman theory. It consists in assuming each numerical phase as a porous media with a variable intrinsic permeability k_i.

Adding the Brinkman term to the equation of motion, fluid and solid phases can be distinguished by varying the value of k_i.

$$\rho\left(\frac{\partial \mathbf{u}}{\partial t} + (\mathbf{u}.\nabla)\mathbf{u}\right) + \mathbf{B}_\mathbf{u}(\mathbf{u} - \mathbf{u}_\infty) + \boxed{\frac{\mu \mathbf{u}}{k_i}} = \rho\mathbf{g} - \nabla p + \nabla.\left[\mu(\nabla\mathbf{u} + \nabla^t\mathbf{u})\right] \quad (2.3)$$

When $k_i \sim +\infty$, the Darcy term disappears in the equation (2.3) and the phase is considered as a fluid. In contrast, if $k_i \sim 0$, the Darcy term becomes significant compared to the other terms in the equation. At these points, the velocity is nil in the two directions and the phase is assumed to be a solid obstacle. In the model, the values of k_i are fixed to 10^{-40} for a solid and 10^{40} for a fluid.

iii) The third method is based on solidifying a fluid by imposing an infinite viscosity. The interactions between fluids and solids can be better represented using this method (Ritz & Caltagirone (1999) and Ducassou et al. (2017)).

2.1.3 Numerical method for NS equations

Temporal discretization

The first step to solve the system (2.2) consists in establishing a temporal discretization of the equations. The total duration of the simulations is divided in time steps Δt^n that is calculated by a dynamic Courant-Friedrichs-Levy (CFL) condition. The CFL condition allows to control the fluid motion in a mesh at each time step. In this way, while the fluid velocity increases, the time step is adjusted depending on the CFL number imposed in the simulations. The temporal discretization of the system of equations (2.2) is carried out by an Euler scheme of order 1 (GEAR1).

Spatial discretization

The NS equations are discretized on a fixed Cartesian grid using a finite volume method. This method consists in integrating the balance equations over a control volume at each time step Δt^n.

The terms of the equations are expressed in conservative form to use the Stokes formula on the control volume (V_Ω):

$$\frac{1}{V_\Omega}\int_\Omega (\nabla.f)dv = \frac{1}{V_\Omega}\int_\Gamma f.\mathbf{n}ds \quad (2.4)$$

with

$$\int_\Gamma f.\mathbf{n}ds = \int_{\Gamma_N} f.\mathbf{n}_N ds + \int_{\Gamma_S} f.\mathbf{n}_S ds + \int_{\Gamma_E} f.\mathbf{n}_E ds + \int_{\Gamma_W} f.\mathbf{n}_W ds \quad (2.5)$$

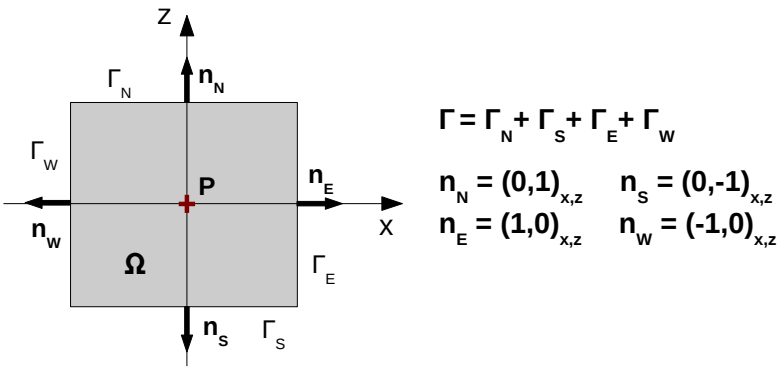

Figure 2.1: Finite volume method - Characteristics

f is the considered variable (velocity and pressure) and the integral is defined as shown in fig.2.1.

Following Patankar (1990), the finite volume formulation is solved using staggered mesh as in the Marker And Cells (MAC) method from Harlow & Welsh (1995). For this reason, THETIS features three grid types: the pressure grid and 2 velocity grids (fig.2.2). The velocity grids are defined by translation of the main grid of a half mesh. The grid displaced along the x axis contains the horizontal component of the velocity field. The red arrows (respectively blue) represent the nodes corresponding to the horizontal grid (respectively vertical). A viscosity grid is also implemented in order to improve the viscosity calculation in multi-phasic simulations. The nodes of the viscosity grid are located at the center of the main grid elements.

Solution of the velocity-pressure coupling

- Augmented Lagrangian method

This is a minimization method under the constraint of the continuity equation, where the pressure which is decoupled to the velocity, appears as a Lagrange multiplier. The incompressibility constraint is directly introduced into the equation of motion as a penalty term $r_u \nabla(\nabla.\mathbf{u})$, that couples the components of speed. With k the iteration of the

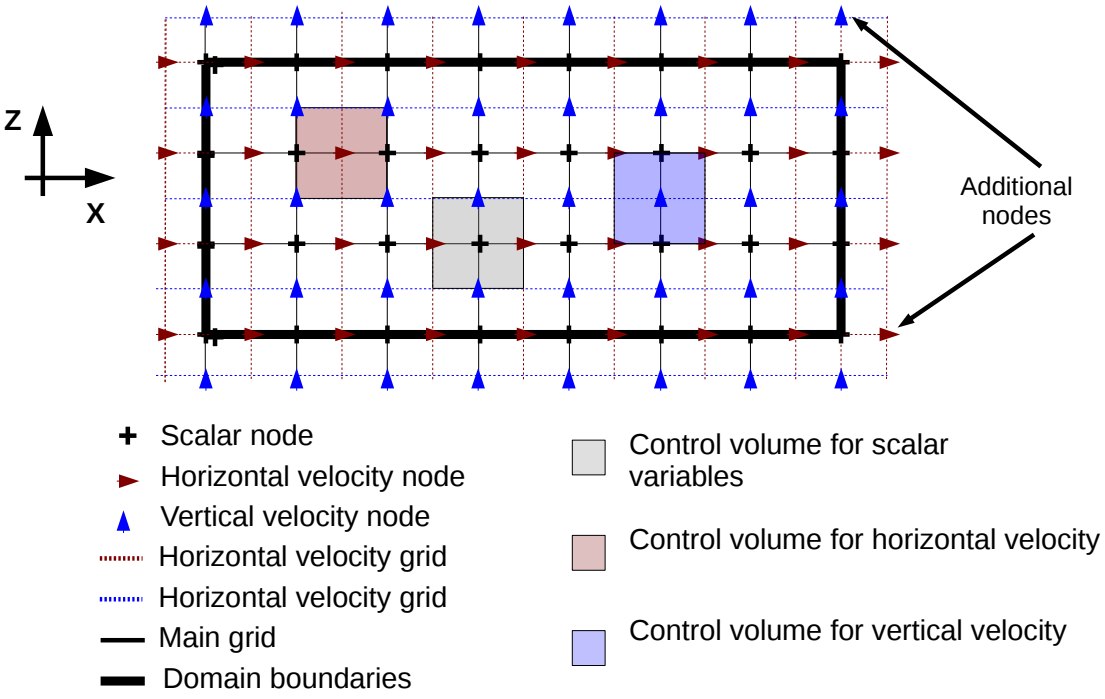

Figure 2.2: Description of the grids and control volumes in THETIS

method, the system is written by:

$$\begin{cases} \rho^n \left(\frac{\mathbf{u}^{k+1}}{\Delta t^n} + (\mathbf{u}^k.\nabla)\mathbf{u}^{k+1} \right) + \mathbf{B}_\mathbf{u}(\mathbf{u}^{k+1} - \mathbf{u}_\infty) \\ + \frac{\mu^n \mathbf{u}^{k+1}}{K} - \rho^n \mathbf{g} - \nabla p^k - \nabla. \left[\mu^n (\nabla \mathbf{u}^{k+1} + \nabla^t \mathbf{u}^{k+1}) \right] - r_u \nabla(\nabla.\mathbf{u}^{k+1}) = \rho^n \frac{\mathbf{u}^n}{\Delta t^n} \\ p^{k+1} = p^k - r_p \nabla.\mathbf{u}^{k+1} \end{cases} \quad (2.6)$$

where r_u and r_p are convergence parameters set automatically in the numerical simulations. The advantage of such a formulation is the explicit calculation of the pressure. It uses only the pressure in the previous temporal iteration and the divergence of speed, no boundary condition on the pressure is required.

- Projection method

The projection method, first introduced by Chorin (1967), comprises two steps:
(i) From the pair $(\mathbf{u}^n, p^n)$, a velocity field $\tilde{\mathbf{u}}$ is calculated using the expression:

$$\tilde{\mathbf{u}} - \mathbf{u}^n = \frac{\Delta t^n}{\rho^n} \left(\rho^n \mathbf{g} - \nabla p^n + \nabla.(\mu^n [\nabla \mathbf{u}^n + \nabla^t \mathbf{u}^n]) - \nabla.(\rho^n \mathbf{u}^n \otimes \mathbf{u}^n) \right) \quad (2.7)$$

(ii) The velocity $\mathbf{u}$ is calculated by projection of $\tilde{\mathbf{u}}$ on a field with no divergence:

$$\mathbf{u}^{n+1} = \tilde{\mathbf{u}} - \frac{\Delta t^n}{\rho^n}\nabla(\mathbf{p}^{n+1} - \mathbf{p}^n) \tag{2.8}$$

This second step (projection step) consists in determining the pressure $\mathbf{p}^{n+1}$. The Poisson equation is used:

$$\nabla.\left(\frac{\Delta t^n}{\rho^n}\nabla(\mathbf{p}^{n+1} - \mathbf{p}^n)\right) = \nabla.\tilde{\mathbf{u}} \tag{2.9}$$

This method is relatively simple to program and easy to solve because it is not an iterative method (contrary to the previous method). However, boundary conditions on the pressure field must be imposed to allow the resolution of (2.9).

2.1.4 Interface tracking and transport

The Volume of fluid (VOF) method proposed by Hirt & Nichols (1981) is implemented in this model. This method introduces a color function F, which indicates the volume fraction occupied by each phase in a mesh cell. The interface position is defined as the iso-line $F = 0.5$. In this case, with two phases, $F = 1$ correspond to water and $F = 0$ correspond to air. When the mesh cell is mixed, the color function F has a value between 0 and 1, equals to the volume fraction of fluid in the cell.

The evolution of the function F during the simulations is obtained by the solution of the advection equation where $\mathbf{u}$ is the local fluid velocity.

$$\frac{\partial F}{\partial t} + \mathbf{u}.\nabla F = 0 \tag{2.10}$$

Different VOF methods are implemented in the THETIS model to calculate the interface transport.

VOF-TVD method

This first method consists in solving equation (2.10) directly using a suitable numerical scheme. Writing the convective term in the conservative form and using a first order discretization in time, the discretization in space over the control volume (i, j) reads:

$$\frac{F_{i,j}^{n+1} - F_{i,j}^n}{\Delta t^n}\Delta X \Delta Z + \Phi_X \Delta Z + \Phi_Z \Delta X = 0 \tag{2.11}$$

With

$$\Phi_X = F_{i+\frac{1}{2},j}^{n+1} u_{i+1,j}^{n+1} - F_{i-\frac{1}{2},j}^{n+1} u_{i,j}^{n+1}$$
$$\Phi_Z = F_{i,j+\frac{1}{2}}^{n+1} u_{i,j+1}^{n+1} - F_{i,j-\frac{1}{2}}^{n+1} u_{i,j}^{n+1}$$

ΔX (respectively ΔZ) represents the horizontal space step (respectively vertical). At this stage, a good approximation of the fluxes Φ_X and Φ_Z is required to obtain an accurate representation of the interface. A TVD scheme typically has two main properties: in the parts of the domain where the solutions are regular, it is equivalent to a high-order scheme that reduces diffusion. But in the parts where there are strong discontinuities it is a first order scheme that prevents oscillations.

VOF-PLIC method

The Piecewise Linear Interface Calculation (PLIC) method is also employed. One of the advantages of this Eulerian/Lagrangian method is to keep the discontinuous nature of the interface between water and air due to the Lagrangian character of the transport method. The five successive steps of the PLIC method are the followings:

- Mixed cells (i.e. $0 < F < 1$) identification.
- In each cell containing air and water, calculation of the interface normal direction using a finite difference approximation on nine points.
- Piecewise linear interface reconstruction, knowing the normal direction in each cell and the volume fraction.
- Lagrangian advection of the interface segments using a linear interpolation of velocities calculated on the staggered mesh.
- Calculation of the new volume fraction distribution.

To ensure the conservative or stability nature of the PLIC method, a sufficient condition is that the segments are not advected over more than half of a cell size during a time step Δt^n (Abadie et al. (1998)).

SVOF-PLIC method

The SVOF-PLIC method consists in slightly smoothing the volume fraction function by introducing a controlled diffusion zone around the interface. This is performed by using an analogy with the thermal diffusion whose governing equation equation reads:

$$\frac{\partial T}{\partial t} - \nabla.(a\nabla T) = 0 \tag{2.12}$$

$a > 0$ is the thermal diffusion coefficient. The smoothed volume fraction function F^S is given with the following equation:

$$-\nabla.a\nabla F^{S,k+1} + F^{S,k+1} = F^{S,k} \tag{2.13}$$

in which the thermal diffusion coefficient a depends on the interface thickness L_i and the local dimension of the considered cell ΔX:

$$a = L_i \Delta X^2 \tag{2.14}$$

This equation is discretized in space by using the finite volume method and a centered scheme. The final smoothed function F^S is obtained iteratively by applying the following algorithm:

$$L^1 = F \tag{2.15}$$

$$\text{For} \quad \text{k} = 1...\text{N} - 1,$$

$$-\nabla.\tau_d^* \nabla F^{S,k+1} + F^{S,k+1} = L^k \tag{2.16}$$

$$L^{k+1} = F^{S,k+1} \tag{2.17}$$

with $\tau_d^* = \frac{L_i \Delta X^2}{N}$. After resolution of (2.15) - (2.17), the condition $F^S = F^{S,k}$ is verified.

The function F^S includes a narrow diffusion zone that represents the interface more regularly. By this way, the discontinuities which may appear with the PLIC algorithm are smeared and the interface is more stable while being a little less accurate. The model can describe high interface distortions during the impact without diverging.

Practically, the parameters L_i and the number of internal iterations N are adjusted to limit the interface fractioning while keeping an accurate description of the interface.

2.1.5 $k - \varepsilon$ turbulence model

Turbulence flows are simulated in THETIS using the $k - \epsilon$ model. This eddy-viscosity model is one of the most used because of its simplicity, robustness and ease of implementation. It is based on transport equations for the turbulence kinematic energy, k, and the dissipation energy, ε. The modified Navier-Stokes equations read now as follows:

$$\begin{cases} \nabla.\mathbf{u} = 0 \\ \rho\left(\dfrac{\partial \mathbf{u}}{\partial t} + (\mathbf{u}.\nabla)\mathbf{u}\right) = \rho\mathbf{g} - \nabla p + \nabla.\left[(\mu + \mu_t)(\nabla\mathbf{u} + \nabla^t\mathbf{u})\right] \end{cases} \tag{2.18}$$

where μ_t is the local turbulent viscosity given by the following relationship:

$$\mu_t = \rho C_\mu \frac{k^2}{\varepsilon} \tag{2.19}$$

The transport equation for the turbulence kinetic energy (k) is derived from the exact equation, while the equation for the rate of dissipation (ε) is obtained using physical reasoning. The two model transport equations for k and ε reads as follows:

$$\rho(\frac{\partial k}{\partial t} + \nabla.(\mathbf{u}k) - k\nabla.\mathbf{u}) = \nabla.\left((\mu + \frac{\mu_t}{\sigma_k})\nabla k\right) + P + G - \rho\varepsilon + \frac{\mu}{k_i}\varepsilon \tag{2.20}$$

$$\rho(\frac{\partial \varepsilon}{\partial t} + \nabla.(\mathbf{u}\varepsilon) - \varepsilon\nabla.\mathbf{u}) = \nabla.\left((\mu + \frac{\mu_t}{\sigma_\varepsilon})\nabla\varepsilon\right) + C_1\frac{\varepsilon}{k}(P + C_3G) - C_2\rho\frac{\varepsilon^2}{k} + \frac{\mu}{k_i}\varepsilon \tag{2.21}$$

where P and G are respectively the generation terms of turbulence kinetic energy due to the mean velocity gradients and buoyancy. These terms can be calculated by the following expressions:

$$P = \mu_t\ (\nabla\mathbf{u}.\nabla\mathbf{u} + \nabla\mathbf{u}.\nabla^t\mathbf{u}) \tag{2.22}$$

$$G = -\frac{\mu_t}{\sigma^t}\beta\mathbf{g}.\nabla T \tag{2.23}$$

where σ^t is the turbulent Prandtl number for energy which value is 0.85 and β is the coefficient of thermal expansion defined as follows:

$$\beta = -\frac{1}{\rho}\left(\frac{\partial\rho}{\partial T}\right)_p \tag{2.24}$$

C_μ, C_1 and C_2 are model constants and σ_k and σ_ε are the turbulent Prandtl coefficients for k and ε. The values of these coefficients in Eq. (2.20) and (2.21) are the followings:

$$C_\mu = 0.09,\ C_1 = 1.44,\ C_2 = 1.92,\ \sigma_k = 1,\ \sigma_\varepsilon = 1.3 \tag{2.25}$$

The C_3 constant determines the influence of buoyancy on the dissipation energy (ε):

$$C_3 = tanh\left(\frac{u_y}{u_x}\right) \tag{2.26}$$

with u_y the velocity component parallel to gravity and u_x the component perpendicular to gravity. In this way, C_3 becomes 1 for flows which main direction is the same as the gravitational vector. In contrast, C_3 is nil for flows perpendicular to the gravitational vector.

2.1.6 Modelling flows through a porous medium

THETIS was extended in order to model multiphase flows inside porous mediums in Desombre (2012) and Desombre et al. (2012). In this work, the porous medium is studied at macro-scale and considered as homogeneous, isotropic and immobile. Consequently, the porosity ϕ and the intrinsic permeability k_i, which characterize the porous mediums in THETIS, are constants.

The porosity ϕ $[m^3/m^3]$ is defined as the relationship between the volume of voids over the total volume:

$$\phi = \frac{Vol_v}{Vol_v + Vol_s} \tag{2.27}$$

where Vol_v is the volume of voids and Vol_s is the volume of solids. The porosity represents the total amount of void space accessible from the surface.

The intrinsic permeability k_i $[m^2]$ is an intensive property that is function of the porous medium characteristics. k_i is estimated from the grain size using the Kozeny-Carmann formulation:

$$k_i = \frac{d_{50}^2}{180} \frac{\phi^3}{(1-\phi)^2} \tag{2.28}$$

with d_{50} is the average diameter of grains.

The Darcy-Forchheimer equation

Different flow regimes can be observed in porous mediums. For slow flows characterized by a low Reynolds number, the Darcy's law can be used:

$$I = \frac{1}{K}\boldsymbol{\nu} \tag{2.29}$$

where I, K and $\boldsymbol{\nu}$ are the hydraulic gradient, the permeability and the Darcy velocity respectively. This velocity is the volume-averaged velocity over the mesh cells, which is linked to the internal pore velocity $\mathbf{u}$ by the Dupuit relationship $\boldsymbol{\nu} = \mathbf{u}\phi$.

In contrast, when the Reynolds number increases, the interaction between the flow and the grains of the porous medium becomes significant and the relation between the pressure gradient and the velocity established by the Darcy equation is not valid any more. To model this kind of flows, Forchheimer proposes to add a quadratic drag term to take into account this phenomenon. The Darcy equation with the Forchheimer term reads as follows:

$$I = a_k\boldsymbol{\nu} + b_k\|\boldsymbol{\nu}\|\boldsymbol{\nu} \tag{2.30}$$

The linear (a_k) and quadratic (b_k) drag coefficients are related to the intrinsic permeability and to the fluid density and viscosity by the respective relations:

$$a_k = \frac{1}{K} = \frac{\mu}{\rho \mathbf{g} k_i} \qquad and \qquad b_k = \frac{\rho C_F}{\rho \mathbf{g} \sqrt{k_i}} \tag{2.31}$$

The Forchheimer equation is added to the equation of motion:

$$0 = \rho \mathbf{g} - \nabla p - \frac{\mu}{k_i} \boldsymbol{\nu} + \frac{\rho C_F}{\sqrt{k_i}} \|\boldsymbol{\nu}\| \boldsymbol{\nu} \tag{2.32}$$

where C_F is the Forchheimer coefficient. The value of the C_F depends on the type of porous media. As we do not dispose of enough information to calibrate this parameter, the universal value of 0.55 given by Ward (1964) is considered in these computations.

Simulation of flows inside and outside the porous medium

The work presented by Desombre (2012) allows to simulate surface and subsurface flows solving only one equation. Special attention needs to be put to model the fluid motion through the porous medium interface.

To ensure continuity of velocity and pressure at the porous medium boundaries, the Brinkman method was implemented in the THETIS model. This method proposes to introduce a term (using μ_{eff}) in the Stokes equation which allows to model the transformation of a subsurface Forchheimer flow into a surface Stokes flow:

$$0 = \rho \mathbf{g} - \nabla p + \mu_{eff} \nabla^2 \boldsymbol{\nu} - \frac{\mu}{k_i} \boldsymbol{\nu} + \frac{\rho C_F}{\sqrt{k_i}} \|\boldsymbol{\nu}\| \boldsymbol{\nu} \tag{2.33}$$

Several studies tried to assess the value of the effective viscosity (μ_{eff}). In this work, the expression proposed by Ochoa-Tapia & Whitaker (1995), $\mu_{eff} = \frac{\mu}{\phi}$, is used.

Integrating the Darcy-Brinkman-Forchheimer formulation, the system of equations (2.2) solved by THETIS is the following:

$$\begin{cases} \nabla . \boldsymbol{\nu} = 0 \\ \\ \rho \left(\frac{1}{\phi} \frac{\partial \boldsymbol{\nu}}{\partial t} + (\frac{\boldsymbol{\nu}}{\phi} . \nabla) \frac{\boldsymbol{\nu}}{\phi} \right) = \rho \mathbf{g} - \nabla p + \mu_{eff} \nabla^2 \boldsymbol{\nu} - \frac{\mu}{k_i} \boldsymbol{\nu} + \frac{\rho C_F}{\sqrt{k_i}} \|\boldsymbol{\nu}\| \boldsymbol{\nu} \end{cases} \tag{2.34}$$

Outside the porous medium, the porosity is $\phi = 1$ and the intrinsic permeability is set to $k_i = \infty$. The equation (2.34) is therefore transformed to the classical NS equations (2.2). Inside the porous medium, the porosity and the permeability are low and Darcy and Forchheimer terms allow to balance the hydraulic gradient.

2.2 BOSZ model

One of the objectives of this work is to investigate the transformation of tsunami waves into undular bores, which needs a numerical model able to handle frequency dispersion. The numerical simulations should also take into account the interaction of waves with irregular bathymetries and offshore breakwaters.

A numerical code based on the Boussinesq equations meets these requirements. Several Boussinesq-type models have been already used for undular bore simulations: the 1D simulations carried out in Madsen et al. (2008), the FUNWAVE-TVD model in Grilli et al. (2012) or the fully nonlinear Boussinesq model used in Kim & Lynett (2010). In this PhD, the BOSZ (Boussinesq Ocean Surf Zone) model is chosen. This code, also based on the Boussinesq equations, proposes an alternative formulation with shock capturing capabilities and uses a conservative numerical scheme to reproduce wave breaking over fringing reefs. Model stability is improved using a formulation that includes the dispersion terms (with time and spatial derivatives) in a new set of evolution variables. An adaptive time step is used in the numerical integration. This model allows to take into account dispersion as the formulation presented in Nwogu (1993), but also contains flux terms as the nonlinear shallow-water equations to simulate discontinuous flows during wave breaking. This numerical code has been shown to be an effective and consistent tool modelling wave propagation, reflection, high-frequency dispersion and flood events in Roeber et al. (2010) and Roeber & Cheung (2012).

The governing equations, the Boussinesq-type equations presented in Nwogu (1993), consist of a continuity equation and two momentum equations:

$$\eta_t + \nabla[(h+\eta)\mathbf{u}] + \nabla.\left[\left(\frac{z_\alpha^2}{2} - \frac{h^2}{6}\right) h\nabla(\nabla.\mathbf{u}) + \left(z_\alpha - \frac{h}{2}\right) h\nabla[\nabla.(h\mathbf{u})]\right] = 0 \qquad (2.35)$$

$$\mathbf{u}_t + \mathbf{u}(\nabla\mathbf{u}) + g\nabla\eta + \left[\frac{z_\alpha^2}{2}\nabla(\nabla\mathbf{u}) + z_\alpha\nabla[\nabla.(h\mathbf{u})]\right]_t = 0 \qquad (2.36)$$

where t denotes partial derivatives with respect to time, h is the water depth, η is the free surface elevation, and $H = h + \eta$ is the flow depth, g is gravity, $\mathbf{u}$ is horizontal flow velocity and z_α is the reference depth.

The Boussinesq-type equations presented in Nwogu (1993) are written by Roeber et al. (2010) in conserved variables. These variables are H, η, ρ, (u, v) that are respectively the total water depth, the free surface elevation, the water density and the flow velocities

in x and y directions. The continuity equation in function of H reads as follows:

$$\begin{aligned}
&H_t + (Hu)_x + (Hv)_y \\
&+\left[\left(\frac{z_\alpha^2}{2} - \frac{h^2}{6}\right) h(u_{xx} + v_{xy}) + \left(z_\alpha + \frac{h}{2}\right) h((hu)_{xx} + (hv)_{xy})\right]_x \\
&+\left[\left(\frac{z_\alpha^2}{2} - \frac{h^2}{6}\right) h(u_{xy} + v_{yy}) + \left(z_\alpha + \frac{h}{2}\right) h((hu)_{xy} + (hv)_{yy})\right]_y = 0
\end{aligned} \tag{2.37}$$

The momentum equations are also expressed in conserved variables (Hu and Hv). These equations are obtained from Eq. 2.36 combined with the continuity equation (Eq. 2.35):

$$\begin{aligned}
(Hu)_t + (Hu^2)_x + (Huv)_y &= H(u_t + uu_x + vu_y) + u(H_t + (Hu)_x + (Hv)_y) \\
(Hv)_t + (Hvu)_x + (Hv^2)_y &= H(v_t + uv_x + vv_y) + v(H_t + (Hv)_y + (Hu)_x)
\end{aligned} \tag{2.38}$$

Replacing the known terms of the continuity equation, the conserved variable momentum equations read as follows:

$$\begin{aligned}
&(Hu)_t + (Hu^2)_x + (Huv)_y + gH\eta_x \\
&+H\left[\frac{z_\alpha^2}{2}[u_{xx} + v_{xy}] + z_\alpha[(hu)_{xx} + (hv)_{xy}]\right]_t \\
&+u\left[\left(\frac{z_\alpha^2}{2} - \frac{h^2}{6}\right) h(u_{xx} + v_{xy}) + \left(z_\alpha + \frac{h}{2}\right) h((hu)_{xx} + (hv)_{xy})\right]_x \\
&+u\left[\left(\frac{z_\alpha^2}{2} - \frac{h^2}{6}\right) h(u_{xy} + v_{yy}) + \left(z_\alpha + \frac{h}{2}\right) h((hu)_{xy} + (hv)_{yy})\right]_y \\
&-g\eta h_x - H_t\psi_P + \tau_x = 0
\end{aligned} \tag{2.39}$$

$$\begin{aligned}
&(Hv)_t + (Hv^2)_y + (Huv)_x + gH\eta_y \\
&+H\left[\frac{z_\alpha^2}{2}[v_{yy} + u_{xy}] + z_\alpha[(hv)_{yy} + (hu)_{xy}]\right]_t \\
&+v\left[\left(\frac{z_\alpha^2}{2} - \frac{h^2}{6}\right) h(u_{xx} + v_{xy}) + \left(z_\alpha + \frac{h}{2}\right) h((hu)_{xx} + (hv)_{xy})\right]_x \\
&+v\left[\left(\frac{z_\alpha^2}{2} - \frac{h^2}{6}\right) h(u_{xy} + v_{yy}) + \left(z_\alpha + \frac{h}{2}\right) h((hu)_{xy} + (hv)_{yy})\right]_y \\
&-g\eta h_y - H_t\psi_Q + \tau_y = 0
\end{aligned} \tag{2.40}$$

Where ψ_P and ψ_Q (P and Q are evolution variables) denote the dispersion terms in the momentum equations and τ_x and τ_y are the frictional drag terms depending on the Manning roughness coefficient.

$$\psi_P = z_\alpha[0.5z_\alpha(u_{xx} + v_{xy}) + (hu)_{xx} + (hv)_{xy}] \tag{2.41}$$

$$\psi_Q = z_\alpha[0.5 z_\alpha(v_{yy} + u_{xy}) + (hv)_{yy} + (hu)_{xy}] \tag{2.42}$$

After this change of variables, the governing equations (2.37), (2.39) and (2.40) in the BOSZ model are composed of the non-linear shallow water equations in the conservative form and the dispersion terms given in Nwogu (1993).

2.2.1 Numerical solution

BOSZ combines the use of the Finite Volume method with the governing equations which is compatible with the second-order Runge-Kutta time integration scheme for dispersion (Gottlieb et al. (2001)). The Runge-Kutta method allows to improve the shock-capturing ability of the model and ensure fast convergence. The numerical domain is discretized in regular cells and the simulations are integrated with an adaptive time step. A Courant number (Cr) condition must be satisfied while calculating the time step. This Cr is set to 0.5 in this work.

A TVD limiter is used in BOSZ (Kim et al. (2008)) to define the flow in either side of the cell. This provides the input to a Riemann solver to determine the interface flow characteristics for the flux and bathymetry terms. A first-order upwind scheme is used to compute these terms and give a correct solution even for steep bathymetries. This numerical method allows to keep solving conservation of mass and momentum even if free surface discontinuities are significant.

2.2.2 Boundary conditions

BOSZ model allows to impose solid reflective walls and dissipative sponge zones as boundary conditions in the domain. The sponge layer is an exponential decay function which allows to absorb the continuity and momentum fluxes through smooth transitioning to zero. Obstacles as coastal structures in the BOSZ model should be integrated in the bathymetry. Permeability and porosity of dykes or breakwaters are not considered. Attention should be paid to the structure slopes in order to avoid numerical instability. BOSZ can handle a maximum slope of 1.0.

Waves are generated giving free surface elevations at any of the boundaries. The wave amplitude time series can be simply imposed using an external file in Matlab format which includes time and free surface height. The wave velocity is automatically calculated depending on the water depth ($v_{wave} = \sqrt{gh}$).

2.2.3 Wave breaking

BOSZ is a depth-integrated model and so wave overturning and breaking can not be described. To avoid numerical instabilities during the transition between subcritical and supercritical flows linked to excessive dispersion, BOSZ deactivates the dispersion terms to allow the Riemann solver to describe the breaking wave as a bore. Dispersion is deactivated in every cell where the following criterion hold:

$$\begin{aligned} |(Hu)_x| &> B\sqrt{gH} \\ |(Hu)_y| &> B\sqrt{gH} \end{aligned} \tag{2.43}$$

where B = 0.5, based on comparison with experimental data. The condition is verified in each time step. In cells with not dispersion, the model solves the hydrostatic shallow water equations.

Another criterion based on the Froude number (Fr) is implemented in the code. The Froude number can be calculated from the free surface velocity ($Fr = \sqrt{u_z^2 + v_z^2}/\sqrt{gH}$):

$$\begin{aligned} u_z &= u_{z_\alpha} + \frac{1}{2}(z_\alpha^2 - z^2)[(u_{z_\alpha})_{xx} + (v_{z_\alpha})_{xy}] + (z_\alpha - z)[(hu_{z_\alpha})_{xx} + (hv_{z_\alpha})_{xy}] \\ v_z &= v_{z_\alpha} + \frac{1}{2}(z_\alpha^2 - z^2)[(u_{z_\alpha})_{xy} + (v_{z_\alpha})_{yy}] + (z_\alpha - z)[(hu_{z_\alpha})_{xy} + (hv_{z_\alpha})_{yy}] \end{aligned} \tag{2.44}$$

In that case, dispersion is deactivated when the Froude number is superior to 1.0.

Chapter 3

Numerical study of the Tohoku tsunami impact on the breakwater of Port of Soma

---

The first work presented in this PhD is the 2-dimensional numerical simulation of the Tohoku tsunami in the Sendai Bay. This study aims to model the propagation of tsunami waves, especially undular bores observed in this bay, and investigate the stability of the offshore breakwater located in Soma. A Boussinesq model (BOSZ) is first validated to simulate the transformation of long waves on undular bores. After that, this code is run to study the arrival of the Tohoku tsunami (first and second waves) to the port of Soma and the interaction between waves and the breakwater. This chapter shows the loads induced by the impact of an undular bore on a composite breakwater that has not been investigated in previous works. This study was carried out in the third year of PhD since the bathymetric and breakwater data were collected during the first two years of doctoral work. A brief description of numerical models are presented again since this chapter is written to be sent for publication in the next months.

3.1 Introduction

The Tohoku tsunami caused great damages on many offshore vertical breakwaters ranging from the erosion of the rubble-mound to the partial displacement or total collapse of caissons. The literature review has shown that breakwater failure mechanisms were function of the tsunami wave types that vary along the Japanese coast according to the

bathymetry features (Mori & Takahashi (2012) and Mikami et al. (2012)). The Iwate coast, characterized by deep water depths and steep slopes, was mainly impacted by tsunami overflow leading in particular to the failure of the world's deepest breakwater at Kamaishi (caisson height between 10 m and 15 m and depth ranges from 60 m to 25 m). In the shallow waters of the Sendai bay, observations showed that breakwaters protecting harbour entrances were impacted by short wave trains resembling undular bores as shown in fig.3.1.

The propagation of undular bores has been observed in many cases: tides propagating in estuaries (Bonneton et al. (2015), Chanson (2010)), dam-break flows (Treske (1994), Soares Frazao & Zech (2002), Kim & Lynett (2010)) and long waves as tsunamis propagating in shallow waters (Matsuyama et al. (2007), Madsen et al. (2008)). In the work presented in Madsen et al. (2008), the phenomenon of disintegration of long waves into wave trains is investigated. The authors identified that when a long wave enters in shallow waters, asymmetry builds up, the wave front becomes very steep and dispersion may lead to an undular bore depending on the bathymetry.

The generation of undular bores while a tsunami wave approaches the coast have been observed during the boxing day tsunami in 2004 (Glimsdal et al. (2006), Horrillo et al. (2006), Grue et al. (2008), Arcas & Segur (2012)) and the tohoku tsunami in 2011 (Murashima et al. (2012), Saito et al. (2014), Baba et al. (2015)).

Glimsdal et al. (2006) and Horrillo et al. (2006) pointed out that the increase of the tsunami steepness in shallow waters enhanced dispersion generating undular bores during the Indian tsunami of December 26, 2004. They also showed that this phenomenon can not be reproduced by standard shallow water equations and non-linear and dispersive models are needed for accurate prediction in near-shore areas. In this way, the formation of undular bores in the shallow Strait of Malacca during the Indian tsunami of 2004 was numerically investigated by Grue et al. (2008) using the fully nonlinear dispersive method and the Korteweg-deVries equation. Two different wave heights (the original one and half of this height) were imposed finding that the wave train appeared for the same wave slope (0.0036 – 0.0038). The dominant period of short waves was observed to be slightly longer than 20s. In the Sendai Bay, helicopter videos (fig.3.1) show a clear undular bore arriving to the coast during the second wave of the Tohoku tsunami in 2011. Baba et al. (2015) used Boussinesq model (dispersive and non dispersive simulations) to reproduce the formation and propagation of the wave train in the bay. The dispersive simulation was able to model the tsunami undular bore, whereas the non dispersive test failed to reproduce the tsunami disintegration and gave a smaller wave amplitude during the shoaling. In terms of inundation, both simulations gave similar results. The role of

dispersion for several tsunami cases was analysed in Glimsdal et al. (2013). This work shows that the formation of undular bores may double the wave height near the coast.

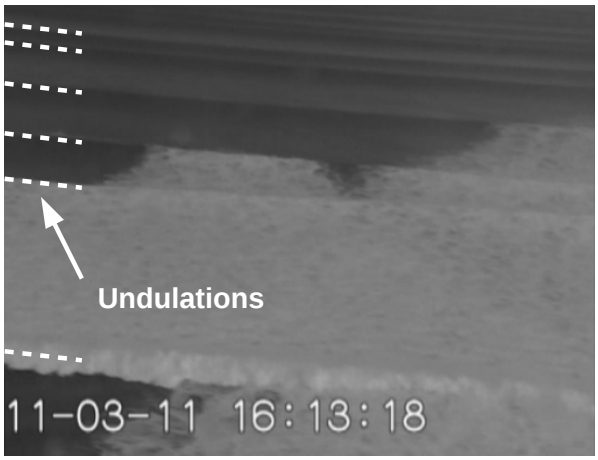

Figure 3.1: Second Tohoku tsunami wave transforming into an undular bore in Sendai Bay (Murashima et al. (2012)).

Focusing on tsunami impacts on coastal structures, several authors made significant efforts trying to assess pressures and forces using laboratory experiments (Cross (1967), Ramsden (1996), Asakura et al. (2003), Ikeno et al. (2007), Nouri et al. (2010), Guler et al. (2015), Kihara et al. (2015)) , or numerical models (Arikawa et al. (2012), Jianhong et al. (2013), McCabe et al. (2014)). Arikawa et al. (2012) run the RANS CADMAS-SURF/3D model to simulate the Kamaishi breakwater stability including the porous media under a realistic signal of the Tohoku tsunami obtaining a very good agreement with large-scale experiments. The authors concluded that the main causes of failure were the water level difference and scouring of the foundation. Further investigations on the Kamaishi breakwater failure are presented in Bricker et al. (2013) where different turbulence models are tested in the RANS InterFOAM VOF code. In the latter study, the bearing pressure on the foundation at the caisson heel was calculated finding that another major cause of breakwater failure could be the punching failure of the rubble-mound.

On the other hand, researchers as Hsiao & Lin (2010) chose solitary waves to experimentally and numerically investigate tsunami impinging coastal structures. In this work, a model based on the RANS equations was successfully validated to simulate forces and free surface for three different solitary wave impacts: the wave collapses before arriving to the seawall, the wave collapses directly into the seawall, the wave collapses after overtopping the seawall. In Jianhong et al. (2013), a VARANS model combined with a Biot

model was used to investigate tsunami impacts on a vertical breakwater. Pressures on the caisson, rubble-mound and seabed are given by these simulations in which solitary waves are also used to approach tsunamis. Similarly to these studies, Jiang et al. (2016) carried out small-scale laboratory experiments of tsunami-like solitary waves impacting a rectangular seawall that were used to validate an OpenFOAM model solving the RANS equations. Then, numerical experiments were conducted to investigate the flow field and wave pressures in function of the seawall dimensions and wave height. Boussinesq models have been used to investigate the wave-structure interaction by several authors (Hu et al. (2000), Engsig-Karup et al. (2008), Roeber et al. (2010)), but few studies have used these models to analyse breakwater stability due to tsunami impacts. In McCabe et al. (2014), the SWAB model solving the Boussinesq equations was shown to be able to properly reproduce run-up, overtopping and forces on vertical walls due to tsunamis approached by solitary waves, but it failed simulating impulsive loads.

Most of the studies of tsunami-structure interaction used the contradictory solitary wave approach whereas this kind of waves seems to better represent storm wave impacts than tsunamis (Madsen et al. (2008)). Furthermore, there is no published work about forces applied on a breakwater by tsunami undular bores. This paper aims to fill the gap of knowledge about the stability of vertical breakwaters submitted to the kind of tsunami waves that were observed during the Indonesian tsunami in 2004 and the Tohoku tsunami in 2011. The offshore breakwater of the port of Soma in the Sendai Bay, which failed due to the impact of the Tohoku tsunami, is numerically studied in this work. First, an 1-dimensional Boussinesq model (BOSZ) is used to generate and propagate the first and second tsunami waves recorded in 2011. The formation of undular bores in the Sendai Bay is also investigated. Then, a 2-dimensional VARANS model (THETIS), which is more widely used for wave-structure interaction, allows to study the failure mechanism of the Soma breakwater analysing the impact pressures and bearing stress at the caisson heel. For these simulations, the upstream boundary conditions, water level and fluid velocity, are given by the 1-dimensional BOSZ model.

The chapter is organized as follows. The numerical experiments carried out with BOSZ and THETIS are described in section (3.2). After this, the first part of section (5.3) shows the propagation of the first and second waves of the Tohoku tsunami. Then, the second part of this section focuses on the tsunami impact on the breakwater. A discussion of these results is proposed in section (5.4). Finally, the conclusion are drawn in section (3.5).

3.2 Methodology

3.2.1 Description of BOSZ model

BOSZ is the proposed model to investigate the transformation of tsunami waves into undular bores. The model is also used to simulate the interaction of waves with irregular bathymetries and offshore breakwaters. The BOSZ code has been shown to be an effective and consistent tool modelling wave propagation, reflection and flood events in Roeber et al. (2010) and Roeber & Cheung (2012). The Boussinesq-type equations presented in Nwogu (1993) written in conserved variables are used in this code (Roeber et al. (2010)).

BOSZ is a depth-integrated model and so wave overturning and breaking can not be described. To avoid numerical instabilities during the transition between subcritical and supercritical flows linked to excessive dispersion, BOSZ deactivates the dispersion terms to allow the Riemann solver to describe the breaking wave as a bore.

Obstacles as coastal structures in the BOSZ model should be integrated in the bathymetry. Permeability and porosity of dykes or breakwaters are not considered. Attention should be paid to the structure slopes in order to avoid numerical instability. BOSZ can handle a maximum slope of 1.0. Waves are generated giving free surface elevations at the left boundary. The wave amplitude time series can be simply imposed using an external file which includes time and free surface height. The wave velocity is automatically calculated depending on the flow depth ($v_{wave} = \sqrt{gH}$).

Validation case: Undular bore generation and propagation with BOSZ

The ability of BOSZ to model the generation of undular bores is tested with the laboratory experiments presented in Matsuyama et al. (2007). This study, which results were also used for numerical validation in Kim & Lynett (2010) and Grilli et al. (2012), aimed to analyse the propagation of long sinusoidal waves over shallow waters and their transformation into undular bores. The wave flume is $205m$ long, $3.4m$ wide and $4m$ deep. In this paper, the results of case 024 are used to validate the numerical model. The wave amplitude and period are respectively $0.03m$ and $20s$ and the continental shelf slope is 1/200. For the numerical simulation, we only simulated the nearest part to the coast (fig. 3.2) due to the lack of knowledge of the wave input. The wave input is analytically given in the paper but it does not correspond to the experimental data. Therefore, the free surface signal recorded at the beginning of the continental shelf during the experiments ($x = 80m$ of fig.3 in Matsuyama et al. (2007)) is imposed as boundary condition. The model grid size is 0.05 m.

The free surface elevations obtained with the laboratory experiments and BOSZ are

compared at two different locations in fig.3.3. At $x = 30m$ from the shoreline, the model accurately reproduces the two undulations on the top of the first wave, but the wave arrives slightly in advance compared to the laboratory experiments. For the second wave, this advance is reduced and the simulated wave train fits better with the experimental data. BOSZ properly predicts the undular bore formation and the propagation of undulations, even if small amplitude differences are observed ($\simeq 1cm$). The number and period of the undulations are also well reproduced with BOSZ. Closer to the shore ($x = 49.2m$), the BOSZ model allows to simulate the amplitude increase of undulations at the first wave and the simulated bore now moves slightly slower than in the laboratory experiments. At this location, the height of the second undular bore ($\eta = 0.05m$) decreased with respect to the previous analysed location ($\eta = 0.08m$). Such behaviour is well modelled by BOSZ despite slight discrepancies in the amplitude and period of short waves.

This validation case shows that the generation of undular bores from long waves and their subsequent evolution are overall correctly simulated by BOSZ despite slight inaccuracies when the undular bore is formed. These differences might be also linked to measure errors due to the small amplitude of waves.

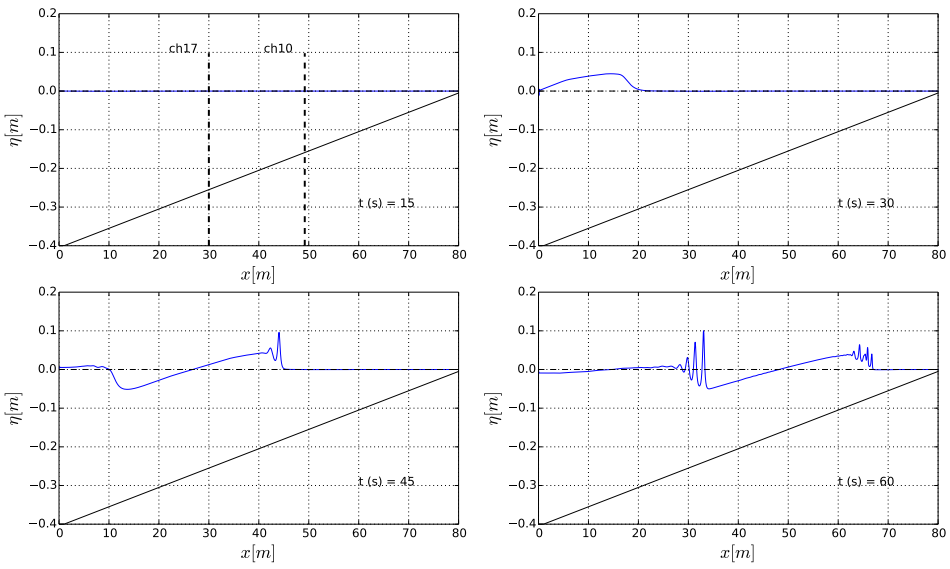

Figure 3.2: BOSZ simulation of the undular bore propagation presented in Matsuyama et al. (2007). The initial water level is set to $0m$. The free surface signal recorded at $x = 0m$ (see fig. 3 in Matsuyama et al. (2007)) during the experiments is imposed as boundary condition.

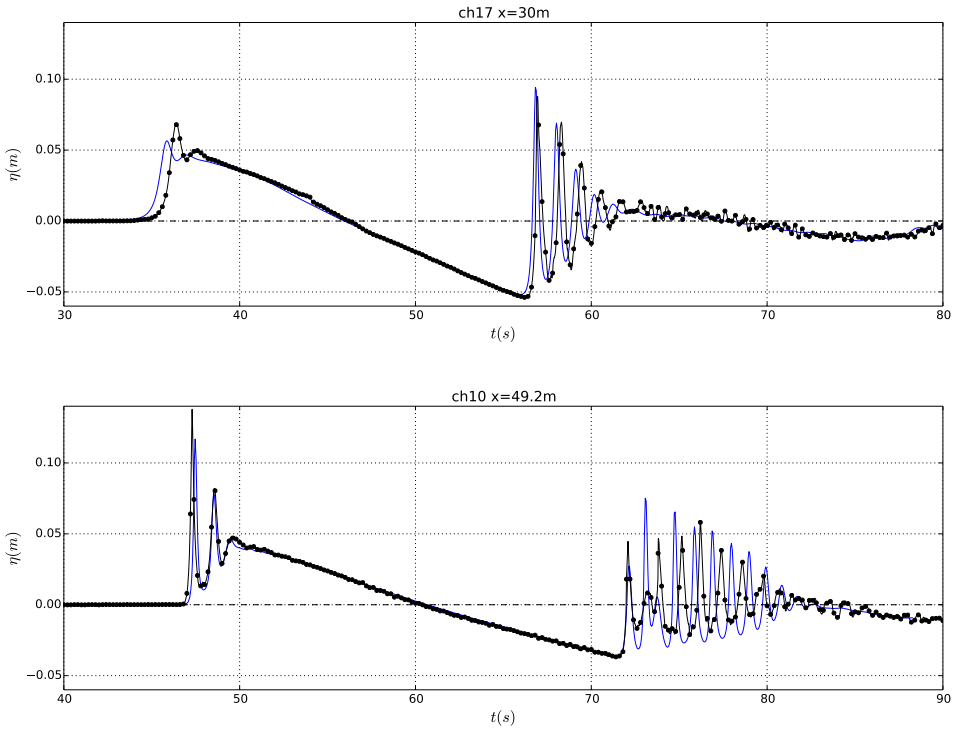

Figure 3.3: Free surface ($\eta(m)$) evolution in time at ch17 ($x = 30m$) and ch10 ($x = 49.2m$). Laboratory experiments (black) and BOSZ simulations (blue).

3.2.2 Description of THETIS

Numerical simulations with THETIS are used to investigate the interaction between waves and structures. This code solves the RANS (Reynolds-Averaged Navier–Stokes) equations with a VOF method to capture the interface evolution. The flow is considered incompressible and the continuity of fluid velocity is assumed through the interface. The turbulent flows are modelled using the $k-\epsilon$ model, which was already chosen in previous similar works (Nakayama & Kuwahara (1999), Hsu et al. (2002) ,del Jesus et al. (2012)).

A Volume of Fluid (VOF) technique allows to calculate the evolution of the volume fraction occupied by one of the fluids (i.e. water) in a cell. A VOF-TVD method is implemented in this simulations. A TVD scheme typically has two main properties: in the parts of the domain where the solutions are regular, it is equivalent to a high-order scheme that reduces diffusion, and in the parts where there are strong discontinuities it is a first order scheme that prevents oscillations.

Several papers (Desombre et al. (2012), Mokrani & Abadie (2016), Kazolea et al. (2016), Martin-Medina, Abadie & Morichon (2017), Martin-Medina, Abadie, Mokrani & Morichon (2017)) have shown an extensive validation of THETIS for the simulations of

wave propagation and impact in coastal structures.

3.2.3 Numerical experiments

BOSZ model set-up

The first numerical experiment consists in modelling in 1D (profile A-B in fig.3.4) the propagation of the Tohoku tsunami in the Sendai Plain using the BOSZ code. The model is 62 Km long and its set-up is described in fig.3.5. The initial water level is set to $-0.16m$ (relative to the mean water level), free surface height when the first tsunami wave arrived to the coast. A fine mesh of 10 m is used to properly reproduced the generation of the undular bore. The tsunami signal recorded in the GPS801 buoy (fig.3.6), which is the closest buoy to the studied area, is imposed at point B in the model. The period and amplitude (a_i) of the first wave are 20 min and 6 m, respectively. After the first wave, there is a significant water level drop up to -5 m, followed by the arrival of the second tsunami wave of 5 m height.

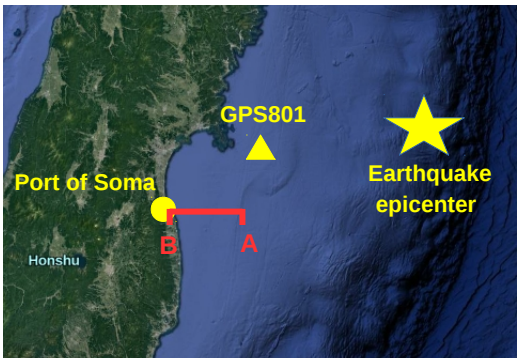

Figure 3.4: Location of the port of soma, profile A-B of the BOSZ simulation and GPS801 buoy in the Sendai Bay.

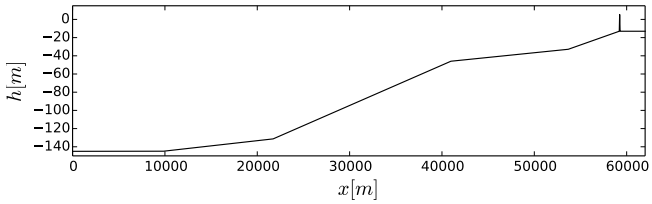

Figure 3.5: Numerical set-up (profile A-B) of the BOSZ simulations. The initial water level is set to $\eta = -0.16m$ and the tsunami signal recorded at GPS801 is imposed at the left boundary.

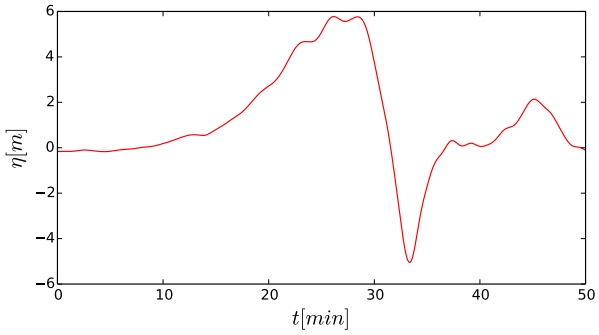

Figure 3.6: Tsunami signal recorded at the GPS801 buoy, the closest buoy to the port of Soma.

Two parameters are calculated to analyze the formation and propagation of undular bores: the maximum elevation slope (α_m) at the wave front and the Froude number (Fr). The maximum elevation slope, which has been already used in the study of tsunami undular bores (Grue et al. (2008)) and tidal bores (Bonneton et al. (2015)), represents the maximum local wave steepness of the wave front at a given time. The Froude number of the front, as in Bonneton et al. (2015), allows to characterize the bore intensity and flow regime. These parameters are defined as follows:

$$\alpha_m = \frac{(\frac{\delta\eta}{\delta t})_{max}}{c_b} = max(\frac{\delta\eta}{\delta x}) \tag{3.1}$$

$$Fr = \frac{|u_0 - c_b|}{\sqrt{gh_0}} \tag{3.2}$$

Where u_0 is the average fluid velocity before the bore arrives, c_b is the bore celerity, h_0 is the water depth at the wave front and η is the free surface height. Fig.3.7 illustrates the definition of maximum elevation slope calculated at the tsunami front.

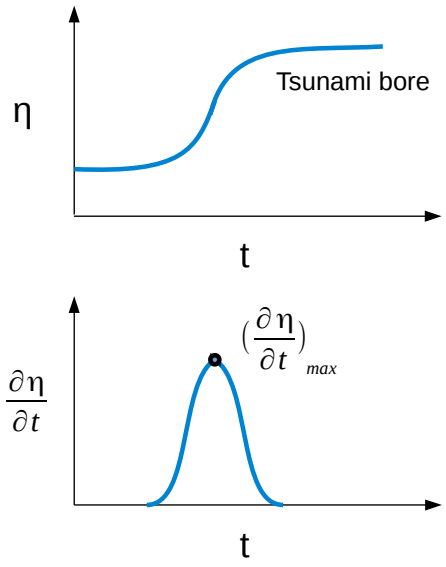

Figure 3.7: Definition of the maximum elevation slope (α_m) at the wave front calculated for the first and second wave.

THETIS model set-up

The set-up of THETIS model and the verical breakwater dimensions are represented in fig.3.8. More informations about the Soma breakwater can be found on the field surveys carried out by the National Institute for Land and Infrastructure Management in Japan. The model is $4500m$ long focusing on the wave arrival to the near-shore area and its interaction with the offshore breakwater. The water level and velocity given by BOSZ are imposed at left. An open boundary condition is established at right. The numerical domain is discretized in 439501 elements by using an irregular mesh whose size is minimum ($20\ cm$) at the breakwater. In the THETIS simulations, the first and second tsunami waves are modelled separately to avoid numerical issues at the boundaries. The initial free surface is set to $-0.16m$ and $-6.5m$ for the two simulations, respectively.

Stability computation

The Safety Factors regarding sliding (S.F.) and overturning (S.F.m) are calculated for the two models and give informations about the caisson stability during the impact:

$$S.F. = \frac{\mu(W - F_u)}{F_h} \tag{3.3}$$

$$S.F.m = \frac{M_w - M_u}{M_h} \tag{3.4}$$

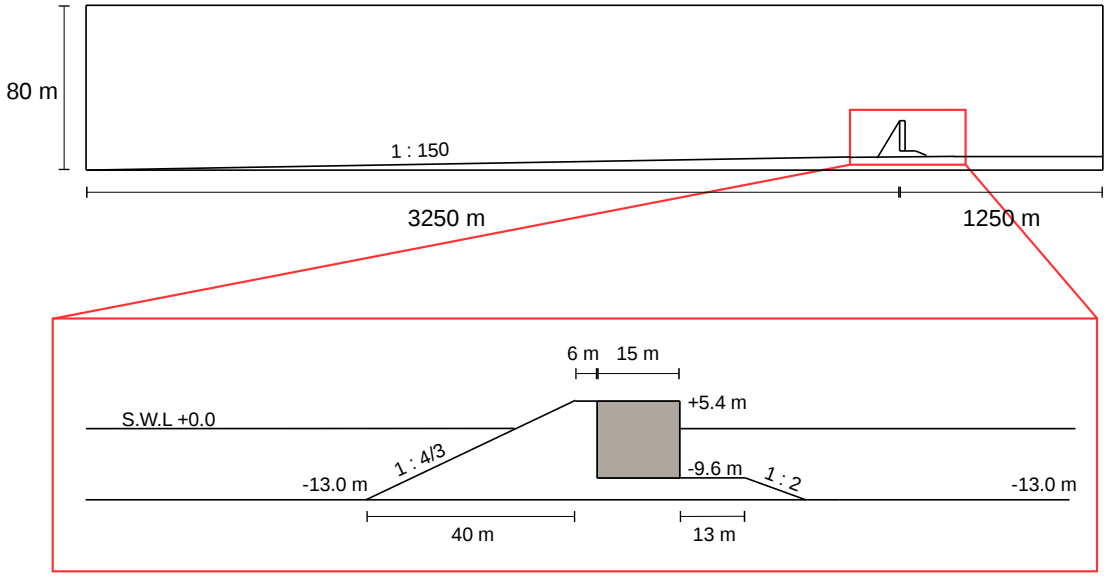

Figure 3.8: Numerical set-up of the Navier-Stokes simulations. The dimensions of Soma vertical breakwater and its porous rubble-mound.

Where μ is the friction coefficient ($\mu = 0.6$), F_h the horizontal force, F_u the vertical force, M_h the horizontal moment, M_u the vertical moment, W the dry weight of the caisson and M_w the stabilizing moment generated by this weight.

The bearing pressure on the breakwater foundation at the heel of the caisson is calculated following the formulation presented in Goda (2010) during the tsunami impact for BOSZ and THETIS. The normal force W_e of the caisson taking into account the uplift induced by the tsunami is given by:

$$W_e = W - F_u \tag{3.5}$$

The moment M_e about the heel of the caisson due to the resultant force of all the loads applied on the caisson reads as follows:

$$M_e = M_w - M_u - M_h \tag{3.6}$$

Knowing the normal force W_e and the moment M_e, the horizontal distance t_e between the heel and the normal force W_e is given by:

$$t_e = \frac{M_e}{W_e} \tag{3.7}$$

Finally, the bearing pressure at the heel p_e is calculated by the following expression (Goda (2010)):

$$p_e = \begin{cases} \frac{2W_e}{3t_e} & \text{if } t_e \leq B/3 \\ \frac{2W_e}{B}(2 - 3\frac{t_e}{B}) & \text{if } t_e > B/3 \end{cases}$$

Where B is the width of the caisson.

3.3 Results

3.3.1 Tsunami propagation

Modelling of the first and second tsunami waves

The free surface elevations computed with the BOSZ model at different times are illustrated in fig.3.9. The first tsunami wave is characterized by a length of $30Km$ and a low steepness. When reaching the breakwater, the first wave starts to overtop ($t = 3500s$) the structure without generating an impulsive collision. No undulation are observed on the top of this first wave. After the first tsunami wave, there is a water level drop followed by a second wave. Unlike the first wave, this second wave becomes shorter and steeper while approaching the coast and clear undulations start to appear at the front at $14Km$ (in the middle of the flat region) from the breakwater. These waves are very short ($\simeq 100m$) and present a large amplitude, around $10m$ ($t = 4250s$) for the first undulation. The height of the second tsunami wave is $5m$ near the shore ($t = 3500s$), but this height is doubled ($10m$) when the undular bore is generated ($t = 4000s$).

Fig.3.10 displays the time evolution of the free surface elevation from offshore to near-shore areas. These plots show little changes at the four first locations when the bathymetry is deep enough. When the water depth decreases, differences are more significant and the tsunami waves become slower and steeper leading to higher values of η. The second wave front becomes almost vertical while arriving the low-slope region ($x = 40000m - 53000m$) and the first undulations appear at $x = 45000m$. After its formation, the amplitude of short waves rapidly increases at $x = 50000m$ and $x = 55000m$. Between $x = 25000m$ and $x = 50000m$, the reflected first wave is observed going back to the ocean after meeting the breakwater and interacting with the incoming waves.

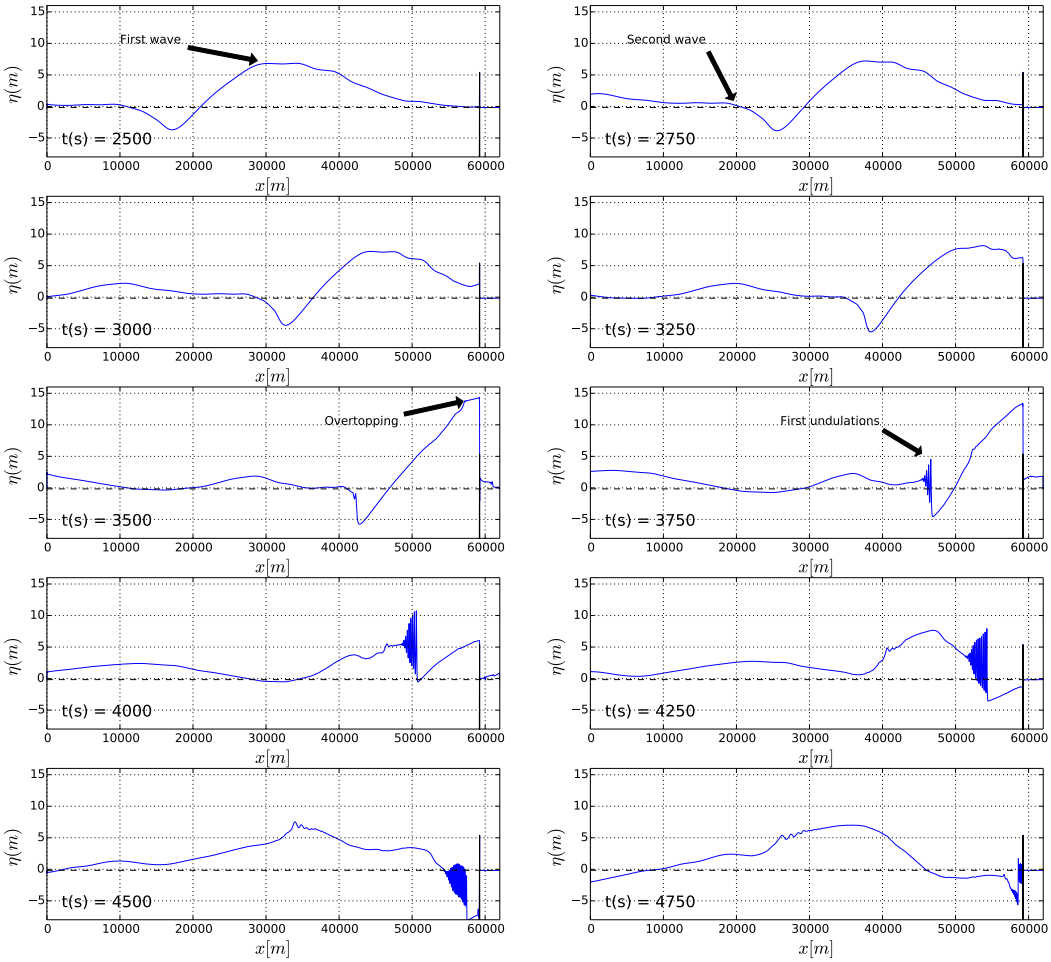

Figure 3.9: Propagation of the first and second tsunami wave with BOSZ. The initial water level is set to $-0.16m$. Time from the beginning of the simulation.

Tsunami undular bore generation

The variation of the maximum elevation slope of the front (α_m) in space and the first undulation bore amplitude adimensionalized by the initial first tsunami wave amplitude (a_u/a_i) are represented in fig.3.11 for the first and second tsunami waves. The first tsunami wave (top) presents an initial α_m of 3×10^{-4} that slowly grows up to the value of 3×10^{-3} when the wave interacts with the breakwater. As shown before, this first wave induced an overflow event and did not involve any undulation. For the second tsunami wave (bottom), the initial α_m is 9×10^{-4}. The values of α_m rapidly increases with x and the first undulations appear when entering in the flat region at $x = 40000m$. α_m reaches 9×10^{-3} when the tsunami undular bore starts to be generated, value that has never been reached in the first wave. Once the short waves appear on the top of the second wave, their amplitude keeps increasing up to $x = 52000m$ when a_u/a_i diminishes

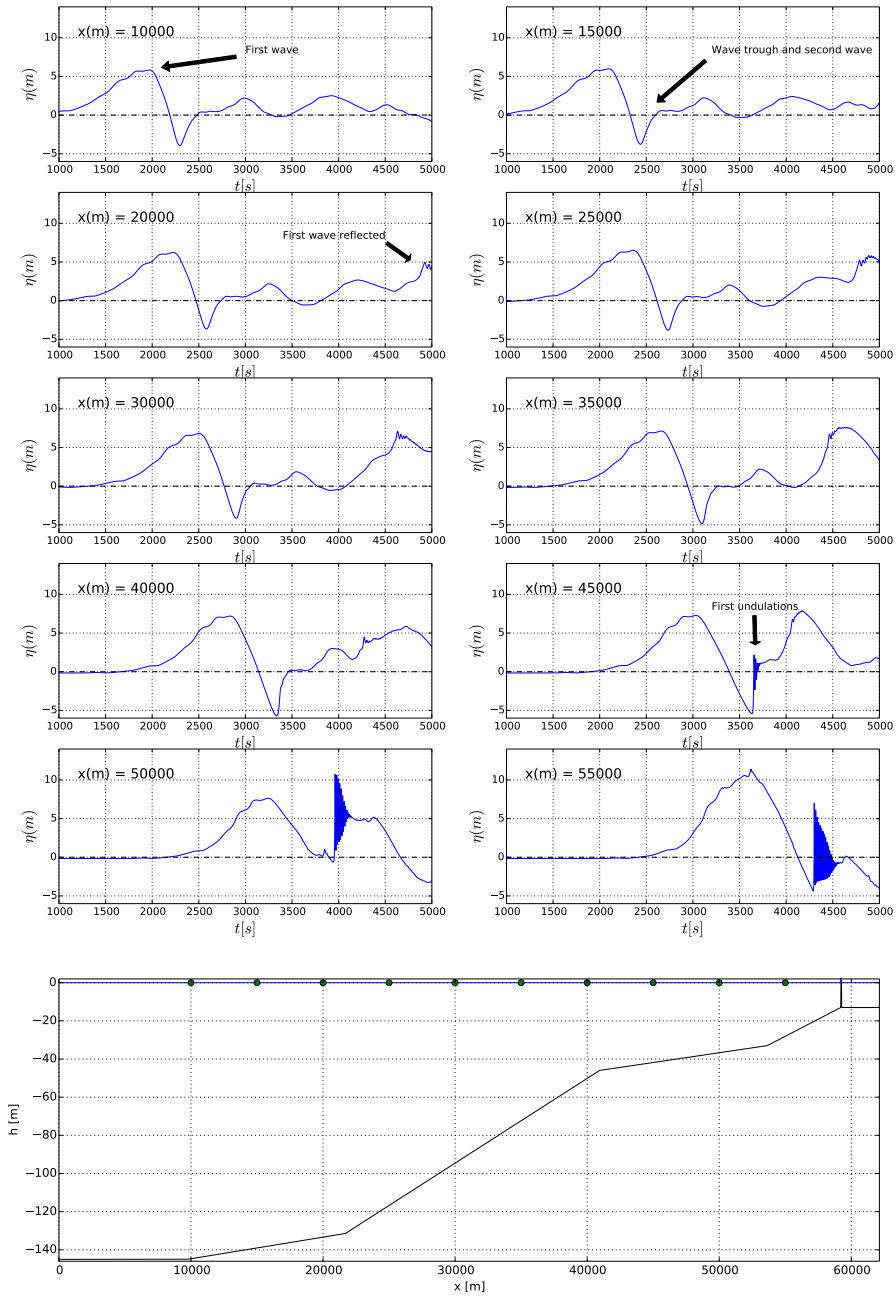

Figure 3.10: Tsunami free surface ($\eta(m)$) evolution in time computed with BOSZ at different locations along the profile A-B.

near the shore due to the breaking process.

Fig.3.12 shows the spatial evolution of the Froude number and α_m. For the two cases, slope changes cause sudden Froude variations. The Fr number for the first wave increases with x and reaches the value of 1.04 at the end of the first slope region ($x = 22000m$).

After this, there is a sudden augmentation of the Fr (more than 1.1) when the wave travels over the second and steepest region. In the third and flat region, the wave slows down and the Fr decreases again up to the value of 1.04. From this moment, the Froude number progressively grows while approaching the coast getting a maximum value of 1.2. A similar evolution of Fr, but with overall lower values, is obtained for the second tsunami wave while propagating far from the coast. In the second slope, an interesting phenomenon is observed where the Froude remains quasi-constant along these $16Km$. After the second slope region, the Fr number decrease below 1. At this location ($x = 42000m$), the wave transforms into an undular bore and Froude number rapidly increases up to the value of 1.27 close to the coast. It is important to mention a Fr drop is observed when the reflected first wave meets the second wave advancing towards the coast at $x = 49000m$.

3.3.2 Tsunami impact on the offshore breakwater

In this section, the Navier-Stokes simulations (THETIS) are also used to investigate the impact of the first and second tsunami wave on the offshore breakwater of the port of Soma. First, the propagation and interaction of the tsunami with the structure ($< 2Km$) is analysed. Then, the impact forces, overturning moments, S.F. values and bearing pressure are calculated in order to clarify the failure mechanism of the breakwater due to Tohoku tsunami impact.

Undular bore interaction with the breakwater

The free surface elevations of the undular bore computed with THETIS are represented at different times in fig. 3.13. Let us recall that the free surface and velocity given by BOSZ are used as input in the Navier-Stokes simulation. For the simulation of the second wave in THETIS, water velocities given by the BOSZ model are initially imposed in the THETIS domain.

For the first wave, fig.3.13(a) shows that the first tsunami wave does not present any short waves and generates a constant overflow. The flow over the caisson gives birth to a large eddy at the back side of the breakwater. The maximum height reached at $t = 3500s$ is $15m$.

Subsequently, the free surface of the undular bore arriving to the vertical breakwater are shown in fig.3.13(b). At $t = 4500s$, the first two waves of the undular bore have broken far from the coast ($2.5Km$) and generated a turbulent front bore in THETIS. When the undular bore reaches the breakwater ($t = 4700s$ and $4800s$ in fig.3.13(b)), the impact process appears to be complex with a mixed front of water and air impacting the

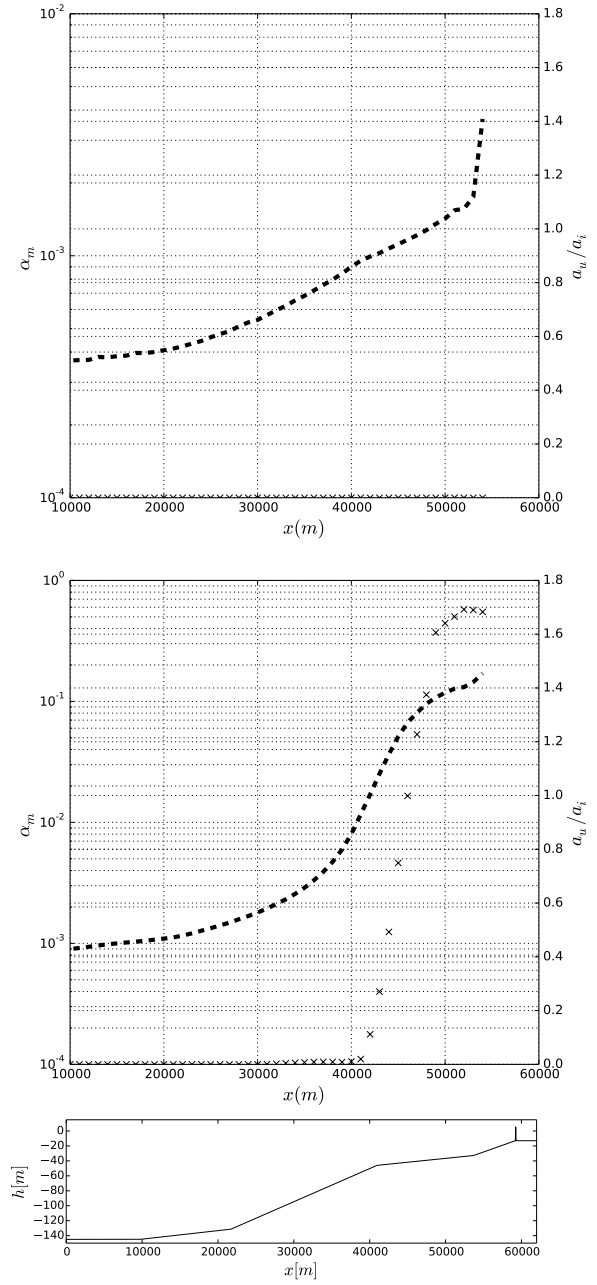

Figure 3.11: Evolution in space of the maximum elevation slope α_m (- -) and first undulation bore amplitude a_u/a_i (x x). First (top) and second (bottom) tsunami waves.

breakwater ($t = 4700s$). The maximum undulation amplitude is $4m$ near shore. These undulations ride on the top of a bore body whose height is about $5m$. After the impact caused by the undulations, the tsunami body back side reaches the breakwater and is reflected ($t = 4900s$ and $5000s$).

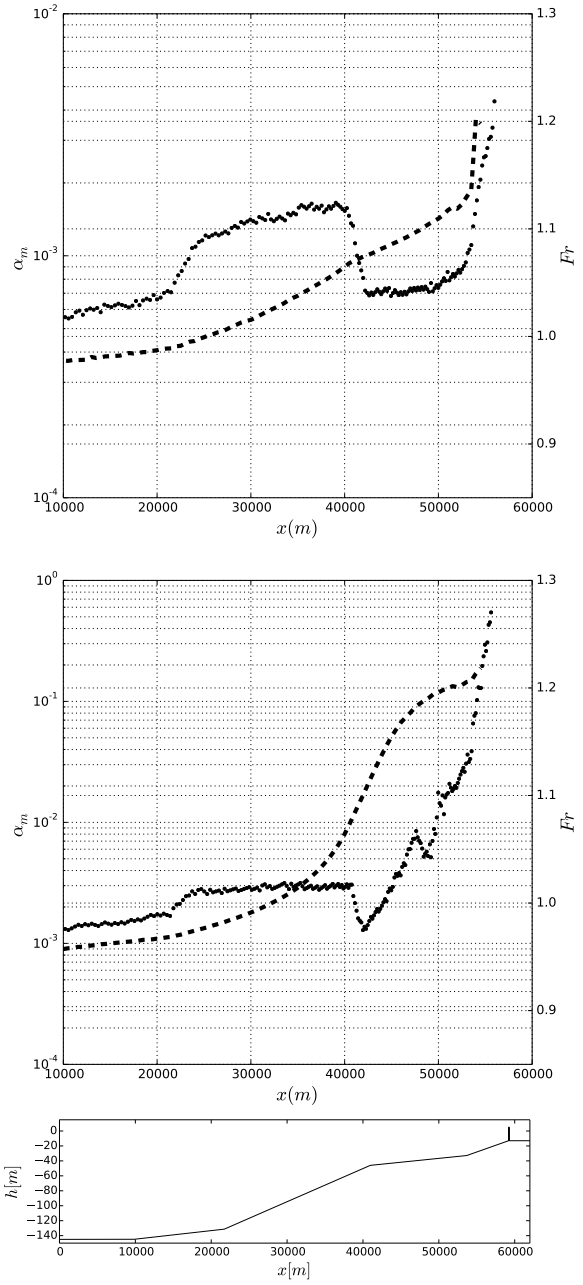

Figure 3.12: Evolution in space of the maximum elevation slope α_m (**- -**) and Froude number Fr (**. .**). First (top) and second (bottom) tsunami waves.

Impact forces, overturning moments and bearing pressure

The horizontal force, uplift and the safety factors calculated for the first and second tsunami wave are plotted in fig.3.14.

Regarding the first wave overtopping, THETIS gives a maximum horizontal force (F_h) of $2400KN$. Significant uplift force values are also obtained ($F_u \simeq 2600KN$) due to the

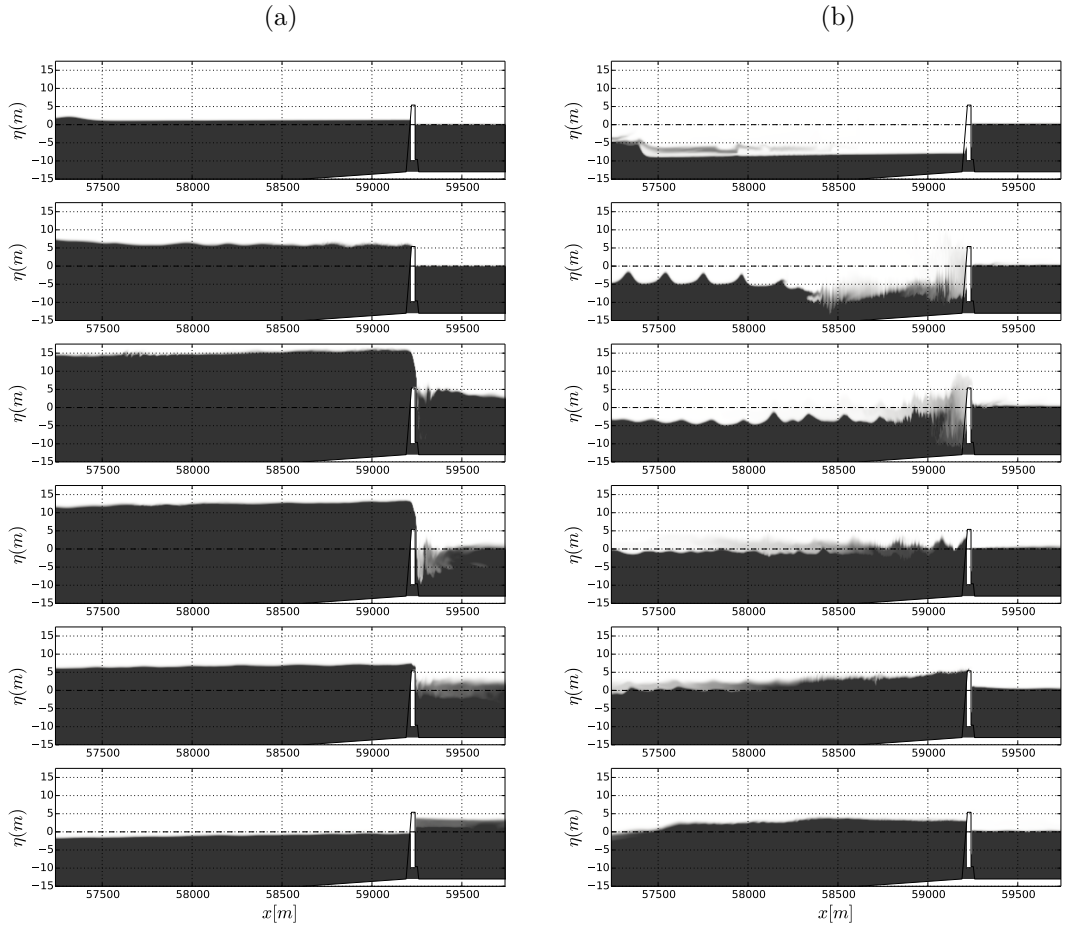

Figure 3.13: First (a) and second (b) tsunami wave (undular bore) propagating near-shore computed with THETIS. Water (dark gray) and air (white). $t = 4500s$, $4600s$, $4700s$, $4800s$, $4900s$ and $5000s$ from top to bottom.

pressure inside the rubble-mound. Fluctuations are observed in the uplift force evolution in time which are caused by the overflow. As mentioned before, this flow generates a large eddy in the harbour side of the breakwater which acts directly on the rubble-mound toe and produces significant pressure variations at this part. For the second wave, the force signal can be divided in two parts: the impact of the tsunami undulations and the arrival of the tsunami body. For the first part, the impact of the undular bore short waves are clearly observed in the force signal where the maximum values are around $500KN$. The uplift force signal also shows the successive impacts of these undulations with a maximum load of $1300KN$. After this, for the second and longer part, larger horizontal force values are obtained during the impact of the tsunami body ($F_h = 900KN$) than during the first part. Such behaviour is also found for the uplift force with maximum

values of $1750KN$.

Once the forces applied to the caisson have been calculated, the Safety Factor related to sliding can be deduced in order to analyse the breakwater stability. We also take into account the stabilizing loads generated by water at rest at the harbour side and the water mass above the caisson due to the overtopping discharge. Safety Factor below 1.0 means that the caisson might be in unstable condition. For the first wave, S.F. values slightly below 1.0 are obtained during a long period of time ($200s$). Higher S.F. values are obtained for the undular bore (around 4) associated to the second wave.

The caisson stability with respect to overturning is plotted in fig.3.15. The overturning moments due to the destabilizing forces present the same behaviour in time than the horizontal and uplift forces illustrated in fig.3.14. The Safety Factor associated to overturning (S.F.m) is calculated as previously taking into account the stabilizing moments generated by the still water at the harbour side and the overtopping discharge. S.F.m values above 1.0 (a minimal value of 1.4) are obtained during the arrival of the first wave. For the second wave, S.F.m values far from the stability limit of 1.0 are estimated (7.0 is the minimal value).

The time evolution of the bearing pressure at the heel of the caisson is shown in fig.3.16. For the first wave, the highest pressure ($780KPa$) is obtained when the overtopping discharge is maximum. This value does not exceed the critical value of $800KPa$ (Uezono (1987)), but the design limit of $600KPa$ (Goda (2010)) is overpassed for a long period of time ($300s$). For the second wave transformed into an undular bore, as for forces and moments, the bearing pressure is less significant than for the first wave and does not overpass the design limit ($\simeq 300KPa$).

3.4 Discussion

This study shows how an undular bore was generated in the Sendai Bay due to the arrival of the second wave of the Tohoku tsunami and why such phenomena was not observed for the first wave. After this, the impact of both tsunami waves into the offshore breakwater of the port of Soma was investigated. Numerical simulations solving the Boussinesq equations (BOSZ) allowed to analyse the first and second tsunami wave evolution in function of the maximum slope of the front and Froude number. The arrival of the Tohoku tsunami to Sendai Bay coast was already studied in previous studies (Baba et al. (2015) and Murashima et al. (2012)), but the present study focused on the generation mechanism and the evolution of the tsunami undulations in the bay. Once the propagation of the first and second tsunami waves is shown, we studied the stability of the

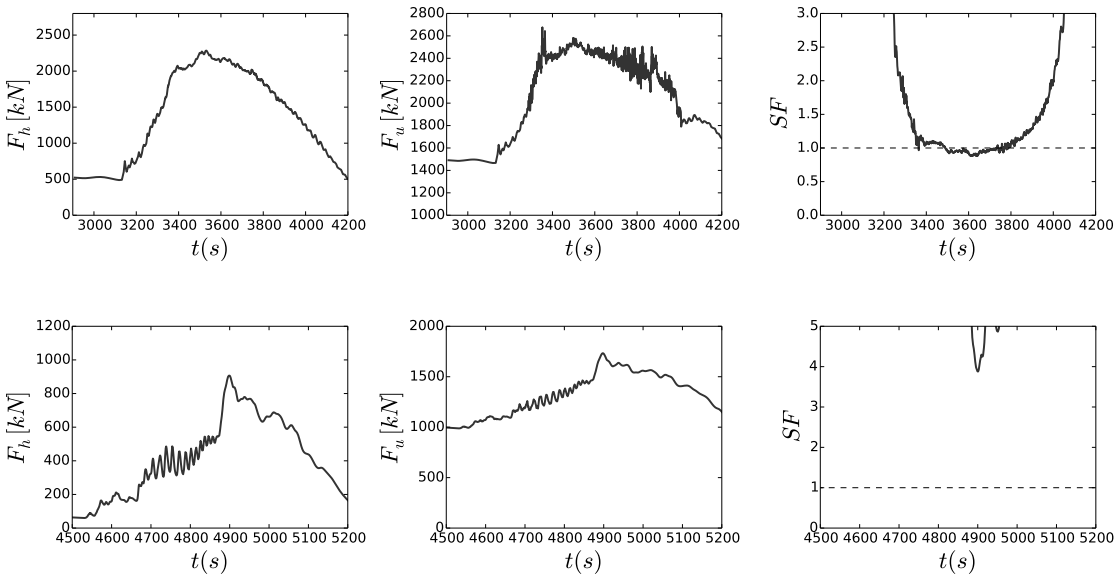

Figure 3.14: Horizontal and uplift forces and S.F. values obtained with BOSZ (blue) and THETIS (black) for the first (top) and second wave (bottom).

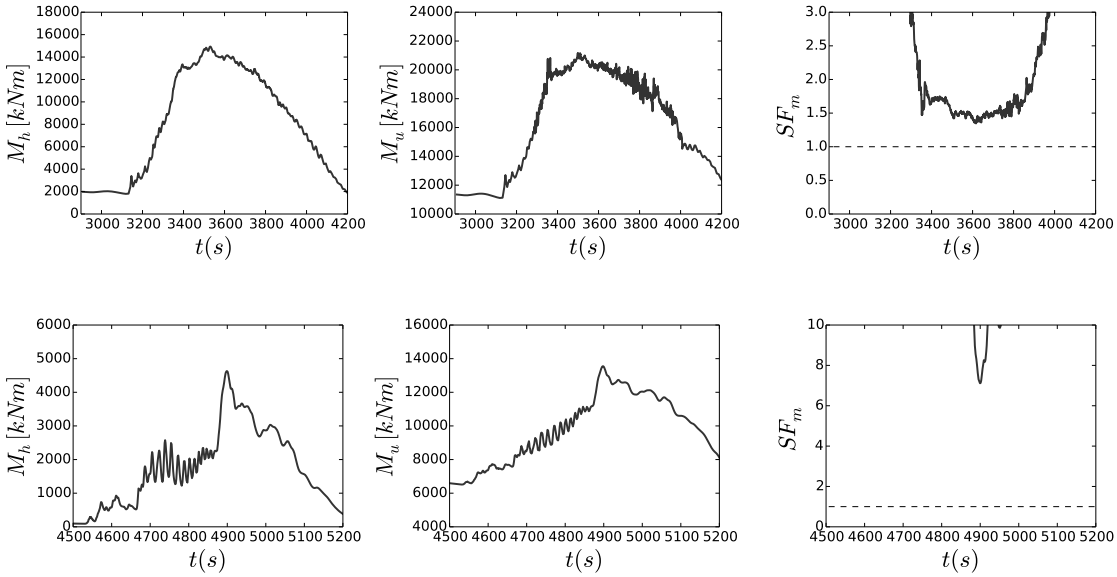

Figure 3.15: Horizontal and uplift moments and S.F.m values obtained with BOSZ (blue) and THETIS (black) for the first (top) and second wave (bottom).

Soma breakwater submitted to the impact of these waves. To our knowledge, this is the first time that the tsunami undular bore interaction with a vertical breakwater is studied in a real configuration. A 2-dimensional Navier-Stokes model (THETIS), commonly proposed to investigate wave-structure interaction problems, was used to investigate the

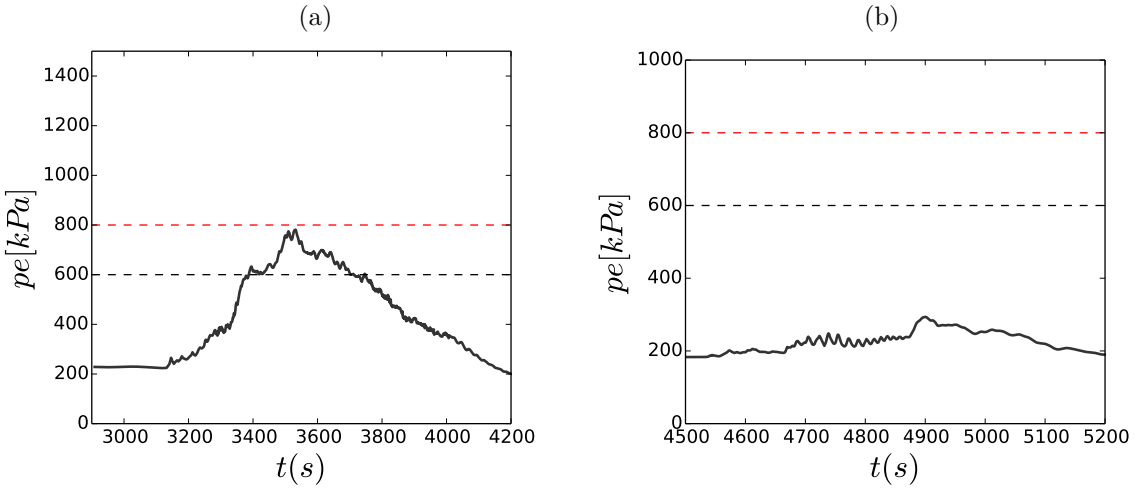

Figure 3.16: Bearing pressure estimated with BOSZ (blue) and THETIS (black) for the first (left) and second wave (right). Design bearing stress (- -) and critical bearing stress (- -).

efforts on the structure induced by the first and second tsunami wave. The water level and fluid velocity provided by BOSZ are imposed as boundary conditions in THETIS.

Comparing to previous studies (Glimsdal et al. (2006), Horrillo et al. (2006), Grue et al. (2008), Saito et al. (2014)) about the tsunami propagation, the dispersion was also shown to play a key role on the transformation of wave regime into undular bore regime when the Tohoku tsunami propagated in the Sendai Bay. The first tsunami wave did not present any undulations even if the wave became shorter and steeper ($\alpha_m = 3 \times 10^{-3}$ close to the breakwater) but not enough to give birth to an undular bore. In contrast, for the second wave with an initial maximum elevation slope (α_m) of 9×10^{-4}, a clear undular bore is generated when α_m increases up to the value of 9×10^{-3}. To clarify if this value of α_m is a limit value for the formation of undular bores in Sendai Bay, two additional numerical tests with BOSZ have been carried out imposing half and double the free surface height of the original tsunami signal. For these cases, the initial α_m are respectively 4.5×10^{-4} and 1.8×10^{-3}, and the undular bores appear again when α_m reaches the values of 9×10^{-3} and 1×10^{-2}. These values are similar to what we obtained for the original tsunami input: $\alpha_m = 9 \times 10^{-3}$. This is consistent with the numerical study of Grue et al. (2008), where the authors showed that undular bores were generated in the Strait of Malacca when the maximum elevation slope exceeded a limit value $(0.0036 - 0.0038)$ for two cases with different wave amplitudes ($5.2m$ and $2.6m$).

Looking at the Froude number evolution in space, we observed that it rapidly increased after the formation of the undular bore while it remained relatively constant for the first wave without undulations. The Fr number at the moment of the undular bore formation

was about 1.0 and the amplitude of undulations kept increasing up to a Fr of 1.2. For values higher than this Fr, the height of short waves started to break. Such behaviour was reported by Treske (1994) and Soares Frazao & Zech (2002) where undulations were generated for Fr between 1.0 and 1.28 and for higher Fr numbers, the undular bores led to steep turbulent fronts. The first tsunami wave also presented Fr values above 1.0 but the front did not become steep enough (low α_m) to form an undular bore. This confirms that the α_m parameter marks the start of the undular bore generation and the Fr characterises the type of wave regime.

Focusing on the tsunami interaction with the breakwater, the largest forces, overturning moments and bearing stress are obtained for the overtopping generated by the first wave. This is mainly due to a high water level (more than $10m$ above the caisson top) during the tsunami overflowing that is prolonged for a long period of time ($\simeq 10min$). Sliding safety factor values below 1.0 were obtained during the first part of the event. In contrast, it seems that during the second wave, the undular bore did not impact the breakwater in the worst scenario and higher S.F. values ($\simeq 4$) were obtained. Even if the structure was almost completely exposed due to the level decrease, the front undular bore broke at $2Km$ from the structure which implies that much energy of the impact was presumably dissipated far from the breakwater. Consequently, the breakwater failure would apparently occur during the overtopping generated by the first wave. However, the S.F. values of the first wave ($0.9 - 1.0$) are not low enough to explain the damages observed during the Tohoku tsunami. This lead us to investigate also other failure processes. We found that excessive bearing pressures generated at the heel of the caisson and significant overturning moments could play a key role weakening the rubble found and favouring the caisson destabilization. Furthermore, the large tsunami overtopping during the first wave could generate scouring of the harbour side of the rubble-mound and diminish the adherence between caisson and foundation.

It is important to mention that the tsunami signal imposed on the BOSZ simulation was recorded in the north of Sendai Bay (GPS801) while Soma is located in the south of the bay. Obviously, closer results to the reality would be obtained if the tsunami signal were recorded closer to the studied area. However, we consider that using the tsunami signal of GPS801 as input in these simulations is acceptable to reproduce what was observed in Soma since there is not significant bathymetry variations between the two locations. We only focused on the 2011 tsunami wave, but it could be also interesting to study the formation of undular bores with different tsunami periods and heights. As other undular bore impact scenarios might be more dangerous in terms of breakwater stability.

The first part of this paper focused on the propagation of the Tohoku tsunami waves in Sendai Bay. The numerical results with BOSZ (Boussinesq model) have shown that the second wave transformed into an undular bore as reported in previous research works and helicopter videos. The importance of the maximum elevation slope has been demonstrated for the formation of tsunami undulations. After that, this study also showed the interaction between the Tohoku tsunami and the offshore breakwater of Port of Soma. A RANS model (THETIS) was used to clarify the causes that might induce the failure of this structure: large overtopping during the first wave, bearing pressures reaching the design limit and significant overturning moments.

3.5 Conclusions

The propagation of the Tohoku tsunami in Sendai Bay has been numerically shown in this study. We have also investigated the impact of the tsunami waves on the offshore breakwater of the port of Soma. The following main conclusions can be drawn from this study:

- Numerical validation: BOSZ (Boussinesq) was validated to model the formation of tsunami undular bores and their propagation towards the coast.

- The generation of undulations on the tsunami top. The second tsunami wave transformed into an undular bore, while the first wave did not present any undulations due to its long period and very low steepness. The first short waves started to appear at $14Km$ from the breakwater in the low-sloping region when the maximum elevation slope (α_m) of the tsunami front overpasses the value of 9×10^{-3}. For the first wave, this limit was not reached and undulations could not develop at the front.

- Propagation of the undular bore in Sendai Bay. Once the tsunami undulations were generated (Fr about 1.0), the amplitude of these short waves increased while travelling towards the coast (up to $Fr = 1.2$). When the tsunami arrived to nearshore areas, its strong interaction with the ocean bottom led to a diminution of amplitude of the undulations.

- Tsunami overtopping due to the first tsunami wave. As no undulations were observed during the arrival of the first wave, the breakwater was not submitted to impulsive impacts. But it was overtopped by this first wave for several minutes. The forces, moments and bearing stress calculated with THETIS reached high values due

to the large overtopping. The safety factor values illustrated that the breakwater caisson would have been likely destabilized after this first tsunami wave.

- Tsunami undular bore impact: Forces and moments applied to the caisson and SF values. During the impact, two phases could be distinguished: a first one due to the undulations and another one due to the tsunami body. The efforts submitted by the tsunami undular bore have been shown to be less significant than for second phase. Sliding and overturning S.F. values have been computed. The minimal values, obtained during the second phase, were above one, so apparently the breakwater would not have failed due to the second wave impact.

- Bearing pressure at the heel of the caisson. We have studied the largest pressure on the foundation generated during the tsunami. THETIS has given maximal pressure values of $780KPa$ for the first tsunami wave. Therefore, the bearing capacity of the soil ($600KPa$) is overpassed for a long period of time ($300s$). These excessive pressures at the heel of the caisson could have weakened the breakwater foundation diminishing the resistance against sliding which could also contribute to the caisson displacements found in 2011.

Chapter 4

Numerical simulation of flip-through impacts of variable steepness on a vertical breakwater

---

This chapter raised the question of studying singular wave impacts generated by tsunami undular bores or storms at a fine scale. The study focuses on the analysis of flip-through impacts which has been shown to be the most extreme kind of wave impact observed in the literature (e.g. Cooker & Peregrine (1992), Hofland et al. (2011)). The THETIS model is used as a numerical wave tank to analyse the influence of interface steepness on pressures and forces generated in the real configuration of a breakwater caisson. The numerical simulations consist in a solitary wave, which represents each undulation riding on the top of undular bores, propagating over a reef and impacting a breakwater caisson placed over a porous rubble mound. After careful validation, the model allows us to make an in-depth investigation of three flip-through impacts with different incidence angles at impact (least steep, medium steep and steepest flip-through impact). The understanding of the process of this extreme impact is improved by analysing velocities and accelerations for the three cases. Horizontal and uplift forces are calculated allowing to estimate the stability of the caisson. The flow field and pressure variations inside the porous rubble mound are also analysed in this part. This study has been sent for publication to the international journal Applied Ocean Research and was welcomed with favourable reviews.

4.1 Introduction

Wave impacts on breakwater caissons may generate high and variable pressures in space and time. The prediction of pressure distributions has been the main objective of several empirical studies (Minikin (1950), Goda (1974), Takahashi et al. (1994), Oumeraci et al. (2001), Cuomo et al. (2010)). Other authors applied CFD models to study the problem of wave impact or wave interaction with breakwater caissons (Hsu et al. (2002), Losada et al. (2005), Lara et al. (2008), Noar & Greenhow (2015), Wen et al. (2016)). So far, most published works aim to give a conservative envelope of the maximum horizontal and uplift forces submitted to the caissons, which is essential for breakwater design. But there is still a lack of knowledge of the impact dynamic at the wave scale.

Focusing on the wave impact dynamics, two phases can be distinguished on the pressure signal generated onto breakwater caissons: first, an impulsive component characterized by a very high magnitude and a short duration, followed by a longer part influenced by the pressure peak value. Impulsive forces have been identified as one of the main causes of coastal structure failure in Takahashi et al. (1992). They are generally associated to storm waves but tsunami bores are also susceptible to produce such violent impacts (Ramsden & Raichlen (1990), Hsiao & Lin (2010), Kato et al. (2006), Nistor et al. (2011)). Many researchers (e.g.,Kirkgöz (1991), Zhou et al. (1991), Oumeraci et al. (1992), Hattori et al. (1994), Hull & Müller (2002), Bullock et al. (2007), Khayyer et al. (2009), Abadie & Mokrani (2012)) highlighted that these impulsive pressures depend strongly on the wave shape at impact.

In general, vertical obstacles may be submitted to three breaking wave impact types: a very aerated impact corresponding to a broken wave; a second one presenting enclosed air between the wall and the wave; and finally, a last kind of wave impact where there is neither air pocket nor mixed air, also called flip-through impact. Bagnold (1939) first stressed the influence of entrapped air observing that pressures were greatest when the amount of air trapped by the wave was small. Mitsuyasu (1966) and Chan (1994) emphasized the sensitivity of peak pressure due to very small changes of parameters such as the kinematic of the breaking wave or the amount of entrapped air. Laboratory experiments were carried out in Hull & Müller (2002) obtaining similar pressure values for several breaking waves with a variable amount of entrapped air, the pressure peak being slightly higher for large air pockets which was contradictory to what was shown by Bagnold (1939). However, when the wave impacts without air trapping (flip-through), even higher pressure peaks can be generated as reported by Cooker & Peregrine (1990) and Cooker & Peregrine (1992).

The flip-through impact (hereinafter referred as FTI) is generated when the conver-

gence of the wave crest and trough flow at the wall is strong enough to give birth to a small scale ascending jet associated to accelerations orders of magnitude larger than in other parts of the wave. It is generated by near-breaking waves presenting very steep faces when meeting the wall. It is therefore an intermediate case between slosh impacts and the developed plunging breaking wave which traps air at the wall. Hattori et al. (1994) have illustrated the importance of the FTI in terms of loading on structures. In this experimental study, several flip-through cases were tested concluding that the most severe impact is produced by a near-breaking wave with a very steep face. Lugni et al. (2006) highlighted the existence of extreme pressures for the FTI. High upward accelerations of the characteristic jet were measured during the laboratory experiments. Lugni et al. (2006) identified three main steps characterising the flow evolution of a FTI: *Wave advancement* is the step when the wave approaches the wall; it is followed by the *focusing* stage, in which wave front and trough move toward each other, generating high vertical flow accelerations; finally, the characteristic upward moving jet is suddenly produced at the beginning of the *flip-through* stage. Bullock et al. (2007) found that low-aerated breaking waves generate higher pressure values than wave impacts enclosing a large amount of air (high-aerated). The low-aerated impacts are defined by containing little if any enclosed air between the wave interface and the structure, and they may, therefore, be considered as close to FTI. An experimental and numerical FTI on a sea-wall placed over an impermeable slope was investigated in Bredmose et al. (2010). The potential-flow model used for these simulations was able to reproduce well the FTI until the stage of jet formation. However, the nature of this model does not allow to simulate the formation of droplets and interaction of fluids observed after the phase of jet formation. Scolan (2010) computed FTIs with a potential-flow model using a desingularized technique. High pressure variations and extreme accelerations of the upward moving jet were reached in a very short time.

Former results obtained on FTI studies were confirmed by Kaminski et al. (2009) and Hofland et al. (2011) who carried out large scale experiments concluding that the most extreme type of impact in terms of peak pressure corresponds to the FTI case. But based on the same laboratory experiments, these authors also pointed out that strong slosh impacts close to FTI may generate intense and long pulsating loads on vertical walls. The literature showed that the limit between slosh impacts and FTIs is not always clearly defined. Cooker & Peregrine (1992) defined first the term "FTI" as corresponding to an impact for which the interface accelerates and finally "flips through" between the wall and the wave crest. Lugni et al. (2006) added that the fluid accelerations are on the order of $100 - 1000g$. Kaminski et al. (2009) and Hofland et al. (2011) tried to differentiate slosh

impact from FTI. These authors stated that the difference between these two types of impact resides on the position of the wave crest when wave trough fills up the impacted zone. In the case of the FTI (fig.4.1(a)), the wave crest is near the vertical obstacle and moves toward the trough converging to a point (focusing), while in the slosh impact (fig.4.1(b)), the wave trough flow goes up at the wall before the wave crest arrives. We will follow the initial definition of FTI given by Cooker & Peregrine (1992), implying a flip through interface motion and the generation of large acceleration in the rising jet compared to the wave acceleration field. So for us there will be non focusing and focusing FTI.

But behind definition inaccuracy, a gap in the knowledge may also be identified. It is still not clear how the pressure field vary for apparently very similar FTI. A related gap is linked to the structure stability and the type of impact (i.e. a longer or a quicker FTI?) which may produce the largest sliding. To answer these questions, one also have to take into account more realistic obstacles than the simple vertical wall almost always considered.

In the present work, we propose a numerical study of extreme non-aerated impacts of FTI type at wave scale in a realistic configuration (i.e. a vertical breakwater) involving a porous basis. The objective of this study is to: 1) give some answers to the question of pressure variability within the FTI class by analysing in detail the influence of the local interface inclination; and 2) document the whole pressure and flow field including the one in the breakwater rubble mound. A numerical model is used as a numerical wave tank to analyse this pressure variability, as well as the fluid dynamic. Solitary waves of a fixed height are used to generate different impact magnitudes. Pressure variations are caused by local interface changes in the wave impact obtained by slightly translating the caisson of the breakwater studied.

The chapter is organized as follows. The numerical experiments are described in section (4.2). The ability of the numerical model to simulate flows through a porous medium and FTIs is also shown. In section (4.3), the influence of the interface inclination angle on pressure distributions is analysed. All the results obtained in this part are discussed in section (4.4). Finally, in section (4.5), the conclusions of the study are drawn.

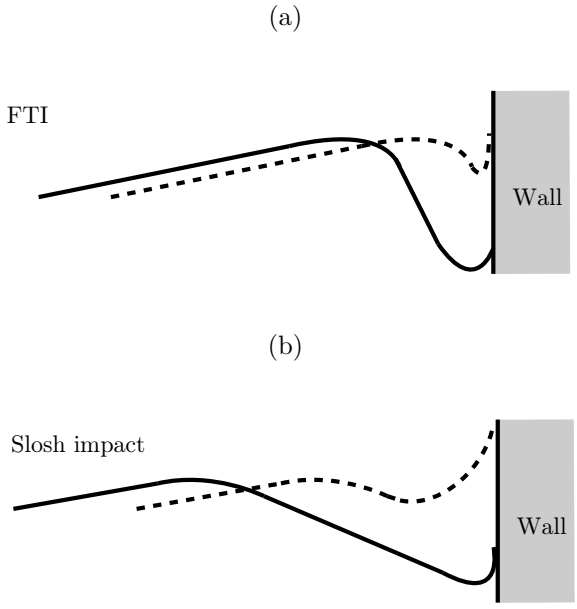

Figure 4.1: Water interface and position of the wave crest and through at the beginning (–) and at the end of impact (- -) – (a): FTI; (b): slosh impact.

4.2 Methodology

4.2.1 Description of the numerical experiment

Numerical simulations are carried out to analyse the pressures on a breakwater caisson submitted to FTI. The set-up of the simulations is described in fig.4.2. A solitary wave of $7m$ height is propagated over a constant slope (1/8) where the breakwater caisson ($h_c = 13m$) is fixed. The third order solution of Fenton (1972) is used to impose the free surface position and fluid velocity in the numerical domain at $t = 0$. Initial water depth is set to $y/h_c = 1$. Three different wave impacts are generated by slightly varying the caisson position: $x/h_c = 15.3$ for the *I1* impact, $x/h_c = 15.6$ for the *I2* impact and $x/h_c = 15.96$ for the *I3* impact. The aim is to study extreme cases with a different steepness of the wave front at impact (*I1*: least steep face; *I2*: medium steep face; *I3*: steepest face). The I3 case may be considered as the most extreme case of non-aerated impacts since air would be entrapped between the wave and wall when moving the caisson to $x/h_c > 15.96$.

The flow in the porous rubble mound breakwater is also solved in order to investigate the uplift force due to pressure changes under the caisson. The porosity and intrinsic permeability of the rubble mound are assumed to be constant with the following values: $\phi = 0.5$ and $k = 10^{-5}m^2$.

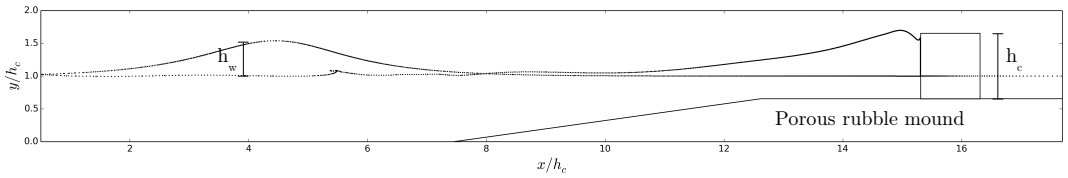

Figure 4.2: Set-up of the numerical experiment. Solitary wave height: $h_w = 7m$, initial water depth: $y/h_c = 1$, reef slope: 1/8, breakwater caisson height $h_c = 13m$ and caisson position: $x/h_c = 15.3$ for the *I1* case, $x/h_c = 15.6$ for the *I2* case and $x/h_c = 15.96$ for the *I3* case

This numerical study is performed with the THETIS code which solves the Navier–Stokes (NS) equations and uses a Volume of Fluid Technique (VOF) method to capture the interface evolution (see Chapter 2). The flow considered incompressible is composed of two phases: water and air. The incompressible version was commonly used in the literature since not air is entrapped between the wave and wall during the impacts. The continuity of fluid velocity is assumed through the interface and surface tension effects are neglected. No turbulence model is used in this study. Turbulence may have an effect on the impact pressure by locally modifying the free surface shape. In the real phenomenon, it will be mainly generated by wave/wave interaction. This phenomenon is here consciously limited by considering a single wave impact.

4.2.2 Validation cases

Test case 1: FTI on a vertical wall

The first test case was chosen to assess the ability of THETIS to reproduce the FTI process on a vertical wall. The reference case is one of the FTI cases modelled in Scolan (2010) using a potential-flow model with a desingularized technique. This case was selected since Scolan (2010) and other authors (Cooker & Peregrine (1992), Bredmose et al. (2010)) demonstrated the consistency and performance of this type of models to reproduce the exact wave interface at the local scale which is essential to simulate the most extreme impacts as the FTI. The initial wave focusing configuration used in the reference case is impossible to establish on laboratory, but it allows to simply initialise numerical simulations for wave impact study (Guilcher et al. (2014), Scolan & Brosset (2016)).

The simulations start from the following initial free surface deformation in a rectan-

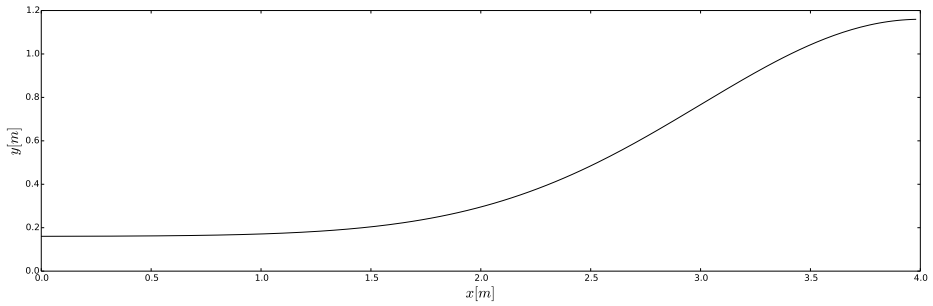

Figure 4.3: Initial free surface deformation in the FTI validation case (from Scolan (2010)). $A = 1$m, $h = 0.16$m, $R = 0.5$m and $L = 4$m.

gular tank over an horizontal bottom:

$$y = h + A\tanh(R(x - L/2)), \qquad 0 < x < L \tag{4.1}$$

where L is the length of the rectangular tank, h is the water depth, A is the amplitude and R controls the slope of the force surface. In this validation case, the impacted wall is located at $x = 0m$ and the wave propagates from right to left. Figure 4.3 shows the numerical set-up of the studied case in this work. Free slip conditions are imposed in all the boundaries of the Navier-Stokes model. An irregular mesh of 640000 elements is used with a minimal size of $0.001m$. The effect of the air is not considered in the potential-flow model. For this reason, we artificially modified the air density value in the Navier-Stokes model (The surrounding fluid density being 1.1768×10^{-8} Kg/m^3). This value is our limit case as simulations performed with even less dense air lead to the same results. This test case was also studied in Martin-Medina, Abadie & Morichon (2017) including an analysis of the effect of air during the impact and the influence of the mesh.

Test case 2: Solitary wave impacts on a porous rubble mound breakwater

The second test case consists in simulating wave impacts on a porous composite breakwater. Numerical results are compared to laboratory experiments carried out in the Coastal Wave, Current and Tsunami Flume (COCOTSU) at the IH Cantabria in the framework of the ASTARTE european project on tsunami risk. The aim of these experiments was to test the model ability to reproduce the complex flow generated by a tsunami wave interacting with a rubble mound breakwater and the uplift forces applied under a caisson breakwater. The model set-up is represented in Fig.4.4. The main characteristics of the experiment are summarized in table 4.1. Solitary waves of several heights were

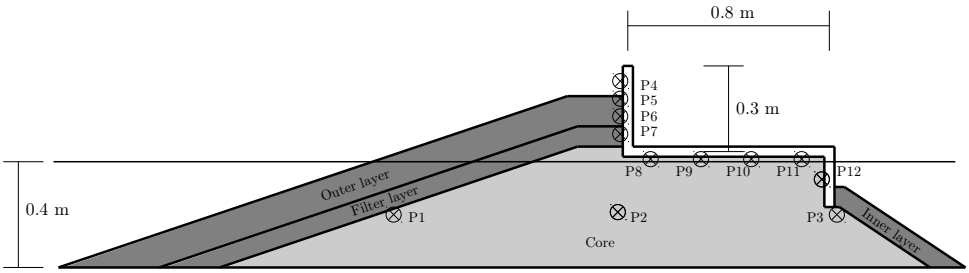

Figure 4.4: Breakwater dimensions and pressure gauges location

tested during the experiments, but we only consider a wave of 0.20 m ($A/SWL = 0.5$) to validate the numerical model. The displacement of the crown is not permitted and its material is considered non permeable. The rubble mound is composed by a permeable core covered by an outer armor and an inner armor. A filter layer is placed between the core and the outer armor layer. 12 pressure gauges (Fig.4.4) inside the rubble mound and over the wave screen allow to measure efforts applied on the breakwater. For the numerical simulations, the domain is discretized in 462000 elements by using an irregular mesh with a minimal size of $0.005m$ in the impact area. Free slip conditions are imposed along the model boundaries. In the present work, we just illustrate the results of a numerical case with the parameters given in table 4.1. More information about the influence of porosity and intrinsic permeability changes on pressures can be found in Martin-Medina, Abadie & Morichon (2017). The solitary waves are modelled using the third order solution given by Fenton (1972). This solution gives the water level position and water velocities to initialize the solitary wave in the numerical model.

Layer	Size stones (D_5 - D_{95}) [m]	Thickness ($2D_{50}$) [m]	ϕ	k [m^2]
Outer armor	0.055 – 0.067	0.123	0.5	10^{-4}
filter-inner armor	0.027 – 0.042	0.072	0.5	10^{-5}
Core	0.011 – 0.052	–	0.5	10^{-5}

Table 4.1: Model characteristics.

4.3 Results

4.3.1 Validation of the model

Test case 1: FTI on a vertical wall

The results of the model validation for FTIs are shown in this subsection. Figure 4.5 illustrates the interface of each model at impact. One can observe that both models are in a good agreement. The steep wave face and the characteristic ascending jet are well generated with the Navier-Stokes code. However, we can observe a slight delay in the numerical interface computed by THETIS with respect to the potential-flow results. It is important to highlight that this delay becomes more significant while the fluid velocity rises along the wall. Figure 4.6 compares pressure distributions for the two models. We observe that the potential-flow model generates a slightly higher pressure peak than the Navier-Stokes model. This is probably due to differences on the interface shape at impact, the wave face being a little bit steeper for the potential-flow model. The main characteristics of flip-through impacts are nevertheless properly modelled by THETIS. The NRMSD (equation (4.2)), calculated for the pressure peak value on the wall in time, is 18.3% for this case. However, it is important to stress that we are comparing a multi-phase model to a single-phase one. Martin-Medina, Abadie & Morichon (2017) showed that air density plays a crucial role on the wave steepness at the impact. Despite our efforts to minimize air effect by diminishing the surrounding fluid density (Martin-Medina, Abadie & Morichon (2017)), this discrepancy may be at least in part due to the intrinsic differences between both models. Note that the NRMSD on the wave force, which has also been calculated, is less important (11.5%). In Martin-Medina, Abadie & Morichon (2017), it is also shown that as long as a sufficient mesh size is used, the grid step has not a very significant influence on the pressure and forces in the FTI simulated in this section.

$$NRMSD = \frac{\sqrt{\frac{\Sigma_{i=1}^{n}(\hat{y}_i - y_i)^2}{n}}}{\hat{y}_i} \tag{4.2}$$

With $\hat{y}_i$ the reference values and y_i the simulated values.

Test case 2: Solitary wave impacts on a porous rubble mound breakwater

As the impact on the screen does not correspond to the kind of impact of our interest, the pressures on the crown wall are, therefore, not analysed here. As pointed out in previous studies, a correct prediction of the pressure field requires a perfect description

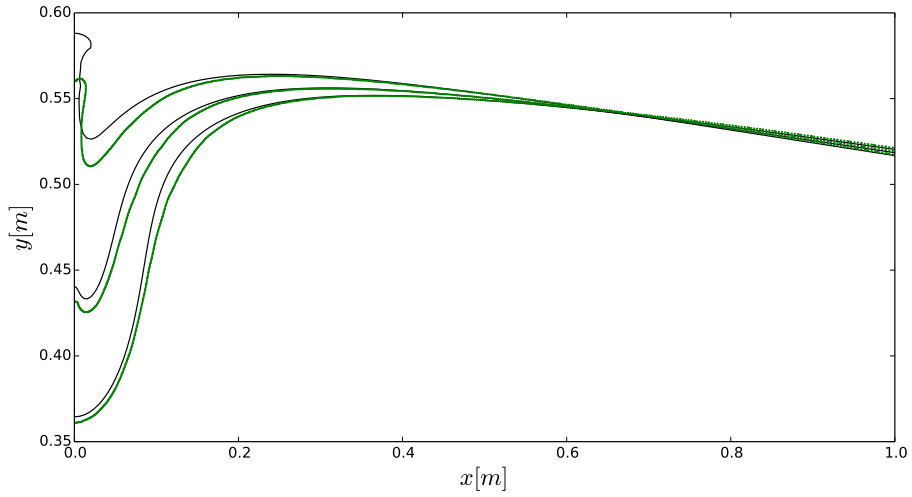

Figure 4.5: Free surface at three different times ($t = 0.97$ s, $t = 0.98$ s, $t = 0.99$ s) during the FTI. Results from Scolan (–) and $\rho_{air} \times 10^{-8}$ (–).

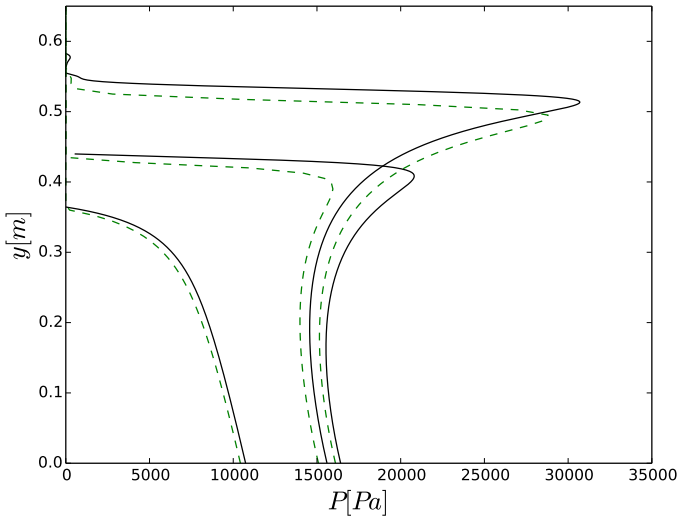

Figure 4.6: Pressure distribution along the wall at three different times ($t = 0.97$ s, $t = 0.98$ s, $t = 0.99$ s). Results from Scolan (–) and $\rho_{air} \times 10^{-8}$ (–). $t = 0.97$ s, $t = 0.98$ s, $t = 0.99$ s.

of the wave shape at impact. In the present experiment, this is very difficult to achieve, as the wave has to propagate and go through the porous medium before impacting the wall. Moreover the impact measured was no strictly a FTI and for that reason, we decided not to show comparisons for the crown wall pressure. Note that in the former subsection, we demonstrated the ability of the code to properly calculate the pressure in FTI provided that the wave shape is correct which what we needed to interpret securely our numerical experiment.

Overall, the model is able to reproduce pressure changes (figure 4.7) in the rubble mound core (P1 and P2) and the energy dissipation inside it (P3). Note that the recorded pressure is not nil before the impact at P2 how it was supposed to be, which leads to differences while comparing to the numerical results. Despite the complexity of the wave screen geometry, satisfactory results are also obtained under the horizontal slab (P8-P12). It is important to mention that very fast pressure variations during the impact may have not been recorded during these laboratory experiments since the recording data frequency is $100Hz$. The NRMSD values (following the equation (4.2)) for the pressure evolution in time are 5.1, 16.9, 16.6, 7.4, 10.1, 20.8, 12.5 and 9.1% for P1-P3 and P8-P12, respectively. The integration of the pressure on the bottom part of the caisson considering a step function gives an error on the uplift force at the peak time of only 1.7%.

4.3.2 Numerical experiment: Impact phase

Identification of FTI

The first step was to identify the limit between FTI and impact with air entrapped. Numerical simulations were carried out placing the breakwater caisson at different locations using a finite spatial step (limited by our spatial resolution). In our simulations, the I3 case appear to be the last FTI. When placing the caisson slightly further away, a slight plunging breaking is observed and air is entrapped (fig.4.8).

The free surface computed with THETIS is plotted at different times in fig.4.9 for the three impact considered in this work. The wave propagation over the slope is similar for the three simulations. Differences only appear when the wave interacts with the caisson, whose position varies for each case. For the next plots, the time origin is fixed for each case before the birth of the vertical ascending jet.

Fig.4.10 shows the free surface evolution and the acceleration field close to the impacted caisson face. All the cases present the FTI dynamic described by Cooker & Peregrine (1992) in which the water interface near the wall rises up, accelerates and flips through giving birth to the small scale moving up jet. In all cases also, the most

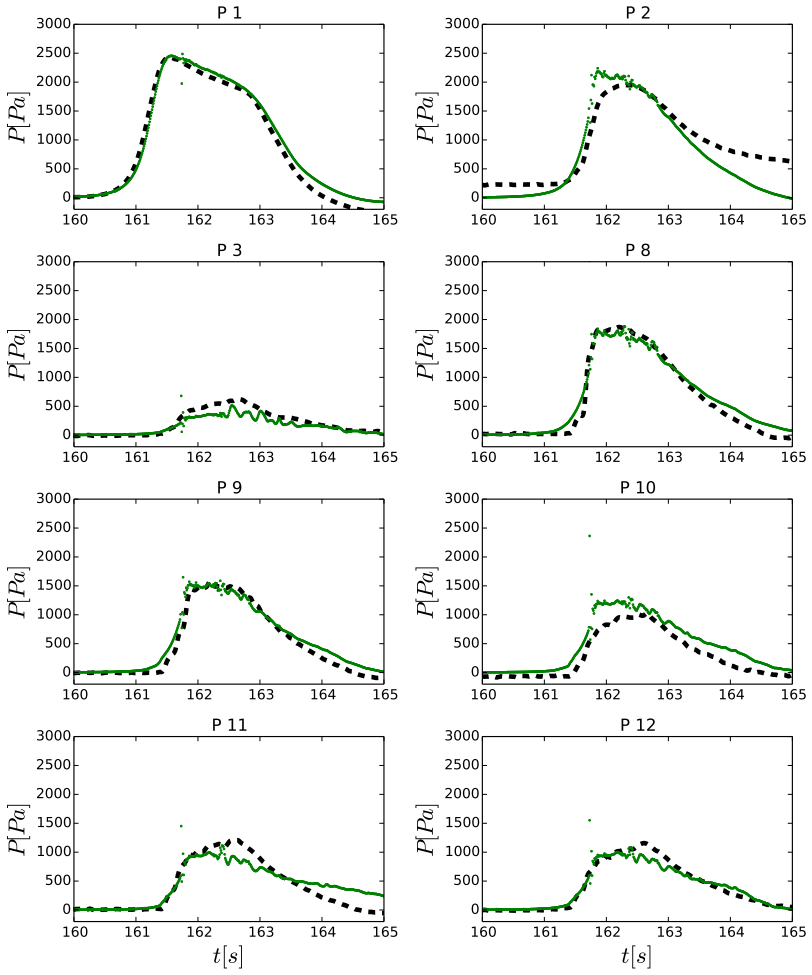

Figure 4.7: Pressure signals in the porous media; (- -) Laboratory experiments. (–) Numerical simulations

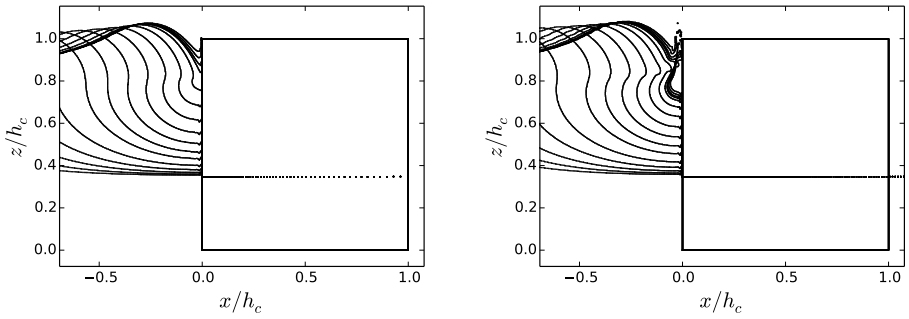

Figure 4.8: Wave interface at different times for the I3 case at left (caisson at $x/h_c = 15.96$) and (right) the impact simulated with the caisson at $x/h_c = 16.25$.

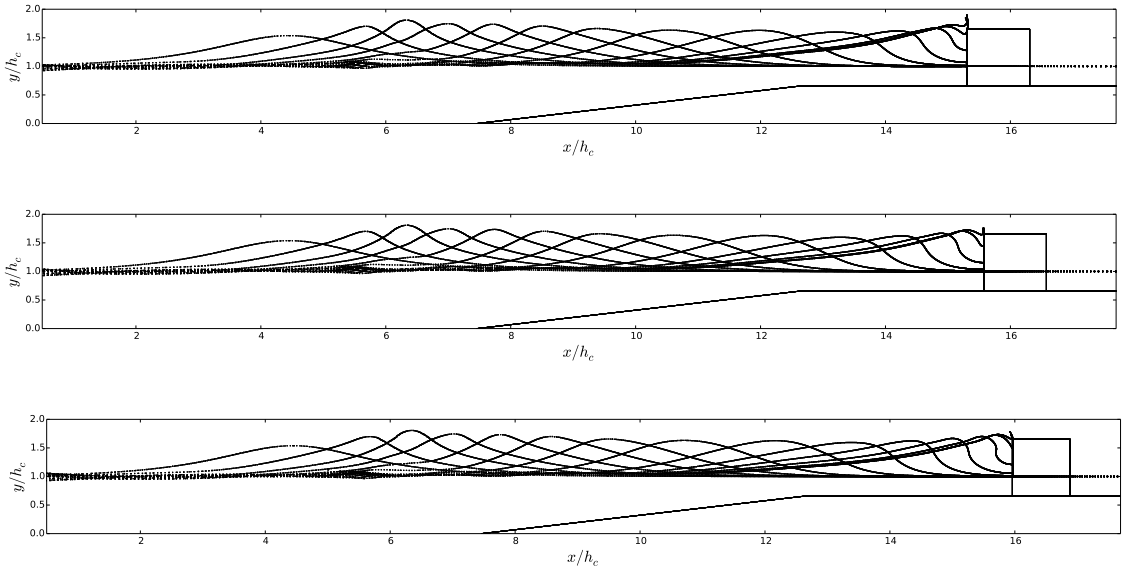

Figure 4.9: Free surface evolution of the three FTIs. I1, I2 and I3 cases from top to bottom. Solitary wave height: $h_w = 7m$. Caisson position: $x/h_c = 15.3$, $x/h_c = 15.6$ and $x/h_c = 15.96$ for the I1, I2 and I3 cases, respectively.

significant fluid accelerations are located in the local ascendant jet close to the caisson breakwater. Fluid accelerations start to increase at $t = 0s$ and reach much higher values during the impact. The largest acceleration values (2900g) are obtained for the steepest breaking wave (fig.4.16), but very high accelerations are also found for the two least steep cases (400g and 650g). A jet deceleration, very pronounced for the *I3* case, is observed at the end of this phase.

For all these reasons, the three impacts simulated in this work belong to the FTI category as defined at the beginning of the paper. Nevertheless, as recalled in the introduction, we may divide the FTI class into two subclasses : the non-focusing and the focusing impacts. Clearly the two first impacts (I1 and I2) belong to the first category. Regarding the I3 case, an incomplete focusing (i.e. involving only the lower part of the wave face) is observed between $t = 0$ and $t = 0.015s$.

Kinematics

The ascending jet tip position and the polynomial of degree four that better fits these points are illustrated in fig.4.11. This polynomial is derived to obtain velocity and acceleration, which directly depend on the steepness of the front. V_c corresponds to the solitary wave celerity at breaking: $V_c = \sqrt{g\left(\frac{h_w}{0.78} + \frac{h_w}{2}\right)}$ (Equation (3) in Tissier et al. (2011)).

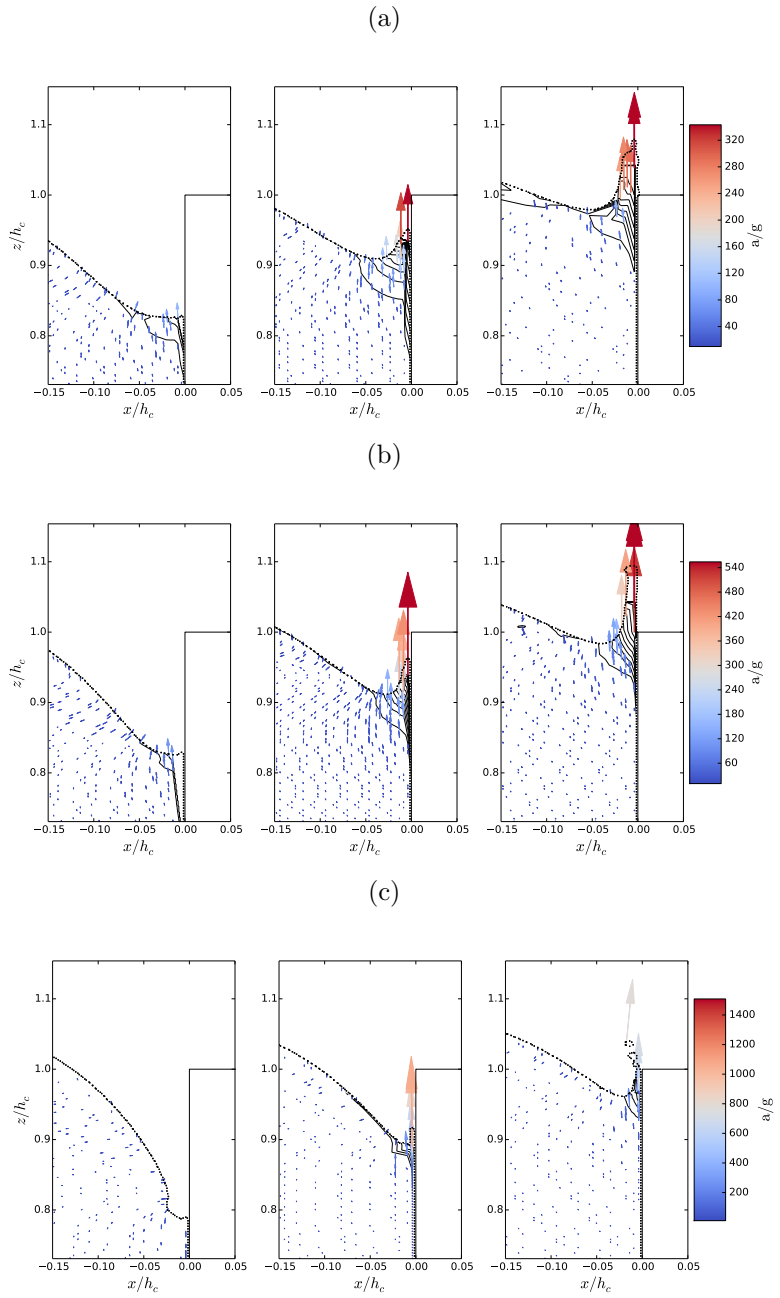

Figure 4.10: Acceleration field during the impact. – (a): *I1* impact. The minimum acceleration contour value is $40g$ and the contour increment is $40g$. $t = 0s$, $0.03s$ and $0.06s$.; (b): *I2* impact. The minimum acceleration contour value is $60g$ and the contour increment is $60g$. $t = 0s$, $0.025s$ and $0.05s$.; (c): *I3* impact. The minimum acceleration contour value is $200g$ and the contour increment is $200g$. $t = 0s$, $0.015s$ and $0.03s$.

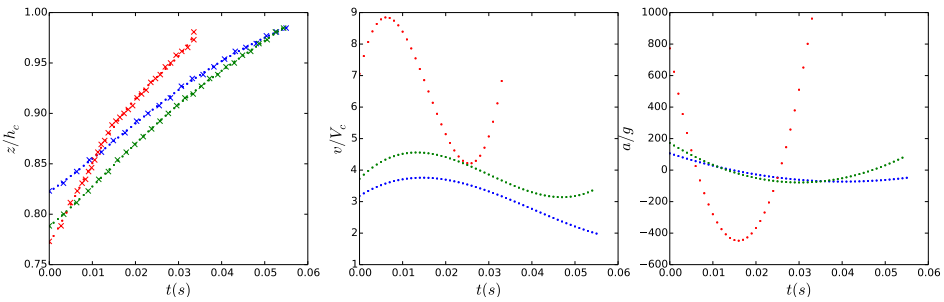

Figure 4.11: Position, velocity and acceleration of the characteristic jet tip during the impact. Position from the numerical simulations (cross) and polynomial of degree four fitting these positions (points line). *I1* (blue), *I2* (green) and *I3* (red) cases.

For the three cases, the ascending jet behaves similarly presenting an initial increase of velocity followed by a decrease and again an increase at the end when the jet reaches the left upper corner of the caisson. The average relative velocity depends on the initial wave steepness, they range from about 3 and 4 (for resp. $I1$ and $I2$) to about 6.5 in the last impact case ($I3$). These velocities are important as they determine the residence time of the peak pressure on the structure. The time evolution of jet tip acceleration (not the maximum fluid acceleration in the flow as described in the former subsection) presents a concave parabolic shape. Associated to the velocity variation, the flow is first accelerated, decelerated and finally accelerated again. The range of acceleration differs strongly depending on the case (two less steep cases ($-50g$ to $150g$) and steepest case ($-450g$ to $800g$). The maximum velocity of $8.8V_c$ is reached during the focusing stage (see Fig 4.10 (c), two first panels), but the strongest acceleration is obtained after the focusing when the jet tip appears.

The velocity field just before the impact phase is shown in Fig.4.12. In the upper part of the flow ($z/h_c > 0.8$), the velocities are globally perpendicular to the interface. For this reason, they are for instance closer to the horizontal direction in the $I3$ case. In the lower part of the flow ($z/h_c < 0.8$), the vertical component is more important and becomes predominant close to the wall. The velocity magnitude gradient is directed toward the point (area) of focus (depending on the case considered) and relative velocity in this area is about 2.5 higher than in the main part of the wave in each impact case.

The velocity field inside the porous rubble mound is shown in Fig.4.13. Similar values are found for the three impacts. Except for the infiltration and exfiltration zones, the velocity under the caisson is horizontal and very weak compared to velocities outside the rubble mound. There are slight differences near the left corner of the caisson where the flow velocity increases for the three cases, the steepest case presenting the largest fluid

velocities.

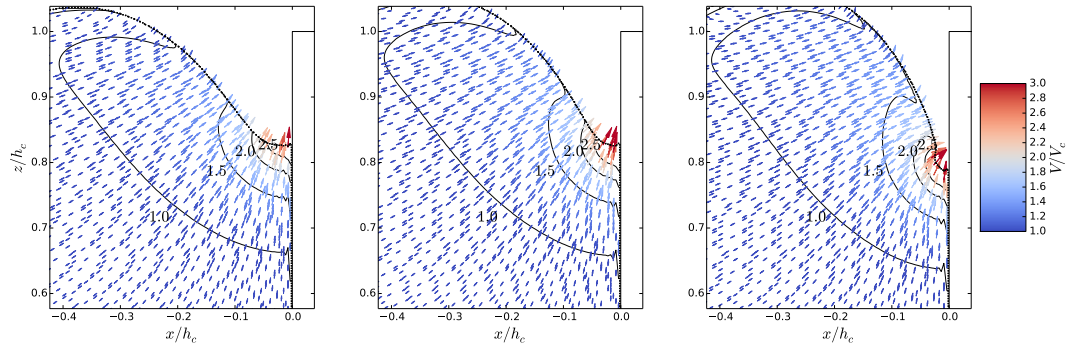

Figure 4.12: Wave velocity for the three cases at the beginning of the impact phase ($t = 0s$). *I1*, *I2* and *I3* cases from left to right. (-) Iso-velocity values (V/V_c).

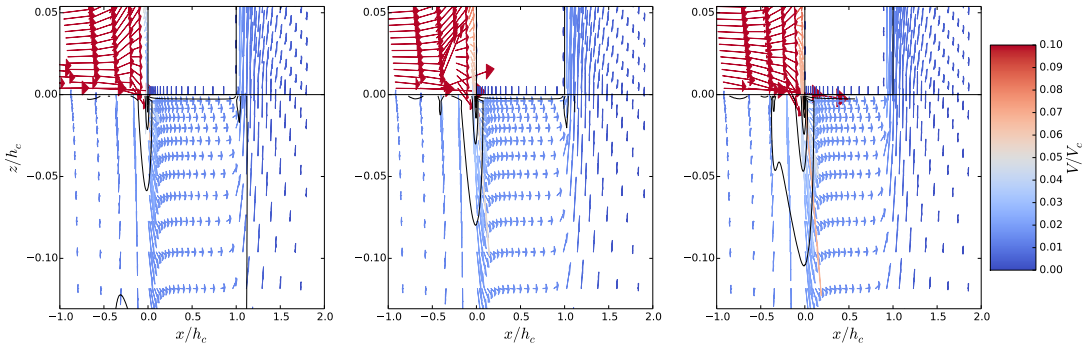

Figure 4.13: Wave velocity for the three cases at the beginning of the impact phase ($t = 0s$) in the rubble mound. *I1*, *I2* and *I3* cases from left to right. (-) Iso-velocity values (V/V_c), the minimum velocity contour value is 0 and the contour increment is 0.01 up to the value of 0.1.

Pressures field

Fig.4.14 illustrates the pressures, normalized by the dynamic pressure $P_0 = \rho_w V_c^2$ (Wu (2007)), along the caisson wall at different times. Three stages (*Wave propagation*, *interaction* and *impact*), characterized by different pressure behaviour, are identified for the three impacts. In the first stage, the pressure field on the wall appears to be mainly controlled by hydrostatic pressure. In contrast, the *interaction* phase, which starts when the trough moves toward the caisson top, induces a remarkable increase of pressure on the whole caisson face. This increase of overall pressure is due partly to the free surface elevation and partly to the fluid acceleration, the pressure profile being clearly no longer hydrostatic. Nevertheless, during this stage,there is no pressure peak. Finally, as soon

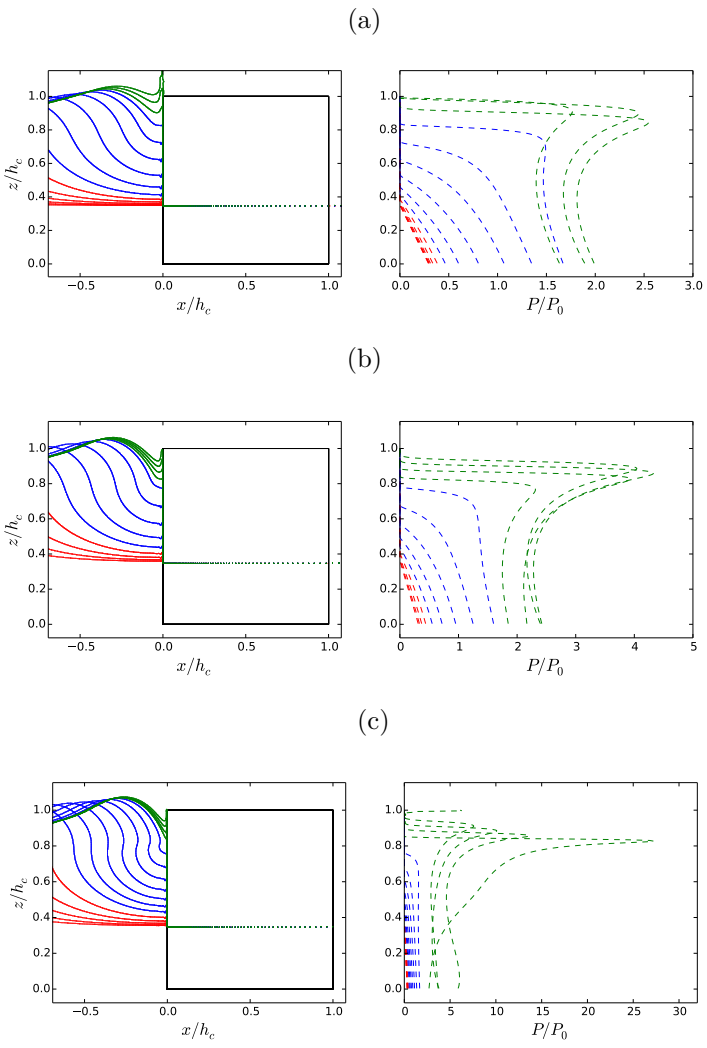

Figure 4.14: *Wave propagation* (–), *interaction* (–) and *impact* phases (–) – (a): *I1* case; (b): *I2* case; (c): *I3* case.

as the ascending small scale jet is generated, (i.e., *impact* stage), a marked pressure peak appears on the caisson. The most important differences in terms of pressure between the three FTI cases are observed during this last stage, the steepest case *I3* giving the highest pressure peak. The pressure distribution under the peak at a given time is almost constant (in space) for each case. But there are also significant differences in the value of this pressure which will play an important role in the impact force.

The spatio-temporal pressure distribution on the caisson wall is represented as a map in Fig.4.15(a) (top panel) for the three studied cases. This representation allows to capture more precisely the pressure characteristics than the snapshots of the preceding figure. In the $I3$ case, the pressure peak reaches $\sim 30P_0$ against $\sim 4P_0$ and $\sim 2.5P_0$ in $I2$ and $I1$ respectively while the corresponding constant pressures are $2P_0 - 6P_0$,

$1.6P_0 - 2.2P_0$ and $1.5P_0 - 2P_0$. The pressure peak appear much more localized in $I3$ than in the two other cases. This peak correspond to the time and location of the focusing process (see Fig. 4.10). Once generated, this pressure peak induces a pressure increase propagating downward to the caisson left bottom corner and upward with the rise of the jet tip. The downward propagation velocity of this pressure pulse is assessed to about 1600 m/s and its presence will be further explained in the discussion.

Fig.4.15(b) (bottom panel) illustrates the uplift pressure distribution in time under the caisson. At a given time, the triangular pressure distribution in space assumed by many authors (i.e.,Goda (1974)) is found in the three cases studied. The *I1* case presents variations of minor amplitude around this distribution while it is more and more variable for increasing free surface inclinations. We also note the presence of the downward pressure pulse at about $0.012s$ for the I3 FTI.

As expected the pressure value at the left corner corresponds to the constant pressure obtained on the impacted face. The hydrostatic pressure is found at the other corner. While the impact process develops, the slope of this triangular distribution increases due to the difference in pressure between the two corners. In the $I3$ case, this pressure increase stage is much shorter than for the two other cases. At $t = 0.038s$, the pressure under the caisson is almost everywhere hydrostatical, whereas, it is still large for the two first impacts studied.

Fig.4.16 represents the peak pressure value on the wall and the maximum fluid acceleration close to the caisson during impact versus time. The peak pressure increases before the fluid acceleration. This is especially very clear for the *I3* FTI case, but this can be also detected at the beginning of the *I1* and *I2* cases. This means that fluid acceleration is logically driven by pressure gradient. The maximum acceleration in the flow is obtained in the $I3$ case with a value of about $2900g$.

Interface inclination

This subsection aims to clarify the link between free surface steepness and pressures on the caisson face. The interface inclination is measured at the inflection point (blue points) of the free surface in fig.4.17. The initial time is taken when the upward moving jet first appears during the simulations. Earlier numerical experiments (Mokrani (2012)) showed that this inflection point plays a key role on the impact dynamics in general and more especially on the peak pressure value. The link between interface inclination and peak pressures (green points) at a given time is presented in fig.4.18. Initial inclination of 48°, 63° and 75° is obtained for *I1*, *I2* and *I3* cases, respectively, illustrating our classification of these three impacts (i.e. least steep, medium steep and steepest impact). From this

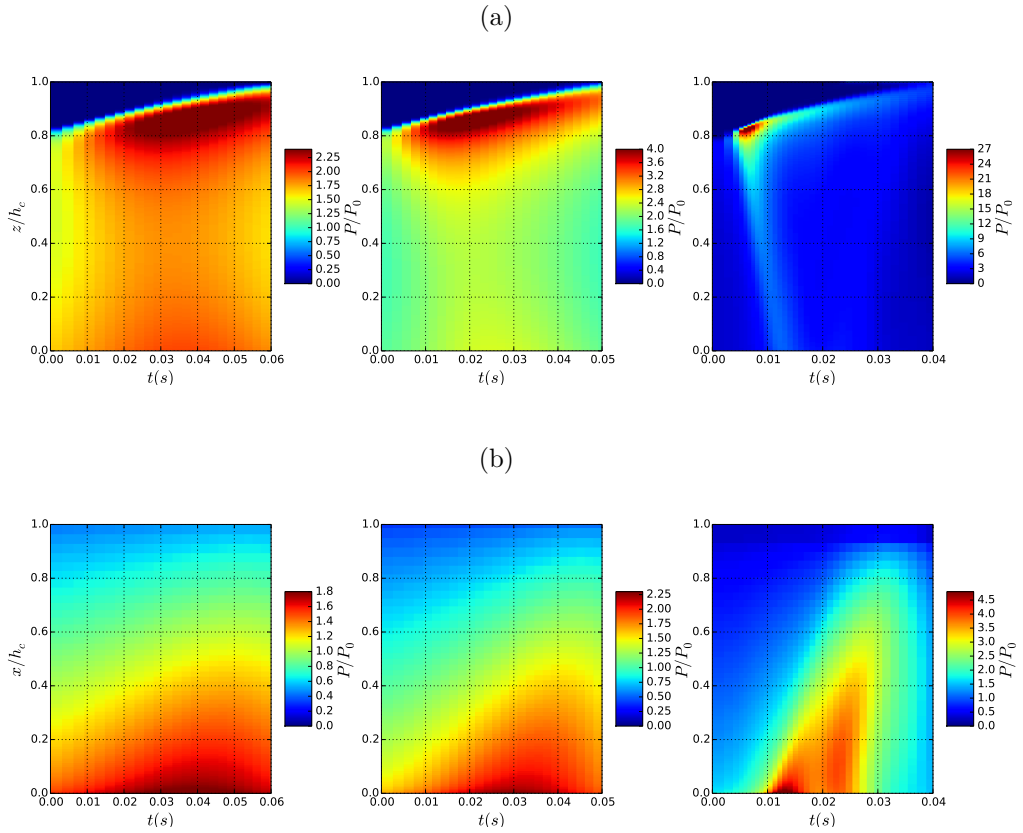

Figure 4.15: Pressure evolution in space and in time. *I1*, *I2* and *I3* cases from left to right. – (a): Caisson screen pressure. ; (b): Pressure under the caisson.

initial value on, the free surface inclination progressively decreases with time in each case (fig.4.17 and fig.4.18). The pressure does not follow this monotonic behaviour and a bell curve is obtained for the maximum pressure value (fig.4.18).

Forces

Fig.4.19 illustrate horizontal and uplift forces in time for the three studied cases. The least steep case presents a maximum horizontal force of 3600 KN. The uplift force is also significant with a maximum value of 2300 KN. For the *I2* case, the horizontal and uplift forces increase to 4700 KN and 2700 KN, respectively. The steepest FTI is the most extreme case in terms of wave loads induced to the structure. A maximum horizontal force of 12200 KN and a maximum uplift force of 5600 KN. For the three cases, the peak force appears in the middle of the *impact* phase. After this peak, a decrease is observed during this phase due to the pressure peak attenuation shown in the latter section. The duration of this force decrease varies from 0.75 to 2.0 times the

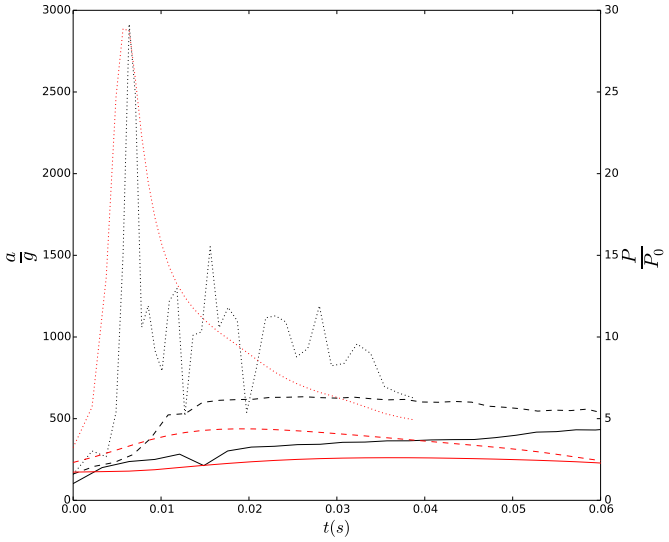

Figure 4.16: Maximum fluid acceleration near the wall (black) and pressure peak evolution on the wall (red) in time for the three flip-through impacts. *I1* (continuous line), *I2* (dashed line) and *I3* (point line) flip-through impacts.

duration of the impact phase depending on the case.

During the force decrease, fig.4.19(b) shows force oscillations that are very clear in the *I3* case, but they can be also seen for the *I1* and *I2* cases. After these oscillations, the three cases converge to the same uplift force value: $\simeq 1000KN$ and $\simeq 1100KN$ for the horizontal and uplift force respectively. The possible origin of these oscillations will be analysed in the section of discussion.

The force impulse, which represents the change in linear momentum, during the impact phase (between the two dashed lines in fig.4.19(a)) is calculated for the three cases. Similar values are obtained for the three studied cases: $154.38Kg\ m/s$, $104.98Kg\ m/s$ and $113.57Kg\ m/s$ for *I1*, *I2* and *I3* cases, respectively.

4.3.3 Numerical experiment: Post-impact phase

Pressure distributions at different times after the *impact* phase are displayed in fig.4.20. The pressure peak is quickly attenuated when the wave starts to overtop the caisson. For the three cases, a common pressure decrease is observed up to a constant value that corresponds to the hydrostatic pressure of the wave overtopping the caisson ($\sim 1P_0$ at the bottom and $\sim 0.2P_0$ at the top).

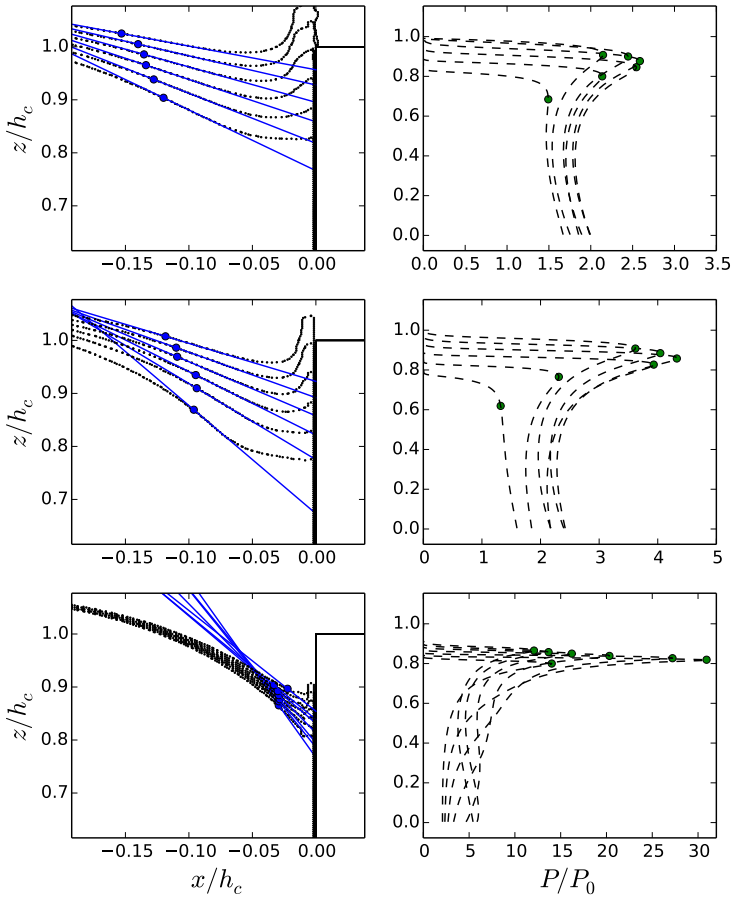

Figure 4.17: Wave interface angle evolution during the *interaction* and *impact* stages. I1, I2 and I3 cases from top to bottom. Inflection point (blue points), interface inclination (blue lines) and pressure peaks (green points) are identified at different times.

4.4 Discussion

The flow field and pressures generated by FTIs are shown in a composite breakwater with a porous rubble mound. It was demonstrated that this kind of extreme impacts can appear with different inclinations. The influence of the FTI inclination at impact on the flow field near the caisson, pressures and loads were analysed in this work.

The main differences between our work and the precedent ones are : first and most important the focus on the effect of the wave front inclination on pressure, and second the real breakwater configuration. The Navier-Stokes model allows us to deal with a real breakwater configuration (including the porous medium) and to show the entire phe-

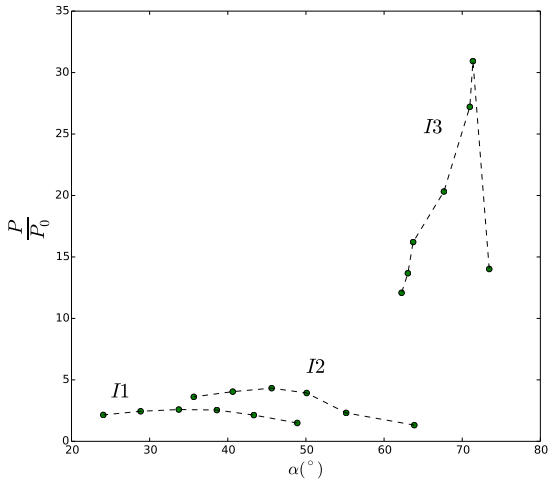

Figure 4.18: Pressure peak value (green points) in function of the instantaneous incidence angle impact at different times during the *impact* phase.

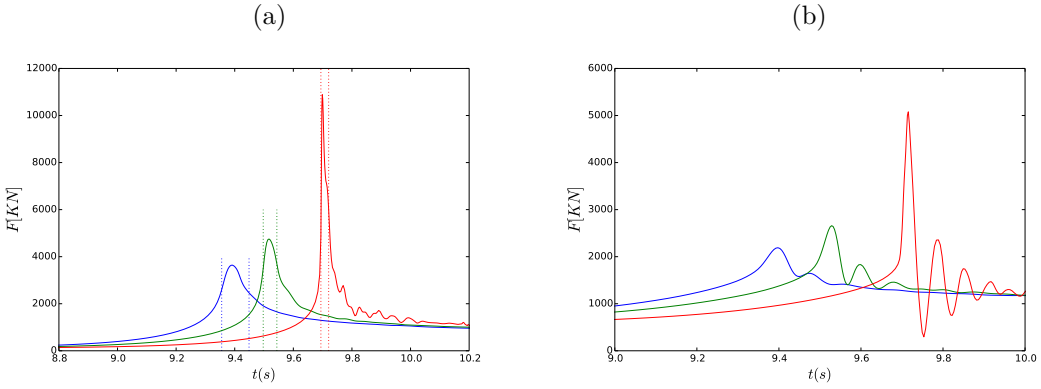

Figure 4.19: Time evolution of the forces acting on the caisson for the three cases of study. *I1* impact (–), *I2* impact (–) and *I3* impact (–). Time from the beginning of the simulations. (a): Horizontal force. The impact phase is delimited by the dashed line.; (b): Uplift force.

(a)

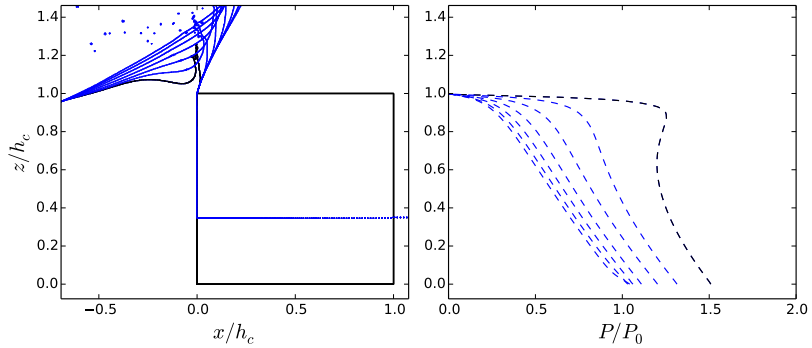

(b)

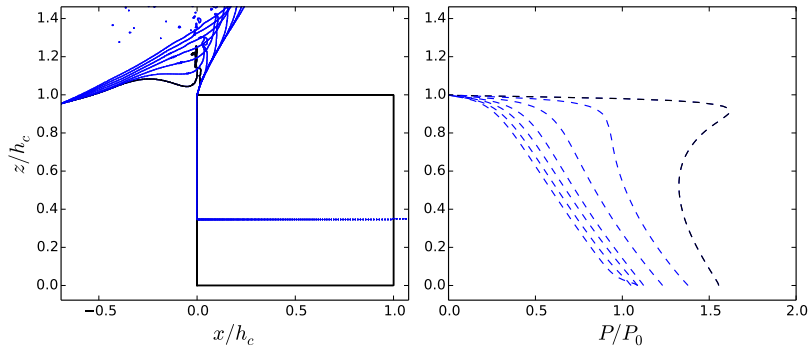

(c)

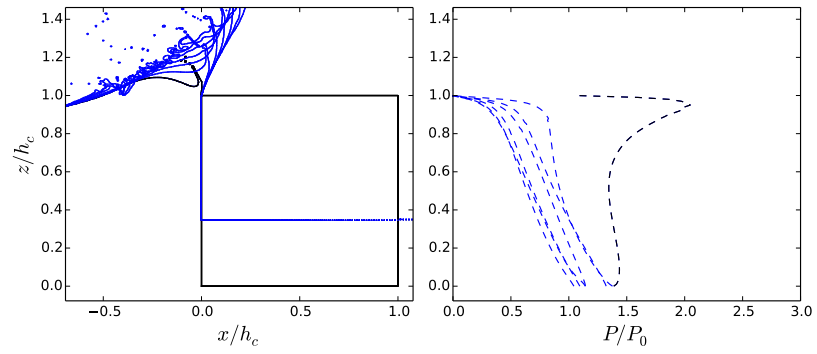

Figure 4.20: Pressure attenuation (- -) until a constant hydrostatic value after the impact. First time steep is in black – (a): *I1* impact; (b): *I2* impact; (c): *I3* impact.

nomenon including the uplift on the caisson. But it is the focus on the wave inclination which allows us to generate such strong FTI. Hence, in terms of pressure magnitude on the vertical wall, we think that for instance a potential model may be able to generate the same kind of results as the one obtained here in the most extreme case as long as the initial conditions are the same. This study allows to enlarge the knowledge of how this phenomenon may vary within this impact class which was not addressed in previous research works. It was shown that slight variations of the wave characteristics can generate FTIs of several intensities in terms of loads applied on the structure. This variability has to be taken into account in breakwater stability studies.

By comparing the wave interface dynamics for the three cases, we observed a clear difference between the I3 case and the other cases. Just before the birth of the small scale moving up jet in the I3 case, there was a clear phase of focusing (defined by Lugni et al. (2006)) in which the wave crest and trough move towards each other. This focusing phase is not observed in the other two less steep impacts. Comparing to the experimental study presented in Kaminski et al. (2009) and Hofland et al. (2011), these non focusing impacts would be considered as slosh impacts since the wave trough reaches the impacted zone slightly before the crest. In the latter papers, small pressures with long durations were measured for slosh impacts while the present work showed a rapid collision with relatively significant pressure peaks for the two less steep impacts. Furthermore, as for the FTI cases investigated in Cooker & Peregrine (1992), Lugni et al. (2006) and Bredmose et al. (2010), I1 and I2 impacts generate a narrow moving up jet with much larger accelerations than everywhere else in the wave.

Analysing the results of pressure presented in this work, two conclusions can be drawn from fig.4.17 and fig.4.18. First, as already pointed out, there is a direct link between the maximum pressure reached during a specific FTI and the initial free surface inclination just before the birth of the ascending jet. With increasing wedge inclination, water has to escape increasingly faster upward which explains the large pressure peaks observed (Mokrani & Abadie (2016)). Secondly, in time, the link between interface inclination and associated maximum pressure is not direct and the behaviour is somehow different (monotonic against non monotonic) even if it is certainly related. An attenuation of the pressure peak value is observed at the end of each impact for the three cases simulated in this work. This attenuation is more noticeable for the *I3* case due to a significant diminution of the instantaneous incidence impact angle (75°-60°) as shown in section (4.3.2). This flip-through impact presents a pressure peak much faster and more variable than the other cases due to abrupt changes of the local interface shape. While, for the less steep cases, the pressure peak seems to be almost constant during the impact even

if there are important angle variations (48°-25° for the *I1* case, 63°-35° for the *I2* case). Pressures on the submerged part of the caisson are found to remain constant in time and in space for a given FTI case. Varying the wave steepness at impact, this remaining pressure on the submerged part increases with the initial free surface inclination. In this part, the pressure values are less variable than for the pressure peak, but they may play an important role when computing the total force submitted to the caisson.

We observed that the maximum fluid accelerations are near $2900g$ and the pressure peak slightly overpasses the value of $30\rho V_h^2$ (V_h being here the horizontal velocity component before impact) for the steepest case presented here. This gives an absolute peak pressure of 3.6 MPa. If we compare the results in terms of acceleration and pressure peak to other published work, Cooker & Peregrine (1992) numerically analysed a FTI with a steep interface at collision. The maximum water acceleration reached $1800g$ and the highest pressure peak value about $4\rho V_h^2$. Lugni et al. (2006) used laboratory experiments to reproduce a similar case to Cooker & Peregrine (1992). Accelerations larger than $1500g$ were found in the moving upward jet and the maximum recorded pressure exceeded the value of $11\rho V_h^2$. As shown in the paper, the significant differences observed between our results and previous studies are explainable by slight variations of the free surface inclination, the FTIs investigated in Cooker & Peregrine (1992) and Lugni et al. (2006) presumably being less steeper than the *I3* case. In terms of absolute peak pressure, our most extreme case gives maximum pressure magnitudes comparable to the one obtained in Hofland et al. (2011) (2.7 MPa) and Bullock et al. (2007) (3.5 MPa).

Concerning the relation between FTI fluid accelerations and pressures on the caisson, we observed that the pressure values increase slightly before fluid accelerations above the pressure peak position as already reported in Cooker (2010). Therefore this is a confirmation that accelerations are driven by pressure gradients.

In terms of forces, the peak appears in the middle of the *impact* phase for the three FTI cases. After this peak, there is a force decrease due to the pressure peak attenuation shown in the latter section. At the end of each FTI, a common force value for the three cases is reached which is controlled by the hydrostatic pressure applied on the caisson.

If we focus now on the porous rubble mound, the maximum pressure under the caisson corresponds to the remaining constant pressure obtained on the submerged part of the caisson. Thus, the breaking wave inclination at impact has a significant role on the horizontal loads applied on the breakwater caisson, but it is also essential to consider the influence of the interface angle on the vertical loads. The maximum pressure values found under the caisson are $5\rho V_h^2$ for the *I3* case. Other works, as Hsu et al. (2002) and Lara et al. (2008), focusing on the numerical validation of wave impact into porous

composite breakwater showed lower maximum uplift pressure values: $\simeq 1.6\rho V_h^2$ and $\simeq 3\rho V_h^2$ respectively.

Regarding the limitations of our study, the present work is only based on a numerical model without any laboratory experiments to test FTIs on breakwater caissons. THETIS has been largely validated to reproduce wave impact on porous rubble mounds and the extreme flow field generated by FTIs. Numerical issues are also still observed during the critical FTI. Indeed, for the I3 case, a marked pressure pulse propagating downward is observed. Logically, this pulse should propagate with infinite celerity if incompressibility is respected. In our case, this infinite velocity is not obtained and divergence is observed to increase during the propagation of this pulse. This means that the computations become slightly pseudo-compressible at this time allowing pressure wave propagation. Note that Peregrine (2003) also obtained such a downward pressure pulses (propagation velocity of about 300 m/s) with compressible computations but in a case of air entrapment. In the latter case, the pulse was later reflected by the bottom as a shock wave. In our case, the pressure pulse generated by pseudo-compressibility effects seems to be trapped within the porous media and reflected back and forth between the approaching wave and the caisson inducing the uplift force oscillations found in fig.4.19(b). The improper behavior of the incompressible model for our most violent impact may be due to the need for physical compressible effects to actually appear in such an impact. Those compressible effects are not explained by the Mach number (less than 0.1) but may be by the huge pressure reached locally by I3 (40 bars) in a very small time scale. These complex processes require further investigations left for future works.

The use of the solitary wave approach is also a limitation. This wave theory has been causing controversy recently in our scientific community when related to long waves as tsunamis. In the present case, it is used as an approximation for storm waves. Note that if we look at the celerity and equivalent wavelength associated to the solitary waves simulated, the equivalent storm waves would be pretty long (about 16-17s period). It is clear that with one unique wave, we miss the interactions between waves which may also be of importance to generate extreme impact. Nevertheless, we consider this interaction as being beyond the scope of this paper and a subject for future investigations.

To conclude, this work has numerically demonstrated the existence of several FTIs on a breakwater caisson. The interface inclination has been found to have an important effect on the flow field, pressures (on the impacted face and inside the porous rubble mound) and forces for three cases representative of FTIs. This work raises the question of the implications of these interface variations in terms of structure stability. Further work will be focused on the study of caisson motion to try to answer this question.

4.5 Conclusions

We investigated the flow field and pressure variations generated by interface changes during FTIs. The main characteristics of FTIs were shown for the three impact cases of this study. But the phase of focusing before the impact described by some authors (Lugni et al. (2006), Kaminski et al. (2009), Hofland et al. (2011)) has been only observed for the I3 FTI. The following main conclusions can be drawn from this study:

- Numerical validation: THETIS was validated for flows inside a porous medium and FTIs on a vertical wall.
- First important conclusion is that the existence of a whole range of FTI driven by the initial wave steepness has been demonstrated. Numerical simulations have shown that pressures directly depend on the interface shape in FTIs. The most severe case corresponds to the steepest breaking wave (75°) impacting the caisson. These results have also showed that the remaining constant pressure varies with the angle through the pressure peak magnitude. In time, nevertheless, the wave incidence angle does not have a direct link on the pressure peak (i.e. a proportional relationship) even if they seem somehow related.
- To our knowledge, this is the first work that has investigated FTIs in the real configuration of a composite breakwater composed of a vertical caisson with a porous rubble mound. The porosity of the rubble mound breakwater has been considered in order to analyze the pressures under the caisson. A triangular pressure distribution has been obtained which values correspond to the constant pressure obtained on the impacted face and the hydrostatic pressure in the other side. It is therefore also highly dependent on the wave steepness.

Chapter 5

Stability study of vertical breakwater submitted to flip-through impacts

---

This chapter aims to analyse the stability of breakwater caissons submitted to flip-through impacts generated by tsunami undulations or storm waves. As in chapter 4, the flip-through cases present three different interface inclinations at impact (least steep, medium steep and steepest face) being representative of all the cases of flip-through. The water wedge approach, also used in Cumberbatch (1960) and Kihara et al. (2015), is here proposed to formulate a semi-analytical model. This method allows to assess efforts and permanent caisson displacements taking into account the wave steepness at impact. This simplified model is applied and compared to the numerical experiment presented in the previous chapter. After this, the water wedge method is used to constitute stability maps for three wave interface inclinations at impact. These graphs give rich informations about forces acting on the caisson, motion durations and maximum caisson displacements in function of the structure dimensions and wave characteristics.

5.1 Introduction

Offshore breakwaters protect important shore areas against storms, typhoons and tsunamis. Vertical breakwaters consisting in a rubble mound and an upright caisson are widely used in several countries. Placed in shallow waters at several hundreds of meters from the coast, they are designed to reduce the impact of extreme events in coastal cities and harbours. These coastal structures may be largely deteriorated after such events.

The main damages encountered for vertical breakwaters are the loss of the global stability of caissons and foundation failures (Oumeraci (1994), Takahashi et al. (2001)). In 1974, Goda (1974) included an historical review of sliding and non-sliding caissons in Japan which was later used in order to test the accuracy of the Goda's stability method. Oumeraci (1994) presented a review of breakwater failures around the world and found that the main causes (ranking them from the most frequent to the least) are sliding of the caisson, seaward tilt and erosion of the rubble mound. Typical failures of vertical breakwater built in Japan were reviewed in Shigeo Takahashi et al. (1999) and Takahashi et al. (2001). These works summarized two field surveys along the Japanese coast where caisson sliding was also found to be the most common failure mode. Emphasis was put on the importance of impulsive pressure as a cause of failure as seen previously in Takahashi et al. (1994).

Many researchers made significant efforts trying to assess the stability of breakwater caissons submitted to wave impacts using physical models (Oumeraci et al. (1992), Klammer et al. (1995) and Wang et al. (2006)) and analytical methods (Oumeraci & Kortenhaus (1994), Oumeraci et al. (1995), Shimosako et al. (1994), Ling et al. (1999) and Cuomo et al. (2011)). Oumeraci et al. (1992) highlighted the dynamic behaviour of caissons when impacted by breaking waves using laboratory experiments. A simplified model to analyse the dynamic response of caissons and its sensitivity to various parameters (mass, damping, stiffness) was presented in Oumeraci & Kortenhaus (1994). This model used the so-called "church roof" load to approach the horizontal force induced by wave impacts. Interesting laboratory experiments were carried out by Klammer et al. (1995) aiming to investigate permanent displacements induced by impulsive wave pressures. This study pointed out the link between permanent displacement and caisson dynamic oscillations. A "Safety Factor" against sliding ($S.F.$) is introduced, permanent displacements occurring when $S.F. < 1$. In the same way, Oumeraci et al. (1995) studied the collapse of breakwater caissons as a result of the repetition of small permanent displacements. The same laboratory tests used in Klammer et al. (1995) allowed to validate a simple numerical model to estimate these cumulative displacements. Experimental data and computed results were in good agreement.

Shimosako et al. (1994) proposed a practical method based on equivalent sliding forces to estimate caisson displacements. This method was compared to laboratory experiments obtaining satisfactory results for impulsive and non impulsive waves. It is also shown that caisson sliding mainly occurred when $S.F.$ is inferior to unity. This method was later updated by Shimosako & Takahashi (2001) in order to better estimate the impulsive and pulsating components of wave load signals. Ling et al. (1999) described a method to

calculate the sliding caisson distance in which the wave force was assumed to vary sinusoidally in time. This method was applied to estimate the caisson displacements of the historical cases presented in Goda (1974). More recently, Wang et al. (2006) presented an experimental and numerical investigation of horizontal and rotational motions of composite breakwater caissons under breaking wave action. These laboratory experiments were used in Rogers et al. (2010) to validate a SPH (Smoothed particle hydrodynamics) model where the permanent displacement of caissons was modelled. The last published work aiming to assess sliding distances of breakwater caissons submitted to wave loads is presented in Cuomo et al. (2011). This new method considered the force variation in time on the coupling between the dynamic response of the caisson breakwater and the bearing capacity of the soil. A comparison was made between predictions and measurements from the physical models of Shimosako et al. (1994) obtaining a good agreement. Even if several of these design methods developed over the past 20 years allow to assess the external stability of vertical breakwater caissons from a practical point of view, they do not provide a link between the exact wave shape at impact and the caisson stability. Besides, there is not study in the literature analysing the breakwater caisson stability under flip-through impacts which have been shown to be the most extreme wave impact (e.g. Cooker & Peregrine (1992), Hofland et al. (2011)).

This chapter aims to propose a first insight of a semi-analytical method to assess the stability of a vertical breakwater caisson submitted to flip-through impacts (hereinafter referred as FTI) with a variable interface inclination (least steep face, medium steep face and steepest face). The analysis of the relation between the interface shape and the pressure evolution in time of the three FTI cases presented in Chapter 4 make us believe that they bear some similarity to water wedges striking a wall. The water wedge approach was already used to characterize breaking wave impacts in Cumberbatch (1960) and Zhang et al. (1996). Wu (2007) and Duan et al. (2009) also studied water wedge impacts on a solid wall varying the interface inclination. Other types of violent impacts as dam break bores may be locally approximated by water wedges (e.g., Mokrani & Abadie (2016) and Kihara et al. (2015)). These studies assumed that the water wedges move over an impermeable bottom, but using the model presented here, pressure variations on permeable mediums may also be assessed.

The first objective is to verify that the water wedge method can be used to estimate pressures, forces and the permanent displacement of a breakwater caisson subject to FTIs. The results obtained with this method are compared with the CFD numerical simulations of Chapter 4. Unlike the coupled CFD-CSD models (Elsafti & Oumeraci (2017)), the THETIS simulations do not consider the coupling wave-caisson-rubble-mound, but

they allow to assess pressures, forces, and therefore, deduct potential caisson sliding. Once this is confirmed, this simplified model allows to build maps that provide information about wave forces, motion duration and caisson sliding in function of the structure dimensions and wave characteristics for FTIs with three wave inclinations. Past studies (Kim et al. (2004), Andersen et al. (2011)) has shown that the sliding-tilting coupling and the relation between the caisson and its rubble mound are necessaries to better calculate caisson displacement. This work neglects these important effects for now, the objective being more to give a first formulation of an powerful method to estimate in a simple manner sliding along the interface between the caisson and the rubble foundation due to FTIs (which is the originality). The latter important processes should be included in this formulation in future works to reproduce realistic displacements.

The chapter is organized as follows. The numerical experiment of FTIs is described in section (5.2.1). Section (5.2.2) contains the formulation of the simplified model using the water wedge approach. A comparison between the numerical experiments and the simplified model is presented in the first part of section (5.3). After this, the stability maps made with the simplified method are included. A discussion of the results is proposed in section (5.4). Finally, in section (5.5), the conclusions of the study are drawn.

5.2 Methodology

5.2.1 Numerical experiment

In the first part of this work (Chapter 4), three FTIs on a caisson have been numerically studied to better understand the role of wave face inclination variations on pressures. These simulations are now used to investigate the stability of a breakwater caisson submitted to these three impacts. As described in Chapter 4, the numerical case consists in a solitary wave propagating over a porous reef and impacting a caisson. The caisson is an unmoving square of $13m$ (h) and the wave height is fixed at $7m$. The initial free surface is located at $y/h = 1.0$. The caisson position is slightly different for each FTI: $x/h = 15.3$ for the least steep wave impact (*I1* case), $x/h = 15.6$ for the medium steep wave impact (*I2* case) and $x/h = 15.96$ for the steepest wave impact (*I3* case). The porosity and intrinsic permeability of the rubble mound are assumed to be constant in these simulations: $\phi = 0.5$ and $k = 10^{-5}m^2$.

Forces and S.F.

Wave loads on the caisson are computed integrating the pressures obtained with the numerical model. The horizontal force (F_h) is calculated using the pressure distributions of the impacted face caisson. The modelling of the porous rubble mound allows to obtain the uplift force (F_u) induced by these impacts. The Safety Factor ("S.F.") is also estimated to evaluate the caisson stability during impacts:

$$S.F. = \frac{\mu(W - F_u)}{F_h} \tag{5.1}$$

Where μ is the friction coefficient ($\mu = 0.6$) and W is the dry weight of the caisson. S.F. values inferior to unity mean that wave loads are higher than the stabilising forces and so the caisson is unstable.

Deduction of caisson motion from the numerical simulations

The displacement is not modelled with THETIS. We have performed CFD calculations of a water wedge impacting a caisson (Martin-Medina et al. (2016), see Annexe 3) considering the coupling between pressures and displacement. The proposed method, which does not take into account this coupling, has been compared to these simulations obtaining similar results in terms of caisson velocity and displacement. Hence, the loss of force due to the motion is not significant and the decoupling between the pressure obtained on the wall and the sliding of the caisson can be assumed to be a valid approximation. The sliding and velocity reached by the caisson can be calculated using the horizontal (F_h) and uplift force (F_u) obtained from the numerical experiments based on the following equations:

$$(m + m_a)\ \ddot{x} = F_h - \mu(W - F_u) \tag{5.2}$$

Where m is the mass and m_a is the hydrodynamic added mass. Integrating once this expression, one obtains the caisson velocity ($\dot{x} = v_x$). The sliding displacement ($x = S$) is then calculated by integrating the velocity expression.

5.2.2 Simplified model to assess caisson stability using the water wedge assumption

The simplified model is based for some part on the water wedge approach and for others, uses numerical results presented in Chapter 4. The advantage of this simplified model with respect to numerical simulations is that it would allow to instantaneously estimate forces, impact durations and caisson motions for any possible case.

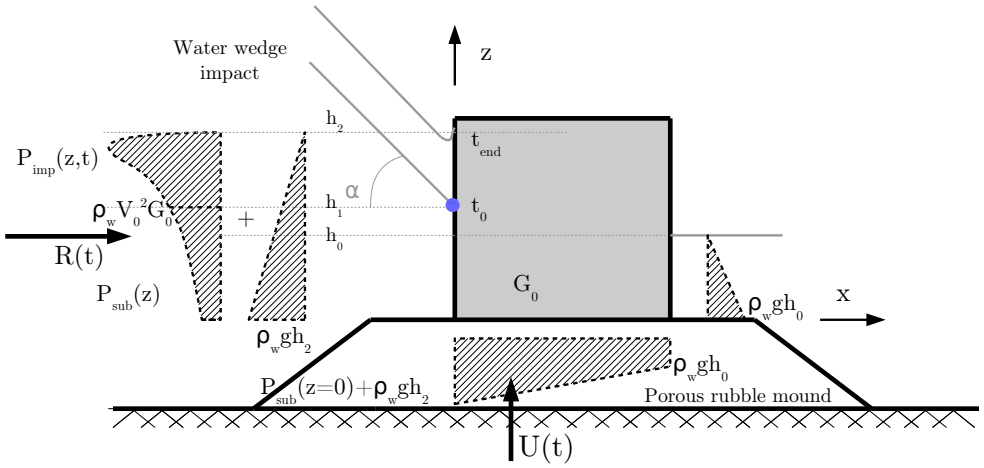

Figure 5.1: Dynamic and hydrostatic pressures on the caisson predicted by the simplified model at $t = t_{end}$. h_0 is the initial free surface and h_1 the water level before the *flip-through* phase. The gray lines represent the free surfaces at $t = t_0$ and $t = t_{end}$

Description of the model

The proposed model allows to estimate force evolution in time during the *flip-through* phase, when the ascending small jet and the pressure peak first appear on the caisson ($[0, t_b]$), and after the end of this phase when the pressure distribution tends to hydrostatic values ($[t_b, t_c]$ and $[t_c, t_d]$). As the force values before the *flip-through* phase are not high enough to induce significant displacements to the caisson, the model will be only applied after the beginning of this phase.

As shown in fig.5.1, this model proposes to approach the pressure evolution in time using the water wedge assumption during the *flip-through* phase (t_0 to t_b). The initial free surface is located at h_0. At $t = 0$, when the *flip-through* phase starts, the water wedge meets the wall at the blue point located at h_1. The pressure profile associated to the water wedge impact develops from this point upward to h_2 (sketched in fig.5.1), height where the impact is considered to finish (h_2 can be smaller than h for some cases, see subsection (5.2.2)).

The water wedge is considered to move constantly and horizontally with velocity V_0. The free surface inclination is denoted by α and the wedge is assumed to be infinite in extent. The fluid is assumed to be incompressible and inviscid. Gravity effect on water wedge dynamic is neglected due to the extreme rapidity of the upward moving jet. Based on the previous assumptions, the problem can be assumed to be self-similar (e.g.,Wu (2007)), which links spatial and temporal coordinates in a simple manner allow-

ing to simplify the problem formulation. This change from real to self-similar plan allows to express the pressure on the wall in any time by the function $G(s)$ with $s = z/V_0 t$. This pressure distribution associated to self-similar water wedge impacts was computed for different angles in Zhang et al. (1996), Wu (2007) and Duan et al. (2009) following different approaches. In this work, we considered the three free surface angle cases (45°, 60° and 80°) that have been studied by Wu (2007). Even if the interface average inclinations are slightly different with respect to FTI cases investigated in the later Chapter (48°, 63° and 75°), we compare to Wu's cases since this study is the only one that focuses on wedge impact with different interface inclinations in the literature obtaining reliable results. The pressure distributions associated to these angles have been numerically computed by two different methods (similarity solution and BEM simulations) giving approximately the same distribution. The results from BEM simulations in Wu (2007) are used in this work.

The dynamic pressure distribution ($P_{imp}(z,t)$)) generated by the water wedge impact ($h > h_1$) is defined by the following expression:

$$P_{imp}(z,t) = \rho_w V_0^2 G(s) \tag{5.3}$$

For the part of the caisson that is not directly impacted by the wave (below the impact, $h < h_1$), the pressure follows an exponential function constant in time as observed in the numerical simulations of Chapter 5 ($P_{sub}(z)$ in fig.5.1). To study the pressures on the submerged part of caissons generated by a FTI case, numerical simulations of a breakwater with a larger water depth in front of the impacted caisson wall have been carried out. The analysis of these simulations allows to formulate this expression:

$$P_{sub}(z) = (20(h_2 - h_1) - h_1 + z)^a \tag{5.4}$$

with

$$a = \frac{\ln(\rho_w V_0^2 G_0)}{\ln(20(h_2 - h_1))} \tag{5.5}$$

In order to calculate the resulting horizontal force $R(t)$ in fig.5.1, let us introduce I, the integral of the pressure profile on the wall $G(s)$ in the self similar plan:

$$I = \int_0^{s_p} G(s) ds \tag{5.6}$$

s_p represents the vertical velocity (relative to the fluid wedge velocity V_0) of the first point of the pressure distribution on the wall whose pressure is zero (or the ascending jet velocity). $\rho_w V_0^2 G_0$ is the constant value of the pressure at $z = h_1$ imposed by the

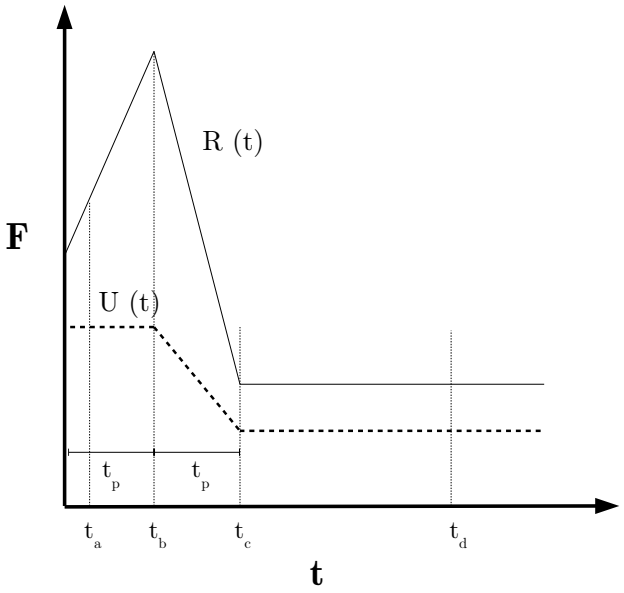

Figure 5.2: Horizontal and uplift forces of a FTI using the simplified model.

water wedge theory. Table 5.1 displays the values obtained of I, s_p and G_0 for the three angles considered in this study.

α	45°	60°	80°
I	3.23	9.57	150.79
s_p	2.4	3.2	11.0
G_0	1.79	2.87	10.67

Table 5.1: Numerical values of I, s_p and G_0 (from Wu (2007)) used in the present work.

Knowing these parameters, the auto-similarity allows to simplify the expression of the force applied on the caisson wall during the *flip-through* phase (see Martin-Medina et al. (2016) for details):

$$R(t) = F_{imp}(t) + F_{sub} + \frac{1}{2}\rho_w g h_2^2 \qquad (t_0 < t \leq t_b) \tag{5.7}$$

with

$$F_{imp}(t) = \rho_w V_0^3 I t \tag{5.8}$$

$$F_{sub} = \frac{(20(h_2 - h_1))^{a+1} - (20(h_2 - h_1) - h_1)^{a+1}}{a+1} \tag{5.9}$$

For the uplift force at the *flip-through* phase, a triangular pressure distribution already used by many authors (i.e.,Goda (1974)) is considered in this model. The pressure value at the left corner is assumed to be the same as the remaining constant pressure of the impacted face ($P_{sub}(z=0)+\rho_w g h_2$). The hydrostatic pressure ($\rho_w g h_0$) is considered at the harbour side of the caisson. The pressure under the caisson at the *flip-through* phase is kept constant in time (fig.5.2). The uplift force denominated by $U(t)$ is then calculated by:

$$U(t)=\frac{1}{2}\rho_w g h_b\left(\frac{P_{sub}(z=0)}{\rho_w g}+h_2+h_0\right) \qquad (t_0<t\leq t_b) \tag{5.10}$$

To keep advantage of the self-similarity, the water wedge theory is applied until the impact pressure peak is attenuated and the pressure distribution is mainly hydrostatic (h_2). The corresponding time is given by:

$$t_b=t_p=\frac{h_2-h_1}{V_0 s_p} \tag{5.11}$$

In the second stage ($[t_b,t_c]$), the wave forces on the caisson diminish linearly from the force peak down to a constant value at t_c (fig.5.2) corresponding to the hydrostatic pressure ($\frac{1}{2}\rho_w g h(2.2h_2-h)$) applied during the last stage as observed in the previous chapter. Between t_b and t_c, the resulting horizontal force is calculated by the following expression:

$$R(t)=\left(R_{peak}-\frac{1}{2}\rho_w g h(2.2h_2-h)\left(\frac{t_c-t}{t_p}\right)+\frac{1}{2}\rho_w g h(2.2h_2-h)\right. \qquad (t_b<t\leq t_c) \tag{5.12}$$

with $R_{peak}=\rho_w V_0^3 I t_b+F_{sub}+\frac{1}{2}\rho_w g h_2^2$.

The uplift force is also assumed to linearly decrease during this stage to a constant value given by a hydrostatic pressure where $1.1\rho_w g h_2$ and $\rho_w g h_0$ are applied at the left corner and right corner, respectively.:

$$U(t)=\left(U_{ab}-\frac{1}{2}\rho_w g h_b(1.1h_2+h_0)\right)\left(\frac{t_c-t}{t_p}\right)+\frac{1}{2}\rho_w g h_b(1.1h_2+h_0) \qquad (t_b<t\leq t_c) \tag{5.13}$$

with $U_{ab}=\frac{1}{2}\rho_w g h_b\left(\frac{P_{sub}(z=0)}{\rho_w g}+h_2+h_0\right)$.

The time t_c, when this force decrease stage is finished, need to be assessed. The numerical simulations presented in Chapter 4 are used to determine the value of this time with respect to the time of the force increase (t_p). This time is found to vary from 0.75 to 2.0 times t_p depending on the interface inclination at impact. But as the force peak is obtained at the end of the *flip-through* phase using the water wedge (see fig.5.2)

while it occurs in the middle of this phase with the numerical simulations, this time t_c is assumed to finish sooner than in the numerical simulations in order to avoid a significant underestimation of force at this phase. Hence, using the proposed model the second stage is proposed to finish at $t_c = 1.75t_p$, value that gives the best results for the three cases.

Finally, the forces converge toward a constant value during the last stage ($[t_c,t_d]$ in fig.5.2) that is controlled by the hydrostatic pressure generated by the wave overtopping the caisson as seen in the numerical simulations presented in Chapter 4:

$$R(t) = \frac{1}{2}\rho_w g h(2.2h_2 - h) \qquad (t_c < t \leq t_d) \tag{5.14}$$

The constant value of the uplift force after t_c is estimated by the following expression:

$$U(t) = \frac{1}{2}\rho_w g h_b(1.1h_2 + h_0) \qquad (t_c < t \leq t_d) \tag{5.15}$$

Motion duration

The impact starts at $t = 0$, but the caisson does not start to slide until t_a (fig.5.2) that can be obtained from equation $R(t) = \mu(W - U_{ab}) + R_{hyd_0}$ (where $R_{hyd_0} = \frac{1}{2}\rho_w g h_0^2$):

$$t_a = \frac{\mu(W - U_{ab}) + R_{hyd_0} - F_{sub} - \frac{1}{2}\rho_w g h_2^2}{\rho_w V_0^3 I} \tag{5.16}$$

With $W = \rho_s g h_b h$.

After t_c, calculated in the latter section, the caisson will continue moving under the action of the whole wave flow. In that phase, the caisson is considered to move with a velocity $v_{bc}(t_c)$ at t_c and the friction force stops it at t_d:

$$t_d = t_c + \frac{-(m + m_a)v_{bc}(t_c)}{R_{hyd} - \mu(W - U_{cd}) - R_{hyd_0}} \tag{5.17}$$

With $R_{hyd} = \frac{1}{2}\rho_w g h(2.2h_2 - h)$, $m = \rho_s h_b h$ and $m_a = 0.543\rho_w h_0^2$ (Oumeraci & Kortenhaus (1994)).

Caisson sliding

The caisson displacement is obtained by expressing the Newton's law of motion. In this work, it is assumed that the impact pressure field is not coupled to the caisson motion allowing a great simplification of the problem (Martin-Medina et al. (2016)). The total

sliding is calculated by summing partial displacements: S_{ab} $(t_a - t_b)$, S_{bc} $(t_b - t_c)$ and S_{cd} $(t_c - t_d)$. The horizontal motion equation for S_{ab} reads:

$$(m + m_a)\ \ddot{x}_{ab} = \rho_w V_0^3 I t + F_{sub} + \frac{1}{2}\rho_w g h_2^2 - (\mu(W - U_{ab}) + R_{hyd_0}) \tag{5.18}$$

Then, integrating the motion equation (5.18), we obtain the following sliding velocity:

$$\begin{gathered} v_{ab}(t) = \dot{x}_{ab}(t) = \\ \frac{1}{(m+m_a)}\left[\frac{1}{2}\rho_w V_0^3 I t^2 - (-F_{sub} - \frac{1}{2}\rho_w g h_2^2 + \mu(W - U_{ab}) + R_{hyd_0})t\right] + C_1 \end{gathered} \tag{5.19}$$

with nil velocity at $t = t_a$:

$$C_1 = -\frac{1}{(m + m_a)}\left[\frac{1}{2}\rho_w V_0^3 I t_a^2 - (-F_{sub} - \frac{1}{2}\rho_w g h_2^2 + \mu(W - U_{ab}) + R_{hyd_0})t_a\right] \tag{5.20}$$

and integrating equation (5.19), the following displacement :

$$\begin{gathered} S_{ab}(t) = x_{ab}(t) = \\ \frac{1}{(m+m_a)}\left[\frac{1}{6}\rho_w V_0^3 I t^3 - (-F_{sub} - \frac{1}{2}\rho_w g h_2^2 + \mu(W - U_{ab}) + R_{hyd_0})\frac{t^2}{2}\right] + C_1 t + C_2 \end{gathered} \tag{5.21}$$

with:

$$C_2 = -\frac{1}{(m + m_a)}\left[\frac{1}{6}\rho_w V_0^3 I t_a^3 - (-F_{sub} - \frac{1}{2}\rho_w g h_2^2 + \mu(W - U_{ab}) + R_{hyd_0})\frac{t_a^2}{2}\right] - C_1 t_a \tag{5.22}$$

t_a has to be positive in equation (5.16) which gives:

$$\mu(W - U_{ab}) + R_{hyd_0} > F_{sub} + \frac{1}{2}\rho_w g h_2^2 \tag{5.23}$$

This condition is not met when the horizontal force at t_a exceeds the friction force. In this case, the sliding motion is considered to start immediately and $t_a = 0$.

Finally, one can write:

$$t_a = max\left(0, \frac{\mu(W - U_{ab}) + R_{hyd_0} - F_{sub} - \frac{1}{2}\rho_w g h_2^2}{\rho_w V_0^3 I}\right) \tag{5.24}$$

t_b keeping the same value as in equation (5.11), the condition for sliding to occur (i.e., $t_a < t_b$) reads:

$$\frac{\mu(W - U_{ab}) + R_{hyd_0} - F_{sub} - \frac{1}{2}\rho_w g h_2^2}{\rho_w V_0^2 I} < \frac{h_2 - h_1}{s_p} \tag{5.25}$$

If this latter condition is not met, the sliding is nil.

The motion equation to estimate horizontal displacement during the stage $t_b - t_c$ reads:

$$\begin{gathered}(m+m_a)\ \ddot{x}_{bc} = (R_{peak} - R_{hyd})(\tfrac{t_c - t}{t_p}) \\ +R_{hyd} - \mu(W - ((U_{ab} - U_{cd})(\tfrac{t_c - t}{t_p}) + U_{cd})) - R_{hyd_0}\end{gathered} \tag{5.26}$$

With $U_{cd} = \frac{1}{2}\rho_w g h_b(1.1h_2 + h_0)$.

Integrating (5.26), one can write:

$$\begin{gathered}v_{bc}(t) = \dot{x}_{bc}(t) = \tfrac{1}{(m+m_a)}[(R_{peak} - R_{hyd})(\tfrac{t_c t - t^2/2}{t_p}) + R_{hyd}t \\ -\mu(Wt - ((U_{ab} - U_{cd})(\tfrac{t_c t - t^2/2}{t_p}) + U_{cd}t)) - R_{hyd_0}t] + C_3\end{gathered} \tag{5.27}$$

and integrating the latter equation, the displacement $S_{bc}(t)$ is obtained:

$$\begin{gathered}S_{bc}(t) = x_{bc}(t) = \tfrac{1}{(m+m_a)}[(R_{peak} - R_{hyd})(\tfrac{t_c t^2/2 - t^3/6}{t_p}) + R_{hyd}\tfrac{t^2}{2} \\ -\mu(W\tfrac{t^2}{2} - ((U_{ab} - U_{cd})(\tfrac{t_c t^2/2 - t^3/6}{t_p}) + U_{cd}\tfrac{t^2}{2})) - R_{hyd_0}\tfrac{t^2}{2}] + C_3 t + C_4\end{gathered} \tag{5.28}$$

With $C_3 = v_{ab}(t_b)$ and $C_4 = 0$.

During the last sliding stage ($t_c - t_d$), the horizontal (R_{hyd}) and uplift forces (U_{cd}) are assumed to be constant using this simplified model.

$$(m+m_a)\ \ddot{x}_{cd} = R_{hyd} - \mu(W - U_{cd}) - R_{hyd_0} \tag{5.29}$$

The caisson sliding velocity in time is obtained as before:

$$v_{cd}(t) = \dot{x}_{cd}(t) = \frac{1}{(m+m_a)}\left[R_{hyd} - \mu(W - U_{cd}) - R_{hyd_0}\right]t + C_5 \tag{5.30}$$

Integrating equation 5.30, the partial displacement between t_c and t_d is written as:

$$S_{cd}(t) = x_{cd}(t) = \frac{1}{(m+m_a)}\left[R_{hyd} - \mu(W - U_{cd}) - R_{hyd_0}\right]\frac{t^2}{2} + C_5 t + C_6 \tag{5.31}$$

With $C_5 = v_{bc}(t_c)$ and $C_6 = 0$.

If $v_{bc}(t_{ci}) = 0$ (being $t_{ci} \in [t_b - t_c]$), the caisson stops before t_c. In that case, the permanent displacement in this stage is $S_{bc}(t_{ci})$ and S_{cd} is nil. But if $v_{bc}(t_c) > 0$, the total sliding S of a caisson breakwater submitted to FTIs is calculated by summing all the partial displacements:

$$S = S_{ab}(t_b) + S_{bc}(t_c) + S_{cd}(t_d) \tag{5.32}$$

Parameters choice and range

The interpretation of the results depends on the choice of the parameters of interest. Some of the caisson parameters have been chosen taking into account the data given in Goda (1974) regarding composite breakwaters in Japan. The idea is to constitute a representative case whose dimensions are function of the caisson height. The average values of h_w, h_b and h_0 (fig.5.3) of the caissons studied in Goda (1974) are summarized in table 5.2. h_1, height where the FTI starts after the *wave approaching* phase, has been estimated analysing the experimental study of the flip-through carried out by Lugni et al. (2006): $h_1 = h_0 + \frac{H_w}{6}$. This height is function of the initial water level (h_0) and the wave height (H_w). Similar values for h_1 were obtained with the Navier-Stokes numerical experiments (Chapter 4). For the maximum height (h_2) reached on the caisson by a FTI still presenting a pressure distribution with a marked peak, numerical simulations have been performed with an infinite obstacle obtaining values between $1.2H_w$ and $1.4H_w$ for the least steep case and the steepest case, respectively. $1.3H_w$ is assumed for the formulation. After this height, the ascending jet would continue moving up, but pressures would be mainly hydrostatic. If $1.3H_w > h - (h_0 - 0.5H_w)$ (the emerged part at impact), the FTI is considered to act in the totality of the emerged part of the caisson ($h_2 = h$). But if the wave does not overtop the caisson, the water wedge model is only applied up to $h_2 = h_0 - 0.5H_w + 1.3H_w = h_0 + 0.8H_w$. Here we take $\rho_s = 2100\ kg.m^{-3}$ and do not consider any inhomogeneous distribution of mass. The coefficient of friction μ is assumed to be 0.6.

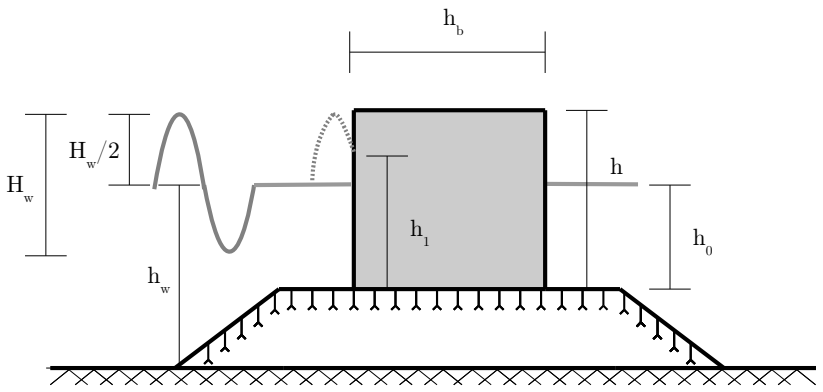

Figure 5.3: Water wedge impacts approaching the flip-through phenomenon.

Parameter	Value
h_b	$1.1h$
h_0	$0.7h$
h_1	$h_0 + \frac{H_w}{6}$
h_2	$min(h, h_0 + 0.8H_w)$
h_w	$1.15h$
β	$1/50$

Table 5.2: Average dimensions considered in this study.

The average value of h in Goda (1974) is 10 m with values varying from 5 m to 17 m. This range is considered in the analysis of the parameter sensitivity. The height of periodic waves that may break directly into the caisson depends on the breaking parameter $\gamma = \frac{H_w}{h_w}$. This parameter is usually considered equal to 0.78, but the literature shows that it may vary. A parametrization of γ in function of local variables is given in Raubenheimer et al. (1997) for values between 0.2 and 1.2:

$$\gamma = 0.19 + 1.05\frac{\beta}{kh_w} \tag{5.33}$$

With β the bottom slope and k the local wave number ($\frac{(2\pi)^2}{gT^2}$). Values near 0.2 represent waves with a short period and length, in contrast, long waves with important period correspond to $\gamma = 1.2$. Wave height values between these boundaries ($0.2h_w \leq H_w \leq 1.2h_w$) are considered in this work.

The impact velocity, represented by the parameter V_0, has also to be assessed. Here, we assume that V_0 is close to the celerity of the wave that the water wedge is supposed to represent. For wave approaching breaking but before the overturning stage, Wei et al. (1995) shows that the maximum fluid velocity at the free surface stays of the order of the wave celerity which justifies our choice. Imposing the value of γ, the wave period is calculated with equation (5.33), and so the wave celerity can be estimated based on the linear wave theory approximation of Guo (2002):

$$V_0 \simeq c = \frac{gT}{2\pi(1 - exp(-((2\pi/T)\sqrt{h_w/g})^{(5/2)}))^{-2/5}} \tag{5.34}$$

5.3 Results

5.3.1 Validation of the water wedge model

A comparison of forces and permanent displacements is now presented to confirm the applicability of this model to approach FTIs. Note that the proposed model was formulated using a periodic wave, but a solitary wave is here imposed to compare with the numerical simulations. This implies that $h_1 = h_0 + \frac{2H_w}{3}$ and $h_2 = min(h, h_0 + 1.3H_w)$.

Impact force signals

The force signals computed using the simplified model are compared to the force signal obtained with the numerical simulations in fig.5.4. Let us recall that the simplified model does not consider the beginning of the force increase (*wave approaching* and *focusing* phases) because loads before the *flip-through* phase are generally not high enough to move the caisson. The horizontal and vertical force peaks are reasonably well estimated for the $I1$ and $I2$ cases. But these forces are overestimated for the $I3$ case. The maximum horizontal force estimated by the proposed model reaches the value of $18500KN$, being 1.5 times higher than the force calculated with the numerical simulations ($11200KN$). The uplift force under the caisson is better estimated by the simplified model ($6200KN$), being 1.1 times larger than the uplift force computed with the THETIS code ($5600KN$). After the peak, the horizontal and uplift forces decrease to hydrostatic pressure values. The horizontal hydrostatic force with THETIS have, therefore, the same value for the three cases ($\simeq 950KN$), which is consistent to the hydrostatic pressure assumed with the simplified model ($\simeq 1000KN$). The same is found for the uplift force which constant hydrostatic pressure is $\simeq 1100KN$ in the numerical simulations and $1140KN$ with the proposed method. It is important to highlight that the transition between the force peak and the remaining hydrostatic force happens in an abrupt manner using the simplified model. But this transition is observed to be more gradual in the numerical simulations.

As the forces of the *I3* case are overestimated using the model with a wedge inclination of 80°, a comparison to a 70° case (the initial wave steepness at impact was 75° in Chapter 4) is displayed in fig.5.5. The parameters I, s_p and G_0 are obtained by simply interpolating linearly between the 60° and 80° cases. The 70° case presents more accurate results in terms of force peak than the 80° case. The maximum horizontal and vertical forces are respectively $13100KN$ and $4300KN$, closer to the numerical results ($11200KN$ and $5600KN$) than the 80° case.

The minimal $S.F.$ values can be estimated for the three numerical cases once the horizontal and uplift forces have been assessed. For the $I1$ and $I2$ cases, numerical

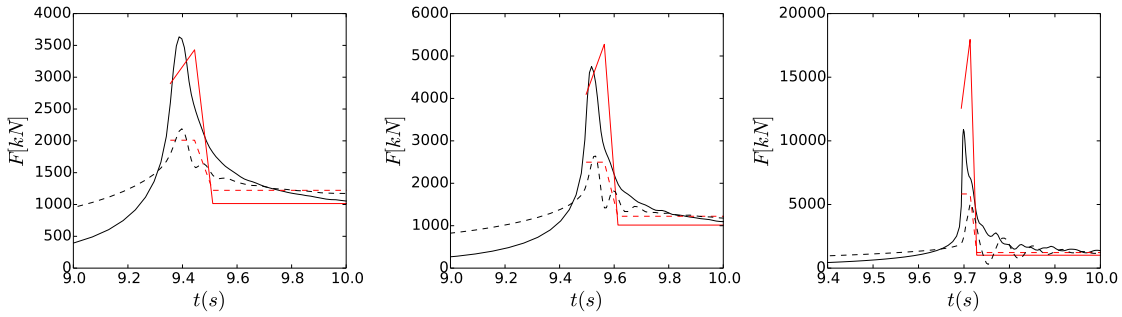

Figure 5.4: Time evolution of horizontal force (continuous line) and uplift force (dashed line) computed by the numerical simulations (black) and the water wedge model (red). *I1*, *I2* and *I3* from the top to the bottom.

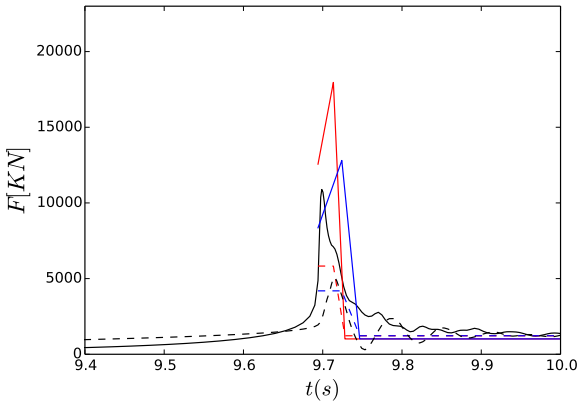

Figure 5.5: *I3* case. Time evolution of horizontal force (continuous line) and uplift force (dashed line) computed by the numerical simulations (black), 70° water wedge (blue) and 80° water wedge (red).

simulations with THETIS give $S.F.$ values of 0.25 and 0.1, respectively. Using the simplified model, the $S.F.$ values are 0.31 and 0.07 giving a good agreement. For the steepest case, the simplified model predicts that the $S.F.$ is negative (-0.19) and gives a similar value to the numerical flip-through (-0.15) even if the horizontal and uplift forces are largely overestimated for the simplified model.

Caisson motion

Fig.5.6 shows a comparison of permanent displacement and sliding velocity computed by the numerical simulations and the proposed model. Overall, similar displacements and caisson velocities are found for the three FTIs. For the least steep case, the displacement given by the model is $0.38m$ underestimating the computed numerical sliding ($0.59m$). A displacement of $0.58m$ is estimated for the *I2* case which numerical simulation generates

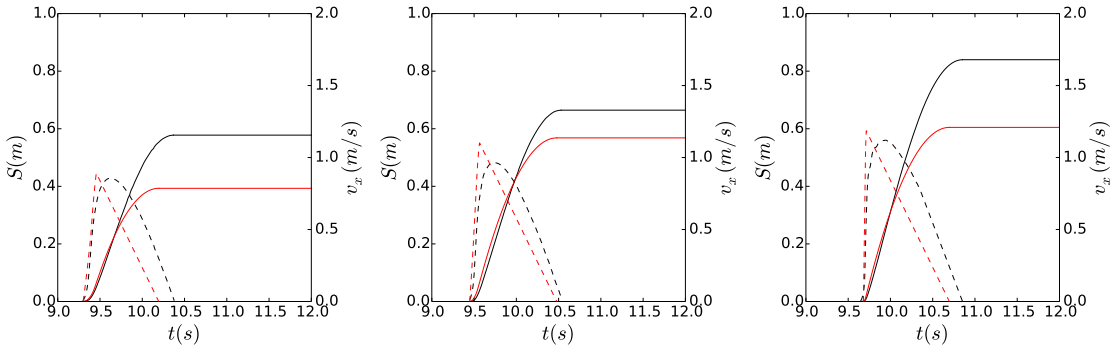

Figure 5.6: Caisson sliding (continuous line) and velocity (dashed line) obtained with the numerical simulations (black) and the water wedge model (red). *I1*, *I2* and *I3* from the left to the right.

a similar value ($0.67m$). The maximum velocities obtained for these cases ($0.85m/s$ and $1.04m/s$) are in good agreement with the simplified model ($0.87m/s$ and $1.12m/s$). For the steepest FTI, the permanent displacement obtained with the numerical simulations reaches a value of $0.83m$ (the maximum value among the three cases) while it is underestimated by the proposed method is $0.61m$. The maximum caisson velocity is slightly overestimated ($v_{x,(NS)} = 1.17m/s$ and $v_{x,(model)} = 1.22m/s$). It is important to note that the sliding durations are reasonably well approached for the three cases.

For the steepest case, the caisson displacement was also calculated using the model with a wedge inclination of 70° but not presented as the results were similar to the 80° case. Even if the resulting forces (shown in fig.5.5) are smaller, the time of application becomes longer and the total sliding increases up to the value of $0.78m$.

5.3.2 Parameter sensitivity

The simplified model using the water wedge approach is now applied to plot maps of forces, motion durations and displacements in function of wave characteristics (H_w) and caisson dimensions (h) for the 3 angles considered in this work: $\alpha = 45°$, 60° and 80°.

Impact resulting forces and S.F.

The maximum horizontal (R_{peak}) and uplift forces (U_{ab}) taken at $t = t_b$ are displayed respectively in fig.5.7 and fig.5.8. The results are plotted for waves that may break directly on the breakwater caisson generating a FTI (see criteria(5.33)). The plot is limited by two areas on the left and on the right where waves do not break or would be already broken. These forces increase for larger caissons (h) because the emerged part impacted by the flip-through is assumed to grow with h. Less significant variations

in terms of force are observed varying the wave height (H_w). For a given wave celerity and caisson dimensions, the largest force values are found for the steepest case (80°). Comparing between the three angles considered in this work, the 80° impact generates horizontal forces that are in average about 4 and 8 times the forces of the 60° and 45° cases.

Focusing on the uplift forces, a similar relation between the three impacts is observed. As the pressures under the caisson are directly linked to the remaining constant pressures on the impacted face caisson, the steepest FTI generates the most extreme vertical forces.

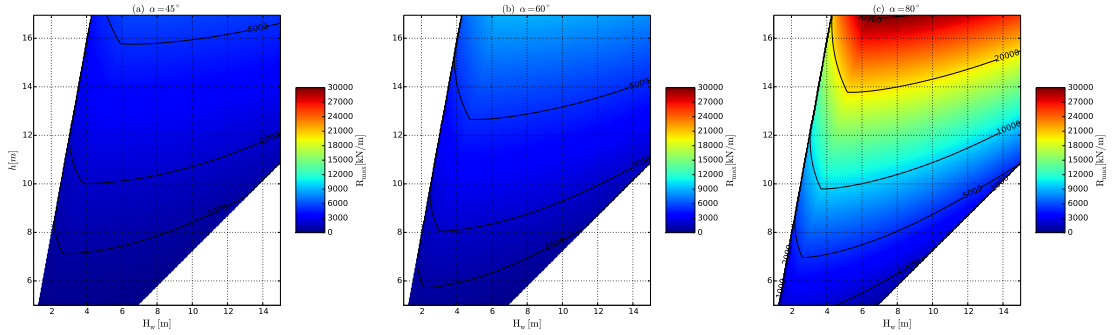

Figure 5.7: Maximum horizontal force (reached at $t = t_b$) for $\alpha = 45°$, 60° and 80°.

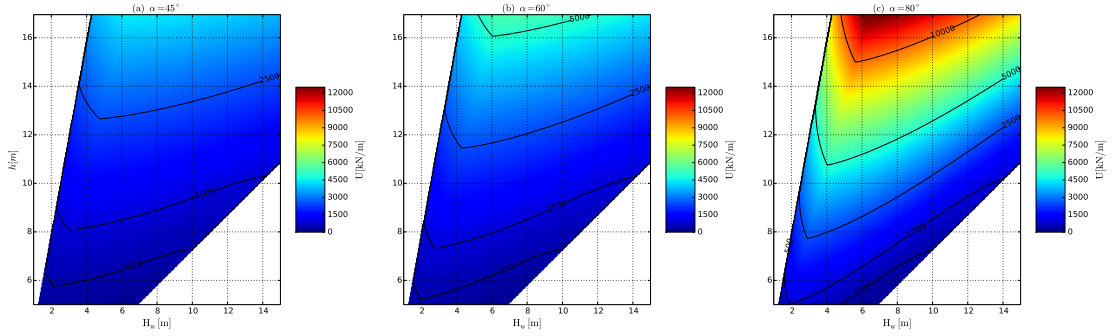

Figure 5.8: Maximum uplift force (reached at $t = t_b$) for $\alpha = 45°$, 60° and 80°.

Once the horizontal and uplift forces have been calculated, the minimum S.F. values can be estimated. The results are not illustrated for different caisson dimensions (h) and wave height (H_w) because very similar values are obtained. As one may guess, the steepest FTI gives the smallest S.F. values obtaining a negative S.F. of ~ -0.10. The 45° and 60° cases also generate low S.F. values: 0.20 and ~ 0.05.

Sliding duration

The duration of the peak force increase (t_p) is plotted in fig.5.9. The highest values of the peak duration are obtained for FTIs whose maximum impact height at the wall matches the height of the caisson ($h_0 + 0.8H_w = h$). The peak duration decreases when the wave impact height is higher than h and the caisson is submitted to only a part of the impact. Comparing the three angles, the steepest wave faces lead to the shortest time duration t_p.

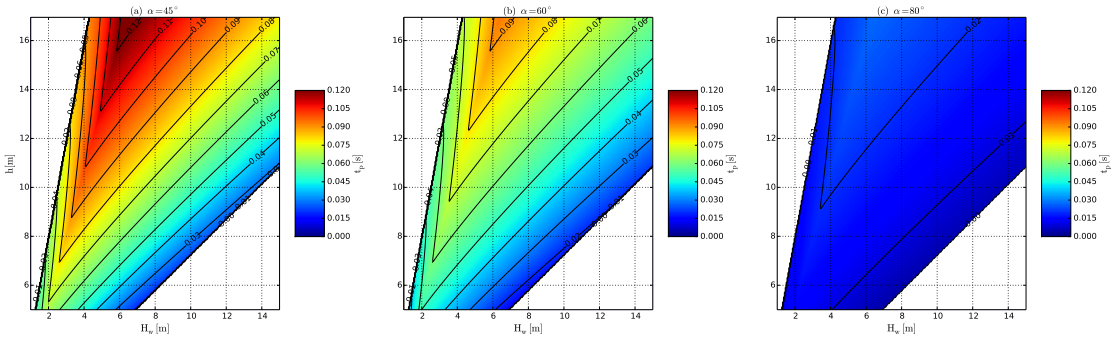

Figure 5.9: Force peak increase duration (t_p) in function of V_0 and h.

Fig.5.10 shows an estimation of the total sliding duration ($t_d - t_a$). Overall, the duration varies with a similar pattern for the three FTI cases. As for the t_p durations, the maximum values are obtained for caissons submitted to waves which impact at the wall reaches the top of the caisson. Similar values are found for the two steepest cases (between $0.20s - 0.75s$) obtaining the larger sliding duration for the 80° FTI. For the least steep case, the sliding durations are shorter varying between $0.15s - 0.60s$.

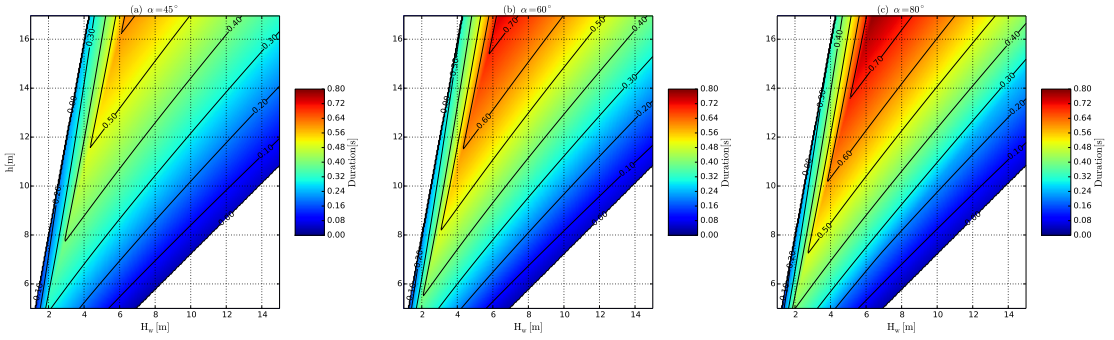

Figure 5.10: Sliding duration ($t_d - t_a$) in function of V_0 and h.

Caisson sliding

The maximum velocity reached by the caisson breakwater during the sliding is plotted in fig.5.11. The largest caisson velocities ($1.20m/s - 1.40m/s$) are obtained for the two steepest cases. For the 45° cases, waves of $6 - 10m$ impacting large caisson can also generate significant caisson velocities ($V_{max} > 0.80m/s$).

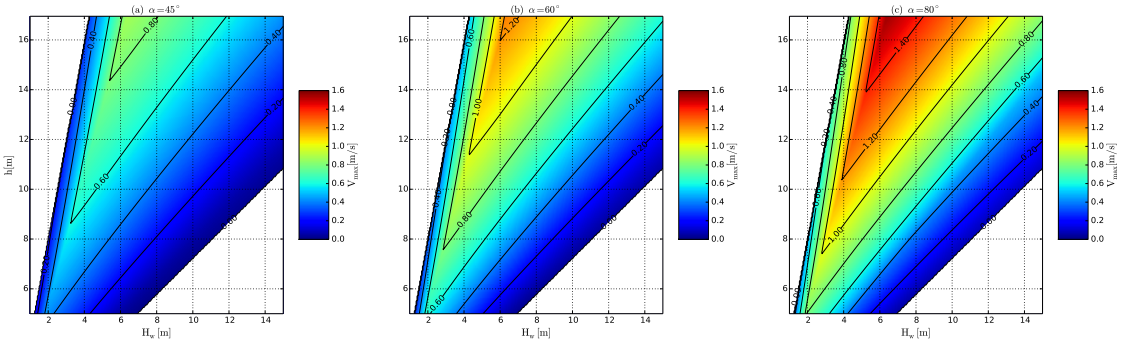

Figure 5.11: Maximum sliding velocity reached by the caisson in function of h and V_0.

Caisson permanent displacements estimated by the proposed model are plotted in fig.5.12. For the smallest waves, the caisson sliding is induced by the action of the whole wave. For this reason, if h is equal to $10m$ (red dashed line in fig.5.12), sliding values increase rapidly with H_w up to a maximum displacement when the caisson is impacted by a wave of $4m$. After this value ($H_w > 4m$), the displacement decreases with the wave height. For the three cases, the permanent displacement is very limited for the biggest waves that may generate a FTI. This is due to the fact that almost the whole wave overtops the caisson and the impact duration (fig.5.9) is very short compared to FTIs generated by smaller wave heights. As observed for the caisson motion velocity, the most significant displacements are observed for the 60° and 80° flip-through cases with a maximal sliding of $0.5m$ and $0.7m$ respectively. The least steep case gives lower displacements than the previous cases, but they may be considerable ($0.30m$) for wave height values between $6m$ and $9m$ impacting the largest caissons ($h = 16m$).

5.4 Discussion

A semi-analytical model was proposed aiming to calculate forces and sliding along the interface between the caisson and the rubble foundation due to FTIs with different steepness at impact. The formulation of this model is based on the water wedge approach and numerical results presented in Chapter 4. Comparing to these numerical experi-

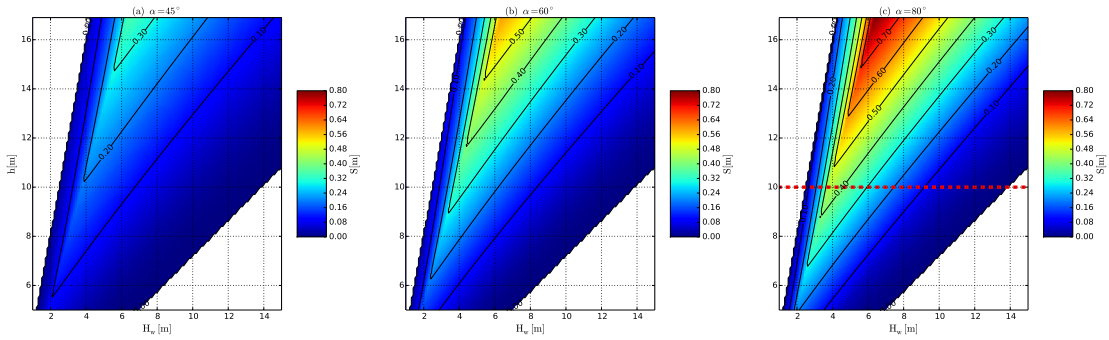

Figure 5.12: Caisson total displacement at t_d for $\alpha = 45°$, $60°$ and $80°$.

ments, a good estimation of horizontal and vertical forces was obtained for the least and medium steep cases, but more discrepancies are found for the steepest case. In terms of caisson sliding, consistent results were obtained for the three FTIs reproducing the tendency of the sliding to increase with the interface inclination at impact. Even for the steepest case, whose loads were overestimated by the water wedge model, the numerical and estimated caisson displacements are in acceptable agreement.

FTIs have been shown to be a very complex phenomenon that generate larger pressures than any other kinds of wave impact. To our knowledge, this is the first study that includes a method to assess the stability of caissons subject to FTIs taking into account the wave inclination at impact. The great advantage of this model with respect to numerical simulations is that, simplifying this phenomenon with the water wedge approach, forces and caisson displacement can be instantaneously obtained. Force, motion duration and caisson displacement maps have been plotted to show how they vary in function of caisson height and wave characteristics.

The water wedge model takes into account the influence of the interface inclination on the forces observed in the numerical simulations, but clear differences are observed between the estimated and simulated force peak for the steepest case. Such differences seem to be due at least in part to the variation between the initial incidence angles of the *I3* FTI case (75°) and the 80° water wedge. The abrupt inclination change encountered in the simulation (see Chapter 4) may also have an influence on the pressure decrease during the *flip-through* phase and this is not considered in the simplified model. The numerical *I3* case was also compared to a 70° water wedge obtaining force signals in better agreement. But still the peak duration was overestimated. Concerning the Safety Factor against sliding, defined by the stabilizing forces divided by the destabilizing forces, very low S.F. values, even negative for the steepest case, were estimated for the numerical simulations and the proposed model meaning that the stability of the caisson is seriously

compromised under such FTIs.

Focusing on the caisson motion, the method formulated in Shimosako & Takahashi (2001) is used to predict the permanent caisson displacement and then compare this value to the results obtained in this paper. A permanent displacement of $9cm$ is estimated while the numerical simulations show larger displacements (0.59, 0.67 and 0.83 m). The simplified water wedge method was more accurate to assess the sliding of the caissons submitted to FTIs (0.38, 0.58 and 0.61 m).

After the validation of the model, sliding distance maps (fig.5.12) have illustrated that the motion of the structure is the result of the combined effect of force magnitude and impact duration, which both strongly depend on wedge inclination. Hence, even if much higher forces are obtained for the steepest case than for the other two cases, this does not mean that the sliding velocity and the caisson displacement would be the largest. The medium steep FTI (60°) induces almost the same displacement than the 80° case even if the forces are four times smaller. Comparing sliding values obtained in these maps to the tolerable sliding limit of $30cm$ given by Shimosako & Takahashi (2001) and Goda & Takagi (2000), we realize how extreme this kind of impact is as most of the cases susceptible of generating a FTI with a very steep interface would induce a displacement up to this tolerable limit. We observe that small waves (e.g., $H_w = 2m$) generating a FTI in relatively large caissons ($h = 7m$) would induce a slight displacement ($\simeq 5cm$). This is mainly due to the extreme pressures and high forces that, according to the water wedge method, are applied during a short time for any FTI case. Under similar conditions, near-breaking and impulsive wave impacts have been experimentally studied in Shimosako et al. (1994) where small caisson displacements ($5 - 10mm$ for a caisson of $1 \times 1.2m$ impacted by a wave of $40cm$) have been measured as it was estimated with the water wedge model.

Caisson sliding has been identified by several authors (Oumeraci (1994), Takahashi et al. (2001)) as a more frequent cause of composite breakwater failure compared to tilting. At this first stage, this work focused on sliding and did not consider tilting, but the method developed is easily adaptable to the tilting motion. Tilting and sliding may also happen at the same time, and in this case, sliding distance would be reduced (Kim et al. (2004)). This effect is not taken into account in the method, which means that caisson sliding results would be on the safe side.

The current version of this model did not consider the dynamic interaction between rubble mound and caisson as well. Oumeraci & Kortenhaus (1994) concluded that the analysis of the dynamic response of the system caisson-rubble mound is necessary to improve the estimation of residual permanent caisson displacements. However, even if

the first oscillatory motion due to the dynamic response of the foundation can not be reproduced in our approach for now, the model is susceptible to give consistent results in terms of permanent displacement similarly to Oumeraci et al. (1995).

This chapter was focused on formulating the first version of a semi-analytical method using the water wedge approach to estimate loads and caisson sliding generated by FTIs in the real configuration of a vertical breakwater. This simplified method was described and validated with respect to the numerical simulation presented in Chapter 4. Interesting results in terms of forces and sliding were then given in maps with many cases of FTI with three different inclinations. These maps showed the wave generating a maximum sliding value for each caisson height. For instance if $h = 10m$ in fig.5.12, the maximum displacement induced by a FTI is generated by a wave of $\sim 4m$. These values coincide with the cases where the maximum impact height is equal to the caisson height ($h_2 = h$). The height of this wave is given by the following expression: $H_w = \frac{3}{8}h$.

Further work will focus on integrating the mentioned simplifications (as the relation between wave, caisson and rubble mound, the pressure-displacement decoupling and the sliding/tilting motion) and updating the formulation to improve the results given by the water wedge method.

5.5 Conclusions

In this chapter, we studied loads and motion of breakwater caissons submitted to Flip Through Impacts (FTI) using a semi-analytical model. The following main conclusions can be drawn from this study :

- Numerical experiment versus water wedge model: It was demonstrated that the presented model is able to approach the FTI dynamic. This method allowed to correctly estimate the horizontal and uplift forces in time for the least and medium steep flip-through cases. But it overestimated the force peak due to the steepest impact ($\alpha = 80°$). The caisson motion was also assessed using this model. A good agreement was found for the three FTIs, even for the steepest case for which the water wedge gave larger acting forces than the numerical cases. Overall, the simplified model gives satisfactory results considering the simplifications of the formulation and the complexity of the problem.

- Parameter sensitivity: Graphs have been plotted to show the variation of forces, motion duration and caisson sliding in function of caisson dimensions and wave height. These plots allow to identify which waves would generate the largest sliding for a given caisson height.

- Permanent displacement in function of the flip-through face inclination: Even though the most dangerous case in terms of structure stability is logically generated by the steepest and fastest 80° inclined water wedge, significant total displacements were also found for the two least inclined FTI. Therefore, if wave shape is an important parameter in this problem, the free surface angle range able to produce dramatic sliding consequences is not as narrow as we may have initially assumed.

- Overall, this work shows that FTIs have the potential to induce structure failure. The structure displacements obtained numerically or analytically are impressive and does not fortunately occur frequently in reality. To better understand the underlying reasons for this difference, there is a need to quantify the occurence frequency of FTIs in-situ by adequate observations.

Chapter 6

General conclusions and future work

This PhD improved the knowledge on wave impact on vertical breakwater. The scope is first put on a large scale study of the Tohoku tsunami interaction with the Soma Breakwater. After that, the flip-through phenomenon, which may be generated by tsunami undular bores or storm waves, is investigated in the real configuration of a vertical breakwater.

The following conclusions are drawn from this research work:

- Numerical validation of BOSZ and THETIS.

  The BOSZ model has been validated to simulate the generation and propagation of tsunami undular bores towards the coast. A large validation of THETIS was made to model the flip-through phenomenon and flows through porous mediums generated by wave impacts. In the framework of the TANDEM project, THETIS model has been further validated for water impacts generated by dam-break flows (see Annexe 1). The model has been also tested to simulate the propagation and breaking process of waves over a coastal reef (see Annexe 2).

- Tsunami transformation into an undular bore.

  Chapter 3 has shown that the second wave of the Tohoku tsunami formed an undular bore when the front maximum elevation slope (α_m) overpassed the value of 9×10^{-3}. This value was shown to be a threshold for the undular bore generation in Sendai Bay. In contrast, for the first wave, this α_m limit value has never been reached and no undulations has appeared during the arrival of this wave to the coast. In Sendai plain, the amplitude of the tsunami bore undulations kept increasing until arriving to very shallow waters where they started to break before impacting the

Soma breakwater. As in Madsen et al. (2008), it has been demonstrated that the use of dispersive codes is essential to model this regime transition.

- Tsunami overtopping vs tsunami undular bore impact.

  Focusing on the effect of the Tohoku tsunami impact on the breakwater of Port of Soma, it has been shown that this structure was submitted to overtopping and successive wave impacts due to the first and second (undular bore) waves. For the tsunami overtopping, numerical models have given large values of force and overturning moment. This led to sliding safety factors between 0.8 and 1.0. Such S.F. values and the excessive bearing stress in the rubble mound could explain the breakwater failure. In the case of the undular bore, the numerical simulation of the tsunami undulation impacts have illustrated that forces and moments applied to the breakwater caissons were not strong enough to compromise the structure stability (S.F. values above 1.0). BOSZ and THETIS were shown to be overall in a good agreement for the tsunami-structure interaction. At large scale, the Navier-Stokes model does not allow to fully simulate the wave impact dynamics and BOSZ might be a useful tool for a first estimation of breakwater stability.

- Flip-through impacts on a vertical breakwater.

  THETIS numerical model has been used to study flip-through impacts in the real configuration of a vertical breakwater for the first time. The existence of a whole range of flip-through cases depending on the front steepness has been proven. The largest pressure have been obtained for the steepest flip-through case. Pressures inside the rubble mound breakwater have been also estimated taking into account flows through porous mediums. It has been demonstrated that the value of this pressure depends on the constant pressure obtained on the impacted caisson face and, therefore, on the flip-through wave inclination.

- Study of the stability of breakwater caissons submitted to flip-through impacts using a simple method based on the water wedge theory.

  The numerical experiment described in Chapter 4 has been used to check the validity of a simplified method using the water wedge approach (already used in Cumberbatch (1960) and Kihara et al. (2015)). Overall, the water wedge method has given satisfactory results in terms of forces and estimated permanent displacement. Once the applicability of the method was validated, plots have been designed which contain rich information to predict impact forces, motion duration and permanent displacement depending on the flip-through case and the breakwater characteristics.

- Permanent displacement of caissons under flip-through impacts.

  This work has shown that flip-through impacts are a very dangerous phenomenon that might lead to the breakwater failure. The most severe case corresponded to the steepest and fastest flip-through. But least steep cases were able to generate very large sliding distance destabilizing breakwater caissons.

As further work, the following points should be addressed in the future:

- Numerical investigation of the formation and impact of different undular bore cases.

  Chapter 3 focused on the numerical study of the Tohoku tsunami propagation and its impact to the Soma offshore breakwater. This chapter raised the question of what would be the destructive effects induced by other tsunami undular bore cases. An interesting contribution would be the investigation of undular bore impacts generated by tsunamis of different characteristics and under several scenarios (water level, bathymetry slope). This study could be also used for engineering purpose since loads on a given breakwater would be predicted for all the possible cases of undular bore. BOSZ has been shown to be a useful tool to carry out this kind of large scale impact studies. However, if the undular bore generates wave aerated impacts or flip-through cases, the use of more detail models (as THETIS) would be needed.

- Field observation of flip-through impacts on vertical breakwaters.

  Laboratory experiments and numerical studies have shown the impact dynamics and pressures of the flip-through phenomenon. However, to the knowledge of the author, this phenomenon has not been identified in real breakwaters yet. A field campaign focusing on the measure of pressures and recording the wave shape at impact would allow to clarify the frequency of such wave impacts and their effects. The Risks and Structure group of SIAME laboratory has monitored with pressure gauges the breakwater of Saint-Jean de Luz (South of France), which is susceptible to be submitted to these extreme impacts. A Phd has just started aiming to analyse this data and new devices will be installed to capture the wave shape.

- Consideration of the caisson-foundation interaction with the water wedge method.

  The aims of Chapter 5 is to give a first estimation of caisson displacements generated by flip-through impacts using a semi-analytical method. But this method would need to be updated to take into account the interaction of caissons with the breakwater foundations. A comparison with laboratory experiments would contribute to a complete validation of the updated method. A new collaboration is been established with the coastal engineering department of Waseda University (Japan),

which disposes of laboratory facilities to carry out this experimental study. Furthermore, this research group has a large experience on wave impact on coastal structures. In this case, the focus would be put on flip-through impacts (recording the exact wave shape at impact) on a vertical breakwater composed by a porous rubble mound and a movable caisson.

Appendix A

Appendix I: TANDEM validation case I01. Dam-break with structure impact

---

In the framework of the TANDEM research project, THETIS and other numerical models have been validated carefully to reproduce violent water impacts. The validation case is based on the laboratory experiments presented in Kleefsman et al. (2005). This case consists in the traditional problem of a dam-break flow impacting a block.

A.1 Description of the case

The experimental system (fig.A.1) is a large tank of about 3 m^3. A certain water volume is maintained by a rigid door in the right part of the tank. The left part is initially dry and contains a small rectangular box. All other tank boundaries are rigid walls. The experiment begins when the door is removed and finishes when equilibrium is reached. The processes studied here are firstly the collapse of the water column, secondly the splash-up on the obstacle, thirdly the interaction with the left wall, and finally the back flow. Measurements are available from Kleefsman et al. (2005).

In this test case, three codes proposed by TANDEM collaborators are compared, all of them solving the

- Navier-Stokes equations.
- Sphynx (SPH method).
- THETIS (multiphase Eulerian VOF).

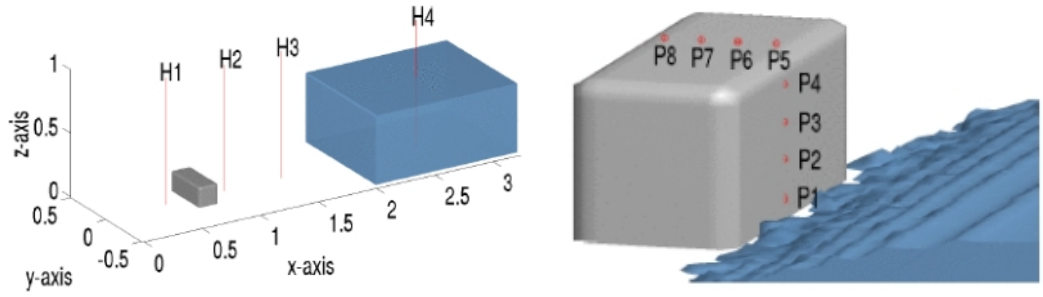

Figure A.1: Set-up of the I01 case.

- EOLENS (Euler equations with interface capturing).

A.2 Main results

On fig.A.2 and fig.A.3, the dam break flow at times 0.40s and 0.56s are shown from a side view, from a volume representation for SPH and with an iso-line of the free surface for the Eulerian codes. The flow is colored by the velocity except for THETIS.

At t = 0.40s (Fig.A.2), all codes give a similar free surface shape. Though, a small delay can be seen on Sphynx and EOLENS simulations compared to the other codes. Furthermore, THETIS seems to highlight some "physical" instabilities of the free surface, probably due to air/liquid flows interactions at the interface.

At t = 0.56s (Fig.A.3), all codes still provide quite comparable results on the whole, although EOLENS and THETIS seem to slightly under predict the height of the splash in comparison with experiments (and with Sphynx' results). Sphynx and EOLENS give the same order of magnitude for the free surface velocity.

Fig.A.1 shows the position of the pressure sensors. Comparisons are done for two sensors on the front face of the obstacle (P1 and P3) and for one on the top of the box (P7). The results on the other sensors are not showed here because they do not bring further information about the benchmarking.

The results are depicted by fig.A.4 and fig.A.5. For all pressure probes, Sphynx gives quite good results despite some discrepancies on the pressure impact (at P1) which is anticipated and smoothed. For THETIS, three simulations are available with several meshes (coarse, middle and fine). Pressure peak values obtained, though not too far away from the experimental data, are found to be grid dependent. It would be interesting to

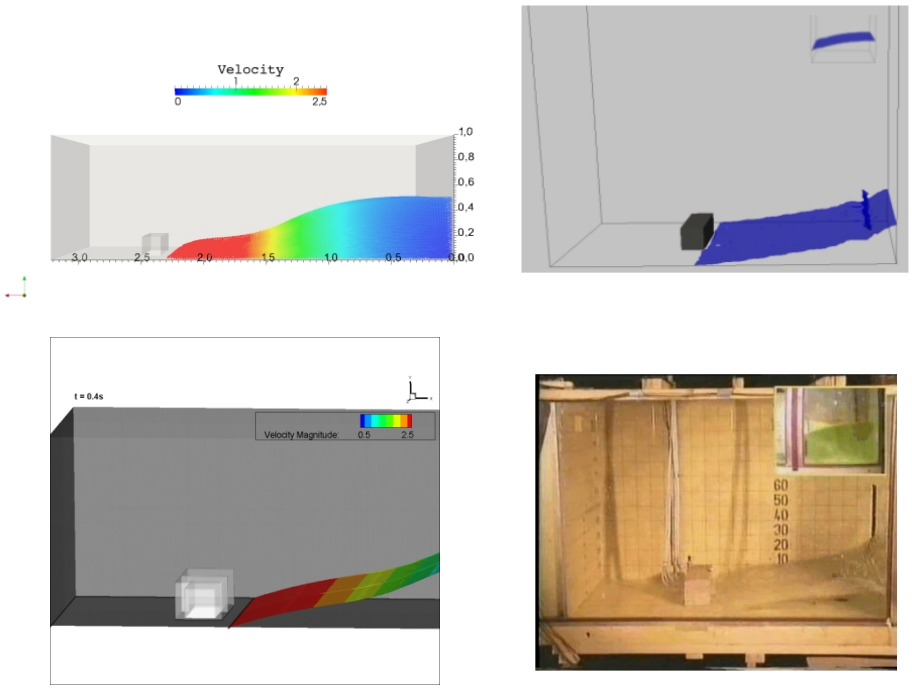

Figure A.2: Shape of the free surface at t = 0.40s. From top to bottom and left to right: Sphynx; THETIS; EOLENS; experiments.

look at the convergence of all incompressible codes used in this benchmark.

Two simulations are carried out with EOLENS on the same mesh, with and without interface compression method. With the compression model, the quick increase of the pressure at the impact is better reproduced than without compression. However for both methods the code under-predicts the pressure at the impact (P1, P3). The global pressure evolution is quite good for the simulation with the interface compression model whereas a too large damping is highlighted without the compression. On the whole, the compression allows a significant improvement of the results.

A.3 Conclusions

All codes have proved their potential ability to simulate the complex physics of this test case, especially the pressure impact problem. Sphynx gives good results on the whole but fails to capture with accuracy the quasi-instantaneous peak pressure at the impact (P1). THETIS gives correct results about elevation but pressure peaks are grid dependent although less than in the P1 case (note that THETIS is the only incompressible model

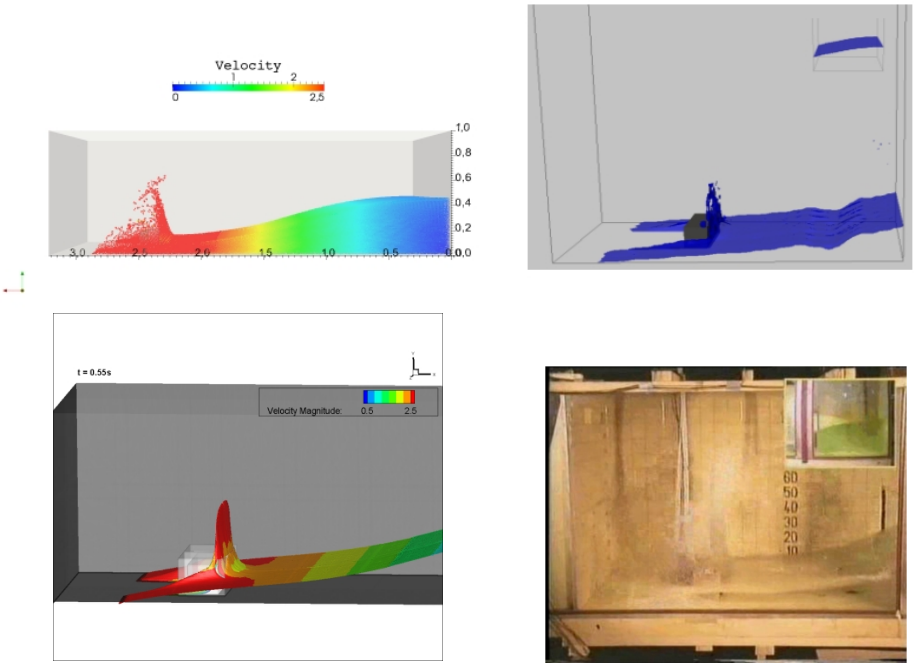

Figure A.3: Shape of the free surface at t = 0.56s. From top to bottom and left to right: Sphynx; THETIS; EOLENS; EOLE; experiments.

providing convergence study here). EOLENS gives quite good results, although the pressure peaks on the front of the obstacle is underestimated. The interface compression method allows a significant improvement of the results.

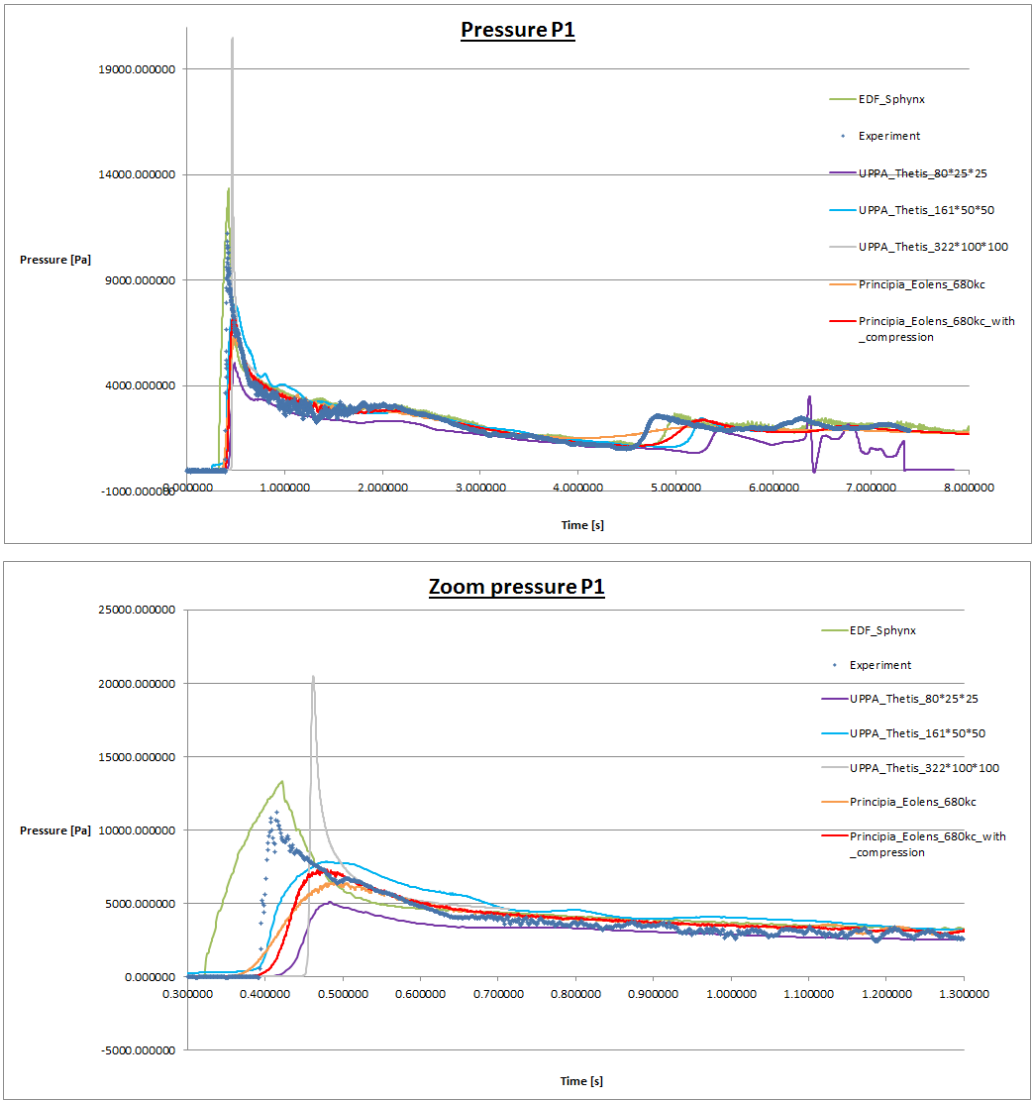

Figure A.4: Time evolution of pressure at P1 (zoom near the main peak on the bottom).

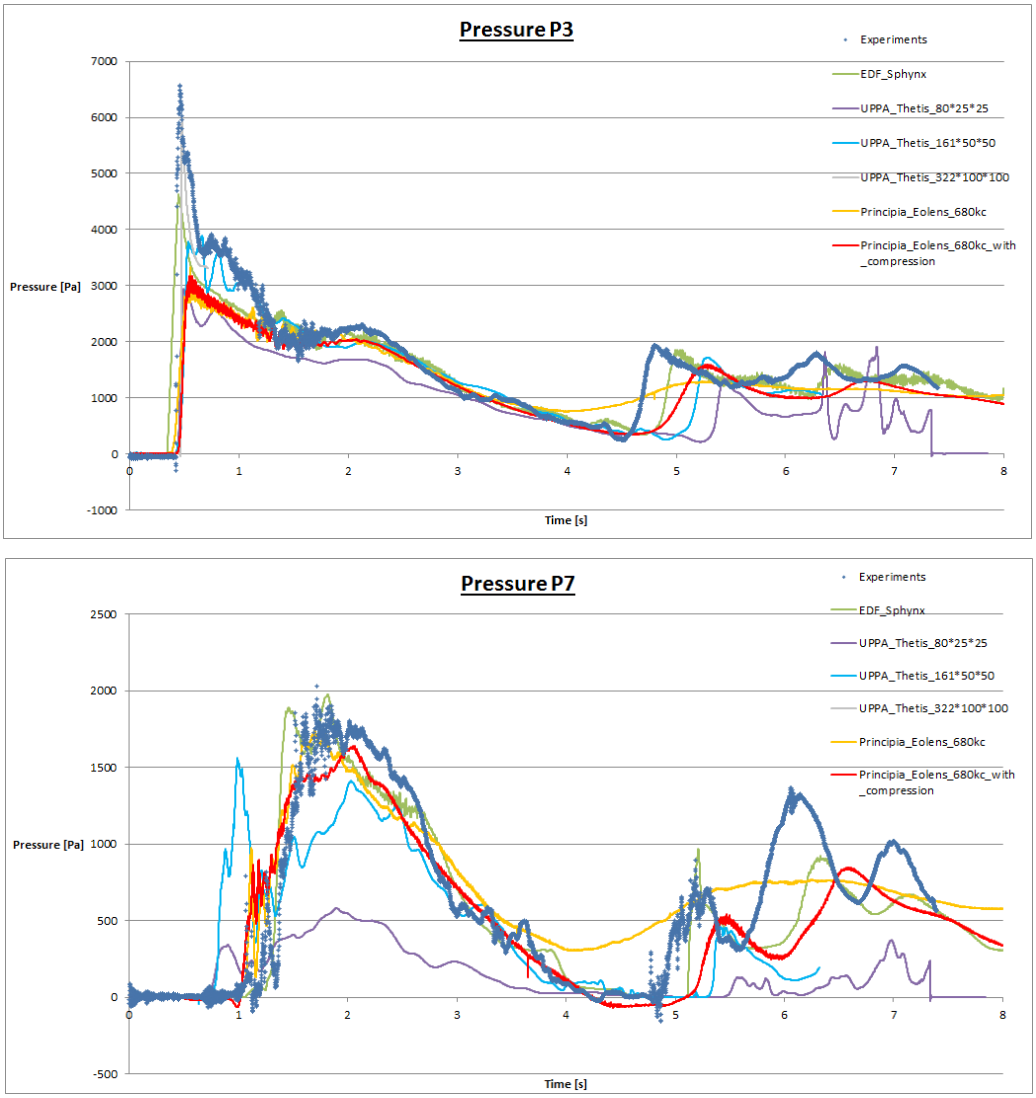

Figure A.5: Time evolution of pressure at P3 (top) and P7 (bottom).

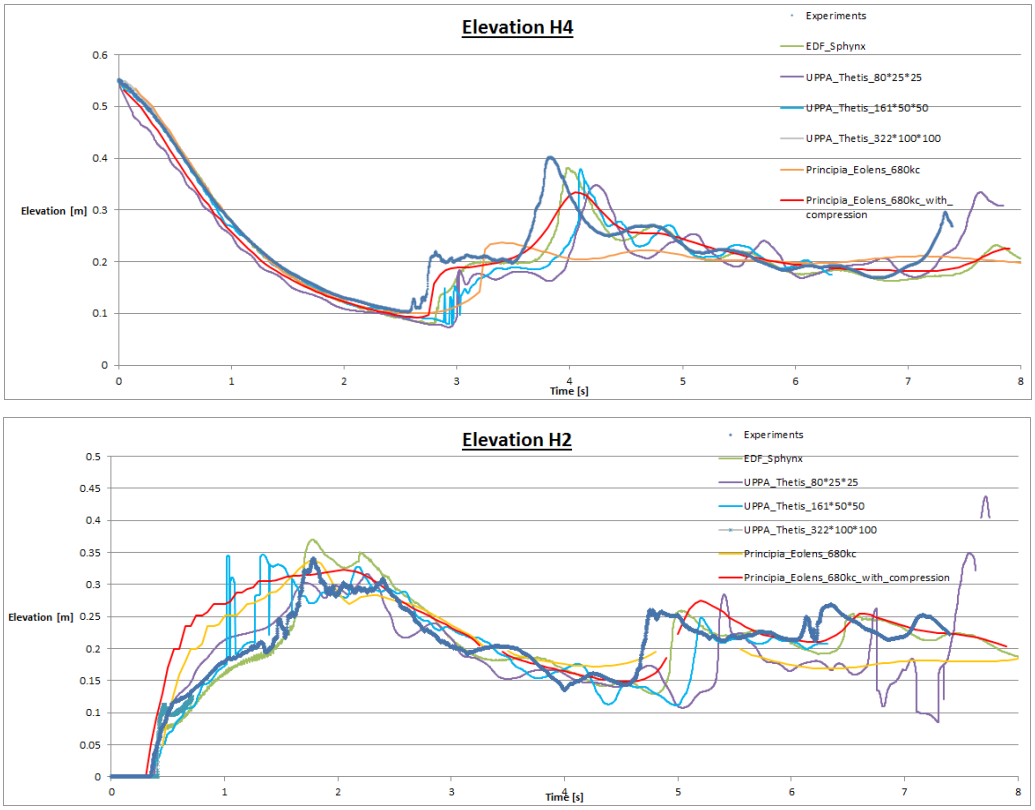

Figure A.6: Time evolution of the water elevation at gauges H4 (top) and H7 (bottom).

Appendix B

Appendix II: TANDEM validation case P02. Solitary wave reflecting on 2D vertical reef

---

During this PhD work, THETIS has been also validated to simulate the propagation, breaking process and transition of sub-critical to super-critical flows using the laboratory experiments presented in Roeber et al. (2010), Roeber & Cheung (2012). Furthermore, the ability of the code to model the reflection of the broken wave is tested. The THETIS model has been compared to other Navier-Stokes and Boussinesq models used by TANDEM collaborators. This comparison has constituted the basis of a paper accepted for publication in the European Journal of Mechanics / B Fluids (Kazolea et al. (2017)).

Wave propagation, breaking, and overtopping on a 2D reef: a comparative evaluation of numerical codes for tsunami modelling

M. Kazolea*, A. Filippini, M. Ricchiuto
Team CARDAMOM, Inria Bordeaux Sud-Ouest,
200 av. de la vieille Tour 33405 Talence-cedex, France

S. Abadie, M. Martin Medina, D. Morichon
Université de Pau et des Pays de l'Adour, Anglet, France

C. Journeau, R. Marcer, K. Pons
Principia, La Ciotat, France

S. LeRoy R. Pedreros, M. Rousseau
BRGM, Orléans, France

Abstract

In the framework of the French research project TANDEM dedicated to tsunami modelling, a series of benchmarks has been set up, addressing the various stages of a tsunami event: generation, propagation, run-up and inundation. We present here the results of five codes, involving both depth-averaged Boussinesq and fully 3D Navier-Stokes equations, aimed at being applicable to tsunami modelling. The codes are evaluated on a flow involving propagation, run-up, overtopping and reflection of the waves on two-dimensional reefs, and compared with the experimental data produced from a set of laboratory experiments carried out at the O.H. Hinsdale Wave Research Laboratory, Oregon State University (OSU, see Roeber et al., 2010 and Roeber and Chung, 2012).

1. Introduction

Fringing reefs exist in many regions around the world. The set-up of the environment such as the extended lagoons and the steep flanks produce unique surf-zone processes such as wave breaking and abruptly transitions of the flow (from dispersion dominated to flux dominated), that are challenging to numerical modeling. Roeber et al. (2010) described two series of flume experiments at Oregon State University in 2007 and 2009 that include 198 tests with 10 two-dimensional reef configurations and ranges of solitary wave height and water depth. These 198 test cases provide a database of hydraulic processes over typical reef configurations in tropical and subtropical environments. The data allows parameterization of the process to understand the effect of the reefs on surf-zone dynamics and to provide guidelines for flood hazard assessment and coastal infrastructure design. This test case has been widely used, from the numerical modeling community, the last few years (Roeber et al. 2010-2012, Tonelli et al. 2012, Kazolea et al. 2013-2014, Filippini et al. 2016) for the validation of wave models and for the understanding of the wave processes in a complex dynamic system. These experiments involve the propagation, run-up, overtopping and reflection of high amplitude solitary waves on two-dimensional reefs. Their purpose is on one hand to investigate processes related to breaking, bore formation, dispersion and passing from sub- to super-critical flows, while

providing, on the other hand, data for validation of near-shore wave models in fringing reef. These characteristics motivated the choice of this case among the set of test-cases built within the French research project PIA-ANR TANDEM on tsunami risk and modeling along the French coasts (TANDEM=Tsunamis in the Atlantic and English chaNnel: Definition of the Effects through numerical modeling, see http://www-tandem.cea.fr). An extensive description of the case studies can be found in Roeber et al. (2010, 2012).

In this work five numerical codes are tested and compared. Three codes are based on depth-averaged Boussinesq models, SLOWS (Filippini et al. 2016, Ricchiuto 2015, Ricchiuto and Fillipini 2014) developed by Inria Bordeaux Sud-Ouest, TUCWave (Kazolea et al. 2012-2014, Kazolea and Delis 2013) co-developed by the Technical University of Crete and Inria Bordeaux Sud-Ouest and FUNWAVE-TVD (Shi et al., 2012) used by BRGM ; and two codes solve Navier-Stokes equations, Thetis (Abadie et al., 1998) used by the Université de Pau et des Pays de l'Adour (UPPA) and EOLE developed by PRINCIPIA. The paper is organized as follows. The test case is presented in section 2 while the numerical models are briefly presented in section 3. Numerical results are demonstrated in section 4 and the main outcomes of the comparison are summarized in the conclusion.

2. Presentation of the benchmark

This study utilizes one of the most challenging test cases that examines the models ability in handling nonlinear dispersive waves together with wave breaking and bore propagation. The test is discussed in (Roeber et al., 2010) and (Roeber and Cheung, 2012). The Large Wave Flume in the O.H. Hinsdale Wave Research Laboratory, used for the experiment, has length of 104m a width of 3.66m and a height of 4.57m with a reef crest (see figure 1). The tank includes a hydraulic piston type wave maker for the solitary wave generation. The set-up of the test includes a fore reef slope of 1/12, a 0.2m reef crest and a water depth of 2.5m. This set-up exposes the reef crest by 6m and submerges the flat with 0.14m of water. Several identical capacitance and acoustic wave gauges placed along the flume in order to measure the free surface elevation. The location of the 14 wave gauges (WG1-14) is depicted on figure 1 also presenting a sketch of the whole domain. It must be noted that the gauges are quite spaced out. So, while providing an interesting validation setting for the large scale behaviour of the flow, this set of data may not capture fine scale physics, especially in presence of complex wave breaking patterns with multiple splash ups and important air entrainment.

As shown on figure 1, the computational domain is 83.8m long, with a rigid (reflecting) wall at the right end. The reef starts at x=25.9m with a nominal slope of 1/12. The actual slope is such that the height of 2.36m is reached after 28.25m. At this station a 0.2m height crest is mounted. The offshore slope of the crest is the same of the reef and the length of its plateau is of 1.25m. The onshore side has a slope of 1/15 giving a nominal length for the crest basis of 6.65m. Using the actual offshore slope a crest basin of 6.64407m is obtained. For the computation, the use of the nominal slope value is prescribed. This gives an offshore length of the crest slope (starting at 28.25m) of 2.4m. For boundary conditions, reflective wall at both ends of the domain (x=0m and x=83.7m) are used. The 0.75m input solitary wave gives a dimensionless wave height of A/h=0.3 since the initial depth at still water is 2.5m. To

simplify the boundary conditions, the solitary is placed initially at x=17.6m which is in reality where the experimental data places the peak at the dimensionless time ($t\sqrt{g/d} = 47.11$). The numerical wave gauges are placed at the same position as the experimental ones. We examine here the free surface elevation recorded in WG2-WG14. The prescribed value of the mesh size used in the PhD of V. Roeber (2010) is 0.05 unless otherwise specified. In the same reference a Courant number of 0.4 is prescribed. The gravity acceleration used is 9.80665m/s^2 and for the friction model a value of the Manning coefficient of 0.014m.s$^{-1/3}$ is prescribed.

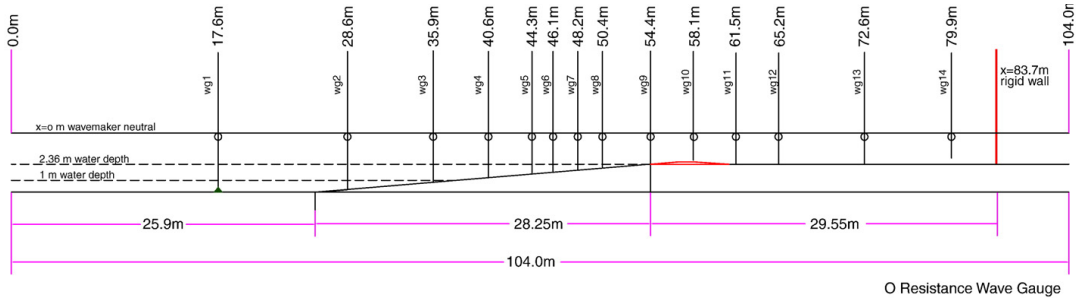

Figure 1 – Schematic of 104m-flume experiment over a fringing reef.

3. Numerical models

In this section we outline the main features of the five numerical models used in this comparison. Additional information on each of these codes can be found in the given references.

3.1 Boussinesq-type code : TUCWave (Inria)

TUCWave code is a high-order well-balanced unstructured finite volume (FV) scheme on triangular meshes for modelling weakly nonlinear and weakly dispersive water waves over slowly varying bathymetries (Kazolea et al. 2012 and Kazolea et al. 2014). It consists of two parts, the 1D solver and the 2D solver. The results here are obtained using the 1D part (Kazolea and Delis, 2013), in which the weakly non-linear weakly dispersive Boussinesq equations of Nwogu (1993) are solved. A formally fourth-order well-balanced hybrid finite volume/difference (FV/FD) numerical scheme for approximating the conservative form the system is used. The FV scheme is of the Godunov type and utilizes Roe's approximate Riemann solver for the advective fluxes along with well-balanced topography source term upwinding, while FD discretizations are applied to the dispersive terms in the systems. All simulations performed with TUCWave were run using the standard fourth order Adams-Bashfoth/Adams-Mouton predictor corrector time integration scheme. A wave breaking mechanism of a hybrid type is also incorporated to the model. Certain criteria along with their proper implementation are established to characterize breaking waves (Kazolea et al. 2014). More precisely, we use the combination of two phase-resolving criteria for the triggering wave breaking modeling: 1. The surface variation criterion: $||\eta_t|| \geq \gamma\sqrt{gh}$ with γ depending on the physical configuration and 2. The local slope angle criterion: $||\nabla\eta||_2 \geq tan\,(\varphi_c)$, where φ_c is the critical front face angle at the initiation of the breaking. η denotes the free surface elevation and h the total water depth. Once breaking waves are recognized, we switch locally in the computational domain from the BT to Nonlinear Sallow Water equations by suppressing the dispersive terms in the vicinity of the wave fronts.

3.2 Green-Naghdi-type code: SLOWS (Inria)

The results of the code SLOWS (Filippini et al. 2016, Ricchiuto 2015, Ricchiuto and Filippini 2014) are obtained by solving the Green-Naghdi (G-N) equations written in the form

$$\begin{aligned} &\partial_t \eta + \partial_x q = 0 \\ &\partial_t q + \partial_x (uq) + gh\partial_x \eta = \Phi \\ &\Phi - \alpha \mathcal{T}(\Phi) = \mathcal{R}(\eta, u, h) \end{aligned} \tag{1}$$

where $q = h\ u$ is the integrated horizontal discharge, h denotes the depth and η is the free surface level. The source term Φ is obtained from the inversion of the elliptic operator in the last line of (1), and account for weakly dispersive-fully nonlinear effects. The model is solved by the technique proposed in Filippini et al. (2016), in which a continuous Galerkin finite element method is used for the elliptic operator, and an upwind stabilized, shock capturing scheme is used for the first two equations. A hybrid approach similar to the one implemented in TUCWave is used to model wave breaking. In this case, this boils down to locally reverting to the nonlinear shallow water equations (first two in the above system) to recover energy dissipation in breaking regions. To this scope we neglect the non-hydrostatic contribution in the hyperbolic phase imposing a tighter coupling of the two phases, with the wave breaking indicator (Kazolea et al. 2014), described also in section 3.1, embedded in the elliptic phase to smoothly turn off the dispersive effects. Time integration has been performed with the standard fourth order Adams-Bashforth/Adams Mouton predictor corrector scheme.

3.3 Thetis (UPPA)

The THETIS code solves the Navier–Stokes equations (NS), with assumed continuity of the velocity through the water-air interface and neglecting surface tension effects. The resulting equations read:

$$\begin{aligned} &\nabla \cdot u = 0 \\ &\rho \left(\frac{\partial u}{\partial t} + (u \cdot \nabla) u \right) = \rho g - \nabla p + \nabla \cdot \left[\mu (\nabla u + \nabla^t u) \right] \\ &\frac{\partial \chi}{\partial t} + u \cdot \nabla \chi = 0 \end{aligned} \tag{2}$$

In which $\chi(x, y, t)$ is a phase characteristic function equal to 1 in water and 0 in air, and ρ and μ are the density and the viscosity of the fluid, respectively. They are spatially varying variables calculated using a linear interpolation based on the average value of in mixed cells. This average value is called the volume fraction F. Surface tension was not taken into account. Nevertheless the Brackbill volume formulation for surface tension (Brackbill et al. 1992) is available in THETIS, but it was not activated because the focus was not on fine scale interface deformation and dynamic but rather on wave propagation features which are not directly dependent on surface tension. The real air and water densities and viscosities are used. The equations are discretized on a fixed staggered Cartesian grid using a finite volume formulation (Patankar 1980). The coupling between velocity and pressure is solved using the augmented Lagrangian method of Fortin and Glowinski (1982). This is a minimization method under the constraint of the continuity equation, where the pressure, which is decoupled from the velocity, appears as a Lagrange multiplier. The interface displacement is solved using a Volume of Fluid (VOF) technique, which calculates the evolution of the volume fraction, occupied by one of the fluids (i.e. water) in a cell. Different VOF methods are implemented in the model THETIS: VOF-TVD and SVOF-PLIC. Simulations have been carried out comparing both methods for this benchmark and the closest results to the experimental data were found with the TVD scheme. The latter is only presented hereafter.

VOF-TVD consists in solving equation (2) directly using a suitable numerical scheme. Using this method, and a first order discretization in time, the convective term of equation (2) is written in the conservative form. A TVD scheme typically has two main properties: in the parts of the domain where the solutions are regular, it is equivalent to a high-order scheme that reduces diffusion, and in the parts where there are strong discontinuities it is a first order scheme that prevents oscillations.
Turbulence is modeled using Large Eddy Simulation. Therefore, the viscosity which appears in equations (2) is in fact the sum of the molecular fluid viscosity and a subgrid scale viscosity, which comes from the LES filtering operation. In this paper, we used the mixed scale subgrid model detailed in Lubin et al. (2006). In this model, the subgrid viscosity is calculated as function of the resolved deformation rate tensor as in Smagorinsky's model and the fluctuating kinetic energy of the subgrid scale evaluated from the resolved field. The advantages of this subgrid model are: a subgrid viscosity depending on large scale but also on small scale flow (i.e., not like Smagorinski's model) and a model which naturally vanishes towards the wall (i.e., no need for specific treatment close to walls). The tests performed on the benchmark presented in this paper show that the turbulence modeling significantly improves the results accuracy in this particular case. More precisely the viscosity in the Navier-Stokes equations is the sum of the molecular viscosity and an additional viscosity calculated by the Large Eddy Simulation (LES) model reported by Sagaut et al. (1996). This physical additional viscosity was found to help to stabilize computations by smoothing very fine interface deformations which may appear during the simulation and which are very difficult to solve properly. The code in this work uses an irregular mesh of 323520 elements with a minimal size of 0.025m

The model is developed at I2M University of Bordeaux. Nevertheless the UPPA project leader contributed to the code at the beginning of its elaboration (by programming the VOF code for instance) and the UPPA team also programs their own additional routines when required.This model was used and validated in several works involving water waves (e.g., Abadie et al., 1998, Lubin et al., 2006, Abadie et al., 2010, Mory et al., 2011, Desombre et al., 2013).

3.4 EOLE (Principia)

The EOLE code developed by Principia since 1990 is a multi-phase URANS model solving the equations on structured curvilinear multi-blocks meshes (possibly moving and deforming). It is based on a pseudo-compressibility technique using a dual time stepping and a second order finite volume scheme for spatial discretization (Guignard et al., 2001). The motion of the interface between the different phases is simulated from an implicit VOF model avoiding any CFL constraint and thus allowing globally large time steps. The transport of the VOF function (actually the displacement of the interface) may be ensured by a classical Eulerian equation or by an improved Eulerian-Lagrangian method developed by Principia, especially for complex wave breaking problem (Guignard et al., 2001; Biausser et al., 2004, R. Marcer et al., 2016). The surface tension is not taken into account because inertia is more important than surface tension (larger Weber number) and real air and water densities and viscosities are used in the simulations (two phase-flow simulations). The code is fully parallelized and uses MPI/OMP libraries and in this work it uses a mesh size of 333 126 cells with mesh grid size Δx=0.05m and Δy=0.04m.

We must mention that concerning all the dispersive models require high-order derivatives of the function that describes the bathymetry. If bottom topography with discontinuous derivatives is included, and the mesh is refined (Δx goes to 0), then a smoothness of the topography is needed since the second derivative of the bathymetry is not valid. But for our case and since we have a finite number of nodes the numerical diffusion introduced by the scheme helps to overcome the above problem and the results obtained are physically correct.

3.5 FUNWAVE-TVD 2D (BRGM)

FUNWAVE-TVD is the most recent implementation of the Boussinesq model FUNWAVE (Wei et al., 1995), initially developed and validated for coastal wave dynamics problems, but however used to perform many successful tsunami case studies. The FUNWAVE-TVD code, that solves the Boussinesq equations of Wei et al. (1995), can work both in Cartesian (Shi et al., 2012) or spherical coordinates with Coriolis effects (Kirby et al., 2012). It uses a Total Variation Diminishing (TVD) shock-capturing algorithm with a hybrid finite-volume and finite-difference scheme to more accurately simulate wave breaking and inundation by turning off dispersive terms (hence solving NLSW during breaking) once wave breaking is detected (detection based on the Froude number of the flow). The code is fully parallelized using the Message Passing Interface (MPI) protocol, using efficient algorithms allowing a substantial acceleration of the computations with the number of cores. For operational uses, FUNWAVE-TVD has received many convenient implementations, such as the use of nested grids to refine the simulations in the interest areas, or the use of Manning coefficients to characterize bottom friction.

In the frame of the U.S. National Tsunami Hazard Mitigation Program (NTHMP), FUNWAVE-TVD has been validated for both tsunami propagation and coastal impact, through an important set of analytical, laboratory and field benchmarks (Tehranirad et al., 2011). Other recent applications have allowed the validation of the model on real cases, such as the Tohoku-Oki tsunami (Grilli et al., 2013).

For completeness, Table 1 presents a summary of the differences and similarities of the codes used in this work.

Name	Model	Numerical scheme	Breaking closure	Parallel
TUCWave	Weakly nonlinear /weakly dispersive	FV/FD	Hybrid	No
SLOWS	Fully nonlinear/weakly dispersive	FV/FE	Hybrid	No
FUNWAVE TVD	Fully nonlinear/weakly dispersive	FV/FD	Hybrid	Yes
Thetis	Navier-Stokes	FV	No	No
EOLE	Navier-Stokes	FV/VOF	No	Yes

Table 1 – Summary of the CODES used in this work

4. Large scale flow: comparison of the different models

This section discusses the large scale features of the flow, as predicted by the different models, comparing with the experimental data. Note that for the Navier-Stokes codes (Thetis and EOLE), this entails a post-processing of the data which is quite delicate, and which will be discussed in some more detail in the next section.

We start by comparing the water level distributions along the flume at different dimensionless times $t^* = t\sqrt{g/d}$. For sake of clarity, we have selected fewer snapshots than those discussed in (Roeber, 2010) and (Roeber and Cheung, 2012), representative of the propagation, breaking, and overtopping phases. The numerical results are compared to the experimental data on figures 2(a) to 2(i). For easier reading, the results have been split in two sets one involving all the Boussinesq models, and the other the two Navier-Stokes codes.

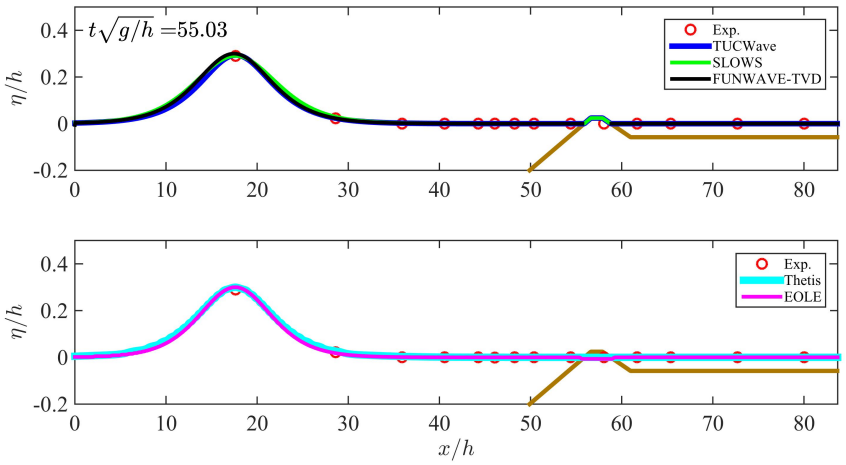

Figure 2(a) – Large scale flow behaviour. Water level at t^* =55.03

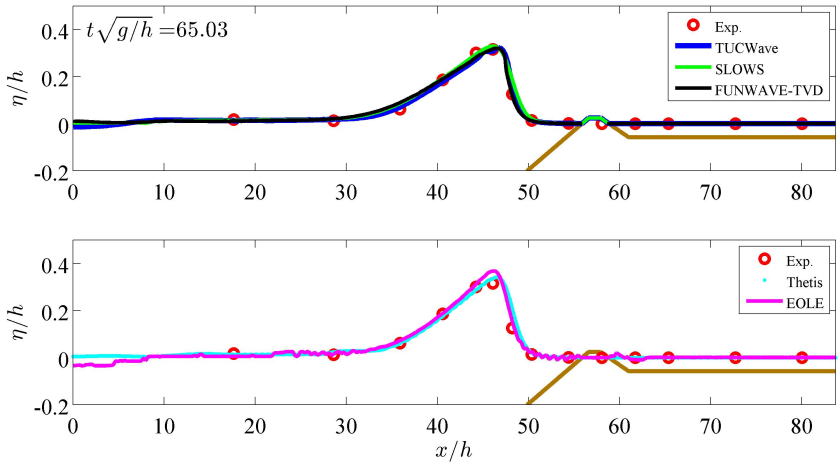

Figure 2(b) – Large scale flow behaviour. Water level at t^* =65.03

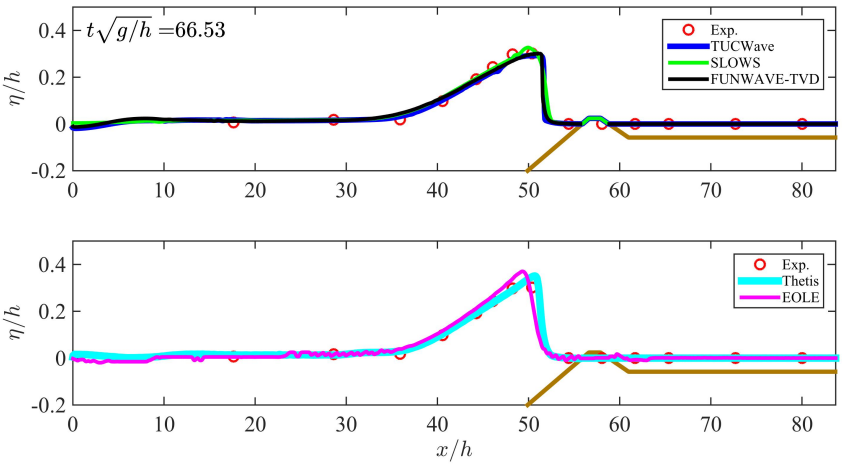

Figure 2(c) – Large scale flow behaviour. Water level at t^* =66.53

Figures 2(a), 2(b), and 2(c) show the propagation and shoaling of the solitary wave. The first figure shows the wave roughly in correspondence of the toe of the slope. At this time the wave is still quite symmetric. The loss of symmetry due to shoaling is clearly visible in figure 2(b), with incipient breaking conditions obtained in FUNWAVE-TVD already at t^*=66.53 in figure 2(c). For this set of snapshots all the models yield very close results. Minor differences can be seen in the sharper and slightly lower profile of FUNWAVE-TVD, especially in the last picture. This is due to the breaking treatment which has been activated, and which turns the wave into a moving bore. In figure 2(c) (and partially in figure 2(b)) we can also see that EOLE provides a peakier wave with regard to all the other models. This may be related to the post-processing of the Navier-Stokes results, as we will discuss later. All the codes agree satisfactorily with the data.

In the next set of figure (2(d) to 2(f)) the wave has broken and overtops the reef. It is known from the experiments that the wave develops into a plunging breaker. All the Boussinesq codes replaced this effect by a moving breaking front treated with the shallow water equations. Instead, the front observed in the figures in the second set is a result of the post-processing of the Navier-Stokes codes. Despite of this, the models provide essentially similar results, especially at t^*=69.13 (figure 2(d)) and t^*=70.68 (figure 2(e)). Visible differences are

present instead in the last figure referring to time t^*=72.48 (figure 2(f)) at which the splashing of the breaker has occurred. The difference observed in the figure is a result of the different treatment of wave breaking. The depth-averaged models clearly provide sharp moving bores, with minor visible differences in the three results. This behaviour is due to the common wave breaking mechanism, which deactivates the dispersion at the wave front, when breaking is detected, and allows to conserve the water's total mass and momentum, while mimicking total energy dissipation via the dissipation in the shallow water shock. The position, and magnitude of the fronts is close to the experiments, validating the breaking detection and dissipation closure. The Navier-Stokes codes, which can resolve the finer scales of the flow, also identify moving fronts, which are more oscillatory when compared to the Boussinesq codes. These instabilities may be possibly artificially accentuated with the post-processing technique implemented to treat the complex flow pattern obtained in the splash-up phase, which we will discuss in the next section. What can be seen from figure 2(e) in this set of figures is that the post-processed data from EOLE accurately represent the plunging position of the wave and the resulting splash-up and bore formation. For the Thetis model, the amplitude of the breakers is well modelled, but the splash-up seems to occur earlier than with the other models. Despite of these differences, the overall agreement with the data is quite satisfactory for all the models.

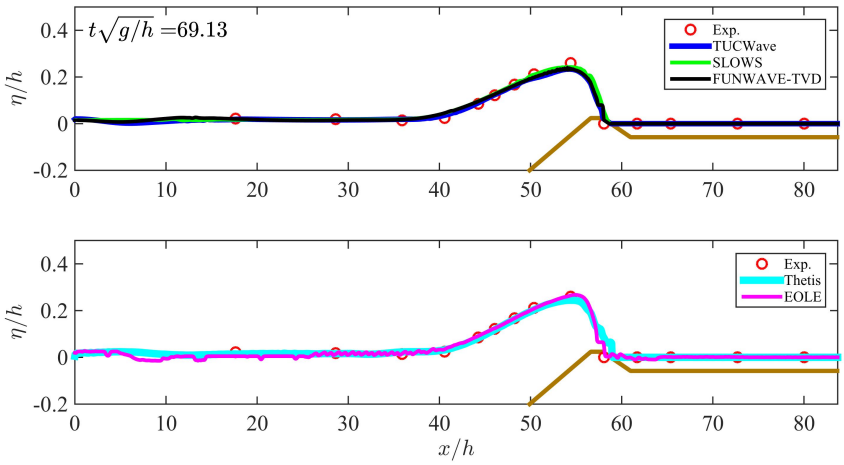

Figure 2(d) – Large scale flow behaviour. Water level at t^* =69.13

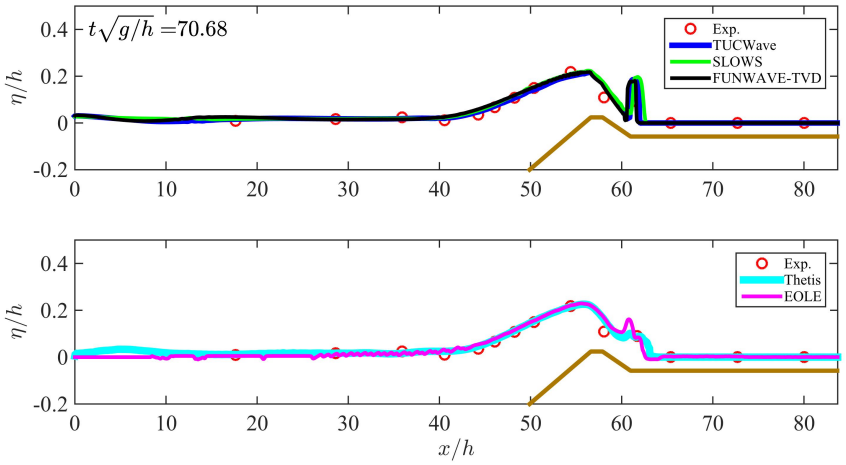

Figure 2(e) – Large scale flow behaviour. Water level at t^* =70.68

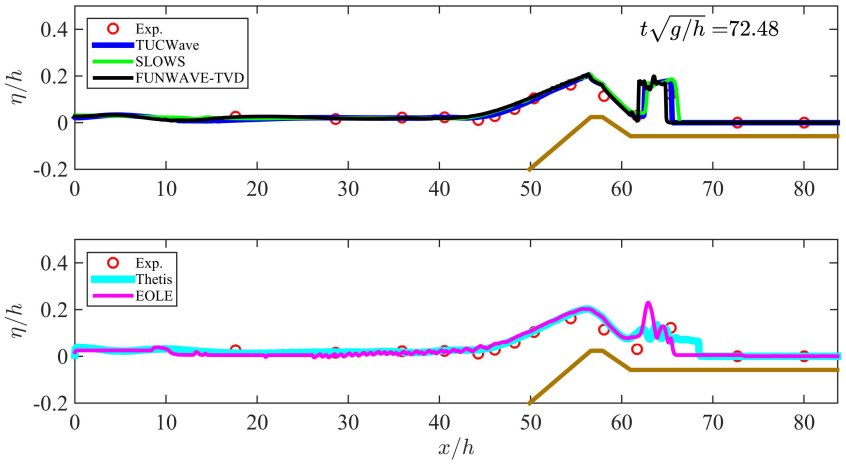

Figure 2(f) – Large scale flow behaviour. Water level at t^* =72.48

The last set of pictures shows the evolution of the supercritical flow and of the bores developed onto the stagnant water. Laboratory observations indicate generation of a hydraulic jump with overturning of the free surface off the back reef and a turbulent bore propagating downstream (Roeber et al. 2012). The deforming bore propagates downstream showing a reduction in amplitude and is reflected by the wall at $t^* \sim 99$. The reflected bore travels downstream and overtops the reef. At this point and as the water rushes down the fore reef, the flow transitions from flux to dispersion-dominated, and a hydraulic jump generated after the second overtopping transforms into an offshore propagating undular bore, ultimately giving a train of dispersive waves over the increasing water depth upstream. The development of this process, which we can see already starting in figure 2(f), can be observed in the results of figures 2(g) to 2(i). In the first two figures, we can see that the three Boussinesq codes provide again sharp moving bores, showing that the breaking model is still on. We can observe a visible phase lag with regard to experimental data for FUNWAVE, and a phase advance for SLOWS, and a more reduced one for TUCWave. Similarly to the previous

pictures, the turbulent propagating bore is described in a more oscillatory way. This is certainly due to the post processing of the 2D flow. Thetis shows a considerable phase advance with regard to all the other models, while EOLE provide a front position in better agreement with the data. Amplitudes are however well described by the two models. Despite of its previous phase advance, Thetis provides an accurate description of the front position and amplitude after the reflection. EOLE gives a slighlty faster reflective wave, very comparable to TUCWave and SLOWS. Finally, after the second overtopping takes places, we can clearly in figure 2(i) see the undulating bore forming in the results of SLOWS and TUCWave, and in those of EOLE. Both FUNWAVE and Thetis fail in providing a description of this feature, which may be related to the breaking detection technique used in FUNWAVE, and in a lack of resolution in the computations performed with Thetis.

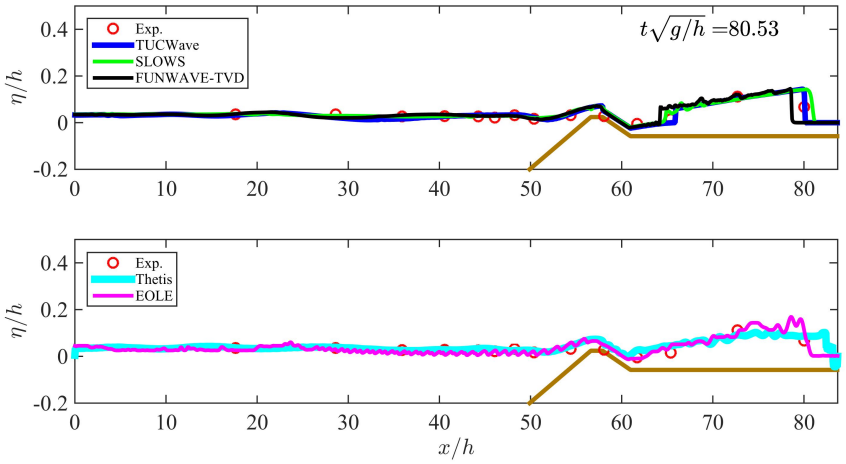

Figure 2(g) – Large scale flow behaviour. Water level at t^* =80.53

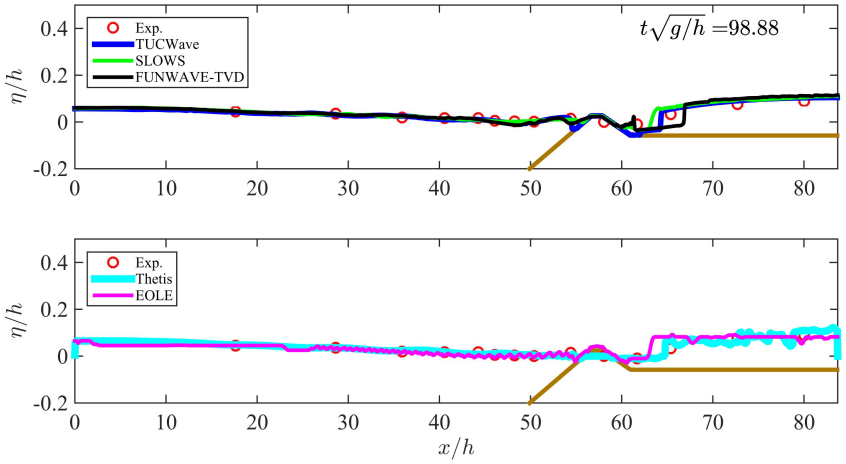

Figure 2(h) – Large scale flow behaviour. Water level at t^* =98.88

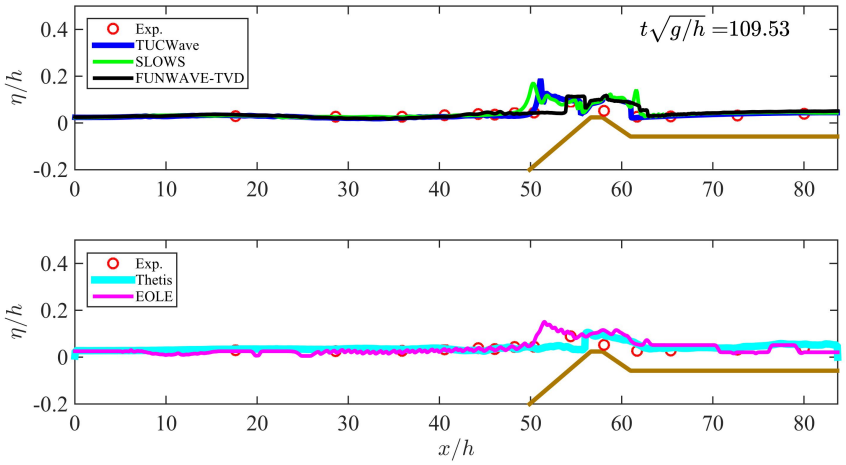

Figure 2(i) – Large scale flow behaviour. Water level at t^* =109.53

We consider now the numerical and experimental time series of the water height in the wave gauges. We will analyse 5 of the 14 gauges. The computed and experimental series corresponding to these probes are reported in figures 3(a) to 3(e). These five gauges allow to somehow single out some of the features of the computed flows, namely:

- WG2 is representative of the initial propagation and final dispersive phases;
- WG5 is representative of the shoaling and final dispersion dominated phase;
- WG9 is representative of the breaking phase and of the formation of the hydraulic jump on the fore reef side;
- WG10 is representative of the overtopping phases;
- WG12 is representative of the propagation of the initial and reflected bores.

Overall, all the models are able to catch-up the flow behaviour, but a closer look reveals some interesting differences. In the propagation phase, we can see from the WG2 data that, while all Boussinesq-type models provide an accurate approximation of the solitary wave movement toward the reef, both the Navier-Stokes solvers overestimate the height of the wave. Moreover, with the resolutions used in the computations both Navier-Stokes simulations seem to miss the higher frequency modes present in the Boussinesq results. These, however, while giving a reasonable reproduction of the amplitude of these modes, all suffer from phase errors, which may be due to the limitations in dispersion accuracy of the models and on the different wave breaking treatments used. The time series in WG5 lead to similar conclusions. In particular, both Navier-Stokes models overestimate the shoaling height, which is well reproduced by all Boussinesq simulations. More importantly, the Navier-Stokes results fail to reproduce the undulating bore originated by the reflected wave overtopping the reef. The EOLE results only capture the first peak, and miss the remaining secondary oscillations. Thetis fails completely to catch this feature. Among the Boussinesq models, one can see that TUCWave overestimates some of the oscillations, as expected with the type of model used in this code. In the breaking phase we can see from WG9 (figure 3(c)) data that all models are able to catch the vertical front of the wave. The BT models underestimate the wave height with FUNWAVE-TVD giving a slightly lower profile compared to the other two BT models due to the different breaking treatment used. Again

both the Navier-Stokes solvers overestimate the height of the wave. Further in time and for the BT models we can see the formation of the undular bore with a visible phase lag with regard to experimental data for FUNWAVE-TVD and a phase advance for SLOWS and TUCWave. EOLE model reproduces the bore satisfactorily but Thetis fails to reproduce the formation of the undular bore maybe due to overestimation of wave energy dissipation over the breakwater.

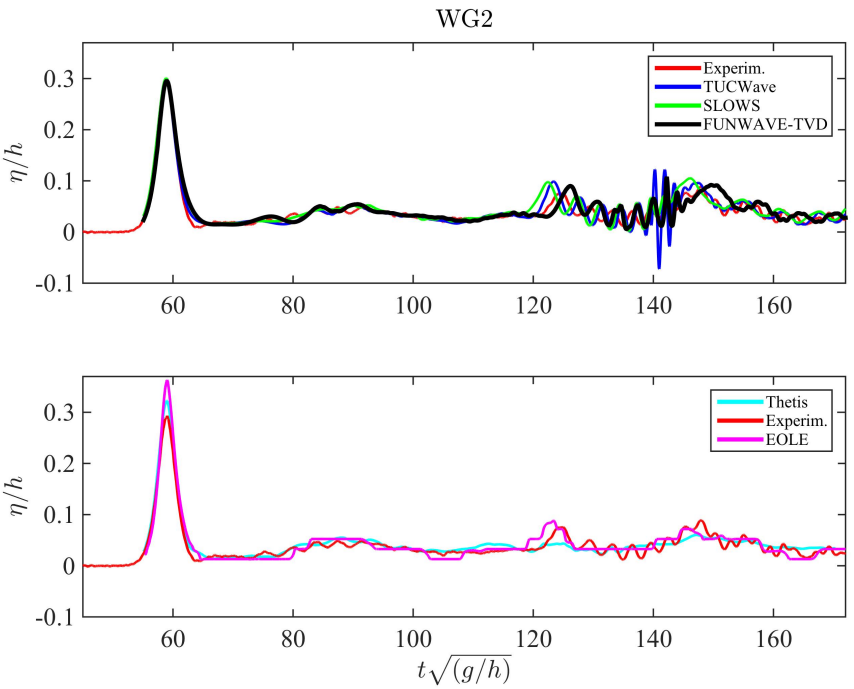

Figure 3(a) – Large scale flow behaviour. Time series in WG2 (propagation)

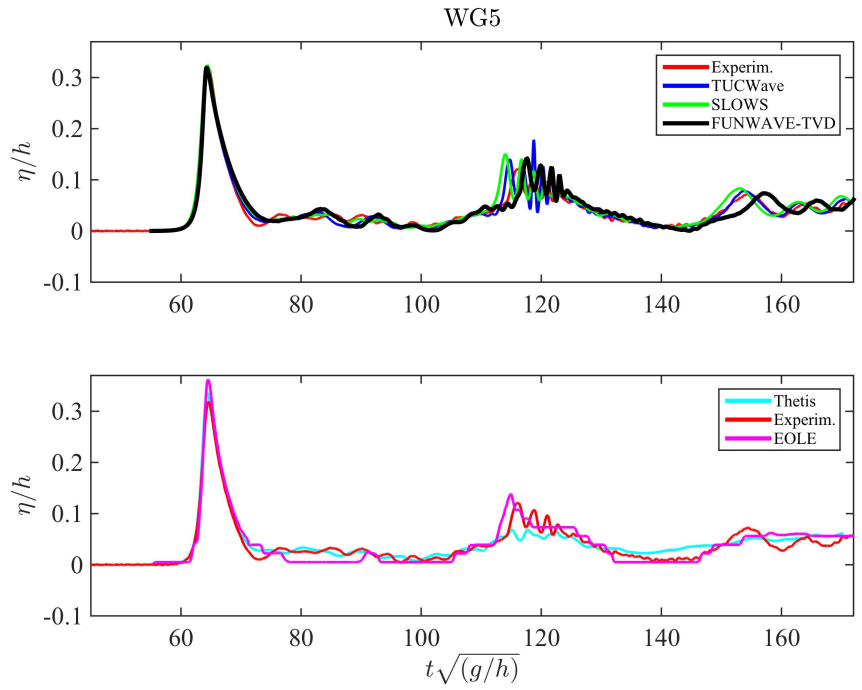

Figure 3(b) – Large scale flow behaviour. Time series in WG5 (shoaling)

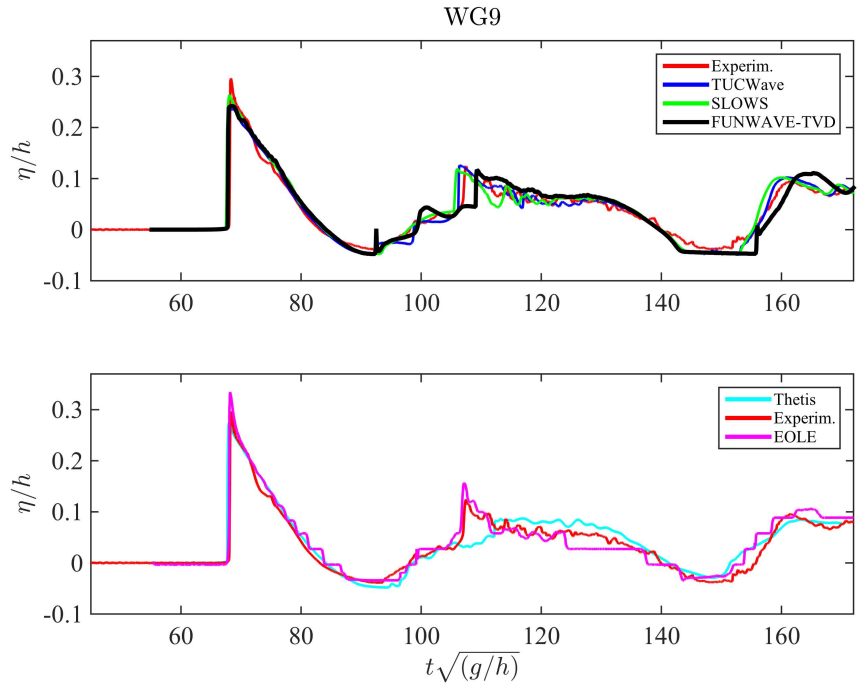

Figure 3(c) – Large scale flow behaviour. Time series in WG9 (breaking)

The time series relative to WG10 are reported on figures 3(d). WG10 is placed on top of the reef and the time series show the overtopping of the first wave, whose amplitude is overestimated by all models, and then the drought of the area, which cannot be reproduced by FUNWAVE-TVD, and EOLE for which the remaining thin water layer is probably due to a lack of grid refinement in this zone. The second overtopping that occurs from the reflected (to the right wall) bore is also overestimated for all codes.

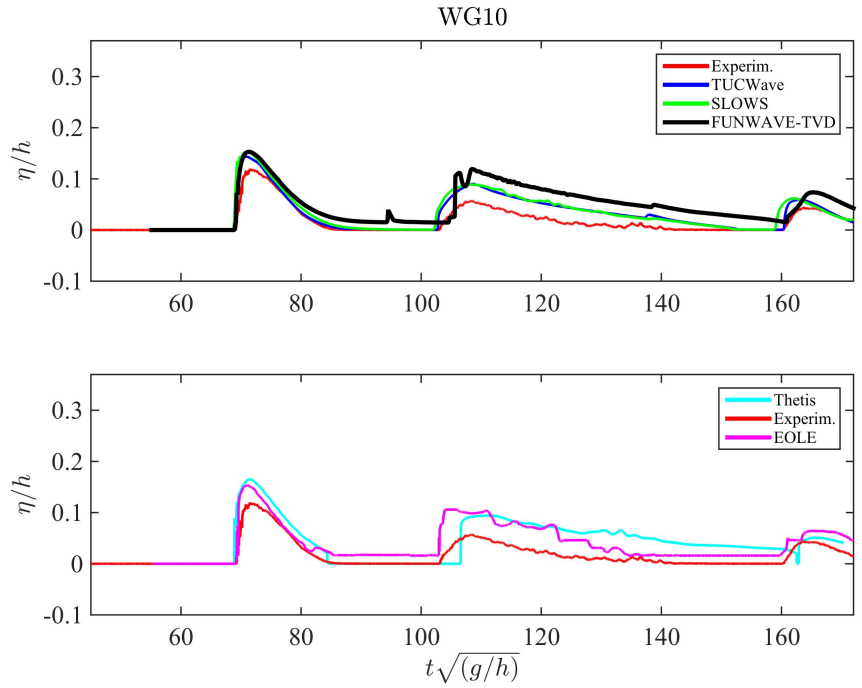

Figure 3(d) – Large scale flow behaviour. Time series in WG10 (overtopping)

Finally, figure 3(e) reports the time series relative to WG12. For the BT models we can see that all models overestimate the initial wave, but the reflected bores are well-reproduced with regard to experimental data, expect a small phase lag on the second wave for the FUNWAVE-TVD model. The numerical results produced by SLOWS are more oscillatory after each propagating bore, which are simulated as moving shocks, due to the nature of the wave breaking mechanism used. In the second set of figures, we can see that even though the Navier-Stokes solvers are able to simulate the amplitude of the first wave better with regard to BT models, their numerical results deviate from the experimental data after the second reflected wave.

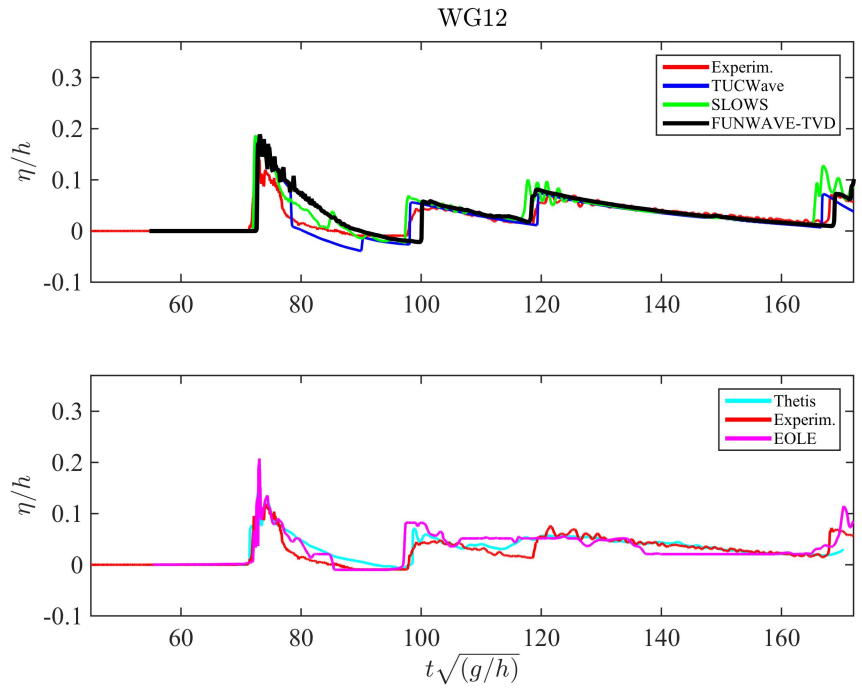

Figure 3(e) – Large scale flow behaviour. Time series in WG12 (bore propagation)

As a next step, we compute the Root Mean Square Deviation (RMSD) in order to measure the differences between the numerical results and the experimental data for each wave gauge. Of course this study shows only a qualitative appreciation of the models since we do not have any error information for the experimental data. Table 1 and figure 4 present the RMSD for each wave gauge and for each model. Overall, all the models give the same order of RMSD, especially for the wave gauges placed before the reef, indicating that all models correctly handle propagation and shoaling of the solitary wave. A closer look at the gauges before the reef reveals that the BT models present a bigger RMSD in the first three gauges with regard to Navier-Stokes solvers for which Thetis code presents the lower RMSD values. The RMSD of the next four wave gauges (WG5 –WG8) for the Navier-Stokes computations grows and is bigger with regard to BT models. This can be attributed to the fact that both Navier-Stokes computations miss the higher frequency modes, which are present in the Boussinesq results. In WG9, Thetis presents the bigger RMSD since it fails to reproduce accurately the undular bore originated by the reflected wave overtopping the reef. The RMSD of the several models vary the most for WG10. This wave gauge indicates the correct wet/dry treatment of the models. FUNWAVE-TVD has the maximum value and TUCWave has the minimum. The next three gauges (WG11-WG13) are representative of the propagation of the initial and reflected bores and we observe more or less the same behavior. Boussinesq models provide almost the same RMSD value, while the Navier-Stokes solvers have a visible difference between them, with Thetis giving the minimum RMSD. This may be related to the post-processing of the Navier-Stokes results, as we will discuss in the next section. The RMSD value for the last wave gauge WG14 indicates in part the correct wall boundary treatment and in part the correct dissipation rate. In this case, Thetis presents the maximum value.

To conclude, we present the CPU time needed for each model in Table 3. The CPU time has been measured for a simulation period of 100s. Of course we must keep in mind that both FUNWAVE-TVD and EOLE are using the parallelized version of the codes.

	EOLE	FUNWAVE TVD	SLOWS	THETIS	TUCWave
WG2	0.0124	0.0131	0.0150	0.0108	0.0157
WG3	0.0114	0.0130	0.0144	0.0122	0.0145
WG4	0.0130	0.0126	0.0131	0.0121	0.0132
WG5	0.0144	0.0139	0.0127	0.0140	0.0128
WG6	0.0145	0.0138	0.0128	0.0143	0.0125
WG7	0.0162	0.0132	0.0133	0.0158	0.0120
WG8	0.0177	0.0149	0.0145	0.0180	0.0147
WG9	0.0191	0.0185	0.0190	0.0235	0.0179
WG10	0.0291	0.0374	0.0229	0.0338	0.0188
WG11	0.0253	0.0210	0.0223	0.0186	0.0227
WG12	0.0208	0.0190	0.0198	0.0143	0.0163
WG13	0.0204	0.0159	0.0167	0.0144	0.0114
WG14	0.0226	0.0206	0.0148	0.0269	0.0146

Table 2 – RMSD values for each model

	EOLE	FUNWAVE TVD	SLOWS	THETIS	TUCWave
CPU time	**1d and 6h**	250sec	71.37sec	1d and 4h	41.33sec
Machine	Linux Redhat 5, 2 processors (Intel® Xeon ® X7460) 6 cores (2.66 GHz), hyper threading (so 24 threads)	1 single processor (AMD Abu Dhabi 2.6GHz)	IMac 3.5Gz, Intel® Core i7	2x8 processors, Nodes - C6100 (x264) 2 processors 6 cores (12 cores/node) 3,06 GHz	IMac 3.5Gz, Intel® Core i7

Table 3– CPU time values for each model

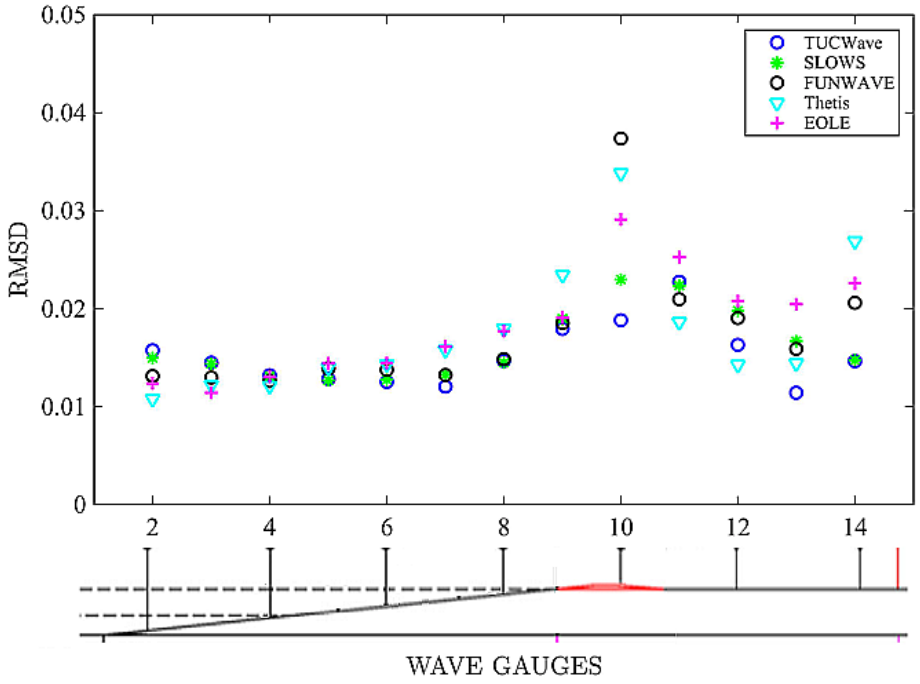

Figure 4 –RMSD in the wave gauges for each model (with a rough sketch of the gauge position)

5. Finer scale features and post-processing

A comparison of the measured and computed wave profiles is first presented in figure . For Navier-Stokes VOF codes, it is necessary to introduce a specific post-treatment algorithm allowing to localize the free surface elevation at each gauge. For exemple in EOLE, for a given position of the gauge the procedure sweeps vertically the VOF field (i.e., the water volume fraction) in all the cells until it detects a partial VOF value (0<VOF<1) meaning the cell containing the interface (knowing that VOF=1 and VOF=0 mean respectively purely liquid and purely air). From the vertical coordinates of the detected cell and its own VOF value a position of the free surface is extracted. The weakness of this algorithm is that the accuracy is strongly meshing size dependence. So the issue is not an exact position of the interface but rather a mean position with an error rounded to the mesh cell size. Other problems may be encountered as well when there are possibly several partial volume fraction values along the same vertical, for instance break-up of droplets from the free surface or air bubble entrainment during splash-up phenomenon (see for example figure 5).

For THETIS, same kind of problems are encountered. Indeed the flow and the water/air interface is very complex in this benchmark due to the strong mixing generated by wave breaking (figure 6). For this reason, the processing of the water/air interface needs to be carefully analysed in Navier-Stokes equations because these models capture at least a certain part of this complexity. This is illustrated in figure 6 which presents the bore propagation over the reservoirs computed by THETIS. White contours represent different fraction of water in cells (10%, 50% and 90%). As shown in this figure, the bore is highly mixed. This has two repercussions: first, the density is equally affected by this mixing and this may play a role in the model behaviour, second the identification of the surface elevation is complicated as no

actual interface can be defined as in Boussinesq models for instance in which this elevation is one of the model parameter. The results presented in this benchmark were computed with a free surface corresponding to F=0,5 (see section 3.3). The following figure 7 shows that this is only a limited view of the available information. Note that this remark also holds for the experimental measurements.

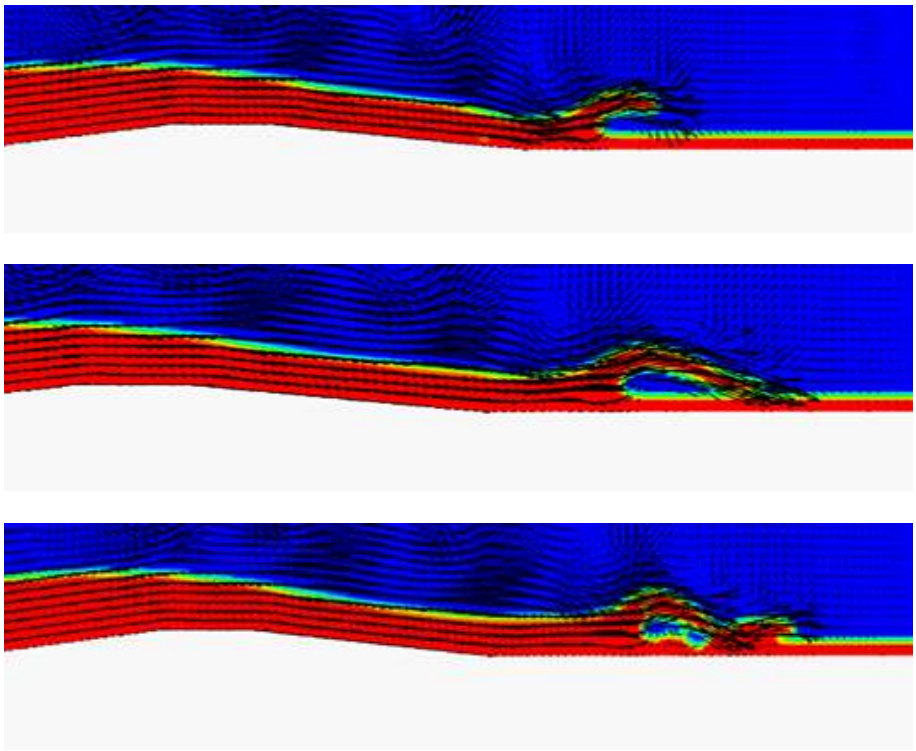

Figure 5: splash-up and air bubble entrainment processes computed by the EOLE model

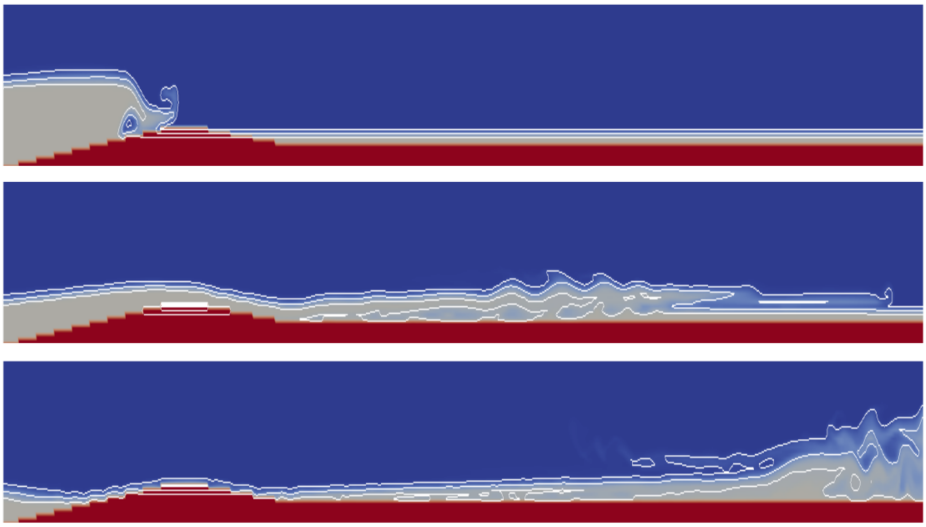

Figure 6: plunging breaking and splash-ups computed by the Thetis model

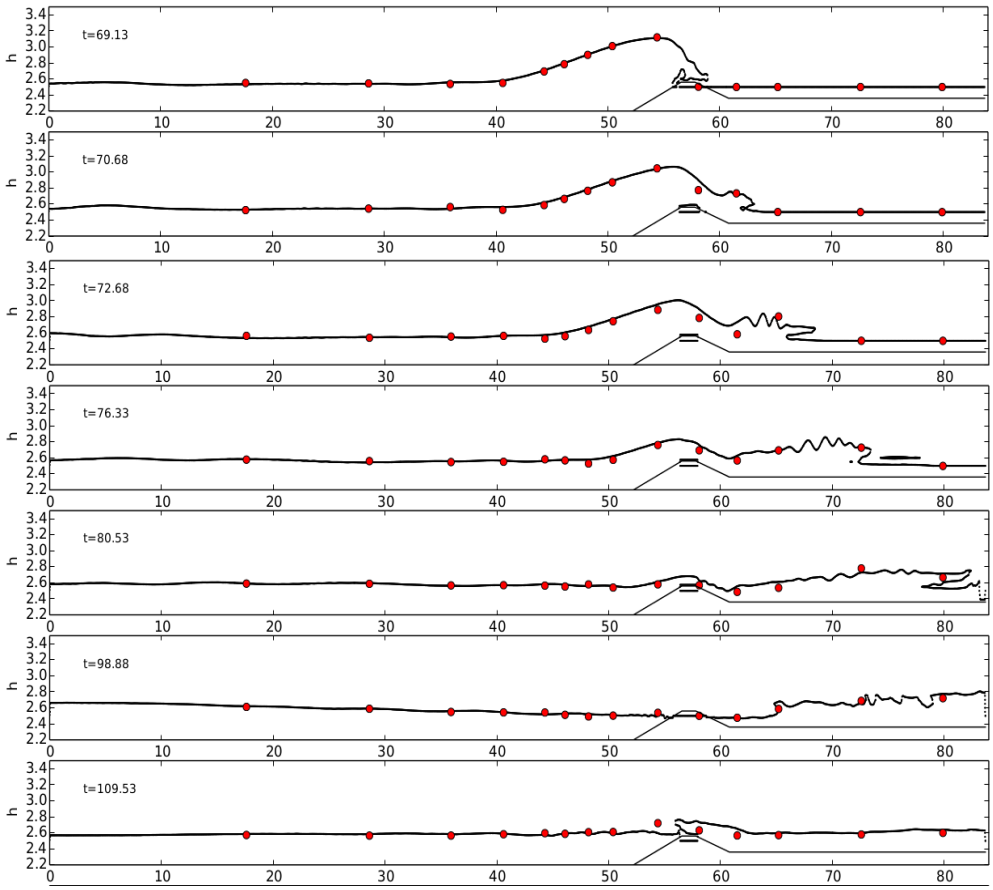

Figure 7: Snaphots of experimental free surface and water/air interface (i.e., F=0.5 computed by Thetis.

6. Summary and conclusions

- Thetis code has the best RMSD for the first three wave gauges where the propagation of the solitary wave, going on-shore, and the propagation of the undular bore, going off-shore, are depicted. Looking closely at the time series of those wave gauges we can see the perfect match of the computational and the experimental data for the solitary wave that travels on-shore while there is a deviation especially on the front of the undular bore, under-predicting the wave's amplitude. During the propagation of the bore on the lake (after the reef) we observe a mismatch of the numerical and experimental data, probably accented by some inaccuracies regarding the surface elevation post-processing treatment and a larger wave energy dissipation than measured.
- EOLE code presents a quite similar behaviour as the Thetis code, especially at the beginning of the process. But if the height of the wave is slightly more overestimated

in the first step of the propagation, a better approximation of the wave's splash-up and associated processes is then observed. Note that, as previously said, the experiment doesn't allow to qualify accurately the corresponding oscillations of the free surface which occur at the wave's splash-up. On the whole, this code provides with a satisfying description of the process, especially of the early phase, and a good prediction of the dispersion dominated undular bore, but with higher frequency oscillations missing in the results probably due to a lack of resolution.

- TUCWave code run with parameter values for CFL 0.2 and for the breaking criterion γ=0.6. The code accurately predicts the propagation of the wave across the channel. During shoaling it slightly over predicts the wave's amplitude, which is expected since the code solves the weakly non-linear weakly dispersive equations of Nwogu (1993). The numerical model accurately predict both time and place of the wave breaking and mimics the breaker as a collapsing bore. The wet/dry front is also accurately simulated since TUCWave is the only code manages to give an error less that 0.02% in wave gauge 10 (where dry reef is placed). The limitation in describing the amplitude of the undular bore deformed after the overtopping of the reflected bore can be attributed to the nature of the equations solved along with the wave breaking technique used.
- SLOWS solves the GN equations with a CFL parameter of 0.2 and γ=0.6 for the breaking criterion. The results are similar to the ones provided by the two others Boussinesq-type models. Like before the breaker is simulated as a collapsing bore that slightly underestimates the wave height but conserves the total mass. We can observe a very good much of the experimental and the numerical data for the undular bore and the dispersive waves that produced as it travels off-shore.
- FUNWAVE –TVD gives almost the same results as the two previous Boussinesq-type models. A time lag between the numerical results and the experimental data is observed during the propagation of the bore on the lake and afterwards.

In conclusion, the five codes can be classified in two main categories. Those based on the Naver-Stokes (NS) model (Thesis and EOLE) and the depth-averaged Boussinesq-type (BT) models (TUCwave, SLOWS, FUNWAVE-TVD). Surprisingly both categories provide very similar and satisfactory results on the whole (according to experiment), in particular a good agreement is observed between EOLE's, SLOW's and TUCWave's results. The computational times of the BT models are significantly less compared to the ones of the NS models. Hence, from the practical point of view, there is no a huge advantage from the NS models compared to the BT models. But we have to keep in mind that the amount of information obtained from NS models is significantly more than the one obtained from the BT models. Among the BT models the results are comparable but there are some differences concerning mainly the phase lag observed. This difference is expected and can be attributed to the fact that the BT models with the hybrid wave breaking closure are very sensitive to the trigger mechanism, which is different in each code. Additionally the trigger mechanism depends on the hydrodynamic quantities provided by the models, which are not the same due to the different nature of the models used. Further more a very crucial point is that we don't have any error measurement on the experimental results (very few experiments exists in the literature) and we can't quantify the behaviour of the codes.

This demanding test case has allowed gaining insight in the capabilities and limitations of five numerical codes aimed at modelling tsunami propagation over long distances. In this test case

multiple wave effects have been considered, as propagation, shoaling due to bottom variations, breaking, reflections and wet-dry front interactions.

Acknowledgements

This comparative study has been performed within the Work Package 1 (Benchmarking of numerical methods) of the TANDEM project (Tsunamis in the Atlantic and the English ChaNnel: Definition of the Effects through numerical Modelling) (2014-2018), with partial funding from the PIA-ANR program (Programme Investissements d'Avenir, Agence Nationale de la Recherche) from the French Government under grant 2013-RSNR-01.

References

Abadie, S., Caltagirone, J.-P., Watremez, P. (1998) Splash-up generation in a plunging breaker. *Comptes Rendus de l'Académie des Sciences - sériés IIB*, 326:556–559.

Abadie, S., Morichon, D., Grilli, S., Glockner, S. (2010) Numerical simulation of waves generated by landslides using a multiple-fluid Navier–Stokes model. *Coastal Engineering* 57: 779–794.

Biausser, B., Guignard, S., Marcer, R., Fraunié, P. (2004) 3-D two phase flows numerical simulations by SL-VOF method, *Int. J. Numer. Meth. Fluids*; 45:581-604.

Biausser, B., Marcer, R., Grilli, S., Fraunié, P. (2004) Numerical Analysis of the Internal Kinematics and Dynamics of 3-D Breaking Waves on Slopes, *International Journal of Offshore and Polar Engineering*, Vol. 14, No. 4, December 2004 (ISSN 1053-5381).

Brackbill, J. U., Kothe, D. B., & Zemach, C. (1992). A continuum method for modeling surface tension. *Journal of computational physics*, *100*(2), 335-354.

Desombre, J, Morichon, J.D., Mory, M. (2013) RANS v2–f simulation of a swash event: Detailed flow structure. *Coastal Engineering*, 71:1-12.

Filippini, A.G., Kazolea, M., Ricchiuto, M. (2016) A flexible genuinely nonlinear approach for nonlinear wave propagation, breaking and run-up. *J. Comp. Phys.*, 310:381–417.

Fortin, M., Glowinski, R. (1982) Méthodes de lagrangien augmenté: applications à la résolution numérique de problèmes aux limites. Dunod.

Grilli, S.T., Harris, J.C., Tajalli Bakhsh, T.S., Masterlark, T.L., Kyriakopoulos, C., Kirby, J.T. and Shi, F. (2013) Numerical Simulation of the 2011 Tohoku Tsunami Based on a New Transient FEM Co-seismic Source: Comparison to Far- and Near-Field Observations, Pure and Applied Geophysics, 170, 1333-1359.

Guignard, S., Marcer, R., Rey, V., Kharif, C., Fraunié, P. (2001) Solitary wave breaking on sloping beaches : 2D two phase flow numerical simulation by SL-VOF method, *Eur. J. Mech. B, Fluids* 20 (2001) 57-74.

Kazolea M., Delis A.I. (2013) A well balanced shock-capturing hybrid finite volume-finite difference numerical scheme for extended 1D Boussinesq models, *Appl.Num. Math*., 67:167-186.

Kazolea M., Delis A.I., Nikolos I.K., Synolakis C.E. (2012) An unstructured finite volume numerical scheme for extended Boussinesq-type equations. *Coastal Engineering,* 69, 42-66.

Kazolea M., Delis A.I., K., Synolakis C.E. (2014) Numerical treatment of wave breaking on unstructured finite volume approximations for extended Boussinesq-type equations. *J.Comp.Phys.,* 271:281-305.

Kirby, J.T., Shi, F., Harris, J.C., Grilli, S.T. (2013) Dispersive tsunami waves in the ocean: Model equations and sensitivity to dispersion and Coriolis effects. *Ocean Modelling*, 62:39-55.

Li, J. (1995) Piecewise Linear Interface Calculation. C.R.Acad.Sci*,* Paris, IIb, 320, 391-396.

Lubin, P., Vincent, S., Abadie, S., Caltagirone, J.-P. (2006) Three-dimensional Large Eddy Simulation of air entrainment under plunging breaking waves. *Coastal Engineering* 53, 631–655.

Marcer, R., Journeau, C., Pons, K. (2016) Tsunami modelling. Validation of EOLE CFD code on academic test cases, XIVèmes Journées Nationales Génie Côtier – Génie Civil, Toulon, 29 juin au 1er juillet 2016.

Mory, M., Abadie, S., Mauriet, S., Lubin, P. (2010) Run-up flow of a collapsing bore over a beach. *European Journal of Mechanics - B/Fluids* ,doi:10.1016/j.euromechflu.2010.11.005.

Nowgu, O. (1993) Alternative form of Boussinesq equations for nearshore wave propagation. *Journal of Waterway, Port, Coastal and Ocean Engineering.* ASCE, 119 (6), 618-638.

Patankar, S.(1980) Numerical heat transfer and fluid flow. CRC Press.

Pianet, G., Vincent, S., Leboi, J., Caltagirone, J. P., Anderhuber, M. (2010) Simulating compressible gas bubbles with a smooth volume tracking 1-fluid method. *International Journal of Multiphase Flow*, *36*(4), 273-283.

Ricchiuto, M. (2015) An explicit residual based approach for shallow water flows. *J. Comp. Phys*, 280, 306-344.

Ricchiuto, M., Filippini, A.G. (2014) Upwind residual discretizations of enhanced Boussinwsq equations for wave propagation over complex bathymetries. *J. Comp. Phys*., 271:306-341.

Roeber, V., Cheung, K.F., Kobayasi, M.H. (2010) Shock-capturing Boussinesq-type model for nearshore wave processes. *Coastal Engineering*, 57:407-423.

Roeber, V., Cheung, K.F. (2012) Boussinesq-type model for energetic breaking waves in fringing reef environments. *Coastal Engineering*, 70:1-20.

Roeber, V., (2010) Boussinesq-type model for nearshore wave processes in fringing reef environment, PhD thesis, University of Hawaii.

Sagaut, P. (1998). Introduction à la simulation des grandes échelles pour les écoulements de fluide incompressible (Vol. 30). Springer Science & Business Media.

Shi, F., Kirby, J.T., Harris, J.C., Geiman, J.D. and Grilli, S.T. (2012) A high-order adaptive time-stepping TVD solver for Boussinesq modeling of breaking waves and coastal inundation. *Ocean Modelling*, 43-44:36-51.

Tehranirad, B., Shi, F., Kirby, J.T., Harris, J. C. and Grilli, S.T. (2011) Tsunami benchmark results for fully nonlinear Boussinesq wave model FUNWAVE-TVD, Version 1.0. Technical report, No. CACR-11-02, Center for Applied Coastal Research, University of Delaware.

Tonelli, M., Petti, M. (2013) Numerical simulation of wave overtopping at coastal dikes and low-crested structures by means of a shock-capturing Boussinesq model, *Coastal Engineering*, 79:75-88.

Wei, G., Kirby, J.T., Grilli, S.T., Subramanya, R. (1995) A fully nonlinear Boussinesq model for surface waves. I. Highly nonlinear, unsteady waves. *J.Fluid Mechanics* 294:71–92.

Appendix C

Appendix III: Proceeding in ISOPE - Sliding of caisson submitted to water wedge impact: analytical calculation and CFD verifications

---

CFD calculations of a water wedge impacting a caisson were carried out considering the coupling between pressures and displacement. These results are compared to the water wedge method included in Chapter 5. This work has been presented in the international conference ISOPE in 2016

Sliding of caisson submitted to water wedge impact: analytical calculation and CFD verifications

M. Martin Medina, S. Abadie*, C. Mokrani**, D. Morichon**
* SIAME EA 4581, Université de Pau et des Pays de l'Adour, Anglet, France
** Civil Engineering Department, Federico Santa María Technical University, Valparaíso, Chile

ABSTRACT

In this work, the impulsive stage of a wave impact on a vertical breakwater is modelled based on the analogy with a water wedge impact. Coupling between pressure along the wall and caisson displacement is neglected. The aim of the present paper is to briefly present the method and verify the uncoupling hypothesis using Navier-Stokes numerical simulations. The water wedge analogy allows us first to analyse the influence of the wedge interface inclination (45°, 60° and 80°) on the sliding. Considering an ideal case without friction and uplift force, caisson sliding motion is found to decrease with wedge angle. Conversely, the velocity acquired by the caisson increases with the wedge inclination. In the 45° case, we show that the sliding simulated with a Navier-Stokes model taking into account the flow/structure coupling is finally close to the one estimated with the analytical method developed in this study, therefore validating the decoupling hypothesis.

KEY WORDS Wave impact, Water wedge, Breakwater caisson, Impulsive pressure, Sliding, Navier-Stokes simulations

INTRODUCTION

Caisson sliding is the predominant cause of vertical breakwater failure based on historical case reviews (Oumeraci (1994) and Takahashi et al. (2001)). Takahashi et al. (1994) was among the firsts to propose a method to evaluate the displacement of a caisson submitted to wave impacts taking into account the impulsive pressure component. Recently, Cuomo et al. (2011) estimated the sliding caisson including the dynamic component. However, the literature review shows a gap in the understanding of the precise role of wave shape on caisson motion.

Pressure signals generated by water wave impacts are typically characterized by two distinct phases: first, an impulsive component identified by a very high magnitude and a short duration followed by a slower one, mainly controlled by hydrostatic pressure. The existence of the impulsive component has been observed and detailed in many studies (e.g.,Kirkgöz (1991), Cuomo et al. (2010)). In wave impact, the peak pressure strongly depends on the wave local free surface shape and its relative position with respect to the wall (e.g., Whillock (1987) or Kirkgöz (1991)).

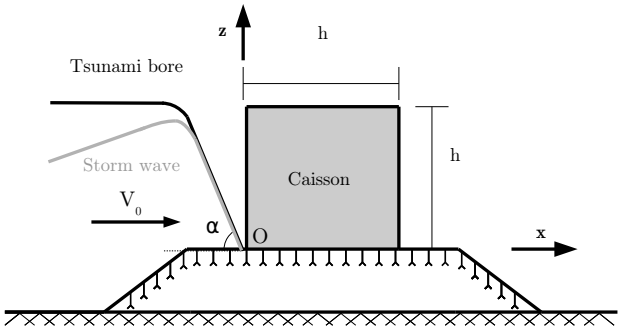

Fig. 1 Water wedge analogy for storm wave and tsunami bore forces considered during impact

A water wedge impact striking a breakwater caisson is studied. This simplified approach was already used to characterize breaking wave impacts in Cumberbatch (1960) and Zhang et al. (1996). Wu (2007) and Duan et al. (2009) also studied water wedge impacts on a solid wall varying the interface inclination. Waves starting breaking and tsunami bores may also be approximated as water wedges. For instance, Kihara et al. (2015) compared experimental results of tsunami bore impacts to results obtained with the water wedge approximation presented in Cumberbatch (1960).

In this work, we first present the method used to estimate the caisson motion. Neglecting the friction and uplift force, the caisson sliding is calculated for three interface inclinations. Finally, the simplified assumption of uncoupling water pressure along the wall and caisson displacement is verified using a computational fluid dynamics (CFD) Navier-Stokes model.

FORMULATION OF THE PROBLEM

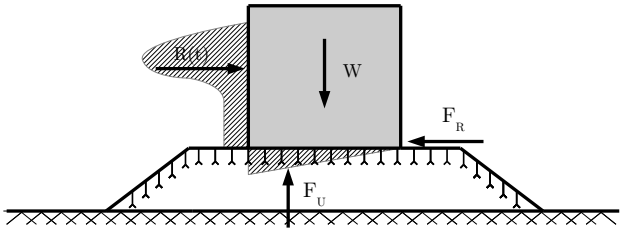

Fig. 2 Forces considered during impact

The caisson considered is a square of side h and weight W. It is submitted to the forces represented on Fig.2. When impacting on the caisson wall, the water wedge (Fig.1) generates a pressure field sketched on Fig.2 and whose resulting force is called $R(t)$. At $t = 0$, the water wedge meets the wall at point O (origin of the frame) located at the bottom left corner of the caisson. This is of course a crude approximation of a real impact as in reality the wave rather strikes somewhere on the front wall. The object of this paper is focused on methodological aspects therefore more realistic representation are left for future improvements. The pressure profile associated to the water wedge impact develops from this point upward. The whole caisson height being impacted is the worst case that can possibly happen. Therefore the results of this study may be considered conservative.

F_R is the bottom friction force acting under the caisson. F_U is the uplift force generated by the water wedge impact. The latter is an unknown and some assumptions will be made to approximate this parameter.

Water wedge impact flow

The water wedge (Fig.1) moves constantly and horizontally with velocity V_0 before impacting the breakwater caisson. The free surface inclination is denoted by α. The wedge is considered infinite in extent. The fluid is assumed to be incompressible and inviscid. Gravity effect on water wedge dynamic is neglected due to the extreme rapidity of the upward flow motion.

Based on the previous assumptions, the problem can be assumed to be self-similar (e.g.,Wu (2007)), which links spatial and temporal coordinates in a simple manner allowing to simplify the problem formulation. To change from real to self-similar plan, the following similarity variables have to be defined :

$$\zeta = \frac{x}{V_0 t} \qquad s = \frac{z}{V_0 t} \tag{1}$$

and the self-similar pressure:

$$g(\zeta, s) = \frac{P(x, z, t)}{\rho_w V_0^2} \tag{2}$$

Pressure on the wall is expressed by the function $g(0, s) = \frac{P(x=0,z,t)}{\rho_w V_0^2}$ also named $G(s)$ for clarity sake. The pressure distribution $G(s)$ associated to self-similar water wedge impacts was computed for different angles in Zhang et al. (1996), Wu (2007) and Duan et al. (2009) following

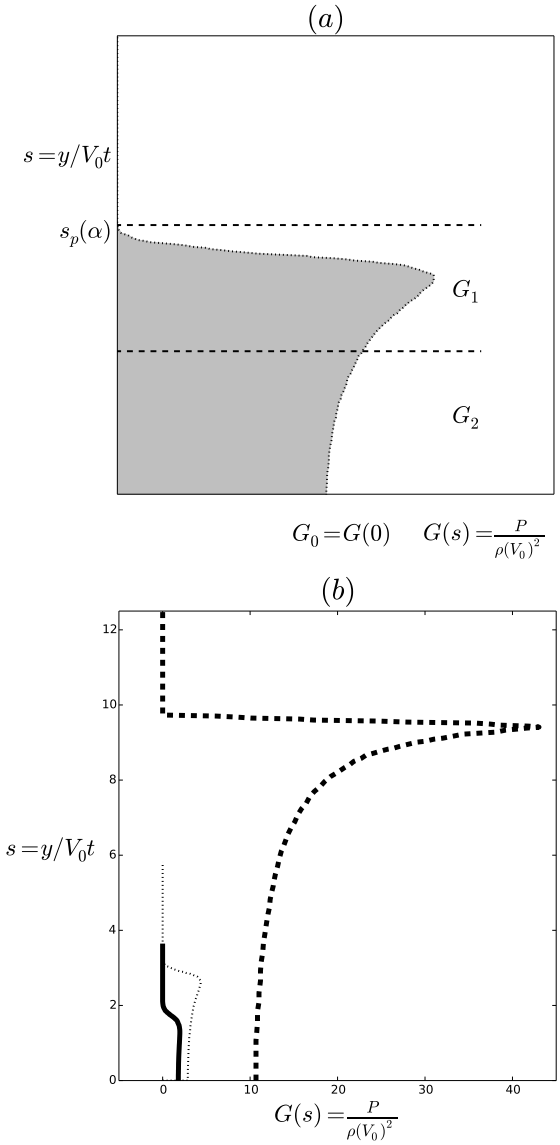

Fig. 3 Pressure distribution associated to water wedge impact (in self-similar coordinate) – (a): Sketch of a typical water wedge impact wall pressure. (b): Pressure signals produced by water wedge impact with different interface angles (from Wu (2007)). – (-) $\alpha = 45°$; (..) $\alpha = 60°$; (- -) $\alpha = 80°$.

different approaches. Fig.3(a) illustrates the typical pressure distribution generated by a water wedge impact. It is constituted by a sharp pressure rise (denoted as G_1 in Fig.3(a)) (i.e., the impulsive component) followed by a constant pressure step (G_2). In this paper, we considered three free surface angle cases: 45°, 60° and 80°. The pressure distributions associated to these angles were numerically computed in Wu (2007) by two different methods giving approximately the same distribution. These pressure signals represented in Fig.3(b), shows that the impulsive component can highly vary for different free surface angles. The results from BEM simulations are used in this work.

$s \times V_0$ represents the vertical velocity with which each point of the pres-

α	45°	60°	80°
s_p	2.4	3.2	11.0
I	3.23	9.57	150.79

Table 1 Numerical values of s_p and I (from Wu (2007)) used in the present paper.

sure distribution moves along the wall. For example, the peak pressure for $\alpha = 80°$ (in Fig.3(b)) is associated to $s \approx 9.5$ which means that its upward velocity, which is constant, is $9.5 \times V_0$. It is then obvious that peak pressures associated to large s values cross the front wall in a very short time.

Impact duration

The impact starts at $t = 0$ with a singularity, the whole pressure profile being gathered in one point, namely the lower left corner of the caisson. For $t > 0$, the pressure profile expands itself while moving up the wall. To keep advantage of the self-similarity, in this study, the impact is supposed to stop when the upper left corner of the structure sees the first pressure increase. The corresponding time is given by:

$$t_b = \frac{h}{V_0 s_p} \tag{3}$$

This time remains the same whatever the case studied. s_p is the relative vertical velocity of the first point on the wall (going up) whose pressure is zero (Fig.3(a)). The time at which the caisson starts to slide is called t_a in the rest of the paper. This time is different depending on the case considered (i.e., whether friction or uplift forces are taken into account or not). Its calculation is detailed in the following subsections. The motion duration D is defined as:

$$D = t_b - t_a \tag{4}$$

Of course, after this duration, the caisson will continue moving under the action of the whole wave flow but this secondary stage is not the topic of the work as we only focus on the displacement during the impulsive impact stage.

Impact resulting force

The resulting force $R(t)$ generated by the impact pressure on the wall can be calculated by integrating the pressure distribution along the wall.

$$R(t) = \int_0^h P(z,t)dz \tag{5}$$

Let us introduce I given by:

$$I = \int_0^{s_p} G(s)ds \tag{6}$$

I can be calculated from the self-similar distribution $G(s)$ given by Wu (2007). Table 1 displays the values obtained for the three angles considered in this study.

For a given time t, the self similarity implies that:

$$P(z) = P(V_0 ts) = \rho_w V_0^2 G(s) \tag{7}$$

Therefore:

$$R(t) = \int_0^h P(z)dz = \int_0^h P(V_0 ts)V_0 t ds = \rho_w V_0^3 t \int_0^{s_p} G(s)ds \tag{8}$$

And finally, subtituting the integral by I according to (6), we get:

$$R(t) = \rho_w V_0^3 It \tag{9}$$

The resulting force $R(t)$ generated by the water wedge impact linearly varies with time. For a given water wedge velocity V_0, the force $R(t)$ is only dependent on the integral value I. Table 1 illustrates that I increases monotonously with the interface angle α. Consequently, V_0 given, $R(t)$ increases with α. But this does not necessary mean that the caisson motion will be larger as the duration over which pressure acts on the wall also depends on α. This duration decreases with increasing α, and it is not straightforward to, *a priori*, guess the behavior of the resulting motion. The maximum pressure resulting force is taken at $t = t_b$ giving:

$$R_{max} = R(t = t_b) = \rho_w V_0^2 \frac{I}{s_p} h \tag{10}$$

Caisson Sliding

Without friction and uplift force

We first study the ideal case without basal friction (i.e., no interaction between caisson and the rubble mound foundation) and uplift force. The caisson displacement is obtained by expressing the Newton's law of motion.

$$m\,\ddot{x} = R(t) \tag{11}$$

with $m = \rho_s h^2$.

In this case, with no friction, the displacement starts as soon as the triangular water wedge strikes the structure (i.e., $t_a = 0$). Therefore, the total duration of the caisson displacement due to water wedge impact is $D = \frac{h}{s_p V_0}$.

By integrating (11), we obtain the caisson velocity:

$$\dot{x}(t) = v(t) = \frac{\rho_w V_0^3 I}{2\rho_s h^2} t^2 \tag{12}$$

and by integrating (12), we get the displacement:

$$x(t) = \frac{\rho_w V_0^3 I}{6\rho_s h^2} t^3 \tag{13}$$

The total displacement reads as:

$$x(t = t_b) = d = \frac{h}{6}\frac{\rho_w}{\rho_s}\frac{I}{s_p^3} \tag{14}$$

Equation 14 shows that the caisson displacement only depends on the ratio $(\frac{I}{s_p^3})$ given h and solid and liquid densities. These variables are constant for a given α and therefore representative of a given wedge inclination. In consequence, the displacement would be the same if the ratio $(\frac{I}{s_p^3})$ were constant no matter the wedge interface angle. The results presented in the next section will show that this is not the case.

With friction

The friction force (F_R) is now taken into account in the calculation of the caisson equilibrium as:

$$F_R = \mu W \tag{15}$$

With $W = \rho_s h^2 g$.

The caisson is assumed to start moving as soon as the force generated by the water wedge pressure exceeds the friction force between ground and caisson. When this is achieved, the motion equation reads:

$$m\,\ddot{x} = R(t) - F_R \tag{16}$$

In this case, t_a is the time when friction equals the wedge pressure resulting force. Equations 15 and 9 give:

$$t_a = \frac{\mu \rho_s h^2 g}{\rho_w V_0^3 I} \tag{17}$$

Therefore, the motion duration D is shortened as compared to the previous ideal case. By integrating equation (16), we can write the sliding velocity:

$$\dot{x}(t) = v(t) = \frac{\rho_w V_0^3 I}{2\rho_s h^2} t^2 - \mu g t + C_1 \tag{18}$$

considering that the velocity is nil at $t = t_a$:

$$C_1 = -\frac{\rho_w V_0^3 I}{2\rho_s h^2} t_a^2 + \mu g t_a \tag{19}$$

and integrating equation (18), we get the caisson displacement:

$$x(t) = \frac{\rho_w V_0^3 I}{6\rho_s h^2} t^3 - \frac{\mu g}{2} t^2 + C_1 t + C_2 \tag{20}$$

with:

$$C_2 = \frac{\rho_w V_0^3 I}{3\rho_s h^2} t_a^3 - \frac{\mu g}{2} t_a^2 \tag{21}$$

Values of t_a higher than t_b correspond to cases for which the pressure resulting force $R(t)$ is not sufficient to compensate the friction force before $t = t_b$. In this case, the caisson displacement due to the wedge impact is nil. This occurs when:

$$h < \frac{1}{s_p} \frac{\rho_w}{\rho_s} \frac{I}{g\mu} V_0^2 \tag{22}$$

With friction and uplift force

Similarly to Goda (1974), the uplift pressure distribution is taken constant and triangular with a maximum value taken from continuity equal to $\rho_w V_0^2 G_0$, the impact pressure found at the bottom left corner of the caisson (cf. Fig.3(a)). The triangular shape is supposed to account for the pressure decrease in the rubble mound porous medium. The resulting uplift force is therefore equal to:

$$F_U = \frac{h G_0 \rho_w V_0^2}{2} \tag{23}$$

The horizontal motion equation reads:

$$m\,\ddot{x} = R(t) - \mu(W - F_U) \tag{24}$$

Then, integrating the motion equation (24) including the uplift force F_U, we obtain the following sliding velocity:

$$\dot{x}(t) = v(t) = \frac{\rho_w V_0^3 I}{2\rho_s h^2} t^2 + \mu \left[\frac{G_0 \rho_w V_0^2}{2\rho_s h} - g \right] t + C_1 \tag{25}$$

with nil velocity at $t = t_a$:

$$C_1 = -\frac{\rho_w V_0^3 I}{2\rho_s h^2} t_a^2 + \left[g - \frac{G_0 \rho_w V_0^2}{2\rho_s h} \right] \mu t_a \tag{26}$$

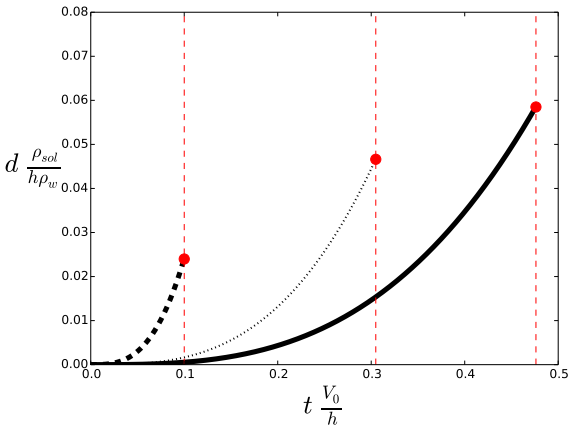

Fig. 4 Caisson displacement for the ideal case (no friction, no uplift) – (-) $\alpha = 45°$; (..) $\alpha = 60°$; (- -) $\alpha = 80°$

and integrating equation (25), the following displacement :

$$x(t) = \frac{\rho_w V_0^3 I}{6\rho_s h^2} t^3 + \frac{\mu}{2} \left[\frac{G_0 \rho_w V_0^2}{2\rho_s h} - g \right] t^2 + C_1 t + C_2 \tag{27}$$

with:

$$C_2 = \frac{\rho_w V_0^3 I}{3\rho_s h^2} t_a^3 - \frac{1}{2} \left[g - \frac{G_0 \rho_w V_0^2}{2\rho_s h} \right] \mu t_a^2 \tag{28}$$

t_a is obtained from equation (24) by setting $\ddot{x}$ to 0:

$$t_a = \frac{\mu h}{V_0 I} \left[\frac{\rho_s h g}{\rho_w V_0^2} - \frac{G_0}{2} \right] \tag{29}$$

and it has to be positive in equation (29) which gives:

$$h > \frac{G_0 \rho_w}{2\rho_s g} V_0^2 \tag{30}$$

The uplifting force exceeds the weight of the caisson when this condition is not met. In this case, the sliding motion is considered to start immediately and $t_a = 0$.

Finally, one can write:

$$t_a = max(0, \frac{\mu h}{V_0 I} \left[\frac{\rho_s h g}{\rho_w V_0^2} - \frac{G_0}{2} \right]) \tag{31}$$

t_b keeping the same value as before, the condition for sliding to occur (i.e., $t_a < t_b$) reads:

$$h < \left(\frac{I}{\mu s_p} + \frac{G_0}{2} \right) \frac{\rho_w V_0^2}{\rho_s g} \tag{32}$$

If this latter condition is not met, the sliding is nil.

SLIDING WITHOUT FRICTION AND UPLIFT FORCE

Figure 4 displays the time evolution of the caisson displacement during the impulsive impact stage (i.e., stopping when the pulsative stage starts) when friction and uplift are neglected. Note that the final displacement does not, in this case, depend on the impact velocity V_0 (cf. equation 14). Red points mark the end of the calculation

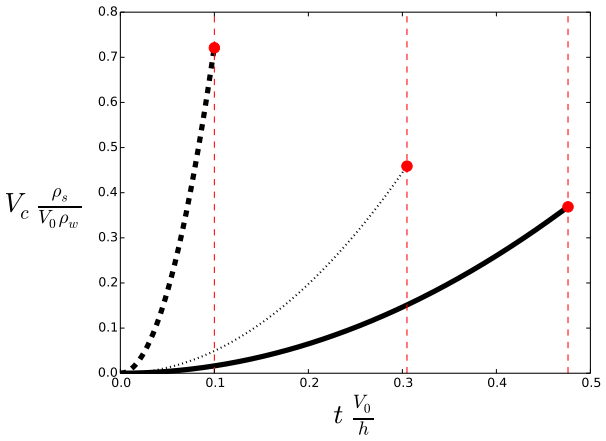

Fig. 5 Caisson sliding velocity for the ideal case (no friction, no uplift) – (-) $\alpha = 45°$; (..) $\alpha = 60°$; (- -) $\alpha = 80°$

(i.e., when the first pressure increase is felt at the left top corner of the wall). Conversely to intuition, the smallest displacement is obtained for the largest α. This displacement is respectively $\approx 0.12h$, $\approx 0.095h$, $\approx 0.05h$ (as $\frac{\rho_s}{\rho_w} = 2.1$) increasing wedge angles. The caisson velocity shown in Fig.5 behaves conversely and increases with wedge inclination. For $\alpha = 80°$, this velocity reaches $\approx 1.5V_0$ which is significant.

As shown previously, the loading on the caisson and therefore the acceleration increases drastically with the angle (equation (9)), while, conversely, the impact duration decreases also with the wedge inclination (equation (3)). In Fig.5, acceleration is the derivative of the plotted curves. It is obvious that this acceleration is much larger for the 80° case than for the 45° one. This allows velocity to reach a larger value even over a shorter duration. Displacement works the other way around. This time, duration controls the result but obviously this won't take long before the situation changes taking into account the values of velocities.

VERIFICATION OF THE DECOUPLING BETWEEN PRESSURE AND CAISSON DISPLACEMENT

In this section, numerical simulations are carried out in order to verify the hypothesis of the decoupling between impact pressure and caisson displacement. The case of triangular water wedge with an inclination of 45° impacting on a caisson of 10 m height is considered. The model set-up is represented in Fig.6(a). The domain is discretized in 117600 elements (Fig.6(b)). Slip conditions are imposed along the model boundaries.

Description of the numerical model

The CFD model used is THETIS, which solves the Navier–Stokes (NS) equations and uses a Volume of Fluid Technique (VOF) method to capture the interface evolution. The flow is considered incompressible composed of two immiscible phases: water and air. The continuity of fluid velocity is assumed through the interface and the surface tension effects are neglected. The system of equations is then the following:

$$\nabla \cdot \mathbf{u} = 0 \tag{33}$$

$$\rho(\frac{\partial \mathbf{u}}{\partial t} + (\mathbf{u} \cdot \nabla)\mathbf{u}) + \nabla p - \nabla \cdot [\mu(\nabla \mathbf{u} + \nabla^t \mathbf{u})] = \rho \mathbf{g} \tag{34}$$

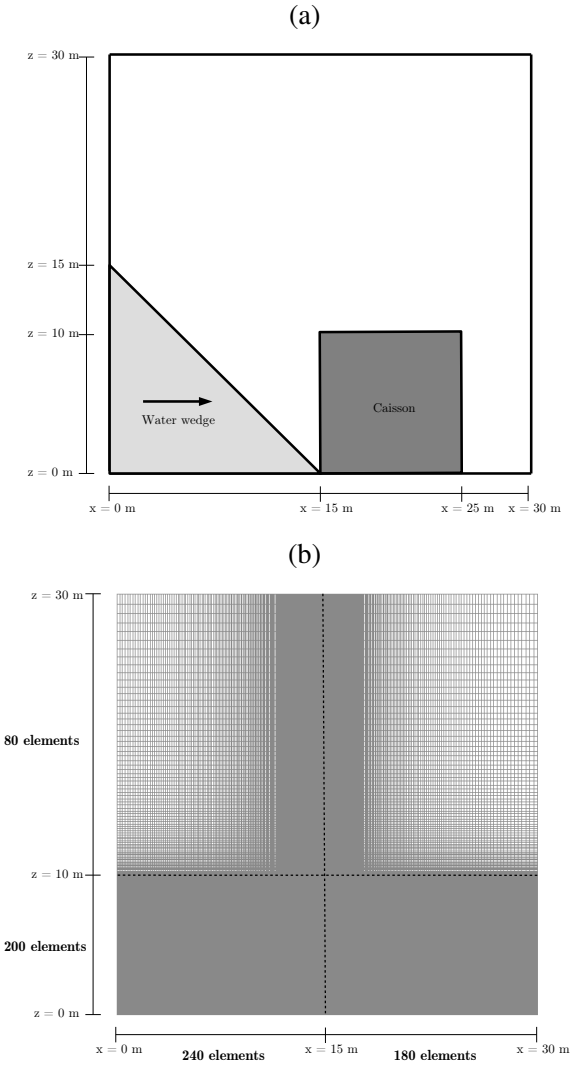

Fig. 6 Numerical simulations with THETIS – (a): Geometry of the numerical model (b): Domain mesh

where, ρ is the fluid density and μ is the fluid viscosity, both spatially varying properties.

The penalisation method described by Ducassou et al. (2015) is used to solve the fluid-solid interaction problems. Equation (33) is solved in the whole domain (fluid and solid domain). A penalty model on the viscosity (Angot et al. (1999); Ritz and Caltagirone (1999)) is proposed to model the solid. The viscosity inside the rigid region is taken large enough to enforce rigid conditions and it acts as penalty factor of the strain-rate tensor. In addition, the interface evolution of the fluid and the solid need to be determined. The motion of each surface is described by:

$$\frac{\partial \Phi_{F,S}}{\partial t} + \mathbf{v} \cdot \nabla \Phi_{F,S} = 0 \tag{35}$$

where $\Phi_{F,S}(x,y,z)$ is a phase function corresponding to the fluid and solid.

The NS equations are discretized on a fixed Cartesian grid using a finite volume formulation. Following Patankar (1980), the finite volume formulation is solved using a staggered mesh known as the Marker And

Cells (MAC) method from Harlow et al. (1965). The coupling between velocity and pressure is solved using the augmented Lagrangian method (Fortin and Glowinski (1982)). This is a minimization method under the constraint of the continuity equation, where the pressure which is decoupled from the velocity, appears as a Lagrange multiplier. The incompressibility constraint is directly introduced into the equation of motion as a penalty term $r_u\nabla(\nabla.\mathbf{v})$, that couples the components of speed. If k is the iteration of the method, the system is written as:

$$\rho^n(\frac{\mathbf{v}^{n,k+1}}{\triangle t^n} + (\mathbf{v}^{n,k}\nabla)\mathbf{v}^{n,k+1}) - \rho^n\mathbf{b} - \nabla p^{n,k} - \nabla[\mu^n(\nabla\mathbf{v}^{n,k+1} + \nabla^t\mathbf{v}^{n,k+1})] - r_u\nabla(\nabla.\mathbf{v}^{n,k+1}) = \rho^n\frac{\mathbf{v}^n}{\triangle t^n} \quad (36)$$

$$p^{n,k+1} = p^{n,k} - r_p\nabla\cdot\mathbf{v}^{n,k+1} \quad (37)$$

where r_u and r_p are convergence parameters set in the present simulations as 1. The advantage of such formulation is the explicit calculation of the pressure. It uses only the pressure in the previous temporal iteration and the divergence of velocity.

Equation (35) is solved introducing a Volume of Fluid (VOF) technique (Hirt and Nichols (1981)) that describes the volume fraction occupied by one of the fluids (i.e. water) in a cell. At the end of each time step, the local cell water volume fraction is used to recalculate local values of density and viscosity necessary to solve the NS equations. The Piecewise Linear Interface Calculation (PLIC) method is employed in these simulations. One of the great advantage of this Eulerian/Lagrangian method is to keep the discontinuous nature of the interface between water and air using the Lagrangian character of the transport method. To ensure the stability of the PLIC method, a sufficient condition is that the volume fraction does not move more than half of a cell during a time step (Abadie et al. (1998)).

Water wedge impact on a fixed caisson

First, the THETIS code is applied to the case of a water wedge impacting a fixed caisson. The configuration is similar to the case described in Fig.6(a). The caisson is fixed to the inferior boundary stopping the motion. The pressure signals obtained with THETIS model are represented in the self-similar plane in Fig.7. Each dashed gray line represents the pressure distribution observed at a specific time. Numerical results show a good agreement with the pressure signal obtained using the complex velocity potential in Wu (2007). However, some differences are found regarding the pressure values recorded on the wall. These differences could be due to the air effect, not considered in Wu (2007).

Water wedge impact on a moving caisson

In the second simulation, the caisson can freely move. The friction between the bloc and the bottom is not considered in the simulations. First, pressure signals corresponding to different instants during the impact are illustrated in Fig.8. As long as the caisson is not moving, the pressure distributions are in good agreement with the results shown in Wu (2007). Nevertheless, the sliding of the caisson causes lower pressure values and therefore a loss of force applied on the caisson as it is shown in Fig.8. Fig.9 illustrates the triangular water wedge impact and the sliding of the caisson simulated in THETIS. t_{s_p} correspond to the end of the impact when s_p reaches the top of the caisson. After the water wedge touches the solid, a diverging jet or splash is developed along the caisson wall as previously shown in Cumberbatch (1960), Zhang et al. (1996) and Wu (2007). During the first period of the impact, $t = t_{s_p}/3$, the sliding of the caisson is not significant. It is in the last period of the impact, $2t_{s_p}/3 < t < t_{s_p}$, when the final displacement is almost totally generated.

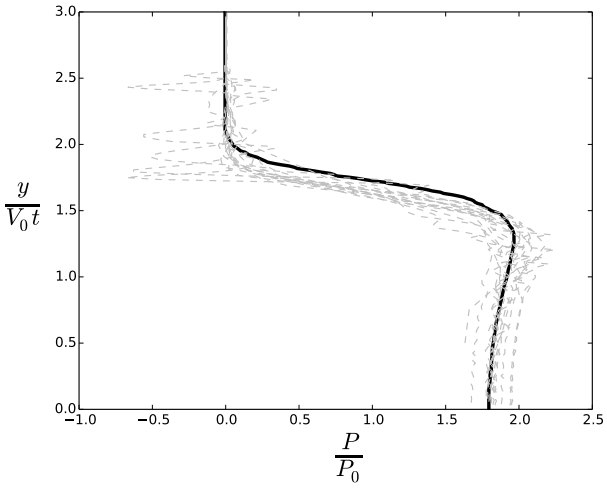

Fig. 7 Pressure distribution ($P_0 = \rho(V_0)^2$) on the breakwater caisson ($\alpha = 45$) – (-) Results from Wu (2007); (- -) Results from numerical simulations on a fixed caisson

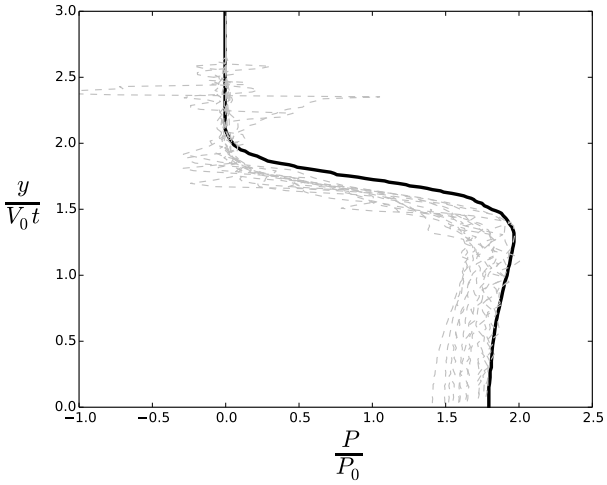

Fig. 8 Pressure distribution ($P_0 = \rho(V_0)^2$) on the breakwater caisson ($\alpha = 45$) – (-) Results from Wu (2007) on a fixed caisson; (- -) Results from numerical simulations on a moving caisson

Despite the differences found in the pressure signals due to the displacement of the caisson, Fig.10 shows that the numerical sliding ($\approx 0.10h$) is very close to the sliding estimated using the method described in this paper ($\approx 0.12h$). This method also gives results in a good agreement with numerical simulations in terms of sliding velocity (Fig.11). Hence, the loss of force mentioned before is not relevant on the sliding of the caisson. Then the decoupling between the pressure obtained on the wall and the sliding of the caisson can be assumed to be a valid approximation.

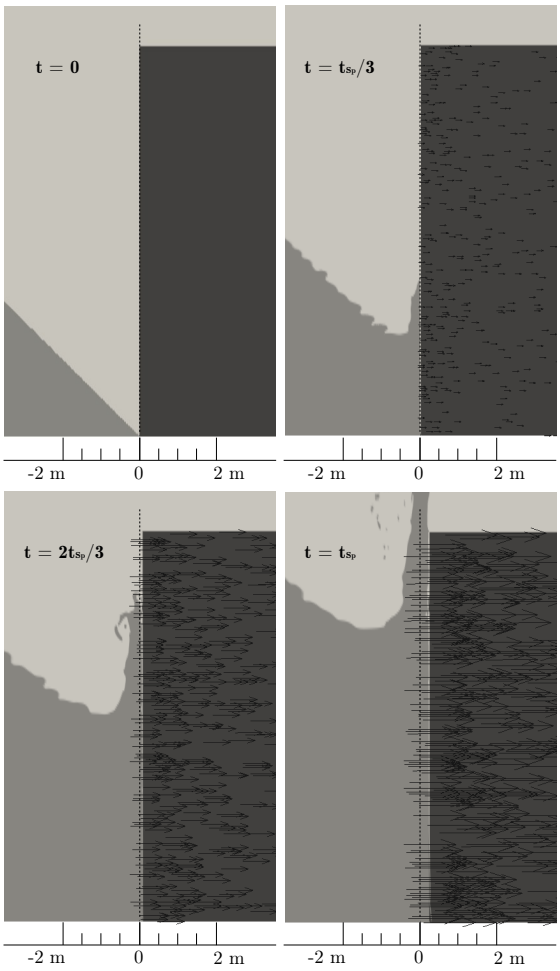

Fig. 9 Breakwater caisson sliding with no friction effect ($\alpha = 45$)

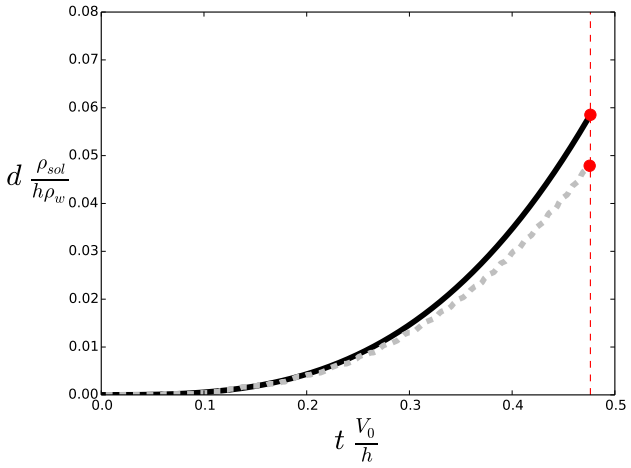

Fig. 10 Breakwater caisson sliding with no friction effect ($\alpha = 45$) – (-) Calculated from pressure distributions obtained in Wu (2007); (- -) Calculated from numerical simulations

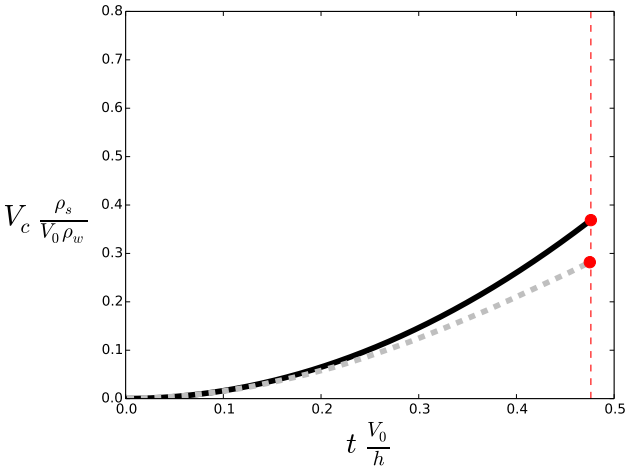

Fig. 11 Breakwater caisson sliding velocity with no friction effect ($\alpha = 45$) – (-) Calculated from pressure distributions obtained in Wu (2007); (- -) Calculated from numerical simulations

CONCLUSIONS

In this paper, the hypothesis of neglecting the coupling between pressure and displacement has been verified using CFD simulations. Furthermore, the sliding of caissons impacted by water wedges impacts has been studied showing the influence of impulsive pressure changes generated by interface variations.

The following main conclusions can be drawn :

- While neglecting friction and uplift force, caisson sliding motion decreases with wedge angle while velocity acquired at impact end increases with this parameter.
- Such violent impacts generate a small displacement due to their short duration but induce a considerable velocity to the caisson. Therefore, velocity acquired by the structure during impact is the most important contribution to the total displacement as compared to displacement during impact.
- Numerical simulations using Navier-Stokes equations allowed us to consolidate the analytical results presented in the first part of the paper.

ACKNOWLEDGMENTS

This work was funded by the FP7 EU research program ASTARTE (Grant No.:603839) and the PIA RSNR French program TANDEM (Grant No.: ANR-11-RSNR-00023-01). The authors would like to thank Dr Mourad Abouzaïd for helpful discussions around the mathematical aspects of this work.

REFERENCES

Abadie, S., Caltagirone, J., and Watremez, P. (1998). Splash-up generation in a plunging breaker. *Comptes Rendus de l'Academie des Sciences Series IIB Mechanics Physics Astronomy*, 326(9):553–559.

Angot, P., Bruneau, C.-H., and Fabrie, P. (1999). A penalization method to take into account obstacles in incompressible viscous flows. *Numerische Mathematik*, 81(4):497–520.

Cumberbatch, E. (1960). The impact of a water wedge on a wall. *Journal of Fluid Mechanics*, 7(03):353–374.

Cuomo, G., Allsop, W., Bruce, T., and Pearson, J. (2010). Breaking wave loads at vertical seawalls and breakwaters. *Coastal Engineering*, 57(4):424–439.

Cuomo, G., Lupoi, G., Shimosako, K.-i., and Takahashi, S. (2011). Dynamic response and sliding distance of composite breakwaters under breaking and non-breaking wave attack. *Coastal Engineering*, 58(10):953–969.

Duan, W., Xu, G., and Wu, G. (2009). Similarity solution of oblique impact of wedge-shaped water column on wedged coastal structures. *Coastal Engineering*, 56(4):400–407.

Ducassou, B., Nuñez, J., Cruchaga, M., and Abadie, S. (2015). A fictitious domain approach based on a viscosity penalty method to simulate wave/structure interaction (submitted). *Journal of Hydraulic Research*, (Submitted).

Fortin, M. and Glowinski, R. (1982). *Méthodes de lagrangien augmenté: applications à la résolution numérique de problèmes aux limites*. Dunod.

Goda, Y. (1974). New wave pressure formulae for composite breakwaters. *Coastal Engineering Proceedings*, 1(14).

Harlow, F. H., Welch, J. E., et al. (1965). Numerical calculation of time-dependent viscous incompressible flow of fluid with free surface. *Physics of fluids*, 8(12):2182.

Hirt, C. W. and Nichols, B. D. (1981). Volume of fluid (vof) method for the dynamics of free boundaries. *Journal of computational physics*, 39(1):201–225.

Kihara, N., Niida, Y., Takabatake, D., Kaida, H., Shibayama, A., and Miyagawa, Y. (2015). Large-scale experiments on tsunami-induced pressure on a vertical tide wall. *Coastal Engineering*, 99:46–63.

Kirkgöz, M. S. (1991). Impact pressure of breaking waves on vertical and sloping walls. *Ocean Engineering*, 18(1):45–59.

Lugni, C., Brocchini, M., and Faltinsen, O. (2006). Wave impact loads: The role of the flip-through. *Physics of Fluids*, 18(12).

Oumeraci, H. (1994). Review and analysis of vertical breakwater failures—lessons learned. *Coastal Engineering*, 22(1):3–29.

Patankar, S. (1980). *Numerical heat transfer and fluid flow*. CRC Press.

Ritz, J. and Caltagirone, J. (1999). A numerical continuous model for the hydrodynamics of fluid particle systems. *International Journal for Numerical Methods in Fluids*, 30(8):1067–1090.

Takahashi, S., Shimosako, K.-i., Kimura, K., and Suzuki, K. (2001). Typical failures of composite breakwaters in japan. In *COASTAL ENGINEERING CONFERENCE*, volume 2, pages 1899–1910. ASCE AMERICAN SOCIETY OF CIVIL ENGINEERS.

Takahashi, S., Tanimoto, K., and Shimosako, K. (1992). Experimental study of impulsive pressures on composite breakwaters. *Report of Port and Harbour Research Institute*, 31(5):35–74.

Takahashi, S., Tanimoto, K., Shimosako, K., et al. (1994). Dynamic response and sliding of breakwater caissons against impulsive breaking wave forces. In *Proc. Intl. Workshop" Wave Barriers in Deep Waters*, pages 362–399.

Whillock, A. (1987). Measurements of forces resulting from normal and oblique wave approaches to small scale sea walls. *Coastal engineering*, 11(4):297–308.

Wu, G. (2007). Fluid impact on a solid boundary. *Journal of fluids and structures*, 23(5):755–765.

Zhang, S., Yue, D. K., and Tanizawa, K. (1996). Simulation of plunging wave impact on a vertical wall. *Journal of Fluid Mechanics*, 327:221–254.

Bibliography

Abadie, S., Caltagirone, J. & Watremez, P. (1998), 'Splash-up generation in a plunging breaker', *Comptes Rendus de l'Academie des Sciences Series IIB Mechanics Physics Astronomy* **326**(9), 553–559.

Abadie, S., Harris, J., Grilli, S. & Fabre, R. (2012), 'Numerical modeling of tsunami waves generated by the flank collapse of the cumbre vieja volcano (la palma, canary islands): tsunami source and near field effects', *Journal of Geophysical Research: Oceans* **117**(C5).

Abadie, S. & Mokrani, C. (2012), 'On the influence of breaking wave local geometry on impulsive loads', *Coastal Engineering Proceedings* **1**(33), 61.

Andersen, L., Burcharth, H. F. & Andersen, T. L. (2011), 'Validity of simplified analysis of stability of caisson breakwaters on rubble foundation exposed to impulsive loads', *Coastal Engineering Proceedings* **1**(32), 46.

Angot, P. (1989), 'Contribution à l'étude des transferts thermiques dans des systèmes complexes, application aux composants electronique. these de doctorat,', *Université Bordeaux I* .

Arcas, D. & Segur, H. (2012), 'Seismically generated tsunamis', *Phil. Trans. R. Soc. A* **370**(1964), 1505–1542.

Arikawa, T. (2009), 'Structural behavior under impulsive tsunami loading', *Journal of Disaster Research* **4**(6), 377–381.

Arikawa, T., Sato, M., Shimosako, K., Hasegawa, I., Yeom, G.-S. & Tomita, T. (2012), 'Failure mechanism of kamaishi breakwaters due to the great east japan earthquake tsunami', *Coastal engineering proceedings* **1**(33), 16.

Asakura, R., Iwase, K., Ikeya, T., Takao, M., Kaneto, T., Fujii, N. & Ohmori, M. (2003), The tsunami wave force acting on land structures, *in* 'Coastal Engineering 2002: Solving Coastal Conundrums', World Scientific, pp. 1191–1202.

Baba, T., Takahashi, N., Kaneda, Y., Ando, K., Matsuoka, D. & Kato, T. (2015), 'Parallel implementation of dispersive tsunami wave modeling with a nesting algorithm for the 2011 tohoku tsunami', *Pure and Applied Geophysics* **172**(12), 3455–3472.

Bagnold, R. (1939), Interim report on wave-pressure research, Technical report, Institution of Civil Engineeris.

Bonneton, P., Bonneton, N., Parisot, J.-P. & Castelle, B. (2015), 'Tidal bore dynamics in funnel-shaped estuaries', *Journal of Geophysical Research: Oceans* **120**(2), 923–941.

Bredmose, H., Hunt-Raby, A., Jayaratne, R. & Bullock, G. (2010), 'The ideal flip-through impact: experimental and numerical investigation', *Journal of engineering mathematics* **67**(1-2), 115–136.

Bricker, J. D., Takagi, H. & Mitsui, J. (2013), Turbulence model effects on vof analysis of breakwater overtopping during the 2011 great east japan tsunami, *in* 'Proceedings of the 2013 IAHR World Congress, Chengdu, Sichuan, China, paper A', Vol. 10153.

Bullock, G., Obhrai, C., Peregrine, D. & Bredmose, H. (2007), 'Violent breaking wave impacts. part 1: Results from large-scale regular wave tests on vertical and sloping walls', *Coastal Engineering* **54**(8), 602–617.

Chan, E.-S. (1994), 'Mechanics of deep water plunging-wave impacts on vertical structures', *Coastal engineering* **22**(1), 115–133.

Chanson, H. (2006), 'Tsunami surges on dry coastal plains: Application of dam break wave equations', *Coastal Engineering Journal* **48**(04), 355–370.

Chanson, H. (2010), 'Undular tidal bores: basic theory and free-surface characteristics', *Journal of Hydraulic Engineering* **136**(11), 940–944.

Chorin, A. (1967), 'A numerical method for solving incompressible viscous flow problem', *J. Comput. Phys.* **2**, 12–26.

Cooker, M. (2010), 'The flip-through of a plane inviscid jet with a free surface', *Journal of Engineering Mathematics* **67**(1-2), 137–152.

Cooker, M. & Peregrine, D. (1990), 'A model for breaking wave impact pressures', *Coastal Engineering Proceedings* **1**(22).

Cooker, M. & Peregrine, D. (1992), 'Wave impact pressure and its effect upon bodies lying on the sea bed', *Coastal Engineering* **18**(3), 205–229.

Cross, R. H. (1967), 'Tsunami surge forces', *Journal of the waterways and harbors division* **93**(4), 201–234.

Cumberbatch, E. (1960), 'The impact of a water wedge on a wall', *Journal of Fluid Mechanics* **7**(03), 353–374.

Cuomo, G., Allsop, W., Bruce, T. & Pearson, J. (2010), 'Breaking wave loads at vertical seawalls and breakwaters', *Coastal Engineering* **57**(4), 424–439.

Cuomo, G., Lupoi, G., Shimosako, K.-i. & Takahashi, S. (2011), 'Dynamic response and sliding distance of composite breakwaters under breaking and non-breaking wave attack', *Coastal Engineering* **58**(10), 953–969.

del Jesus, M., Lara, J. L. & Losada, I. J. (2012), 'Three-dimensional interaction of waves and porous coastal structures: Part i: Numerical model formulation', *Coastal Engineering* **64**, 57–72.

Desombre, J. (2012), Modélisation vof de l'écoulement de jet de rive en surface et dans une plage perméable, PhD thesis, Pau.

Desombre, J., Morichon, D. & Mory, M. (2012), 'Simultaneous surface and subsurface air and water flows modelling in the swash zone', *Coastal Engineering Proceedings* **1**(33), 56.

Duan, W., Xu, G. & Wu, G. (2009), 'Similarity solution of oblique impact of wedge-shaped water column on wedged coastal structures', *Coastal Engineering* **56**(4), 400–407.

Ducassou, B., Nuñez, J., Cruchaga, M. & Abadie, S. (2017), 'A fictitious domain approach based on a viscosity penalty method to simulate wave/structure interaction', *Journal of Hydraulic Research* pp. 1–16.

Elsafti, H. & Oumeraci, H. (2017), 'Analysis and classification of stepwise failure of monolithic breakwaters', *Coastal Engineering* **121**, 221–239.

Engsig-Karup, A. P., Hesthaven, J. S., Bingham, H. B. & Warburton, T. (2008), 'Dg-fem solution for nonlinear wave-structure interaction using boussinesq-type equations', *Coastal Engineering* **55**(3), 197–208.

Fenton, J. (1972), 'A ninth-order solution for the solitary wave', *Journal of Fluid Mechanics* **53**(02), 257–271.
URL: *http://journals.cambridge.org/article_S002211207200014X*

Glimsdal, S., Harbitz, C., Løvholt, F. et al. (2013), 'Dispersion of tsunamis: does it really matter?', *Natural Hazards and Earth System Sciences* **13**(6), 1507.

Glimsdal, S., Pedersen, G., Atakan, K., Harbitz, C., Langtangen, H. & Lovholt, F. (2006), 'Propagation of the dec. 26, 2004, indian ocean tsunami: Effects of dispersion and source characteristics', *International Journal of Fluid Mechanics Research* **33**(1).

Goda, Y. (1974), 'New wave pressure formulae for composite breakwaters', *Coastal Engineering Proceedings* **1**(14).

Goda, Y. (2010), *Random seas and design of maritime structures*, World scientific.

Goda, Y. & Takagi, H. (2000), 'A reliability design method of caisson breakwaters with optimal wave heights', *Coastal Engineering Journal* **42**(04), 357–387.

Gottlieb, S., Shu, C.-W. & Tadmor, E. (2001), 'Strong stability-preserving high-order time discretization methods', *SIAM review* **43**(1), 89–112.

Grilli, S. T., Harris, J. C., Shi, F., Kirby, J. T., Bakhsh, T. S. T., Estibals, E. & Tehranirad, B. (2012), 'Numerical modeling of coastal tsunami impact dissipation and impact', *Coastal Engineering Proceedings* **1**(33), 9.

Grilli, S. T., Losada, M. A. & Martin, F. (1994), 'Characteristics of solitary wave breaking induced by breakwaters', *Journal of Waterway, Port, Coastal, and Ocean Engineering* **120**(1), 74–92.

Grue, J., Pelinovsky, E., Fructus, D., Talipova, T. & Kharif, C. (2008), 'Formation of undular bores and solitary waves in the strait of malacca caused by the 26 december 2004 indian ocean tsunami', *Journal of Geophysical Research: Oceans* **113**(C5).

Guilcher, P., Jus, Y., Couty, N., Brosset, L., Scolan, Y.-M., Le Touzé, D. et al. (2014), 2d simulations of breaking wave impacts on a flat rigid wall–part 1: Influence of the wave shape, *in* 'The Twenty-fourth International Ocean and Polar Engineering Conference', International Society of Offshore and Polar Engineers.

Guler, H. G., Arikawa, T., Oei, T. & Yalciner, A. C. (2015), 'Performance of rubble mound breakwaters under tsunami attack, a case study: Haydarpasa port, istanbul, turkey', *Coastal Engineering* **104**, 43–53.

Guo, J. (2002), 'Simple and explicit solution of wave dispersion equation', *Coastal Engineering* **45**(2), 71 – 74.

Harlow, F. H. & Welsh, J. E. (1995), 'Numerical calculation of time dependent viscous incompressible flow with free surface .', *Physics of Fluids* **8**, 21–82.

Hattori, M., Arami, A. & Yui, T. (1994), 'Wave impact pressure on vertical walls under breaking waves of various types', *Coastal Engineering* **22**(1), 79–114.

Hirt, C. & Nichols, B. (1981), 'Volume of fluid (vof) method for the dynamics of free boundaries', *Journal of Computational Physics* **39 (1)**, 201–225.

Hofland, B., Kaminski, M. & Wolters, G. (2011), 'Large scale wave impacts on a vertical wall', *Coastal Engineering Proceedings* **1**(32), 15.

Horrillo, J., Kowalik, Z. & Shigihara, Y. (2006), 'Wave dispersion study in the indian ocean-tsunami of december 26, 2004', *Marine Geodesy* **29**(3), 149–166.

Hsiao, S.-C. & Lin, T.-C. (2010), 'Tsunami-like solitary waves impinging and overtopping an impermeable seawall: Experiment and rans modeling', *Coastal Engineering* **57**(1), 1–18.

Hsu, T.-J., Sakakiyama, T. & Liu, P. L.-F. (2002), 'A numerical model for wave motions and turbulence flows in front of a composite breakwater', *Coastal Engineering* **46**(1), 25–50.

Hu, K., Mingham, C. G. & Causon, D. M. (2000), 'Numerical simulation of wave overtopping of coastal structures using the non-linear shallow water equations', *Coastal Engineering* **41**(4), 433–465.

Hull, P. & Müller, G. (2002), 'An investigation of breaker heights, shapes and pressures', *Ocean Engineering* **29**(1), 59–79.

Ikeno, M., Matsuyama, M., Sakakiyama, T. & Yanagisawa, K. (2007), Effects of soliton fission and wave breaking on tsunami force acting on breakwater, *in* 'Coastal Engineering 2006: (In 5 Volumes)', World Scientific, pp. 5162–5174.

Jayaratne, R., Abimola, A., Mikami, T., Matsuba, S., Esteban, M. & Shibayama, T. (2014), 'Predictive model for scour depth of coastal structure failures due to tsunamis', *Coastal Engineering Proceedings* **1**(34), 56.

Jiang, C., Liu, X., Yao, Y., Deng, B. & Chen, J. (2016), 'Numerical investigation of tsunami-like solitary wave interaction with a seawall', *Journal of Earthquake and Tsunami* p. 1740006.

Jianhong, Y., Dongsheng, J., Ren, W. & Changqi, Z. (2013), 'Numerical study of the stability of breakwater built on a sloped porous seabed under tsunami loading', *Applied Mathematical Modelling* **37**(23), 9575–9590.

Kaminski, M., Bogaert, H. et al. (2009), Full scale sloshing impact tests, *in* 'The Nineteenth International Offshore and Polar Engineering Conference', International Society of Offshore and Polar Engineers.

Kato, F., Inagaki, S. & Fukuhama, M. (2006), Wave force on coastal dike due to tsunami, *in* 'COASTAL ENGINEERING CONFERENCE', Vol. 30, World Scientific, p. 5150.

Kazolea, M., Filippini, A. G., Ricchiuto, M., Abadie, S., Medina, M. M., Morichon, D., Journeau, C., Marcer, R., Pons, K., Le Roy, S. et al. (2016), 'Wave propagation breaking, and overtoping on a 2d reef: a comparative evaluation of numerical codes for tsunami modelling', *European Journal of Mechanics-B/Fluids (accepted)* .

Kazolea, M., Filippini, A., Ricchiuto, M., Abadie, S., Medina, M. M., Morichon, D., Journeau, C., Marcer, R., Pons, K., LeRoy, S. et al. (2017), 'Wave propagation, breaking, and overtopping on a 2d reef: A comparative evaluation of numerical codes for tsunami modelling', *European Journal of Mechanics-B/Fluids* .

Khadra, K. (1994), 'Méthodes adaptatives de raffinement local multigrille, applications aux équations de navier-stokes et de l'énergie'.

Khayyer, A., Gotoh, H. & Shao, S. (2009), 'Enhanced predictions of wave impact pressure by improved incompressible sph methods', *Applied Ocean Research* **31**(2), 111–131.

Kihara, N., Niida, Y., Takabatake, D., Kaida, H., Shibayama, A. & Miyagawa, Y. (2015), 'Large-scale experiments on tsunami-induced pressure on a vertical tide wall', *Coastal Engineering* **99**, 46–63.

Kim, D.-H. & Lynett, P. J. (2010), 'Dispersive and nonhydrostatic pressure effects at the front of surge', *Journal of Hydraulic Engineering* **137**(7), 754–765.

Kim, S., Lee, S. & Kim, K. H. (2008), 'Wavenumber-extended high-order oscillation control finite volume schemes for multi-dimensional aeroacoustic computations', *Journal of Computational Physics* **227**(8), 4089–4122.

Kim, T., Takayama, T. & Miyawaki, Y. (2004), Laboratory experiments on the sliding distance and tilting angle of a caisson breakwater subject to wave impact, *in* 'COASTAL ENGINEERING CONFERENCE', Vol. 29, World Scientific, p. 3762.

Kirkgöz, M. S. (1991), 'Impact pressure of breaking waves on vertical and sloping walls', *Ocean Engineering* **18**(1), 45–59.

Klammer, P., Oumeraci, H. & Partenscky, H. (1995), Oscillatory motions and permanent displacements of caisson breakwaters subject to impulsive breaking wave loads, *in* 'COASTAL ENGINEERING CONFERENCE', Vol. 2, ASCE AMERICAN SOCIETY OF CIVIL ENGINEERS, pp. 1255–1255.

Kleefsman, K., Fekken, G., Veldman, A., Iwanowski, B. & Buchner, B. (2005), 'A volume-of-fluid based simulation method for wave impact problems', *Journal of Computational Physics* **206**(1), 363–393.

Lara, J., Losada, I. & Guanche, R. (2008), 'Wave interaction with low-mound breakwaters using a rans model', *Ocean engineering* **35**(13), 1388–1400.

Li, Y. & Raichlen, F. (2001), 'Solitary wave runup on plane slopes', *Journal of Waterway, Port, Coastal, and Ocean Engineering* **127**(1), 33–44.

Ling, H. I., Cheng, A. H.-D., Mohri, Y. & Kawabata, T. (1999), 'Permanent displacement of composite breakwaters subject to wave impact', *Journal of waterway, port, coastal, and ocean engineering* **125**(1), 1–8.

Losada, I., Lara, J., Christensen, E. & Garcia, N. (2005), 'Modelling of velocity and turbulence fields around and within low-crested rubble-mound breakwaters', *Coastal Engineering* **52**(10), 887–913.

Lugni, C., Brocchini, M. & Faltinsen, O. (2006), 'Wave impact loads: The role of the flip-through', *Physics of Fluids* **18**(12).

Madsen, P. A., Fuhrman, D. R. & Schäffer, H. A. (2008), 'On the solitary wave paradigm for tsunamis', *Journal of Geophysical Research: Oceans (1978–2012)* **113**(C12).

Mano, A., Iida, T., Udo, K. & Tanaka, H. (2013), 'Breaking process and mechanism of coastal levees on sendai bay coast hit by the 2011 mega tsunami', *Journal of Coastal Research, Special Issue* (65), 772–777.

Martin-Medina, M., Abadie, S., Mokrani, C. & Morichon, D. (2017), 'Numerical simulation of flip-through impacts of variable steepness on a vertical breakwater'.

Martin-Medina, M., Abadie, S., Mokrani, C., Morichon, D. et al. (2016), Sliding of caisson submitted to water wedge impact: analytical calculation and cfd verifications, *in* 'The 26th International Ocean and Polar Engineering Conference', International Society of Offshore and Polar Engineers.

Martin-Medina, M., Abadie, S. & Morichon, D. (2017), Validation of a navier-stokes model to study flip-through impacts on a composite breakwater, *in* 'La Houille Blanche'.

Matsuyama, M., Ikeno, M., Sakakiyama, T. & Takeda, T. (2007), A study of tsunami wave fission in an undistorted experiment, *in* 'Tsunami and Its Hazards in the Indian and Pacific Oceans', Springer, pp. 617–631.

McCabe, M., Stansby, P. K., Rogers, B. D. & Cunningham, L. S. (2014), 'Boussinesq modelling of tsunami and storm wave impact', *Proceedings of the Institution of Civil Engineers-Engineering and Computational Mechanics* **167**(3), 106–116.

Mikami, T. & Shibayama, T. (2013), Numerical analysis of tsunami flow around coastal dike, *in* 'Proceedings of 7th International Conference on Asian and Pacific Coasts', pp. 654–659.

Mikami, T., Shibayama, T., Esteban, M. & Matsumaru, R. (2012), 'Field survey of the 2011 tohoku earthquake and tsunami in miyagi and fukushima prefectures', *Coastal Engineering Journal* **54**(01), 1250011.

Minikin, R. (1950), *Winds, waves and maritime structures*, Charles Griffin and Company Limited.

Mitsuyasu, H. (1966), 'Shock pressure of breaking wave', *Coastal Engineering Proceedings* **1**(10).

Mokrani, C. (2012), Impacts de vagues déferlantes sur un obstacle vertical. Modèle théorique et calcul numérique des pics de pression, PhD thesis, Pau.

Mokrani, C. & Abadie, S. (2016), 'Conditions for peak pressure stability in vof simulations of dam break flow impact', *Journal of Fluids and Structures* **62**, 86–103.

Mori, N., Cox, D., Yasuda, T. & Mase, H. (2013), 'Overview of the 2011 tohoku earthquake tsunami damage and its relation to coastal protection along the sanriku coast', *Earthquake Spectra* **29**(SUPPL.1), S127–S143.

Mori, N. & Takahashi, T. (2012), 'Nationwide post event survey and analysis of the 2011 tohoku earthquake tsunami', *Coastal Engineering Journal* **54**(01), 1250001.

Murashima, Y., Koshimura, S., Oka, H., Murata, Y., Fujima, K., Sugino, H. & Iwabuchi, Y. (2012), 'Numerical simulation of soliton fission in 2011 tohoku tsunami using nonlinear dispersive wave model, (in japanese with english abstract)', *Journal of Japan Society of Civil Engineers, Ser. B2 (Coastal Engineering)* **68**(2), I_206–I_210.

Nakayama, A. & Kuwahara, F. (1999), 'A macroscopic turbulence model for flow in a porous medium', *TRANSACTIONS-AMERICAN SOCIETY OF MECHANICAL ENGINEERS JOURNAL OF FLUIDS ENGINEERING* **121**, 427–433.

Nistor, I., Palermo, D., Cornett, A. & Al-Faesly, T. (2011), 'Experimental and numerical modeling of tsunami loading on structures', *Coastal Engineering Proceedings* **1**(32), 2.

Noar, N. & Greenhow, M. (2015), 'Wave impacts on structures with rectangular geometries: Part 1. seawalls', *Applied Ocean Research* **53**, 132–141.

Nouri, Y., Nistor, I., Palermo, D. & Cornett, A. (2010), 'Experimental investigation of tsunami impact on free standing structures', *Coastal Engineering Journal* **52**(01), 43–70.

Nwogu, O. (1993), 'Alternative form of boussinesq equations for nearshore wave propagation', *Journal of waterway, port, coastal, and ocean engineering* **119**(6), 618–638.

Ochoa-Tapia, J. A. & Whitaker, S. (1995), 'Momentum transfer at the boundary between a porous medium and a homogeneous fluid—i. theoretical development', *International Journal of Heat and Mass Transfer* **38**(14), 2635–2646.

Oumeraci, H. (1994), 'Review and analysis of vertical breakwater failures—lessons learned', *Coastal Engineering* **22**(1), 3–29.

Oumeraci, H. & Kortenhaus, A. (1994), 'Analysis of the dynamic response of caisson breakwaters', *Coastal Engineering* **22**(1), 159–183.

Oumeraci, H., Kortenhaus, A., Allsop, W., de Groot, M., Crouch, R., Vrijling, H. & Voortman, H. (2001), *Probabilistic design tools for vertical breakwaters*, CRC Press.

Oumeraci, H., Kortenhaus, A. & Klammer, P. (1995), Displacement of caisson breakwaters induced by breaking wave impacts, *in* 'Proceedings of the International Conference of the Institution of Civil Engineers-Advances in coastal structures and breakwaters', pp. 50–63.

Oumeraci, H., Partenscky, H., Kohlhase, S. & Klammer, P. (1992), 'Impact loading and dynamic response of caisson breakwaters', *Coastal Engineering Proceedings* **1**(23).

Patankar, S. (1990), 'Numerical heat transfert and fluid flow', *Hemisphere publishing Corporation, New york* .

Peregrine, D. (2003), 'Water-wave impact on walls', *Annual review of fluid mechanics* **35**(1), 23–43.

Peregrine, D. H. (1972), 'Equations for water waves and the approximations behind them', *Waves on beaches and resulting sediment transport* pp. 95–121.

Ramsden, J. D. (1996), 'Forces on a vertical wall due to long waves, bores, and dry-bed surges', *Journal of waterway, port, coastal, and ocean engineering* **122**(3), 134–141.

Ramsden, J. D. & Raichlen, F. (1990), 'Forces on vertical wall caused by incident bores', *Journal of Waterway, Port, Coastal, and Ocean Engineering* **116**(5), 592–613.

Raubenheimer, B., Guza, R. & Elgar, S. (1997), 'Wave transformation across the inner surf zone', *Oceanographic Literature Review* **6**(44), 538.

Ritz, J. & Caltagirone, J. (1999), 'A numerical continuous model for the hydrodynamics of fluid particle systems', *International Journal for Numerical Methods in Fluids* **30**(8), 1067–1090.

Roeber, V. & Cheung, K. F. (2012), 'Boussinesq-type model for energetic breaking waves in fringing reef environments', *Coastal Engineering* **70**, 1–20.

Roeber, V., Cheung, K. F. & Kobayashi, M. H. (2010), 'Shock-capturing boussinesq-type model for nearshore wave processes', *Coastal Engineering* **57**(4), 407–423.

Rogers, B. D., Dalrymple, R. A. & Stansby, P. K. (2010), 'Simulation of caisson breakwater movement using 2-d sph', *Journal of Hydraulic Research* **48**(S1), 135–141.

Saito, T., Inazu, D., Miyoshi, T. & Hino, R. (2014), 'Dispersion and nonlinear effects in the 2011 tohoku-oki earthquake tsunami', *Journal of Geophysical Research: Oceans* **119**(8), 5160–5180.

Scolan, Y. (2010), 'Some aspects of the flip-through phenomenon: A numerical study based on the desingularized technique', *Journal of fluids and structures* **26**(6), 918–953.

Scolan, Y. & Brosset, L. (2016), Numerical simulation of highly nonlinear sloshing in a tank due to forced motion, *in* 'The 26th International Ocean and Polar Engineering Conference', International Society of Offshore and Polar Engineers.

Shigeo Takahashi, M. T., Suzuki, K. & Shimosako, K.-i. (1999), 'Experimental and fem simulation of the dynamic response of a caisson wall against breaking wave impulsive pressures'.

Shimosako, K. & Takahashi, S. (2001), Application of expected sliding distance method for composite breakwaters design, *in* 'COASTAL ENGINEERING CONFERENCE', Vol. 2, ASCE AMERICAN SOCIETY OF CIVIL ENGINEERS, pp. 1885–1898.

Shimosako, K., Takahashi, S. & Tanimoto, K. (1994), 'Estimating the sliding distance of composite breakwaters due to wave forces inclusive of impulsive forces', *Coastal Engineering Proceedings* **1**(24).

Soares Frazao, S. & Zech, Y. (2002), 'Undular bores and secondary waves-experiments and hybrid finite-volume modelling', *Journal of hydraulic research* **40**(1), 33–43.

St-Germain, P., Nistor, I., Townsend, R. & Shibayama, T. (2013), 'Smoothed-particle hydrodynamics numerical modeling of structures impacted by tsunami bores', *Journal of Waterway, Port, Coastal, and Ocean Engineering* **140**(1), 66–81.

Suppasri, A., Koshimura, S., Imai, K., Mas, E., Gokon, H., Muhari, A. & Imamura, F. (2012), 'Damage characteristic and field survey of the 2011 great east japan tsunami in miyagi prefecture', *Coastal Engineering Journal* **54**(01), 1250005.

Synolakis, C. E. (1987), 'The runup of solitary waves', *Journal of Fluid Mechanics* **185**, 523–545.

Takahashi, S., Shimosako, K.-i., Kimura, K. & Suzuki, K. (2001), Typical failures of composite breakwaters in japan, *in* 'COASTAL ENGINEERING CONFERENCE', Vol. 2, ASCE AMERICAN SOCIETY OF CIVIL ENGINEERS, pp. 1899–1910.

Takahashi, S., Tanimoto, K. & Shimosako, K. (1992), 'Experimental study of impulsive pressures on composite breakwaters', *Report of Port and Harbour Research Institute* **31**(5), 35–74.

Takahashi, S., Tanimoto, K. & Shimosako, K. (1994), A proposal of impulsive pressure coefficient for the design of composite breakwaters, *in* 'Proc. of the International Conference of Hydro-Technical Engineering for Port and Harbour Construction', pp. 489–504.

Tissier, M., Bonneton, P., Almar, R., Castelle, B., Bonneton, N. & Nahon, A. (2011), 'Field measurements and non-linear prediction of wave celerity in the surf zone', *European Journal of Mechanics-B/Fluids* **30**(6), 635–641.

Treske, A. (1994), 'Undular bores (favre-waves) in open channels-experimental studies', *Journal of Hydraulic Research* **32**(3), 355–370.

Tsimopoulou, V. (2011), The great eastern japan earthquake and tsunami: Field observations on the coast of tohoku six month later, Technical report, Delft University of technology, Section Hydraulic Engineering.

Uezono, A., O. H. (1987), 'Planning and construction of the rubble mound for a deep water breakwater: the case of the kamaishi bay mouth breakwater.', *Chapter 4.1 of Coastal and Ocean Geotechnical Engineering. The Japanese Geotechnical Society.* .

Wang, Y.-Z., Nan-Nan, C. & Li-Hua, C. (2006), 'Numerical simulation on joint motion process of various modes of caisson breakwater under wave excitation', *International Journal for Numerical Methods in Biomedical Engineering* **22**(6), 535–545.

Ward, J. (1964), 'Turbulent flow in porous media', *Journal of the Hydraulics Division* **90**(5), 1–12.

Wei, G., Kirby, J. T., Grilli, S. T. & Subramanya, R. (1995), 'A fully nonlinear boussinesq model for surface waves. part 1. highly nonlinear unsteady waves', *Journal of Fluid Mechanics* **294**, 71–92.

Wei, Z., Dalrymple, R. A., Hérault, A., Bilotta, G., Rustico, E. & Yeh, H. (2015), 'Sph modeling of dynamic impact of tsunami bore on bridge piers', *Coastal Engineering* **104**, 26–42.

Wen, H., Ren, B., Dong, P. & Wang, Y. (2016), 'A sph numerical wave basin for modeling wave-structure interactions', *Applied Ocean Research* **59**, 366–377.

Wu, G. (2007), 'Fluid impact on a solid boundary', *Journal of fluids and structures* **23**(5), 755–765.

Zhang, S., Yue, D. K. & Tanizawa, K. (1996), 'Simulation of plunging wave impact on a vertical wall', *Journal of Fluid Mechanics* **327**, 221–254.

Zhou, D., Chan, E. & Melville, W. (1991), 'Wave impact pressures on vertical cylinders', *Applied Ocean Research* **13**(5), 220–234.